This is to certify that the

dissertation entitled

TRANSIENT SCATTERING OF ELECTROMAGNETIC WAVES
IN AN OCEAN ENVIRONMENT

presented by

ADAM J. NORMAN

has been accepted towards fulfillment
of the requirements for

PhD degree in Electrical Engineering

Dennis P. Nyquist
Major professor

Date Sept. 17, 1996

TRANSIENT SCATTERING OF ELECTROMAGNETIC WAVES IN AN OCEAN ENVIRONMENT

By

Adam J. Norman

A DISSERTATION

Submitted to
Michigan State University
in partial fulfillment of the requirements
for the degree of

DOCTOR OF PHILOSOPHY

Department of Electrical Engineering

1996

ABSTRACT

TRANSIENT SCATTERING OF ELECTROMAGNETIC WAVES IN AN OCEAN ENVIRONMENT

By

Adam J. Norman

A short pulse of an electromagnetic wave is illuminated upon a simulated ocean surface. The incident wave is then scattered resulting in complex, geometry dependent electromagnetic fields. Frequency domain techniques are employed in the solution of the scattered fields. The transient short pulse results are synthesized from the spectral returns. Numerous ocean models are considered and compared. Experimental results have also been obtained and validate the scattering theory developed. New findings regarding the physics and nature of transient scattering from ocean surfaces are reported, which could be of great interest to future researchers.

In memory of my Grandma Norman, who taught me the importance of school

ACKNOWLEDGEMENTS

I would like to acknowledge my guidance committee members. The Big 3 Dr. Chen, Dr. Nyquist, and Dr. Rothwell, whom not only taught and encouraged me, but also were my friends. I would also like to give special thanks to Jack Ross and Ponniah Ilavarasan whom went out of their way to welcome me and get me started. I would like to acknowledge all the electromagnetics graduate students for all their help and ideas.

The most important factor in the completion of this dissertation was the unceasing support of my family. My father and mother, John and Lynne, provided me with love, support and guidance throughout my studies. And, my wife Jennifer, who keeps me smiling all my days.

Table of Contents

List of Tables viii

List of Figures ix

List of Abbreviations xvii

Chapter 1 1
Introduction 1

Chapter 2 5
Experimental Measurements 5

2.1 Scattering Range Descriptions 5
2.2 Comparison and Analysis of Measurement Systems. 12
2.3 Conclusions. 22

Chapter 3 28
Transient Scattering from a Conducting Sinusoidal Surface 28

3.1 Introduction 28
3.2 TE Scattering from Conducting Sinusoidal Surface 29
3.2.1 Infinite PEC Surface 30
3.2.2 Preliminary results of TE infinite case. 40
3.2.3 TE Scattering from a finite conducting surface. 48
3.2.4 Preliminary results of TE finite case. 49
3.3 TM polarization 51
3.3.1 Infinite Surface 51
3.3.2 Preliminary results for the TM infinite case 57
3.3.3 TM finite surface scattering 63
3.3.4 Preliminary results for the TM finite case 63
3.4 Cut-off frequency phenomena 65
3.5 Results and Experimental Confirmation 67
3.5.1 Infinite surface results 67
3.5.2 Finite surface results 84
3.6 Conclusions 88

Chapter 4 97
Transient Scattering from an Imperfectly Conducting Sinusoidal Surface . 97

4.1 Introduction 97
4.2 Floquet-Mode Matching Analysis 98
4.3 Integral Equation Formulation 106
4.3.1 Moment-Method Numerical Solution 110
4.3.2 Scattered fields 112
4.4 Duality of TE and TM polarizations 113
4.5 Numerical Examples 114
4.6 Experimental Results 137
4.7 Conclusions 141

Chapter 5 152
Transient Scattering from Non-Sinusoidal Surfaces 152

5.1 Introduction 152
5.2 Extensions to theory to accommodate non-sinusoidal surface. . . . 153
5.2.1 Floquet mode-matching/Rayleigh Hypothesis 153
5.2.2 Integral Equation Formulation 155
5.3 Non-sinusoidal sea-surface models 157
5.4 Preliminary numerical results 158
5.5 Scattering from PEC surfaces for TM excitation 169
5.5.1 Experimental Results for TM Excitation 169
5.5.1a TM Measurements performed in time domain 185
5.5.2 Theoretical Response for TM Excitation 191
5.5.3 Comparison/Evaluation of TM results 194
5.6 Scattering from PEC surfaces for TE excitation 199
5.6.1 Experimental Results for TE Excitation. 199
5.6.1a Measurements performed in time domain 208
5.6.2 Theoretical Results for TE Excitation 212
5.6.3 Comparison/Evaluation of TE results. 221
5.7. Conclusions 226

Chapter 6 227
Transient Scattering of a Beam from Infinite Periodic Surfaces 227

6.1 Introduction 227
6.2 Application of Scattering Theory 228
6.3 Beam Synthesis Techniques 229
6.3.1 Examples of Gaussian Beam. 233
6.4 Transient Scattering Results. 236
6.5 Conclusions 238

Chapter 7 250
Transient Scattering from a Three Layer Medium 250

7.1 Introduction 250
7.2 Floquet mode-matching/Rayleigh hypothesis. 251
7.3 PGF IE Technique 255
7.5 Numerical Results 259
7.6 Conclusions 264

Chapter 8 265
Conclusions and Future Study 265

8.1 Summary 265
8.2 Major contributions and findings. 266
8.3 Future research 267

Appendix A 269
Periodic Green's Function Derivation 269

Appendix B 272
Sea Surface Realizations 272

Appendix C 275
Extinction theorem integral equation formulation 275

Bibliography 278

List of Tables

Table 3.1 Low frequency cutoff and maximal frequency of backward Floquet modes. L=0.1016m, 85° incidence angle. 66

Table 3.2 Low frequency cutoff and maximal frequency of backward Floquet modes. L=0.1016m, 67° incidence angle. 66

List of Figures

Figure 1.1 Scattering terms in an ocean environment. 4

Figure 1.2 Qualitative plot of target detection capabilities in the ocean environment. 4

Figure 2.1 Configuration of the ground-plane time-domain measurement system at MSU. 9

Figure 2.2 Configuration of the anechoic chamber measurement system at MSU. 10

Figure 2.3 Configuration of the free-field arch-range scattering system at MSU. 11

Figure 2.4 Spectrum of an ideal baseband incident short pulse with 3 GHz bandwidth. 15

Figure 2.5 Ideal baseband incident short pulses with 3 GHz bandwidth. 16

Figure 2.6 Spectrum and transient nature of ideal incident short pulse with 8 GHz bandwidth. 17

Figure 2.7 Spectrum and transient nature of ideal incident short pulses with 16 GHz bandwidth. 18

Figure 2.8 Block diagram model of measurement system. 23

Figure 2.9 Graphical representation of the calibration procedure. 24

Figure 2.10 Transient backscattered field from 6 inch sphere (background subtracted). 25

Figure 2.11 Transient backscattered field from a 6 inch sphere. 25

Figure 2.12 Spectrum of backscattered field from a 6 inch sphere. 26

Figure 2.13 Transient backscattered field from a 1:72 scale B52 airplane. . . . 27

Figure 3.1 Infinite, conducting sinusoidal surface scattering geometry. 35

Figure 3.2 Graphical representation of Floquet-mode scattered waves. 35

Figure 3.3 Partitioning scheme for MoM numerical solution. 39

Figure 3.4 Modal amplitudes for a mode-matching solution using differing numbers of terms. 42

Figure 3.5 Induced surface current on one period of infinite, conducting sinusoidal surface for TE and TM excitation at 4 GHz. 43

Figure 3.6 Dependence of currents induced on a PEC sinusoid for TE excitation for various incidence angles. 44

Figure 3.7 Dependence of currents induced on a PEC sinusoid for TE excitation for various surface heights. 45

Figure 3.8 Dependence of currents induced on a PEC sinusoid for TE excitation for various surface period lengths (L). 46

Figure 3.9 Dependence of currents induced on a PEC sinusoid for various TE excitation frequencies. 47

Figure 3.10 Finite, conducting sinusoidal surface scattering geometry. 48

Figure 3.11 Comparison of induced surface currents on finite and infinite surfaces for TE excitation. 50

Figure 3.12 Dependence of currents induced on a PEC sinusoid for TM excitation for various incidence angles. 59

Figure 3.13 Dependence of currents induced on a PEC sinusoid for TM excitation for various surface heights. 60

Figure 3.14 Dependence of currents induced on a PEC sinusoid for TM excitation for various surface period lengths (L). 61

Figure 3.15 Dependence of currents induced on a PEC sinusoid for various TM excitation frequencies. 62

Figure 3.16 Comparison of induced surface currents on finite and infinite surfaces for TM excitation. 64

Figure 3.17 Magnitude of total scattered electric field from infinite, conducting sinusoidal surface as a function of frequency for TE excitation. . . 71

Figure 3.18 Magnitude of backscattered electric field from infinite, conducting sinusoidal surface for TE excitation as a function of frequency. . . 72

Figure 3.19 Synthesized pulses used for interrogation of conducting sinusoidal surfaces. 73

Figure 3.20 Total scattered electric field created by a GMC pulse from infinite, conducting sinusoidal surface for TE excitation. 74

Figure 3.21 Comparison of transient total scattered electric fields created by a GMC pulse for various incidence angles upon an infinite sinusoidal surface for TE excitation. 75

Figure 3.22 Transient backscattered electric field created by a 1/8 cosine pulse from infinite, conducting sinusoidal surface for TE excitation. . . 76

Figure 3.23 Comparison of transient backscattered electric fields created by a short pulse of various incidence angles upon an infinite sinusoidal surface for TE excitation. 77

Figure 3.24 Comparison of transient backscaterred electric fields created by a short pulse from various height infinite sinusoidal surfaces for TE excitation. 78

Figure 3.25 Comparison of transient backscattered electric fields created by a short TE pulse from infinite sinusoidal surfaces of differing periods. 79

Figure 3.26 Total scattered magnetic field for TM excitation of a PEC sinusoid. 80

Figure 3.27 Total scattered magnetic field created by a GMC pulse from infinite, conducting sinusoidal surface for TM excitation. 81

Figure 3.28 Backscattered magnetic field for TM excitation of a PEC sinusoid. 82

Figure 3.29 Transient backscattered magnetic field created by a 1/8 cosine pulse from infinite, conducting sinusoidal surface for TM excitation. 83

Figure 3.30 Construction of sinusoidal sea-surface model. 84

Figure 3.31 Experimental measurements of a PEC sinusoid with TE excitation. The measured spectral response and the synthesized transient returns are shown for numerous incidence angles. 86

Figure 3.32 Spectral amplitudes of theoretical and experimental backscattered electric fields from a finite surface for TE excitation. 89

Figure 3.33 Theoretical and experimental transient backscattered electric fields created by a short pulse from a finite surface for TE excitation. . 90

Figure 3.34 Comparison of experimental backscatter (finite surface) results to theoretical backscatter from an infinite surface for TE excitation. 91

Figure 3.35 Comparison of transient backscatter created by a short pulse from an infinite surface (theoretical) and a finite surface (experimental) for TE excitation. 92

Figure 3.36 Comparison of transient backscattered electric field created by a short pulse from an infinite and finite surface for TE excitation. . 93

Figure 3.37 Comparison of spectral domain backscattered magnetic field from an infinite surface (theory) and a finite surface (experiment) for TM excitation. 94

Figure 3.38 Comparison of transient backscattered magnetic field created by a short pulse from an infinite surface (theory) and a finite surface (experiment) for TM excitation. 95

Figure 3.39 Theoretical transient backscattered magnetic field created by a short pulse from an infinite surface and a finite surface for TM excitation. 96

Figure 4.1 Geometry for two media scattering problem. 98

Figure 4.2 Surface field calculations using Rayleigh-mode-matching method compared to MFIE PGF method for various h/L ratios. 119

Figure 4.3 Surface H-fields on an infinite sea-water sinusoid for a TM incident plane wave. Excitation frequency dependence is shown. . 120

Figure 4.4 Surface H-fields on an infinite sea-water sinusoid due to TM excitation at 2 GHz. The dependence on sinusoid interface amplitude (h) is examined. 121

Figure 4.5 Surface H-fields on smaller height sea-water sinusoids. 121

Figure 4.6 Surface H-fields on an infinite sinusoid for TM excitation at 2 GHz. The dependence on incidence angle is examined. 122

Figure 4.7 Surface H-fields on an infinite sea-water sinusoid due to TM excitation at 2 GHz. The dependence on sea-surface period is shown. 123

Figure 4.8 Surface H-fields on an infinite sinusoid due to TM excitation at 2 GHz. The effects of conductivity are shown. 124

Figure 4.9 Surface H-fields on a infinite sinusoid excited by a 6 GHz TM wave. The effects of conductivity are shown. 125

Figure 4.10 Identification of a Brewster angle for TM incidence. Comparison with TE excitation is shown. 126

Figure 4.11 Identification of Brewster's angle for lossless dielectric (ϵ=80,σ=0) surface. 127

Figure 4.12 Identification of Brewster angle for lossy dielectric surface (ϵ=80,σ=4) for various h/L. 128

Figure 4.13 Identification of a Brewster angle for TM incidence. The effects of excitation frequency are shown. 129

Figure 4.14 Identification of a Brewster angle for TM incidence. The effects of sea-water sinusoid amplitude are examined. 130

Figure 4.15 The backscattered H-field around the Brewster angle for TM incidence. 130

Figure 4.16 Backscattered H-field from an infinite sea-water sinusoid. The effects of field point location are examined. 131

Figure 4.17 Backscattered H-field from an infinite sea-water sinusoid. The effects of field point location are examined. 132

Figure 4.18 Forward scattered H-field from an infinite sea-water sinusoid. The effects of field point location are examined. 133

Figure 4.19 Forward scattered H-field from an infinite sea-water sinusoid. The effects of field point location are examined. 134

Figure 4.20 Comparison of Rayleigh and MFIE-PGF method for computing total scattered field spectrum from imperfectly conducting surface. 135

Figure 4.21 Transient TM response of imperfectly conducting sinusoidal surface. 135

Figure 4.22 Comparison of Rayleigh and MFIE PGF methods for computing backscattered field spectrum for imperfectly conducting surface. . 136

Figure 4.23 Backscattered transient response of imperfectly conducting surface. 136

Figure 4.24 Configuration of sea-water sinusoid for experimental measurements. 137

Figure 4.25 Theoretical backscattered H-field from an infinite sinusoid. Comparison of PEC and sea-water models for TM excitation at 60°. 142

Figure 4.26 Theoretical backscattered E-field from an infinite sinusoid. Comparison of PEC and sea-water models for TE excitation at 60°. 143

Figure 4.27 Theoretical backscattered H-field from an infinite sinusoid. Comparison of PEC and sea-water models for TM excitation at 85°. 144

Figure 4.28 Theoretical backscattered E-field from an infinite sinusoid. Comparison of PEC and sea-water models for TE excitation at 85°. 145

Figure 4.29 Theoretical transient backscatter for TM excitation. 146

Figure 4.30 Experimentally measured transient backscatter for TM excitation. 146

Figure 4.31 Theoretical transient backscatter for TE excitation. 147

Figure 4.32 Experimentally measured transient backscatter for TE excitation. . 147

Figure 4.33 Theoretical time-gated backscatter for TM excitation. 148

Figure 4.34 Experimentally measured backscatter for TM excitation. 148

Figure 4.35 Theoretical time-gated backscatter for TE excitation. 149

Figure 4.36 Experimentally measured backscatter for TE excitation. 149

Figure 4.37 Comparison of theoretical and measured TM backscatter from a sea-water sinusoid. 150

Figure 4.38 Experimentally measured forward scatter from a finite sea-water sinusoid. Both transient and spectral results are shown of a number of incidence angles. 151

Figure 5.1 Partition scheme for sea-surface interface. 154

Figure 5.2 Comparison of sea-surface models. 160

Figure 5.3 Surface current on PEC double sinusoid with increasing ripple height. 161

Figure 5.4 Surface current induced on the Stokes wave model for a TE incident plane wave at 85° with frequency of 2 GHz. 162

Figure 5.5 Surface current induced on the double sinusoid wave model for a TE incident plane wave at 85° with frequency of 2 GHz. 163

Figure 5.6 Comparison of induce surface currents on the Stokes and double sinusoid wave models. 164

Figure 5.7 Spectrum of backscatter for TE incident wave at 85°, L=.3m at field point x/L=0, z/L=20 165

Figure 5.8 Spectrum of backscatter for TE incident wave at 85°, L=.3m at field point x/L=0, z/L=20 166

Figure 5.9 Transient backscatter from PEC surface with TE incident wave at 85°, L=0.3m, x/L=0, z/L=20 167

Figure 5.10 Transient backscatter from PEC surface with TE incident wave at 85°, L=0.3m, x/L=0, z/L=20 168

Figure 5.11 Angular dependence of TM scattered fields of the Stokes wave model. 174

Figure 5.12 Angular dependence of TM scattered fields of the double sinusoid wave model. 175

Figure 5.13 Angular dependence of TM scattered fields of the Donelan Pierson wave model. 176

Figure 5.14 Angular dependence of TM scattered fields of the Donelan Pierson wave model. 177

Figure 5.15 Experimental TM scattering from various wave models for an incidence angle of 70°. 178

Figure 5.16 Experimental TM transient scattering from various wave models for an incidence angle of 70°. Synthesized with a 1/8 cosine taper. 179

Figure 5.17 TM backscattered fields from the Stokes wave model. Experimentally measured response at 60° and 80°. 180

Figure 5.18 TM backscattered fields from the double sinusoid wave model. Experimentally measured response at 60° and 80°. 181

Figure 5.19 TM synthesized transient backscattered fields from the Stokes wave model. Experimentally measured response at 60° and 80°. Spectral returns were weighted with 1/8 cosine taper before IFFT. 182

Figure 5.20 TM synthesized transient backscattered fields from the double sinusoid wave model. Experimentally measured response at 60° and 80°. Spectral returns were weighted with 1/8 cosine taper before IFFT. 183

Figure 5.21 TM synthesized transient backscattered fields from the Donelan Pierson wave model. Experimentally measured response at 60° and 80°. Spectral returns were weighted with 1/8 cosine taper before IFFT. 184

Figure 5.22 Transient TM backscatter response for the Stokes wave model. A comparison of frequency-domain synthesis and time-domain techniques. 186

Figure 5.23 Transient TM backscatter response for the double sinusoid wave model. A comparison of frequency-domain synthesis technique and time-domain technique. 187

Figure 5.24 Transient TM backscatter response for the Donelan Pierson wave model. A comparison of frequency-domain synthesis technique and time-domain technique. 188

Figure 5.25 Spectrum of TM backscatter response for the Stokes wave model. A comparison of frequency-domain synthesis technique and time-domain technique. 189

Figure 5.26 Spectra of TM backscatter response for the Stokes and double sinusoid wave models. Measurements were performed using the time-domain technique. 190

Figure 5.27 TM backscattered magnetic field for the Stokes wave model. Comparison theoretical responses for 60° and 85° incidence. 192

Figure 5.28 Synthesized transient TM backscattered magnetic field for Stokes wave. 192

Figure 5.29 TM backscattered magnetic field for the double sinusoid wave model. Comparison theoretical responses for 60° and 85° incidence. 193

Figure 5.30 Synthesized transient TM backscattered magnetic field for double sinusoid. 193

Figure 5.31 TM backscattered magnetic field for the Stokes wave model. Comparison of theoretical and measured responses for 60° incidence. 195

Figure 5.32 Synthesized transient TM backscattered magnetic field for the Stokes wave model. Comparison of theoretical and measured responses for 60° incidence. 196

Figure 5.33 TM backscattered magnetic field for the double sinusoid wave model. Comparison of theoretical and measured responses for 60° incidence. 197

Figure 5.34 Synthesized transient TM backscattered magnetic field for the double sinusoid wave model. Comparison of theoretical and measured responses for 60° incidence. 198

Figure 5.35 Angular dependence of TE scattered fields of the Stokes wave model. 201

Figure 5.36 Angular dependence of TE scattered field spectrum of the double-sinusoid wave model. 202

Figure 5.37 Angular dependence of TE scattered fields of the Donelan Pierson wave model. 203

Figure 5.38 Angular dependence of TE scattered fields of the Donelan Pierson wave model. 204

Figure 5.39 Comparison of synthesized transient scattering from the Stokes wave and double sinusoid wave for near grazing incidence angles. 205

Figure 5.40 Experimental TE scattering from various wave models for an incidence angle of 70°. 206

Figure 5.41 Experimental synthesized transient TE scattering from various wave models for an incidence angle of 70°. GMC weighting applied to spectrum before IFFT. 207

Figure 5.42 Comparison of frequency-domain synthesis measurement with time- domain measurement. Both spectral and transient returns for Stokes Wave interrogated at 60°. 209

Figure 5.43 Spectra of TE backscatter response for the Stokes and double sinusoid wave models. Measurements were performed using the frequency-domain technique. 210

Figure 5.44 Transient TE backscatter response for the double-sinusoid wave model. A comparison of frequency-domain synthesis the time-domain techniques. 211

Figure 5.45 Theoretical synthesized transient TE backscattered fields from the Stokes wave model. The response at 85° incidence for two field points is shown. 213

Figure 5.46 Theoretical synthesized transient TE backscattered fields from the Stokes wave model. The response at 60° incidence for two field points is shown. 214

Figure 5.47 Theoretical synthesized transient TE backscattered fields from the double- sinusoid wave model. The response at 85° incidence for two field points is shown. 215

Figure 5.48 Theoretical synthesized transient TE backscattered fields from the double- sinusoid wave model. The response at 60° incidence for two field points is shown. 216

Figure 5.49 Theoretical transient scattering from double-sinusoid wave at 85°, with the effect of GMC window width examined. 217

Figure 5.50 Theoretical transient scattering from double-sinusoid wave at 85°, with the effect of GMC window center frequency examined. . . . 218

Figure 5.51 Theoretical transient scattering from Stokes wave at 85°, with the effect of GMC window width examined. 219

Figure 5.52 Theoretical transient scattering from Stokes wave at 85°, with the effect of GMC window center frequency examined. 220

Figure 5.53 Comparison of synthesized transient scattering from Stokes wave with theoretical transient scattering at 60°. Using 0.8-7.2 GHz GMC windowed spectral content. 222

Figure 5.54 Comparison of TE scattering from Stokes wave with theoretical scattering at 60°. 223

Figure 5.55 Comparison of theoretical and measured transient scattering from the double-sinusoid wave. Angle of incidence is 60°. 224

Figure 5.56 Comparison of theoretical and measured scattering from the Donelan Pierson wave. Angle of incidence is 60°. 225

Figure 6.1 Geometry of Beam Synthesis Apertures. 229

Figure 6.2 Beam synthesis and scattering geometry. 231

Figure 6.3 Spectral Amplitudes for a Gaussian Incident Beam Parameters are L=5.0m and w =.5m. 234

Figure 6.4 Gaussian Incident beam created from 21 terms of the Fourier Series, where L=5.0 m, w=.5 m, and θ =70° 235

Figure 6.5 Induced Surface currents on PEC surface, for 30° Gaussian beam illumination. 240

Figure 6.6 Induced surface currents on PEC surface for 70° beam illumination. 240

Figure 6.7 Induced surface currents on PEC surface for 30° beam illumination. 241

Figure 6.8 Induced surface currents on PEC surface for 70° beam illumination. 241

Figure 6.9 Frequency response of backscatter from a PEC surface for a single plane wave. 242

Figure 6.10 Transient backscatter from a PEC surface for single plane wave pulse illumination. 243

Figure 6.11 Transient backscatter for single plane wave incident. 244

Figure 6.12 Spectrum of backscattered field for an incident Gaussian beam (θ=30°) 245

Figure 6.13 Frequency response of backscattered field for an incident Gaussian beam (L=5.0m, w=0.5m, n=21 θ=70°) 245

Figure 6.14 Transient backscattered field for an incident Gaussian beam pulse (θ=30°). 246

Figure 6.15 Transient backscattered field for an incident Gaussian beam pulse (θ=70°). 246

Figure 6.16 Transient backscattered field for an incident Gaussian beam pulse (L=5.0m, w=0.5m, θ=30°) 247

Figure 6.17 Synthesized transient backscatter response for Gaussian beam pulse incident at 30° and 70°. (Beam parameters: n=21, w=.5m, L=5m Surface parameters : P=0.1m, h=0.007m, PEC sinusoid) 248

Figure 6.18 Synthesized transient total scatter response for Gaussian beam pulse incident at 30°. (Beam parameters : n=21, w=.5m, L=5m) (Surface parameters : P=0.1m, h=0.007m, PEC sinusoid) 249

Figure 7.1 Configuration of three medium scattering problem. 251

Figure 7.2 Comparison of induced surface fields for TM excitation of three layered medium where the upper layer has a sinusoidal interface (PGF IE). 260

Figure 7.3 Frequency response of backscattered fields for a TM plane wave incident upon a three layer medium. 261

Figure 7.4 Transient backscattered fields from a three layer medium where the upper interface is sinusoidal. 262

Figure 7.5 Transient total scattered field inside the middle layer of a three layer medium where the upper layer has a sinusoidal interface. . . 263

Figure B.1 The Donelan Pierson spectrum of wind driven waves for various wind speeds. 274

Figure C.1 Generic configuration of a 2-D two-region problem. 277

List of Abbreviations

UWB	Ultra Wide-band
SP	Short Pulse
CW	Continuous Wave
FMM	Floquet Mode Matching
PGF	Periodic Green's Function
IE	Integral Equation
MoM	Method of Moments
EFIE	Electric Field Integral Equation
MFIE	Magnetic Field Integral Equation
BS	Backscatter
TS	Total Scatter
FFT	Fast Fourier Transform
IFFT	Inverse Fast Fourier Transform
GMC	Gaussian Modulated Cosine

Chapter 1
Introduction

The radar detection and identification of targets in the ocean environment is a venerable subject. The large and unpredictable (over time) clutter produced by the ocean has limited the usefulness of conventional, narrow band (CW) radars [1-7], thereby allowing targets (missiles, planes) to pass through radar coverage undetected. New hope has arisen with the advent of feasible ultra-wideband/short-pulse (UWB/SP) radar systems [8,9]. UWB/SP radar provides a much higher range resolution or target feature resolution and may reduce the multipath effect. There is also hope that UWB/SP radar may have the ability to not only determine a target's speed and location, but also identify the target's shape and size. The greater spectral content allows for entirely new identification and detection schemes, including the use of time-frequency analysis.

A shipboard radar system, as shown in Figure 1.1, has to contend with a number of scattering mechanisms [10,11]. The target response will be masked by clutter (or backscatter) and could also be deteriorated by multipath scattering. The clutter term will be most detrimental when the ocean is roughest. This is due to the large slopes occurring on the ocean waves. The multipath effect is prominent for smooth ocean surfaces. A qualitative plot of the problem facing radar target detection in the ocean environment is shown in Figure 1.2. These are the problems associated with conventional CW type radar used in detection. The ability of the UWB/SP radar to overcome these drawbacks will be discussed throughout the following chapters.

Although the clutter description for CW type excitation in an ocean environment has been studied by a great many researchers [1-7,12-36], the clutter descriptions for UWB/SP have never been examined. This thesis will provide theoretical and

experimental descriptions of UWB/SP scattering responses in an ocean environment. These basic building blocks will allow future workers to fully exploit the UWB/SP radar systems for target identification and detection.

The thesis will be broken up into chapters that logically develop the UWB/SP description of clutter in an ocean environment. Both the ocean models and interrogating wave shape will be methodically evolved from simple (ideal) cases to complex (real-world) models. The initial ocean simulation that will be considered in chapter 3, is the perfectly electric conducting (PEC) sinusoidal surface illuminated by a plane wave. Both a finite and an infinite interface will be considered. A frequency-domain integral-equation formulation is utilized, and is subsequently implemented numerically via the Method of Moments (MoM). The transient scattered fields are obtained through the use of an Inverse Fast Fourier Transform (IFFT). The infinite sinusoidal surface can also be treated more classically by a mode-matching technique in conjunction with the Rayleigh hypothesis. The important feature of the solutions is that there are no approximations made, such as the Kirchoff approximation (physical optics). This rigor is needed to fully include all the physical effects that could arise. It is this complete understanding of the underlying physics of the problem that could open new avenues for target detection and identification.

In chapter 4, the ocean surface model will be improved, and will be modelled as a two-layer (non-PEC) system. The two layers will be air and sea (ϵ_r=80, σ=4 S/m) separated by a sinusoidal interface. This model relies on a similar frequency-domain integral-equation formulation, which is also quite rigorous. The mode-matching technique is also extended to the two-layer model. The effects of an imperfectly conducting layer will be examined and compared to the PEC case. The possibility of a Brewster's angle phenomenon is also investigated and its implications are discussed.

The interface will then, in chapter 5, be allowed to have any (non-sinusoidal) shape, but it must remain periodic for the infinite-surface case. The non-sinusoidal

surfaces will be constructed to more accurately depict real ocean waves. The analytical techniques developed in the previous chapters are well equipped to handle the non-sinusoidal surface. The enhanced range resolution of the UWB/SP transient radar is fully utilized with the finer structure of the non-sinusoidal waves.

The ideal incident plane wave restriction is removed in chapter 6, when a limited-footprint beam wave is assumed incident. For the infinite surfaces this beam is constructed from the superposition of a finite number of plane waves; therefore the scattering theory developed in the prior chapters will still hold. Beam excitation is an important step in modelling a realistic radar system.

In chapter 7, the ocean model is once again improved with the addition of a third layer, this layer could represent the ocean floor, a large submerged object, or a ducting (guiding) region above the ocean surface. The additional layer is considered to be planar, which minimizes the numerical complexity for a three layer structure.

In the chapters described above, experimental results will accompany many of the theoretical findings. This will serve to validate both the theoretical and experimental techniques that are developed. To facilitate these discussions on the experimental results, a preliminary chapter is needed to introduce the measurement techniques and processing methods used throughout the thesis. Chapter 2 will serve as this preliminary chapter.

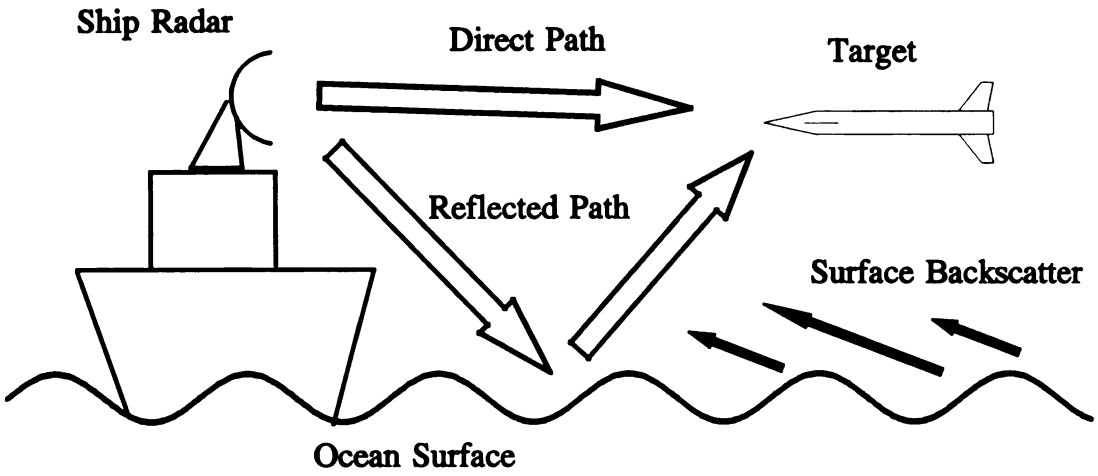

Figure 1.1 Scattering terms in an ocean environment.

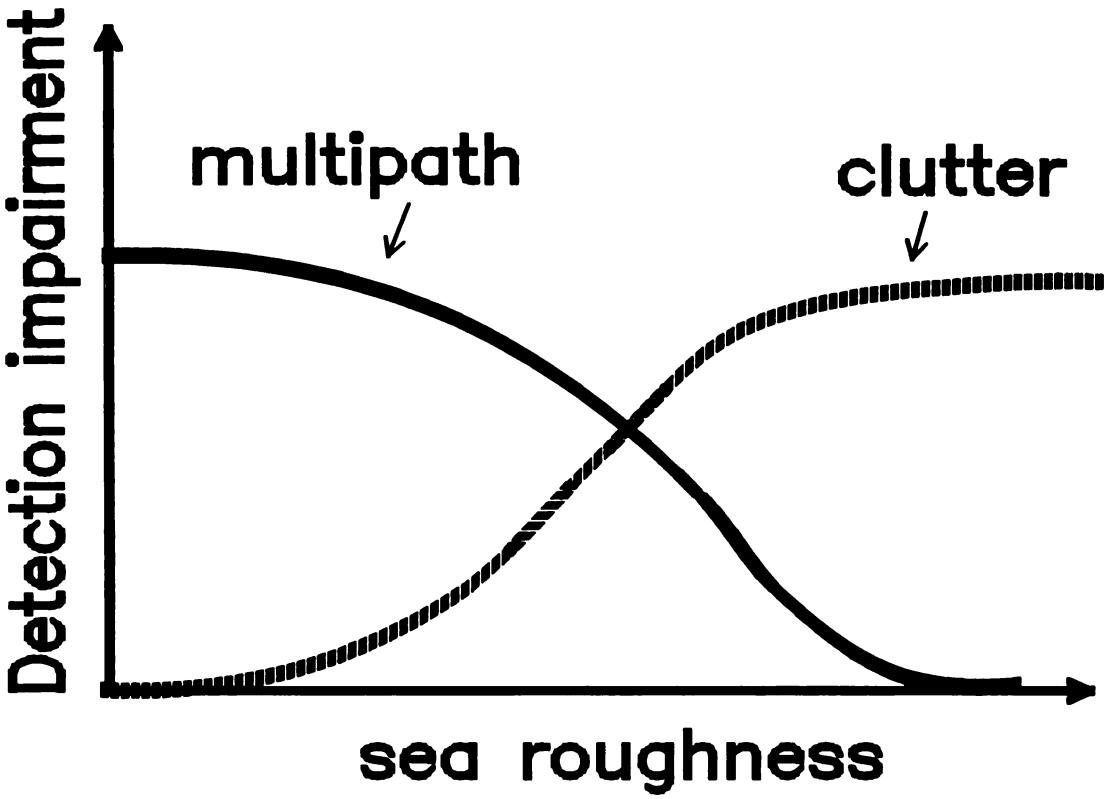

Figure 1.2 Qualitative plot of target detection capabilities in the ocean environment.

Chapter 2
Experimental Measurements

In this chapter the techniques employed in measuring the transient scattered fields from ocean surface models will be examined. In-depth discussions of specific results will be found throughout the thesis as the scattering theory is developed. This chapter will expound on the technical aspects of performing such measurements.

There are three scattering measurement ranges located at MSU from which transient results can be obtained. There are two free-field ranges (Arch Range and Anechoic Chamber) which operate on the same basic principles, that is frequency-domain synthesis [37-39]. There is also a large ground plane on which true base-band time-domain measurements are performed. The arch range and the anechoic chamber may also be used in performing true transient measurements, but the transmitting and receiving horns are not optimal for such measurements. The operating principles of each range will be explained and sample measurements will be performed on the systems for comparison purposes and to illuminate the explanations.

2.1 Scattering Range Descriptions

Historically transient measurements were performed solely in the time domain, that is a pulse (or step) generator creates a train of pulses which is radiated by some antenna, and is then received by another (or the same) antenna and measured by a sampling oscilloscope. At Michigan State the experimental setup is as in Figure 2.1, of note is the large ground plane which serves to reduce the physical size (imaging) of the range and as shield for the feeding and receiving lines and connectors. A Picosecond Pulse Labs (PPL 1000B) pulse generator creates the incident pulse and is radiated by a

8 foot Bi-Conical Antenna with a 16° apex angle. This type of complementary antenna was chosen for its frequency independence, which is required for short pulse transmission and ease of calibration. The receiving antenna is a short probe monopole, which acts a differentiator [40], therefore a step incident wavefront would result in a pulse response from the probe. A Tektronix 7854 Sampling oscilloscope is used to measure the return signal, and is connected via HPIB to a PC. This data acquisition system allows for post processing of the measured results.

The current system is currently limited to roughly a 1/2 nanosecond pulse, which corresponds to a 2 Ghz wide baseband radar. This restriction is caused by the PPL generator, which can only produce 2 GHz of bandwidth. However, the system does produce high quality results over the operating bandwidth. The system is also an excellent instructional tool due to the immediate results obtained and intuitive nature of the time-domain reflected waves.

Due to the geometry of the ground plane and bi-conical antenna length, the effective measurement time window of the system is roughly 12 nanoseconds. This implies that the target must be sufficiently physically small and placed in close proximity to the probe. The measurements that are performed later in the dissertation do not lend themselves well to the ground plane system, therefore little emphasis will be placed on it and the above discussion is only included for completeness.

The pulse generator and sampling oscilloscope can also be utilized in the anechoic chamber to perform true short-pulse time-domain measurements. The transmitting and receiving antennas are American Electronic Laboratories (AEL) model H-1734 TEM wideband (0.5-6.0 GHz) horns. These antennas have non-ideal transfer functions that reduce the fidelity of the measurement system. The anechoic chamber setup does, however, lend itself well to the measurements to be performed later in the dissertation, and therefore will be used as the primary comparison tool in this thesis. The non-ideal characteristics of the horns must be compensated for through calibration and spectral

weighting. The short-pulse time-domain method in the anechoic chamber has roughly a 10 ns quiet zone (similar to ground-plane system), and this limits the physical size of the scatterer.

In order to overcome the bandwidth limitations of the time-domain systems mentioned above, a frequency-domain synthesis technique was developed [37,38]. This development was aided by the advancement of highly-stable large-bandwidth CW signal sources and similar amplifiers and detectors. The basic idea behind the frequency-domain synthesis technique is to repeatedly measure the target (stationary) response at a large number of frequencies. These frequencies should be chosen and weighted to simulate a short pulse when synthesized to the time-domain using the inverse fast-Fourier transform (IFFT). Therefore an IFFT performed on the measured return signal should accurately describe the time-domain pulse response.

The principles and techniques behind performing these transient measurements (synthesized) in an anechoic chamber are well established [37]. MSU's anechoic chamber (See Figure 2.2) is 12' x 12' x 24' and is lined with pyramidal absorbers having a pyramid depth of 6 inches. The frequency-domain measurements are performed using a HP 8720B automatic network analyser (ANA) with a HP 8349B Amplifier, which has a gain of 20 dB over a bandwidth of 2-20 GHz, connected between the ANA and the transmitting antenna. Because of the wide bandwidth of needed measurements, a true monostatic system is not feasible due to the large reflection at the transmit horn antenna. Therefore a bi-static system consisting of two closely spaced AEL H-1734 pyramidal horn antennas is used to simulate a monostatic system. The backscattered field is then proportional to the S_{21} scattering-parameter measurement obtained with the network analyser.

The general idea behind the measurement system is to measure the response of an unknown target (ocean surface model) followed by a similar measurement for a known target or calibrator (sphere). From the information obtained with the known target, any

effects due to the system response can be eliminated from the unknown target measurement. The latter results are then taken to the time domain via an IFFT, yielding the transient backscattered response due to a plane-wave incident pulse. A quantitative analysis of this measurement technique can also be performed the details of which appear in [37]. The procedure is summarized on p.19 where a sample measurement is performed and analyzed.

The arch range (See Figure 2.3) is a large (20 ft diameter) horn-supporting structure, which allows the horn-antennas to be arbitrarily located by rotation about its periphery. The measurements are very similar to those of the anechoic chamber, in that this is also a frequency domain system which utilizes the HP 8720B in the S_{21} mode. Once again, due to the large bandwidth, a bi-static horn system is used to simulate a mono-static radar. However, the arch range also offers the advantage of providing for true bi-static measurements (large horn separation) with precise horn locations. However, the lack of absorbers introduces many difficulties, associated with undesired reflected waves, which aren't present in the anechoic chamber. These difficulties include both the unwanted reflections from the surrounding environment and the interaction of target with that environment. These interactions limit the size and placement of the target. To minimize the interaction of the horns with the supporting structure and floor, dielectric lenses are used to collimate the transmitted wave. Additionally, after much experimentation, pyramidal absorbers where placed in the most problematic regions, including the floor in front of the target and wall behind the target.

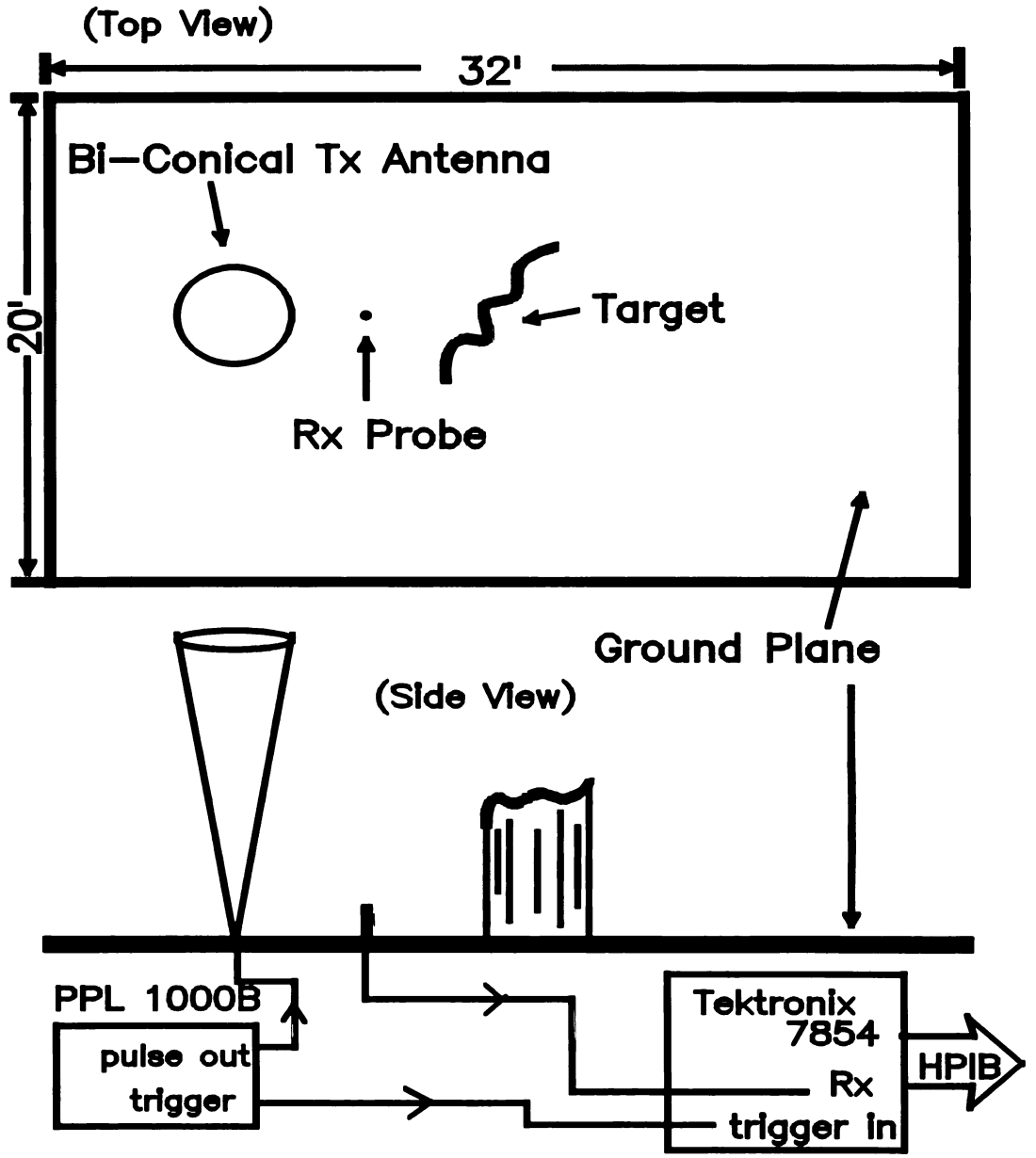

Figure 2.1 Configuration of the ground-plane time-domain measurement system at MSU.

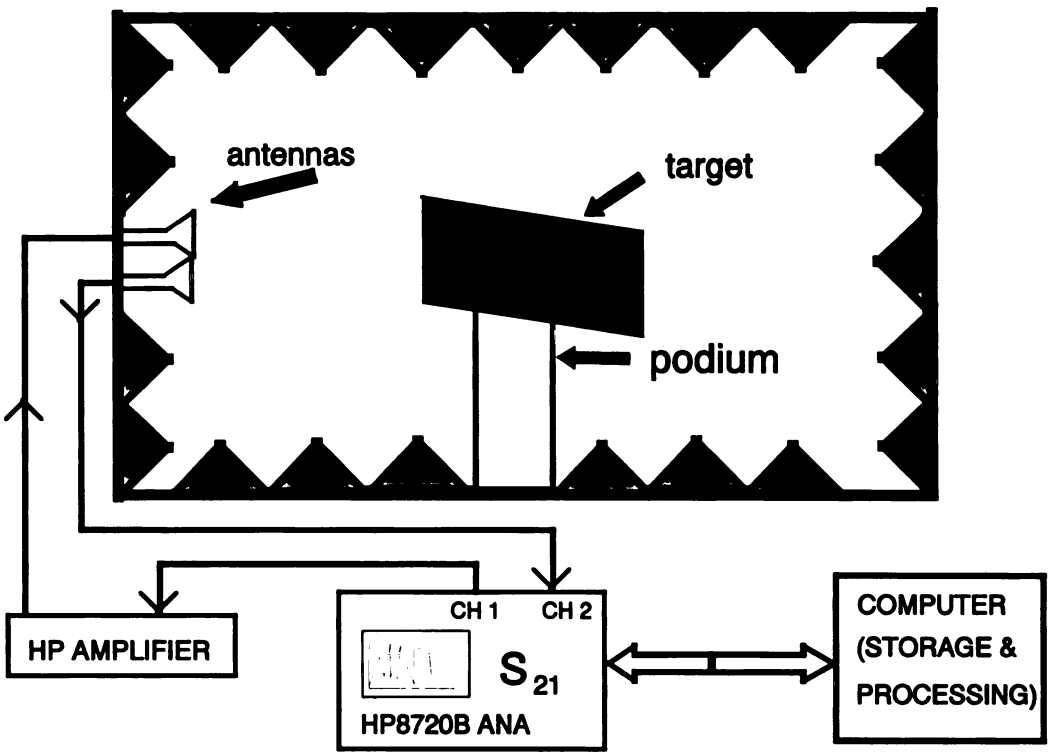

Figure 2.2 Configuration of the anechoic chamber measurement system at MSU.

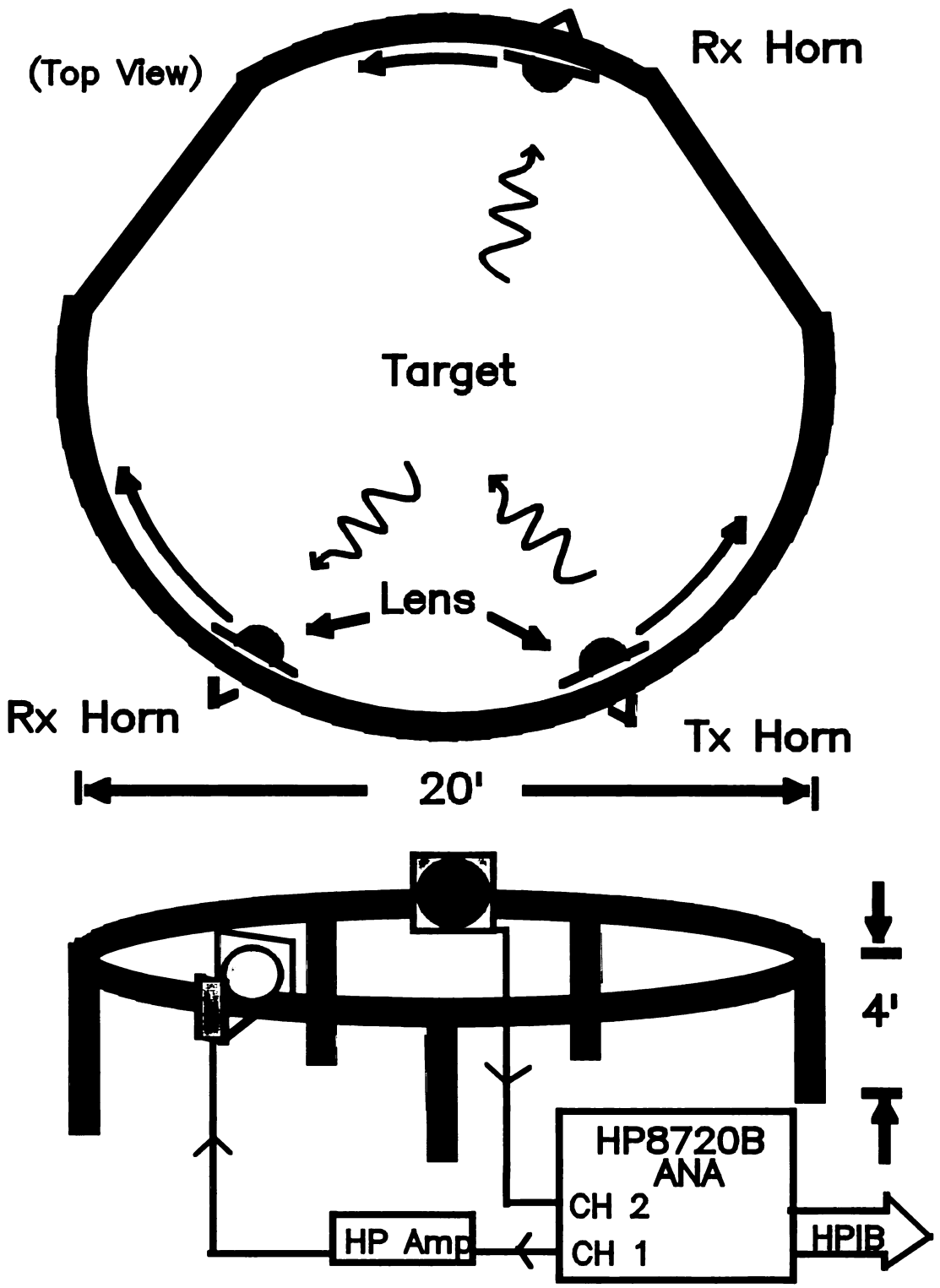

Figure 2.3 Configuration of the free-field arch-range scattering system at MSU.

2.2 Comparison and Analysis of Measurement Systems.

As a general statement regarding the performance of the three measurement systems, the anechoic chamber (frequency domain) yields the highest quality, largest bandwidth results. Therefore, most of the results in the following chapters are obtained via the anechoic chamber. There are number of cases in which the arch range is the system of choice, such as measuring forward scattered fields or any bi-static measurement. The time-domain systems provide primarily a confirmation of the frequency-domain synthesis measurement responses.

The frequency domain synthesis technique, although somewhat paradoxical in that a number of sinusoidal steady-state measurements can yield a transient result, is important to understand in a practical application context. There will be a great number of synthesized results presented in the remainder of the thesis, and a quick refresher on weighting, bandwidth and other related topics will be provided in the form of examples. This will also serve to provide examples of measurements from the various systems.

The need for a weighting function or window, arises when there are discontinuities at the endpoints of a waveform. The waveform must be weighted before transformation into another domain (IFFT or FFT). The discontinuities would produce unwanted, non-causal oscillations. A weighting function that removes the discontinuities would also remove the unwanted oscillations in the transformed waveform.

A weighting function usually tapers the waveform at the endpoints down to zero magnitude, which would be continuous. The rate and shape of the roll-off greatly effects the resultant transformed waveform, hence there are a great number of weighting functions. There are two weighting functions that are extensively used throughout the thesis, and they are the Gaussian modulated cosine (GMC) and the cosine taper.

In the frequency domain the GMC window is bell-shaped, where the center of the bell and the width of the bell can be controlled by f_c and τ, respectively. The window

has a rather gentle roll-off which greatly dampens the oscillations due to the edge discontinuities. The GMC window in the time domain is given by

$$w(t) = \cos(\pi f_c t)\, e^{-\pi(t/\tau)^2} \tag{2.1}$$

and in the frequency domain (via a Fourier Transform) by

$$W(f) = \tau\left\{ e^{-\pi[(f-f_c)\tau]^2} + e^{-\pi[(f+f_c)\tau]^2} \right\} \tag{2.2}$$

where f_c is the center frequency of the window and τ is the shape or width of the window.

The cosine taper is rather rectangular looking, with a rather steep roll-off at the edges. The rate of the roll-off is controlled by τ, where a larger τ results in a steeper roll-off. The cosine taper will generally have more oscillations as compared to the GMC window, but the cosine taper retains more of the spectral information. The cosine taper or Tukey window in the frequency domain is given by

$$W(f) = \begin{cases} \sin^2\left(\frac{\tau}{2}\pi\frac{f-F_L}{\Delta F}\right) & \ldots\ f > \frac{\tau-1}{\tau}F_H \ \ or \ \ f < \frac{F_L}{\tau} \\ 1 & \ldots\ f < \frac{\tau-1}{\tau}F_H \ \ and \ \ f > \frac{F_L}{\tau} \end{cases} \tag{2.3}$$

where F_H is the highest frequency of the band-limited spectrum and F_L is the lowest frequency, ΔF is $F_H - F_L$, and τ is the shape or roll-off factor and must be even. The standard notation for the cosine taper is : $\frac{1}{\tau}$ cosine taper.

The effects of bandwidth and weighting functions can best be explained through examining ideal incident short pulses. These are the pulses that an UWB/SP radar would be transmitting. A baseband short-pulse radar, which can be simulated with the ground-plane time-domain measurement system, contains spectral information down to DC (0 Hz). In Figure 2.4 the Gaussian modulated cosine (GMC) weighted spectrum is representative of a baseband radar and is very close to the output of the PPL pulse generator. The actual shape of the resulting time-domain pulse is shown in Figure 2.5

(solid line), this pulse is compared to another ideal short pulse containing the same spectral bandwidth but weighted differently. A cosine taper was applied to the spectrum (See Figure 2.4), which eliminates any dc component (i.e. oscillations occur).

The GMC is a double-edged sword; it creates smooth transient results, because of the gentle roll-off at the band edges, but there is also information lost at the band edges. The cosine taper allows for more information (spectral content) to be preserved but, due to the relatively steep roll-off at the band edges, there exist more oscillations in the transient results. This point can be visualized by considering a rectangular pulse weighted in the frequency domain which would transform to a sinc function in the time domain. The conclusion is that it is important to understand when and why to use the various weighting functions. These points are further illustrated in the next figures.

In Figure 2.6 a larger bandwidth (8 Ghz) incident pulse is considered, and the pulse is not baseband. Increasing the bandwidth results in a shorter pulse, which would produce better feature resolution. The effects of the weighting functions discussed above are also obvious. The GMC weighted pulse now contains some oscillations because it is not a baseband pulse. The inset figure shows the respective spectra of the incident pulses, and the differences in the roll-offs, which effect the oscillations, can be seen in this figure.

To further examine the effects of bandwidth, in Figure 2.7 that bandwidth is increased to 16 GHz. The resulting pulses are seen to be much shorter in duration. The 2-18 GHz bandwidth in this figure coincides with the limits imposed by equipment at MSU radiation laboratory. Therefore, the pulses shown in Figure 2.7 represent the shortest pulses that can be produced in our laboratory.

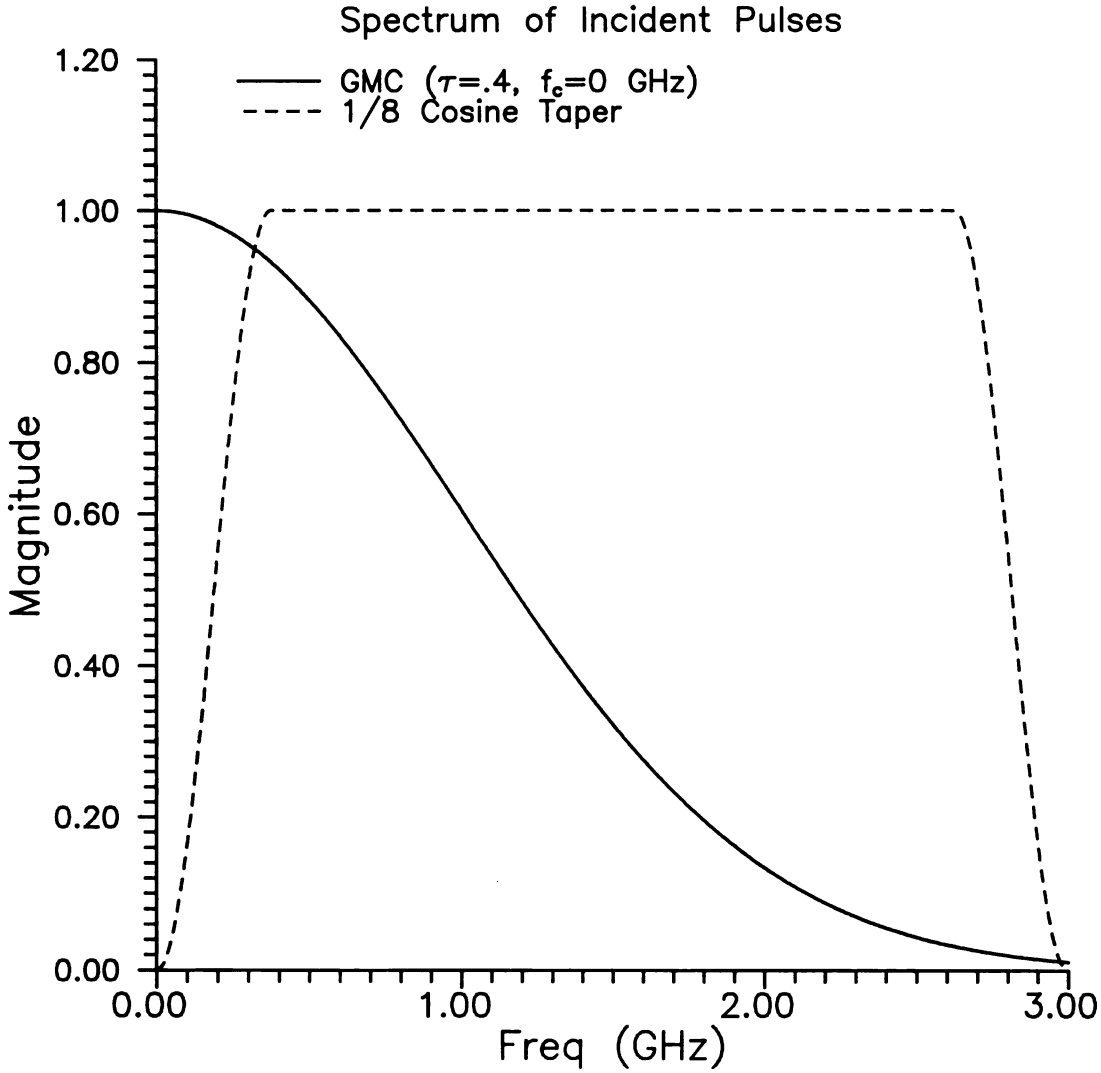

Figure 2.4 Spectrum of an ideal baseband incident short pulse with 3 GHz bandwidth.

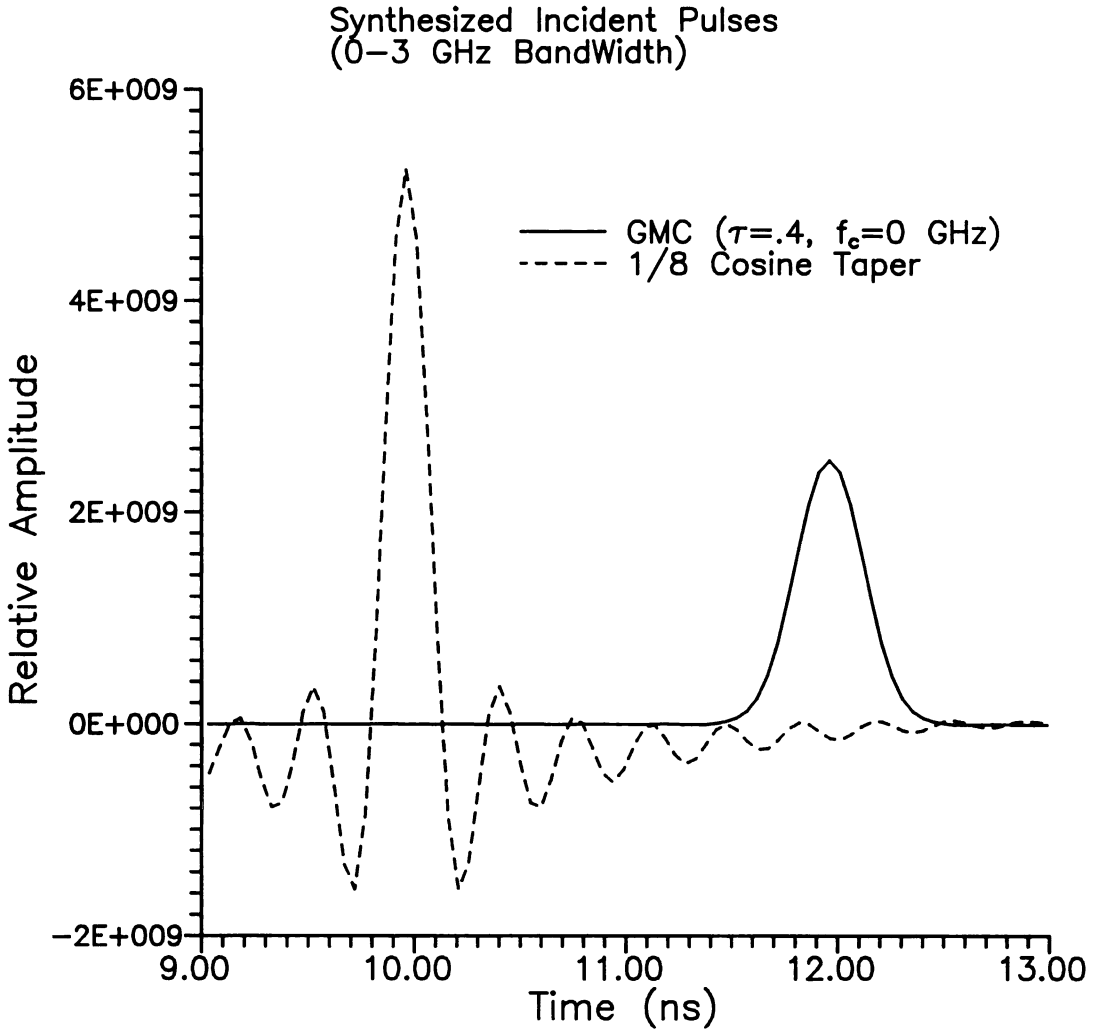

Figure 2.5 Ideal baseband incident short pulses with 3 GHz bandwidth.

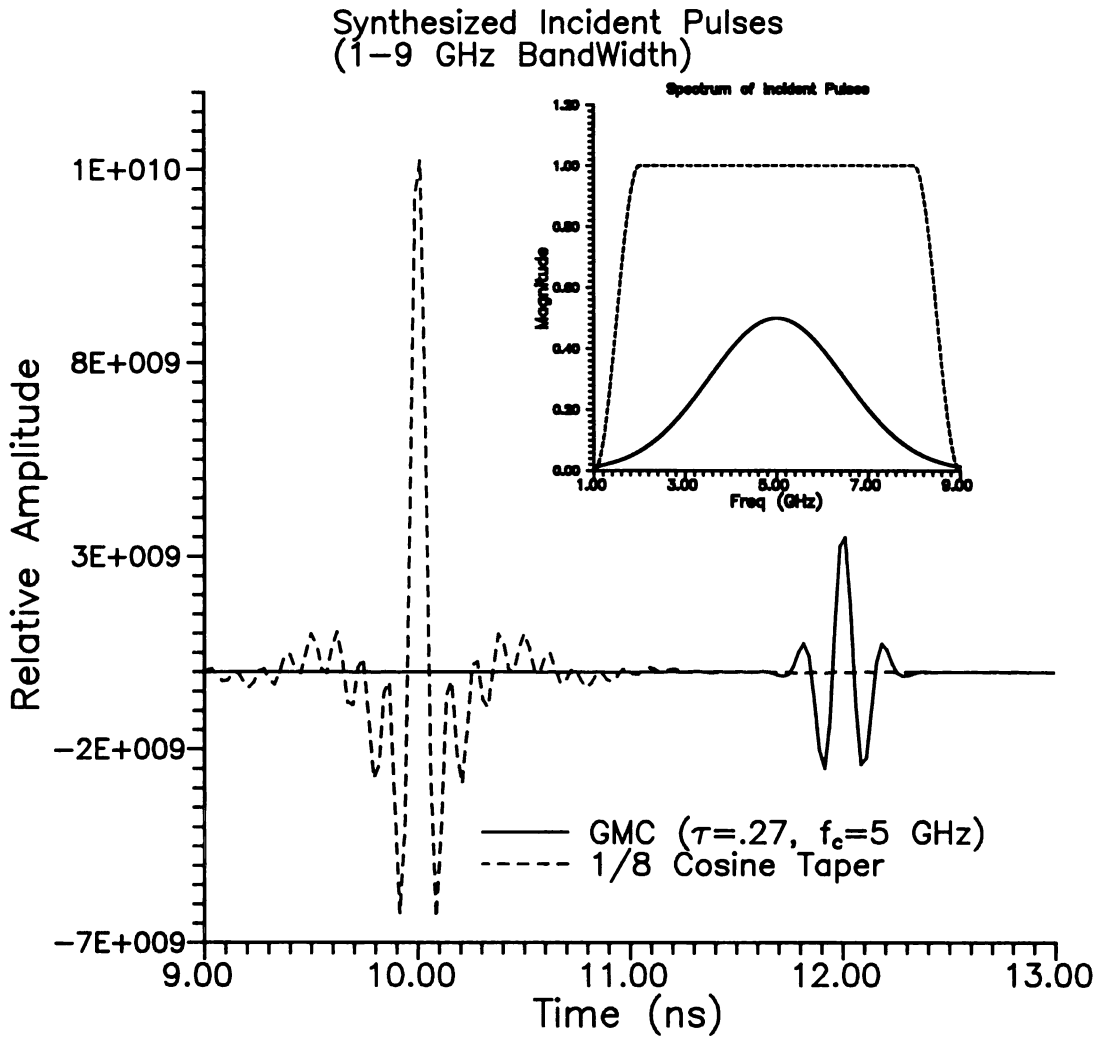

Figure 2.6 Spectrum and transient nature of ideal incident short pulse with 8 GHz bandwidth.

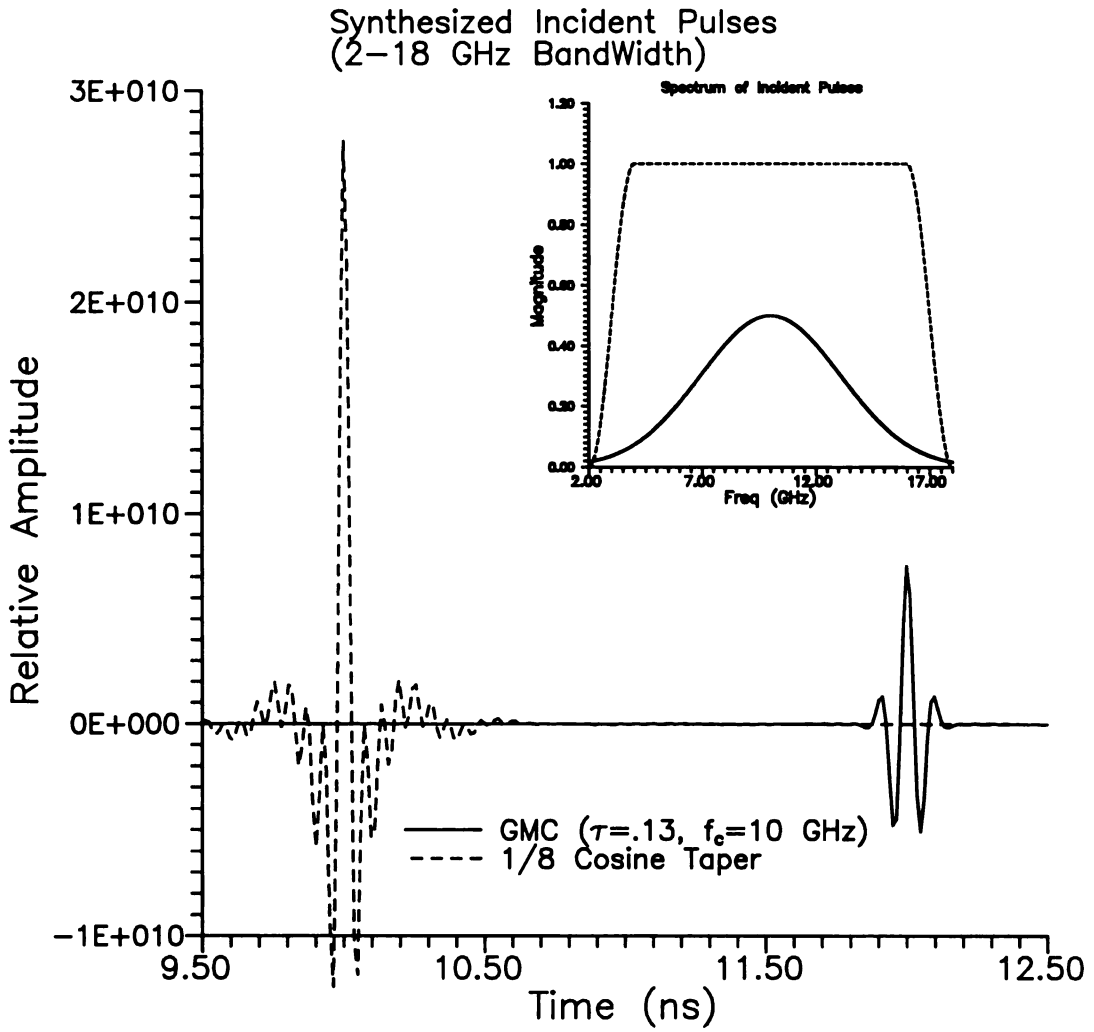

Figure 2.7 Spectrum and transient nature of ideal incident short pulses with 16 GHz bandwidth.

An illustrative example of a measurement in the anechoic chamber (frequency domain) will provide a glimpse at the quality of the chamber and is an excellent means of explaining the calibration procedure. The end goal of a measurement is to find the transfer function of an unknown target ($H_s(f)$). However, simply obtaining the measurement response of the unknown target does not yield the transfer function. There are numerous unknown transfer functions associated with the measurement system. These transfer functions are given in a system block diagram in Figure 2.8. To determine the unknown system transfer function another measurement is required, and this measurement is called the calibration measurement.

Referring to Figure 2.8, a measurement ($R(f)$) consists of a number of transfer functions acting upon an excitation ($E(f)$). There is also an additive noise factor, that is negligible for a high quality anechoic chamber, such as the chamber at MSU.

A calibrated measurement in the anechoic chamber consists minimally of three individual measurements; a background measurement response ($R^b(f)$), a calibrator measurement response ($R^{c+b}(f)$), and finally a target measurement response ($R^{t+b}(f)$). Sometimes it is necessary to perform two background measurements if the background has changed between calibrator and target measurements. These responses can be mathematically described as

$$R^b(f) = S(f)\{H_a(f) + H_c(f)\} \qquad \ldots \; S(f) = H_r(f)H_t(f)E(f) \tag{2.4}$$

$$R^{c+b}(f) = S(f)\{H_a(f) + H_c(f) + H_s^c(f) + H_{sc}^c(f)\} \tag{2.5}$$

$$R^{t+b}(f) = S(f)\{H_a(f) + H_c(f) + H_s^t(f) + H_{sc}^t(f)\} \tag{2.6}$$

where $S(f)$ is the system transfer function and is composed of the antenna transfer functions ($H_r(f)$, $H_t(f)$) and the excitation source transfer function ($E(f)$). There is also a clutter term ($H_c(f)$), a coupling term ($H_a(f)$) and an interaction term ($H_{sc}(f)$). It is important to note that the system, coupling and clutter transfer functions remain the same

for all three measurements, therefore a background subtraction will eliminate the coupling and clutter terms. The background measurements are then subtracted from the respective calibrator and target returns ($R^c = R^{c+b} - R^b$). There remains two resultant sets of spectral waveform data, the subtracted calibrator ($R^c(f)$) and the subtracted target ($R^t(f)$)

$$R^c(f) = S(f)\{H_s^c(f) + H_{sc}^c(f)\} \tag{2.7}$$

$$R^t(f) = S(f)\{H_s^t(f) + H_{sc}^t(f)\} \tag{2.8}$$

At this point the calibrator is used to remove the effects of the measuring system. This is accomplished by using a calibrator that has a known response. A useful calibrator is a sphere, since the scattered field from the sphere can be represented in closed form by the Mie series, and the sphere is impervious to orientation/aspect/polarization. Therefore a sphere is used for nearly all the subsequent measurements in this dissertation.

The system can now be calibrated using the known response of the sphere. By dividing (in the frequency domain) the measured sphere or calibrator response ($R^c(f)$ or eqn. (2.7)) by the theoretical model ($H_s^c(f)$), a calibration waveform is created. We have assumed that the mutual interaction term ($H_{sc}^c(f)$) is negligible, which is the case for a high quality chamber. The calibration waveform ($S(f)$) represents the differences between an ideal measuring system and the actual measuring system and is the transfer function of the system. Those differences include transfer functions of the amplifier, the horns, the connectors and the cables and the propagation paths.

$$S(f) = \frac{R^c(f)}{H_s^c(f)} \tag{2.9}$$

The calibration waveform or system transfer function is then divided out of the subtracted target measurement response ($R^t(f)$ or eqn. (2.8)), which results in the theoretical target spectrum

$$H_s'(f) = \frac{R'(f)}{S(f)} \tag{2.10}$$

This set of steps is illustrated in Figure 2.9. A six (6) inch sphere is used as a target in Figure 2.9, and a 14 inch sphere is used as the calibrator. The subtracted spectrum of the 6 inch sphere is shown as the top waveform, after calibration with the 14 inch sphere the resulting calibrated return is shown in the middle waveform. It can be seen that the frequency responses are much different. This is attributable to the system transfer function which has been removed in the calibrated waveform. The lower waveform is a "cleaned-up" version of the calibrated waveform. This clean-up process was performed in the time domain, by time gating the causal noise in the chamber.

The transient response can be synthesized via an IFFT, and that waveform for the subtracted 6 inch sphere data is shown in Figure 2.10 and corresponds the upper spectrum in Figure 2.9. This transient result was obtained after applying a 1/8 cosine taper to the spectral return, and is therefore the short-pulse response of an incident pulse similar to Figure 2.6. This transient result can be compared to the calculated transient result in Figure 2.11. In Figure 2.11 the measured 6 inch sphere response is compared very favorably with the theoretical transient backscatter. There are noticeable differences between the subtracted (Figure 2.10) and the calibrated (Figure 2.11) transient backscatter from the 6 inch sphere. The shapes of these waveforms are different; this is due to the non-ideal system transfer function still present in the subtracted waveform. The differences in the spectral results (Figure 2.9) shows the actual effect of the system transfer function. The time bases of the two measurements are also different; this is due to the cables, which are eliminated in the calibrated response.

The transient result of the 6 inch sphere shows a large pulse which is a specular reflection from the front of the sphere. Later in time there is another smaller pulse, this pulse is due to the creeping wave and occurs at predicted time ($2\pi r/c$). Beyond that point in time there should be negligible return, but the measured response contains noise (not

fully shown) after the first creeping-wave pulse, this noise corrupts the spectral result as shown in Figure 2.8. This noise can be time gated with the a-priori knowledge of the theoretical transient response, and then subsequently transformed (FFT) back to the frequency domain. In Figure 2.12 the time-gated spectrum is compared very favorably with the theoretical backscatter spectrum. The difference is attributable to imperfections in the 6 inch sphere (constructed by hand) and measurement system errors.

The quality and resolution of the transient radar of .8-7.2 GHz bandwidth is revealed in Figure 2.13. The transient response of a nose-on 1:72 scale B52 airplane is shown, and the scattering centers are easily distinguishable. The calibration was performed with the 14 inch sphere.

A quantitative discussion of the calibration procedure can be found in [37,38], but the short summary and qualitative analysis above should suffice the needs for this dissertation. A very similar procedure is used in calibrating the arch range measurement system, but in that case time gating is essential to eliminate undesired scattering. When performing a time-domain measurement in the arch range or the anechoic chamber it is necessary to calibrate in the same fashion. This, however, can only be performed after the initial transient measurements are transformed to the frequency domain. In the ground plane transient measurements, a calibration is not required because there is no amplifier transfer function, the antennas have known transfer functions and the cables are assumed to be distortionless.

2.3 Conclusions.

The measurement systems and the calibration procedures, which will be used extensively in the following chapters, have been described above. The important concepts of synthesized transient response, bandwidth and weighting have been discussed and set the stage for interpretation of the measured target responses in future chapters.

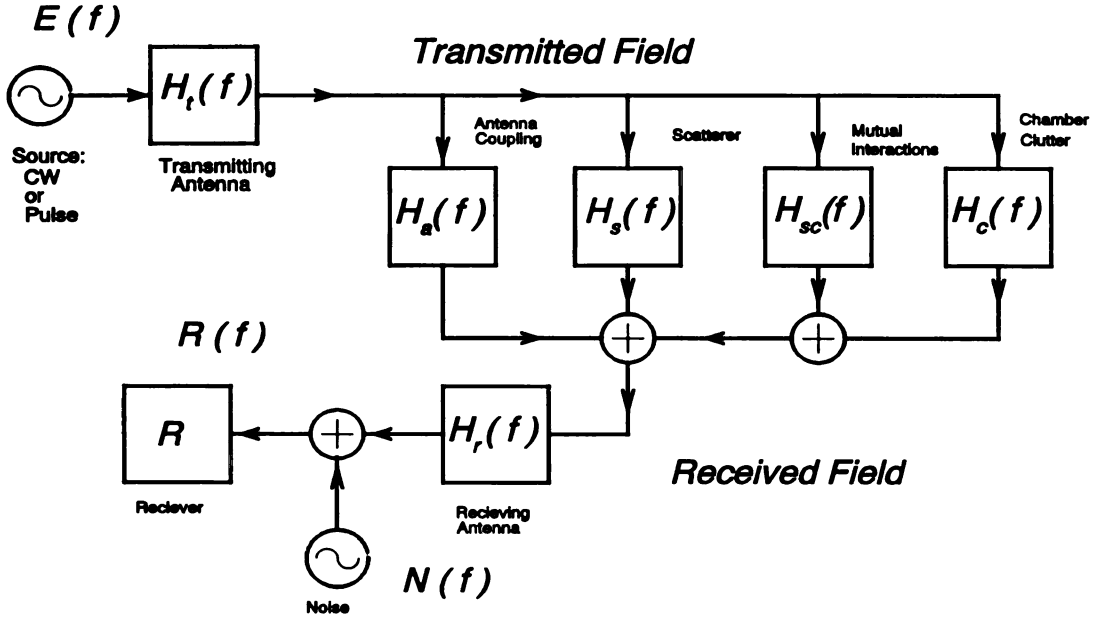

Figure 2.8 Block diagram model of measurement system.

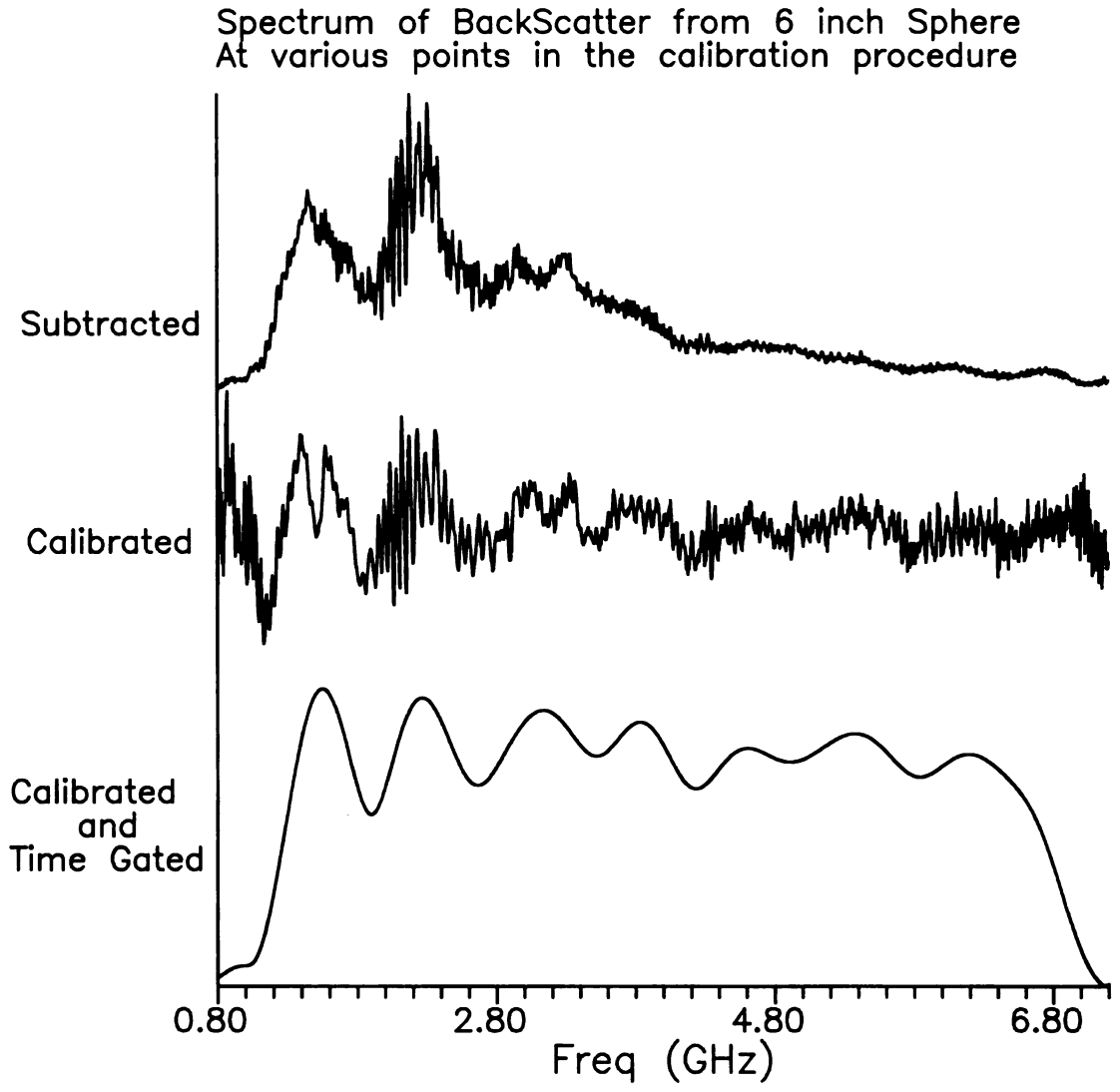

Figure 2.9 Graphical representation of the calibration procedure.

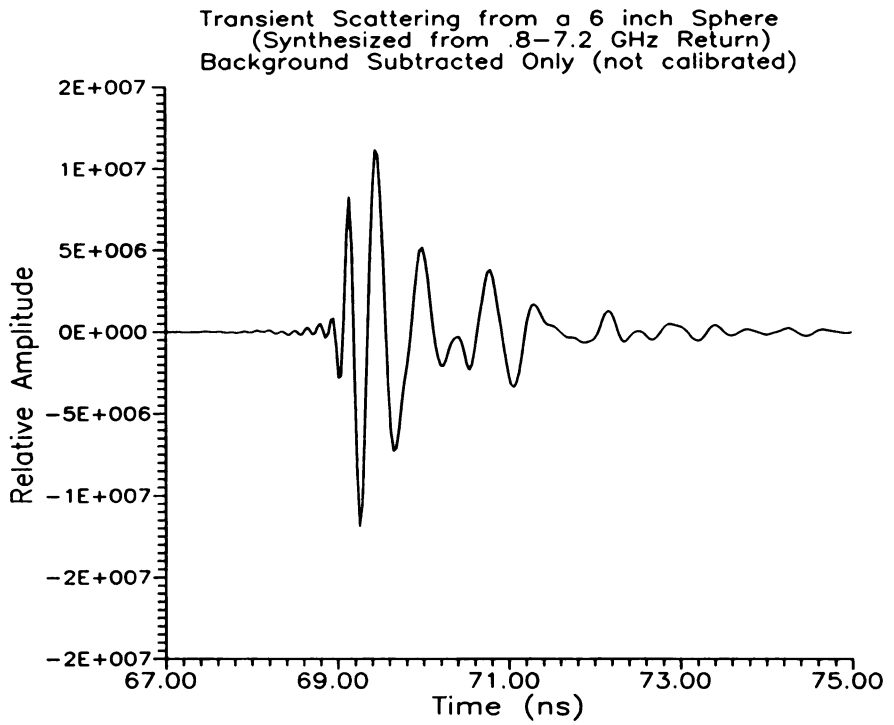

Figure 2.10 Transient backscattered field from 6 inch sphere (background subtracted).

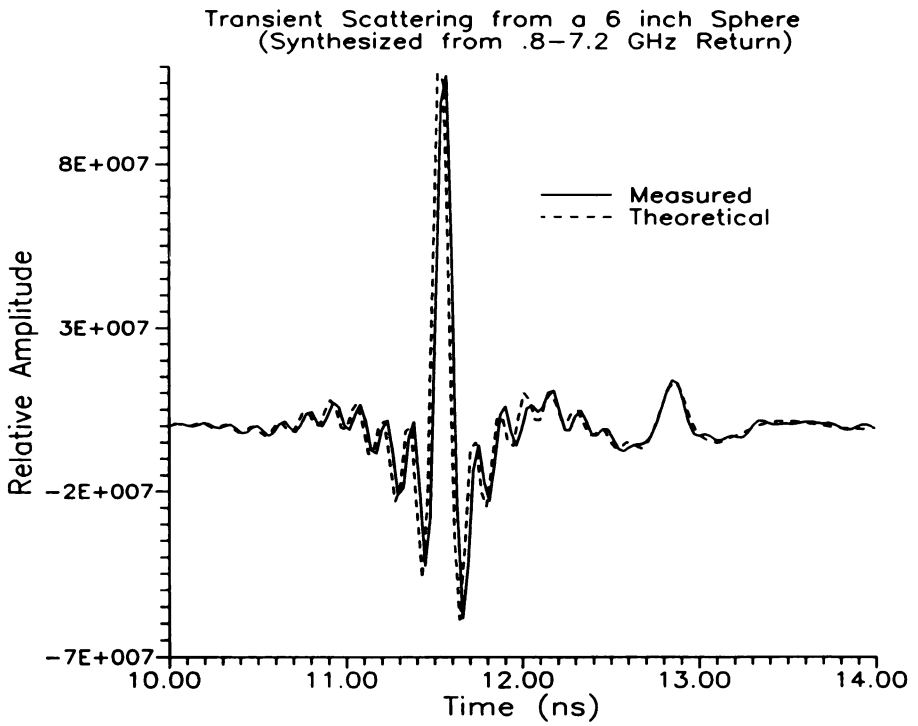

Figure 2.11 Transient backscattered field from a 6 inch sphere.

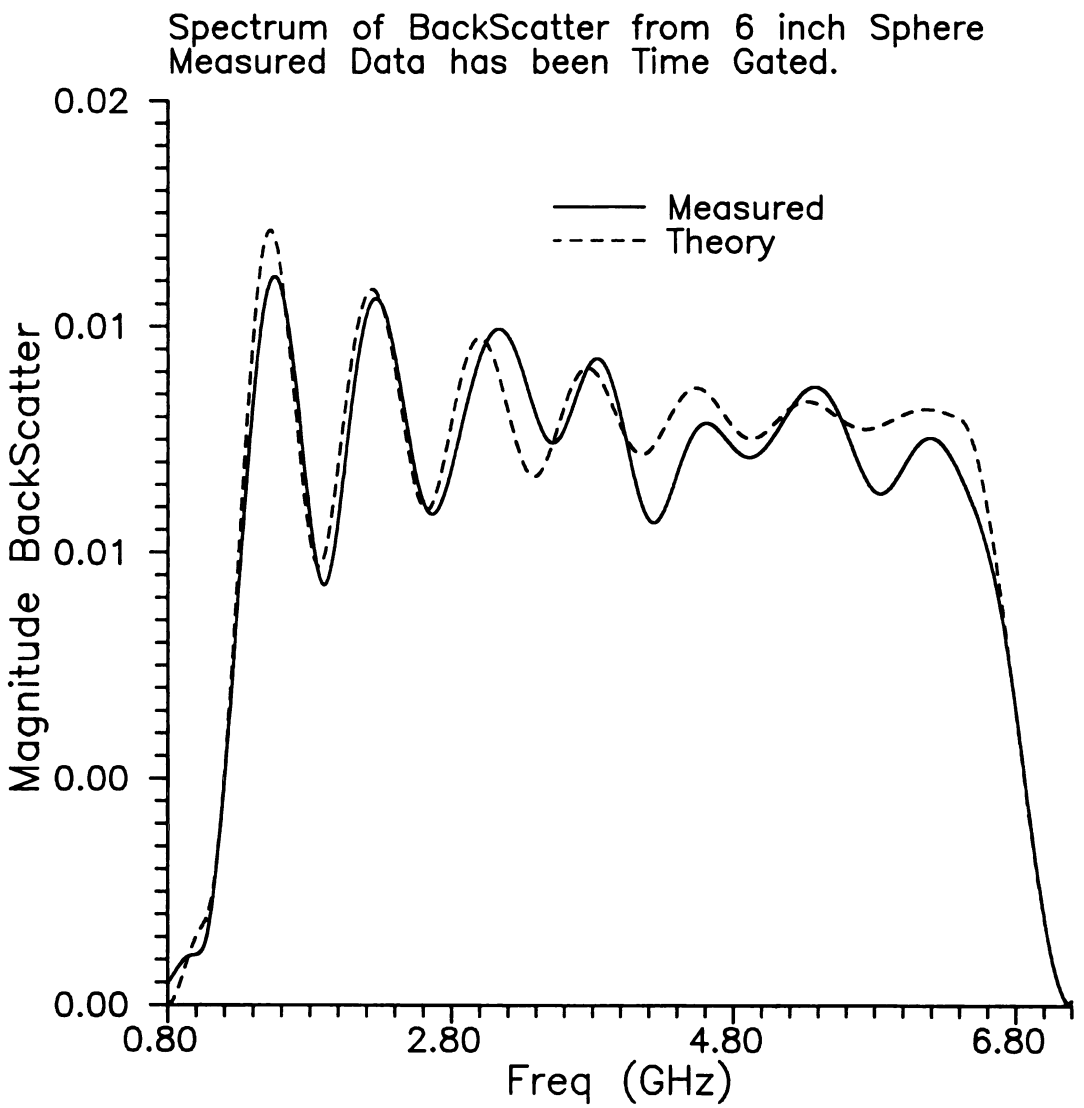

Figure 2.12 Spectrum of backscattered field from a 6 inch sphere.

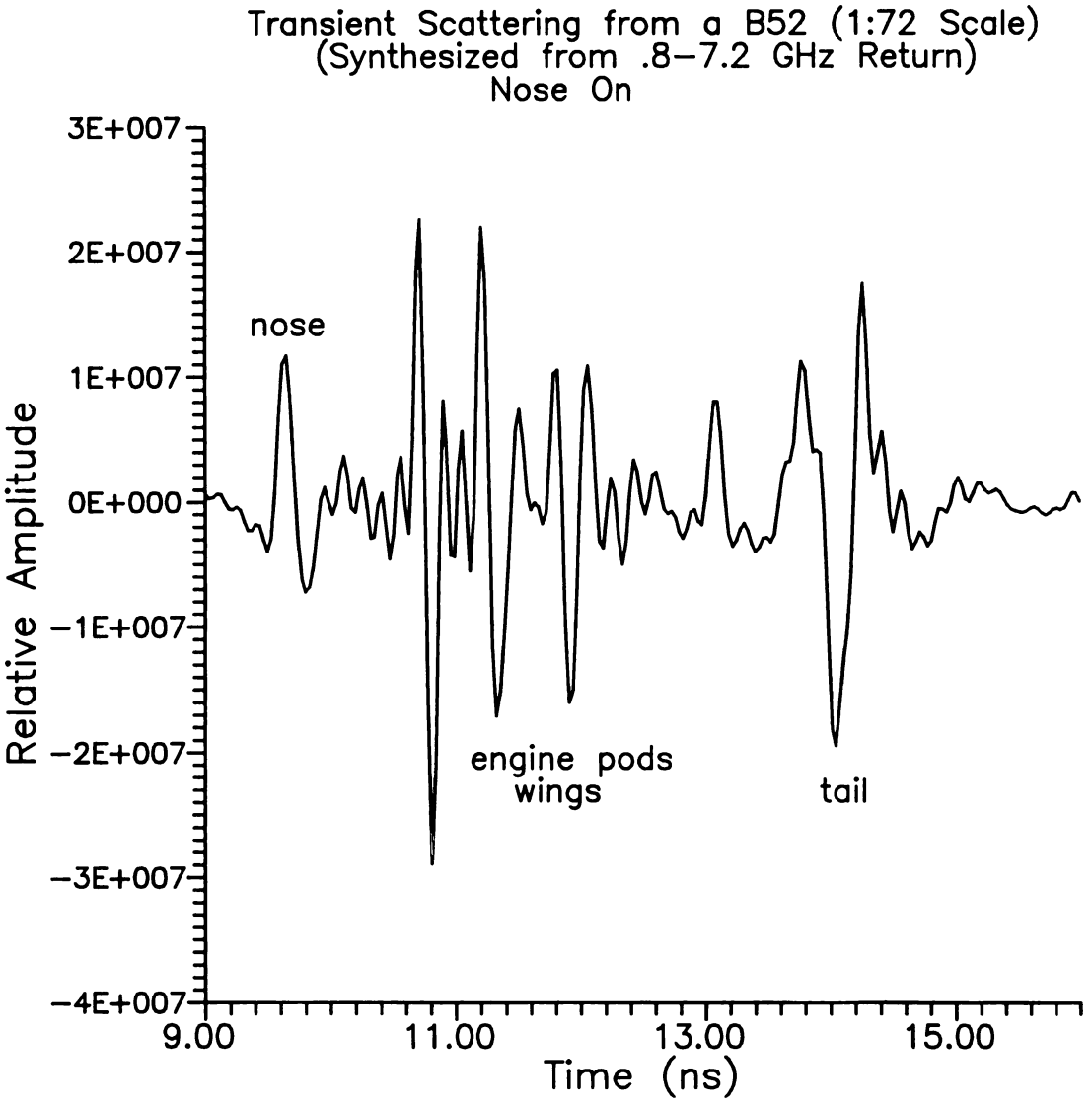

Figure 2.13 Transient backscattered field from a 1:72 scale B52 airplane.

Chapter 3

Transient Scattering from a Conducting Sinusoidal Surface

3.1 Introduction

In this chapter an in depth treatment of transient scattering from a perfectly conducting (PEC) sinusoidal surface will be considered. The PEC sinusoidal surface is a first approximation to an ocean surface, and is periodic. This is an excellent surface to begin the thesis, it introduces many important concepts and phenomena that will also be present in the more complex surface configurations. Floquet mode propagation and cut-off and multiple scattering are two phenomena that will be introduced and discussed in conjunction with the sinusoidal interface.

In addition to theoretical analyses, experimental results will be presented. These experimental results will draw from the ideas of chapter 2, and will verify the developing scattering theory.

The scattering of continuous wave (CW) radiation from a perfectly conducting (PEC) sinusoidal surface has been analyzed by many authors [12,15,25-29], but few have produced results on transient scattering [41,42,43]. This is due to the availability of CW and doppler radar systems for which the clutter analysis therefore tended to become statistical (averaging over time) in nature. The UWB/SP radar allows for snap-shot modelling of the clutter, due to the short pulse interrogation of the sea-surface. It is this property that allows for static sea models to be used in analysis and in experimental measurements.

Both finite and infinite PEC sinusoidal surfaces will be considered. The approaches will include two different polarization states (TE and TM) and will use an Integral Equation (IE) type formulation in conjunction with the Method of Moments.

The infinite surface can also be analyzed more classically using the Rayleigh hypothesis, and results from this method will be included as a confirmation of the IE method. Both methods yield frequency-domain solutions, therefore the transient results will be synthesized using the inverse Fourier transform (IFFT).

Due to the periodicity of the infinite surface the analysis techniques for this surface are centered around Floquet's theorem. The Rayleigh hypothesis method directly uses the theorem to expand the scattered fields, in the IE method the periodicity is embedded in the periodic Green's function. The infinite spatial extent of the surface can therefore be reduced to just one period. This truncation solves one problem, the infinite domain of integration is modified to a domain of one single period. The periodic Green's function, however, creates another problem in its convergence rate [44]. The convergence problem of the PGF is accentuated for shallow (low height) sinusoids, this is another reason for the inclusion of the Rayleigh-hypothesis method.

Research directed towards the finite surface has not been as active as the infinite surface; this is due in part to the strictly numerical nature of the problem, and the lack of apparent applications (sea surfaces, gratings, etc. can usually be considered infinite for most purposes). There are few workers examining this and similar problems [45-47].

Insights are gained regarding the nature of scattering from a PEC periodic surface, which can be extended to the other surfaces that will be considered in the following chapters. For both TE and TM polarizations, the forward and backscattered time and spectral domain fields are calculated. For the backscatter case, which is of primary interest for many applications (sea clutter, etc) the results exhibit a periodic return of pulses dependent upon the period of the surface. This result was expected, and illustrates the feature extraction capabilities of an UWB/SP radar system.

3.2 TE Scattering from Conducting Sinusoidal Surface

Scattering of a plane wave with transversely polarized electric field [$E_y(x,z)$], as indicated in Figure 3.1, is analyzed in the spectral domain. To simplify the problem

(numerically) the surface will be invariant along the y-direction. This approximation will not be lifted throughout the thesis, and is an area of future interest. As stressed earlier the transient response is to be obtained; this can be accomplished by utilizing the IFFT on spectral results of appropriate bandwidth.

3.2.1 Infinite PEC Surface

The first scattering problem that will be analyzed is the case of a sinusoidal surface of infinite extent. Two techniques are utilized in solving for the scattered fields due to plane wave excitation.

Method I) Floquet Mode Matching\Rayleigh-Hypothesis Analysis

The classical method known as the Rayleigh hypothesis can be applied to this problem. Combining the Rayleigh hypothesis with Floquet's theorem permits a solution via a mode-matching technique. The frequency-domain Floquet analysis is found in graduate level electromagnetics texts [12].

It is assumed that the ocean surface described by $z = \rho(x) = -h\cos(2\pi x/L)$ is cosinusoidally periodic in the x coordinate with height h and period L (See Figure 3.1). The y-invariance of the surface and orientation of the TE incident wave result in only one non-vanishing component of the electric field [$E_y(x,z)$], this can be seen from Maxwell's equations. Therefore $E_y(x,z)$ is the generating wave-function for the TE case, and the non-vanishing magnetic field components can be found directly from $E_y(x,z)$. The generating wave function [$E_y(x,z)$] will be denoted by $\psi(x,z)$ for bookkeeping purposes.

The wave function (electric field) must satisfy Helmholtz's equation in the air region above the PEC sinusoid, where there are no sources

$$(\nabla^2+k^2)\,\psi(x,z) = 0 \qquad (3.1)$$

subject to $\psi=0$ on the conducting surface S.

The incident plane wave can be written as

$$\psi_i(x,z) = A_0 e^{-j\vec{k}\cdot\vec{r}} = A_0 e^{-j(k_x x + k_z z)} = A_0 e^{-j(\beta x - qz)} \tag{3.2}$$

where $\beta = k_x = k\sin\theta_i$, $q = -k_z = k\cos\theta_i$ and $k = \omega\sqrt{\epsilon_o \mu_o}$.

Given a periodic structure with period L along the x-direction, Floquet's theorem states that

$$\psi(x) = \sum_{n=-\infty}^{\infty} A_n e^{-j\beta_n x} \qquad \beta_n = \beta + \frac{2n\pi}{L} \tag{3.3}$$

where $\psi(x)$ is a wavefunction and $A_n e^{-j\beta_n x}$ is referred to as the n^{th} space or Hartree harmonic. A proof of this theorem is available in [12].

The scattered wavefunctions are then written using Floquet's theorem as

$$\psi_s(x,z) = \sum_{n=-\infty}^{\infty} e^{-j\beta_n x} f_n(z) \tag{3.4}$$

where $\beta = k\sin\theta_i$ is necessary to match the phase progression of the scattered wave to that of the incident wave. Substituting (3.4) into (3.1) results in

$$\sum_{n=-\infty}^{\infty} \left[\frac{\partial^2 f_n}{\partial z^2} + (-\beta_n^2 + k^2) f_n \right] e^{-j\beta_n x} = 0 \tag{3.5}$$

Note also that

$$\int_0^L e^{j\beta_m x} e^{-j\beta_n x} dx = L\delta_{mn} \tag{3.6}$$

where δ_{mn} is the Kroneker delta function. Therefore,

$$\frac{\partial^2 f_n}{\partial z^2} + q_n^2 f_n = 0 \tag{3.7}$$

where $q_n^2 = k^2 - \beta_n^2$. This differential equation has the usual solutions

$$f_n(z) = B_n e^{-jq_n z} + C_n e^{jq_n z} \tag{3.8}$$

Then, according to the Rayleigh Hypothesis, the scattered field consists of space harmonics which travel only outward in the +z direction, hence $C_n=0$. This "approximation" is valid provided that

$$\left(\frac{\partial \rho}{\partial x}\right)_{max} = \frac{2\pi h}{L} < 0.448 \tag{3.9}$$

There has been a considerable amount of controversy surrounding the legitimacy of the Rayleigh hypothesis. Lord Rayleigh originally stated (without proof) the theorem in conjunction with the scattering of sound waves from a corrugated surface. It was not until fairly recently [34] that Rayleigh was questioned, with the argument that inside the troughs there must exist a downgoing wave. The existence of a downgoing wave does seem intuitively needed, and it was proven that the Rayleigh Hypothesis did indeed fail when the surface slopes exceeded 0.448. However, the legitimacy of the Rayleigh hypothesis still remained in question for surface slopes less than 0.448. Then, through a number of analytical methods [31-33] the Rayleigh Hypothesis was finally proven to be rigorous for slopes less than 0.448. It is, however, impossible to prove experimentally, due to the fact that an ideal plane wave is required and a perfectly periodic and smooth infinite surface is needed. But, the technique still remains to be quite powerful, and numerically useful.

The scattered wavefunctions, using the Rayleigh hypothesis are therefore

$$\psi_s(x,z) = \sum_{n=-\infty}^{\infty} B_n e^{-j\beta_n x} e^{-jq_n z} \tag{3.10}$$

which is periodic in x as expected.

Physically the scattered field is made up of an infinite summation of plane waves. These plane waves are either propagating or evanescent in nature. The propagating modes are characterized by a real valued q_n or $k > |\beta_n|$. The evanescent modes occur when q_n is imaginary or $k < |\beta_n|$. Note that the branch cut on q_n is chosen so that the scattered wave decays exponentially in the +z direction. There are only a finite number

of propagating modes and that number depends on the sea-surface period (L), the excitation frequency and incidence angle. The scattered modes can be thought of as plane waves scattered at various angles (See Figure 3.2). The angles are determined by β_n and q_n, which depend on the Floquet mode number (n). The n=0 mode is the specular reflection ($\theta_s = -\theta_i$). The backscattered field therefore consists of all the Floquet modes that are scattered in the -x direction, which would be the n=-2 and n=-3 modes in Figure 3.2. These topics and their implications will be discussed further in section 3.4.

In order to determine the unknown coefficients of all the scattered Floquet modes (B_n) the boundary conditions must be used. Enforcing the Dirichlet boundary condition ($\psi_i + \psi_s = 0$) at the surface ($z = \rho$) results in

$$A_0 e^{jq\rho} e^{-j\beta x} + \sum_{n=-\infty}^{\infty} B_n e^{-j\beta_n x} e^{-jq_n \rho} = 0 \tag{3.11}$$

One then divides out the $e^{-j\beta x}$ dependence and applies Galerkin's method using a testing operator of the form

$$\int_0^L \{...\}\ e^{j2\pi mx/L}\, dx \tag{3.12}$$

to yield

$$A_0 \int_0^L e^{jq\rho} e^{j2\pi m\frac{x}{L}} dx + \sum_{n=-\infty}^{\infty} B_n \int_0^L e^{-jq_n\rho} e^{j2\pi(m-n)\frac{x}{L}} dx = 0 \tag{3.13}$$

This can be rewritten as

$$\sum_{n=-\infty}^{\infty} \bar{K}_{mn} B_n = A_0 \bar{A}_m \qquad 0 \le |m| < \infty \tag{3.14}$$

where

$$\bar{A}_m = -\int_0^L e^{jq\rho} e^{j2\pi m\frac{x}{L}} dx \tag{3.15}$$

which can be shown to be equivalent to

$$\bar{A}_m = -Lj^{|m|}(-1)^{|m|}J_{|m|}(qh) \tag{3.16}$$

and

$$\bar{K}_{mn} = \int_0^L e^{-jq_n\rho}e^{j2\pi(m-n)\frac{x}{L}}dx \tag{3.17}$$

which can be seen to be equivalent to

$$\bar{K}_{mn} = j^{|m-n|}J_{|m-n|}(q_nh) \tag{3.18}$$

Both of the above integrations ((3.15) and (3.17)) where performed in closed form because of the specialization of the surface (ρ) to a sinusoid. These integrals could be numerically evaluated for any surface shape, provided the surface slope remains within the Rayleigh hypothesis regime.

These simplifications result in

$$\sum_{n=-\infty}^{\infty} K_{mn}B_n = A_0A_m \qquad 0 \le |m| < \infty \tag{3.19}$$

with

$$A_m = -j^{-|m|}J_{|m|}(qh) \tag{3.20}$$

$$K_{mn} = j^{|m-n|}J_{|m-n|}(q_nh) \tag{3.21}$$

This infinitely large matrix equation can be truncated (-N to N) to obtain an approximate solution for the spatial harmonic amplitudes. According to [12], if the height is small compared with a wavelength and the period L is much greater than a wavelength, the matrix can be truncated without too much error.

Subsequent to the determination of the spatial harmonic amplitudes the scattered field in the air region can be found using (3.10).

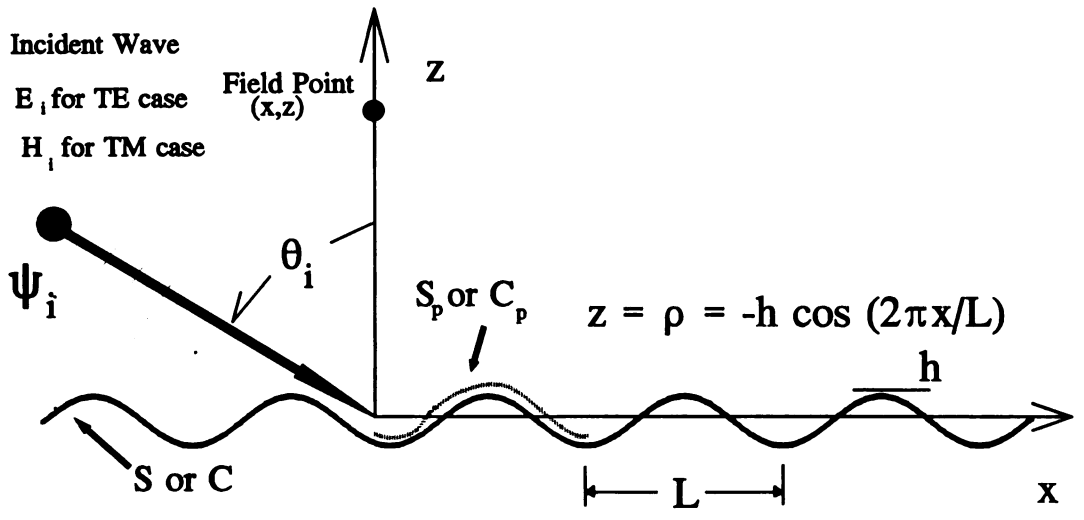

Figure 3.1 Infinite, conducting sinusoidal surface scattering geometry.

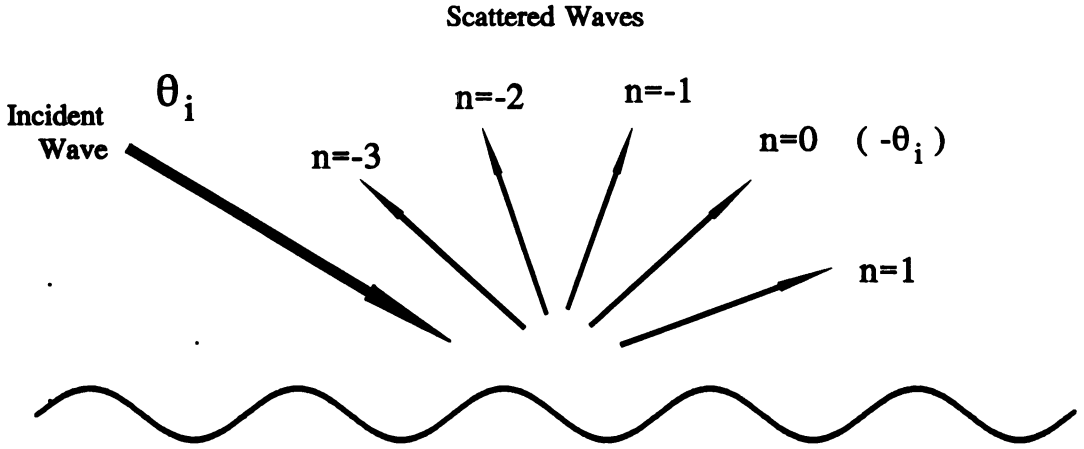

Figure 3.2 Graphical representation of Floquet-mode scattered waves.

Method II) EFIE-MoM Analysis

A rigorous and more general treatment for the scattering of plane waves from a PEC periodic surface has been developed. The technique sets no restrictions on the surface slope and in fact the surface need not be sinusoidal. An integral-operator-based analysis has been employed for this analysis, and will be referred to as EFIE-MoM method. The currents induced on the PEC sea surface are calculated as solutions to an EFIE with a periodic Green's-function (PGF) kernel. With the surface currents known, it is then possible to determine the scattered fields once again making use of the PGF.

The electric field $E_y(x,z)$ associated with the two-dimensional (2-D) TE scattering problem satisfies the 2-D Helmholtz equation

$$\frac{\partial^2 E_y}{\partial x^2} + \frac{\partial^2 E_y}{\partial z^2} + k^2 E_y = j\omega\mu J_y \tag{3.22}$$

where $k = \omega\sqrt{\mu\epsilon} = 2\pi/\lambda$ is the wavenumber in the space region above the ocean surface and $J_y(x,z)$ is the source current density. The incident wave is defined by (3.2).

As a consequence of the infinite periodicity of the ocean surface, the induced current must be similarly periodic, except for a progressive phase shift of βL radians per period to match that of the incident wave, such that $J_y(x+mL,z) = \exp(-jm\beta L)J_y(x,z)$ with m integer valued. The induced currents maintain a scattered field having the similar periodicity $E_y(x+mL,z) = \exp(-jm\beta L)E_y(x,z)$.

The above nature of the induced current prompts the definition of a periodic Green's function to accommodate the periodicity of the scattered field. If a 2-D current point source $\delta(x-x')\delta(z-z')$ is located at (x',z') in the first period of the ocean surface, then the periodic Green's function is the field maintained by that point source as well as its infinite translation $\exp(-jm\beta L)\delta[x-(x'+mL)]\delta(z-z')$ into the remaining ocean periods for $-\infty<m<\infty$. The periodic Green's function $G(x,z|x',z')$ is defined by

$$\frac{\partial^2 G}{\partial x^2} + \frac{\partial^2 G}{\partial z^2} + k^2 G = -\sum_{m=-\infty}^{\infty} e^{-jm\beta L}\delta[x-(x'+mL)]\,\delta(z-z') \tag{3.23}$$

and has periodicity property $G(x+mL,z|x',z') = \exp(-jm\beta L)G(x,z|x',z')$.

It is demonstrated in Appendix A that definition (3.23) leads to

$$G(x,z|x',z') = -\frac{j}{2L}\sum_{n=-\infty}^{\infty}\frac{e^{-j\beta_n(x-x')}e^{-jq_n|z-z'|}}{q_n} \tag{3.24}$$

where $\beta_n = \beta + 2n\pi/L$ and $q_n^2 = k^2 - \beta_n^2$ so $q_n = -j\sqrt{\beta_n^2 - k^2}$ where the branch cut is chosen such that $Im\{q_n\}<0$. The periodic Green's function innately accommodates the periodicity of scattered field $E_y^s(x,z)$, which is obtained by integrating that Green's function into the current which resides only on the first period of the surface to yield

$$E_y^s(x,z) = -j\omega\mu\int_{S_P} J_y(x',z')G(x,z|x',z')\,dx'dz' \tag{3.25}$$

where S_P designates the cross section of the first ocean period.

The boundary condition at any point on the conducting ocean surface requires that $E_y(x,z) = E_y^i(x,z) + E_y^s(x,z) = 0$ there. Using (3.2) for E_y^i and the specialization of (3.25) for E_y^s maintained by the surface current K_y induced on the ocean surface leads to

$$\int_{C_P} K_y(x',z')G(x,z|x',z')dl' = \frac{A}{j\omega\mu}e^{-j\beta x}e^{jqz} \quad \ldots \forall\ (x,z)\in C_P \tag{3.26}$$

where C_P designates the contour of the ocean surface in its first period. Exploiting representation (3.24) for the periodic Green's function leads to

$$\int_{C_P} K_y(x',z')\bar{G}(x,z|x',z')dl' = \frac{2LA}{k\eta}e^{-j\beta x}e^{jqz} \quad \ldots \forall\ (x,z)\in C_P \tag{3.27}$$

where $\eta = \sqrt{\mu/\epsilon}$ is the intrinsic impedance, and kernel $\bar{G}(x,z|x',z')$ is defined by

$$\bar{G}(x,z|x',z') = \sum_{n=-\infty}^{\infty}\frac{e^{-j\beta_n(x-x')}e^{-jq_n|z-z'|}}{q_n} \tag{3.28}$$

Equation (3.27) is an EFIE for the unknown current K_y.

A MoM numerical solution is implemented by expanding the unknown current K_y in basis set $\{f_q\}$ as

$$K_y(x,z) = \sum_{q=1}^{N} a_q f_q(x,z) \tag{3.29}$$

and point matching (3.27) at N points $(\bar{x}_p,\bar{y}_p)$ on the first ocean-surface period C_p. This leads to the matrix equation

$$\sum_{q=1}^{N} A_{pq} a_q = F_p \quad \ldots\ p = 1,2,\cdots,N \tag{3.30}$$

where the matrix elements are given by

$$A_{pq} = \int_{C_p} f_q(x',z')\,\bar{G}(\bar{x}_p,\bar{z}_p|x',z')\,dl' \tag{3.31}$$

and the forcing vector is

$$F_p = \frac{2LA}{k\eta}\, e^{-j\beta\bar{x}_p} e^{jq\bar{z}_p} \tag{3.32}$$

A pulse-function basis set was used to implement the numerical solution. The first period $0 \le x \le L$ of the ocean surface is partitioned into N segments, each of length $\Delta x = L/N$, between end points $x_q = (q-1)\Delta x$ for $q = 1,2,\cdots,N+1$. Corresponding points on the surface are located by $z_q = \rho(x_q)$. The pulse functions are then defined by

$$f_q(x,z) = \begin{cases} 1 & \ldots\ for\ x_q < x < x_{q+1} \\ 0 & \ldots\ otherwise \end{cases} \tag{3.33}$$

For the purpose of evaluating the integrals in matrix elements (3.31), the ocean surface is modelled as piecewise linear between partition end points x_q with slope $m_q = (x_{q+1} - x_q)/\Delta x$. An element of displacement along the ocean surface is $dl = S(x)\,dx$ with $S(x) = \sqrt{1 + (dz/dx)^2}$ such that within the q'th partition $dl' = S_q\,dx'$ with $S_q = \sqrt{1 + m_q^2}$. The MoM partitioning scheme can be visualized in Figure 3.3. The matching points are located by $\bar{x}_p = x_p + \Delta x/2$, $\bar{z}_p = z_p + m_p \Delta x/2$. Matrix elements (3.31) are calculated from

$$A_{pq} = S_q \int_{x_q}^{x_q+\Delta x} \bar{G}(\bar{x}_p, \bar{z}_p | x', z')\, dx'$$

$$= S_q \sum_{n=-\infty}^{\infty} \frac{e^{-j\beta_n \bar{x}_p}}{q_n} \int_{x_q}^{x_q+\Delta x} e^{j\beta_n x'} e^{-jq_n|\bar{z}_p - z_q - m_q(x'-x_q)|}\, dx' \tag{3.34}$$

The integrals in (3.34) can be evaluated in closed form, leading to:

CASE 1: $\bar{z}_p \neq \bar{z}_q$, $\chi_{nq} = \beta_n + q_n m_q$ ... for $\bar{z}_p > \bar{z}_q$, $\chi_{nq} = \beta_n - q_n m_q$ ... for $\bar{z}_p < \bar{z}_q$

$$A_{pq} = S_q \sum_{n=-\infty}^{\infty} \frac{e^{-j\beta_n(\bar{x}_p - \bar{x}_q)} e^{-jq_n(\bar{z}_p - \bar{z}_q)}}{q_n} \frac{2\sin(\chi_{nq}\Delta x/2)}{\chi_{nq}} \tag{3.35}$$

CASE 2: $\bar{z}_p = \bar{z}_q$, $\bar{m}_q = |m_q|$

$$A_{pq} = S_q \sum_{n=-\infty}^{\infty} \frac{e^{-j\beta_n(\bar{x}_p - \bar{x}_q)}}{jq_n\left[\beta_n^2 - (q_n \bar{m}_q)^2\right]} \left\{-2q_n\bar{m}_q\left[1 - e^{-jq_n\bar{m}_q\Delta x/2}\cos(\beta_n \Delta x/2)\right]\right.$$
$$\left. + j2\beta_n e^{-jq_n\bar{m}_q\Delta x/2}\sin(\beta_n \Delta x/2)\right\} \tag{3.36}$$

Subsequent to solution of the MOM matrix equation (3.30) for a_q, the scattered field at points above the ocean surface can be obtained from expression (3.25) as

$$E_y^s(x,z) = -\frac{k\eta}{L} \sum_{q=1}^{N} a_q S_q \sum_{n=-\infty}^{\infty} \frac{e^{-j\beta_n(x-\bar{x}_q)} e^{-jq_n(z-\bar{z}_q)}}{q_n} \frac{\sin[(\beta_n + q_n m_q)\Delta x/2]}{\beta_n + q_n m_q} \tag{3.37}$$

The backscattered field is obtained from (3.37) by restricting the sum over n to include only those Floquet modes which are propagating (q_n real) in the -x direction ($\beta_n < 0$).

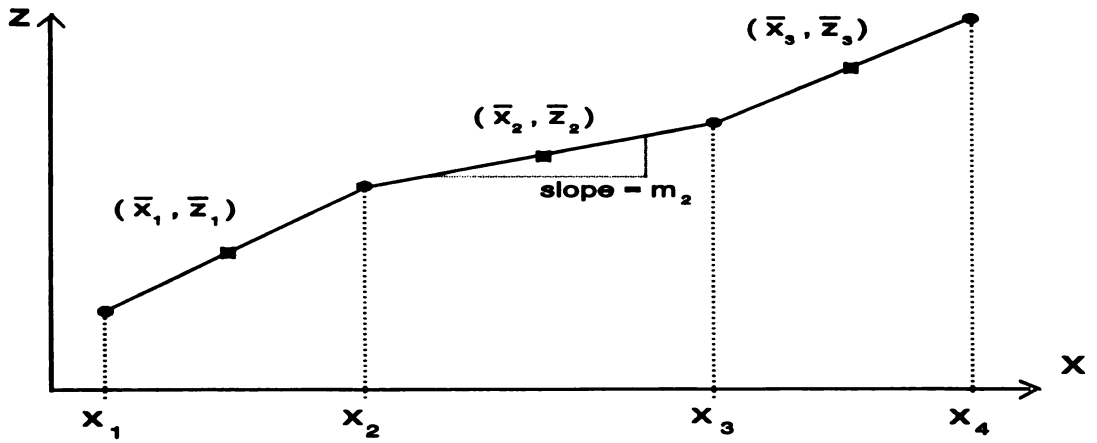

Figure 3.3 Partitioning scheme for MoM numerical solution.

3.2.2 Preliminary results of TE infinite case.

The preliminary results are concerned with the currents which are induced on the PEC sinusoid due to the TE plane wave excitation. The Floquet mode-matching technique relies on matching the modal amplitudes of the scattered field modes (3.10) at the sinusoidal boundary. There are an infinite number of these modes, but the numerical solution requires truncation of the modes to a finite number of terms. From the discussion on propagating and evanescent modes it might seem that the number of modes could be truncated to contain only the propagating modes, which describe the far-field scattering. This is incorrect because the evanescent modes do contribute to the surface currents. If the surface currents are incorrectly obtained then the modal amplitudes of the propagating modes must also be wrong. This idea can be seen in Figure 3.4, where the number of terms (N) is varied. This figure shows that even if all the propagating modes are considered (N=2 case), there are changes in the modal amplitudes as more modes are included (N=6 and N=10) in the solution. For the surface characteristics that are present in this thesis it was found that a N of 15 to 20 is sufficient.

As a preliminary check of the two methods developed above the surface currents on a PEC sinusoid (L=0.1016 and h/L=0.0625) are compared for both methods. The sinusoids were illuminated with a 6 GHz TE plane wave at an incidence angle of 85°. The results in Figure 3.5 show a very good agreement between the mode-matching and integral equation techniques. This lends credibility to the methods and the numerical implementations. There is also a noticeable shadowing effect in the trough area behind the illuminated crest.

It will be assumed from this point that the FMM-RH method is used when the sinusoidal surface is within the Rayleigh-hypothesis regime, unless specifically noted. The IE method will be used for all other cases.

A further examination of the surface currents is provided. In Figure 3.6 the currents are compared for a number of incidence angles. The normally incident case

displays a symmetric current distribution as expected. As the incidence angle is increased the maximum current moves towards the illuminated region and the shadow zone becomes apparent. The magnitudes of the current decrease as the incidence angle is increased. This was an unexpected result. The expectation was that the magnitudes would remain constant for all the incidences, but would shift maximal locations. The results, however, indicate that the current tends to redistribute itself and since the higher incidence angles intercept less surface area there is less total current (energy) induced.

The dependence of induced current on sinusoid height (h) is observed in Figure 3.7. As the height of the sinusoid is increased the induced current is seen to grow at the crest of the sinusoid. The shadow region also becomes more defined at the height is increased. These observations were expected and increase the confidence in the numerical solution.

In Figure 3.8 the period length (L) of the surface is varied with the resulting induced currents being compared. The results are quite intuitive. As the period length is increased the slope of the sinusoid is decreased, which results in a smaller maximum magnitude. The shadow region becomes less distinct as L is increased, which is expected.

The last figure in this section (Figure 3.9) is quite important. This figure shows the dependence of the induced surface current on excitation frequency. Since the eventual scattered fields will require this large bandwidth of returns it is interesting to observe the effect on the surface currents. As the excitation frequency is increased the magnitude of the current maximum increases and the shadow region becomes more defined. This is expected because in the physical-optics limit (high frequency) the current would vanish in the shadow region. The frequencies around 1.5 GHz and 2.95 GHz show a slight roughness in the current. This phenomenon is due to a Floquet mode moving from evanescent to propagating (or vice-versa) and will be discussed in section 3.4.

The preliminary results lend faith to the theoretical developments, through the agreement with physics and intuition and the convergence of the two analytical methods.

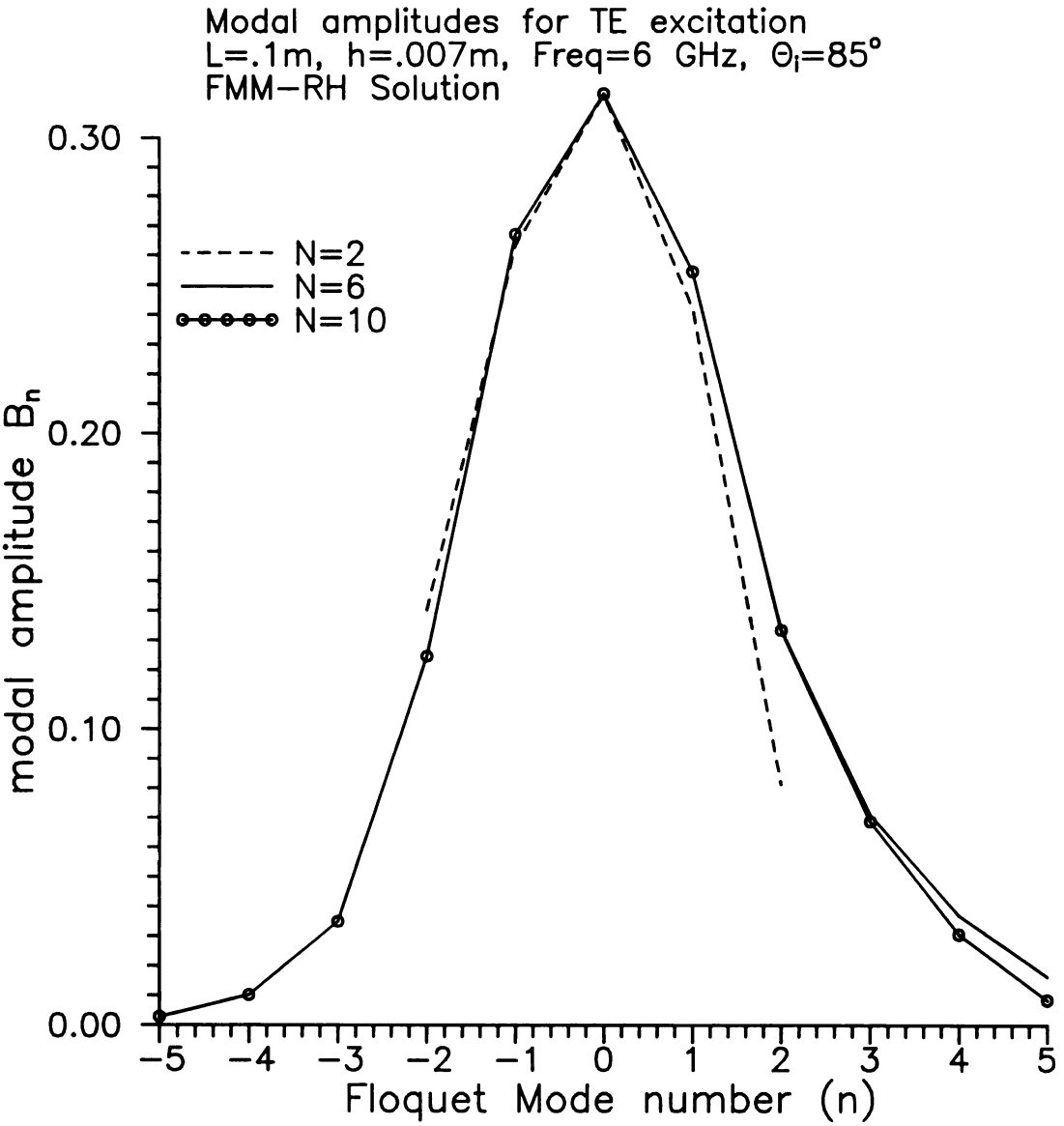

Figure 3.4 Modal amplitudes for a mode-matching solution using differing numbers of terms.

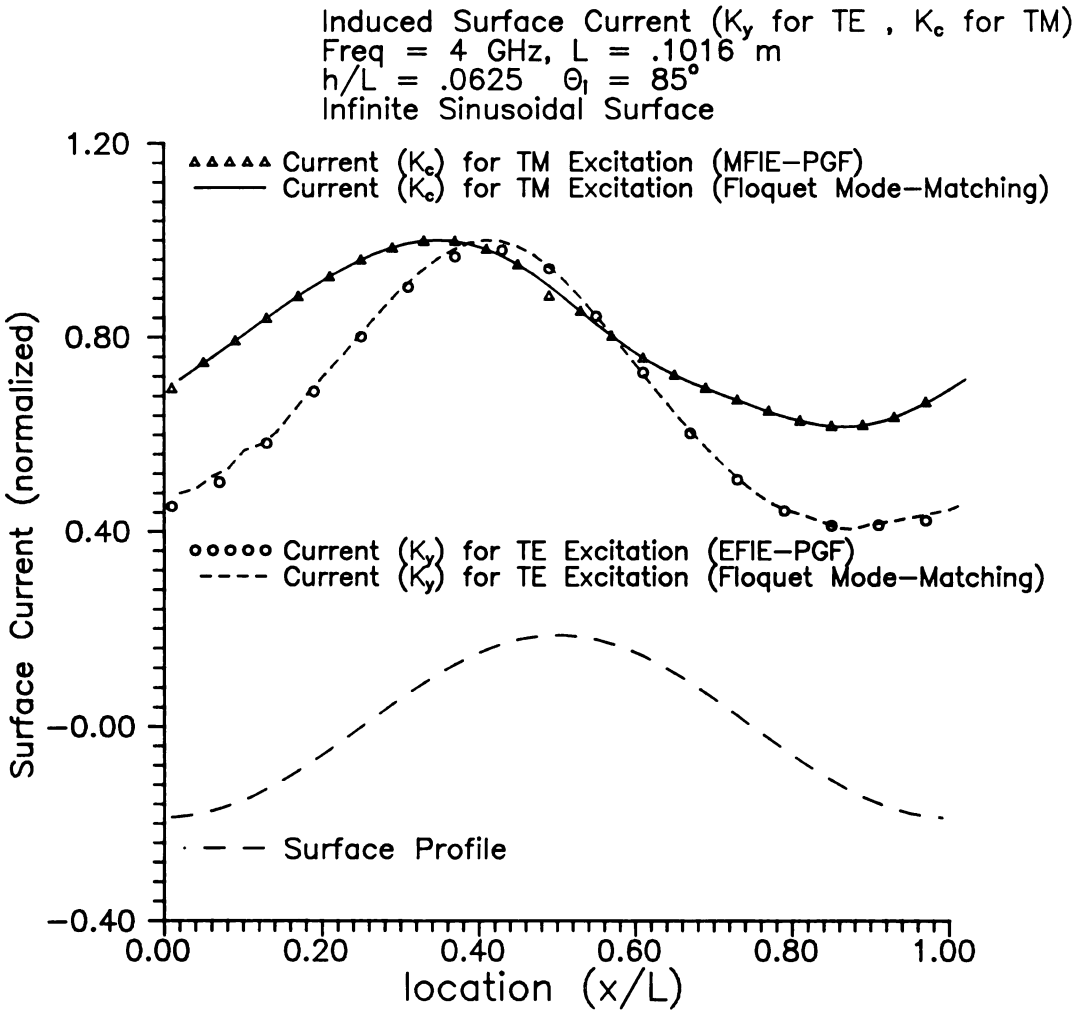

Figure 3.5 Induced surface current on one period of infinite, conducting sinusoidal surface for TE and TM excitation at 4 GHz.

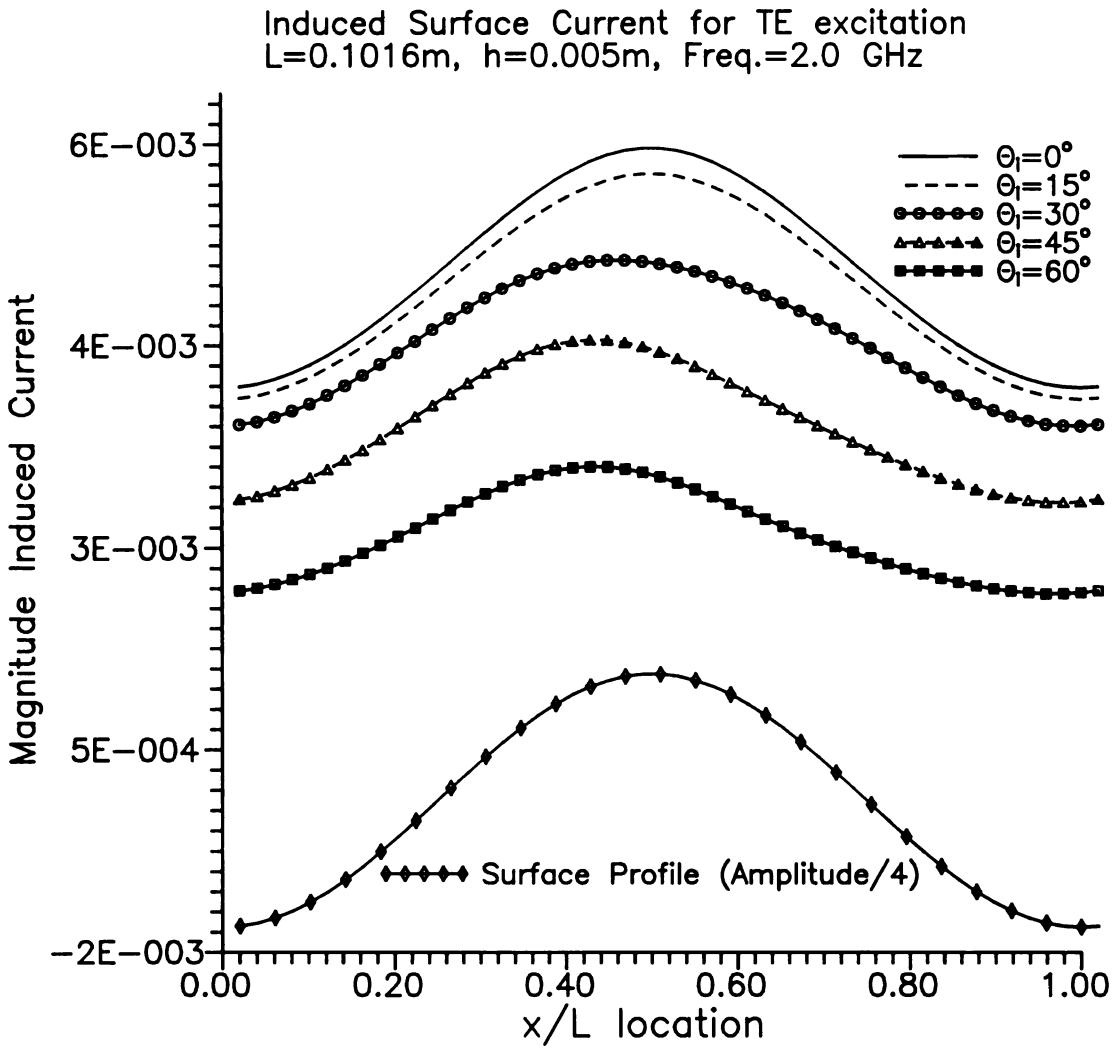

Figure 3.6 Dependence of currents induced on a PEC sinusoid for TE excitation for various incidence angles.

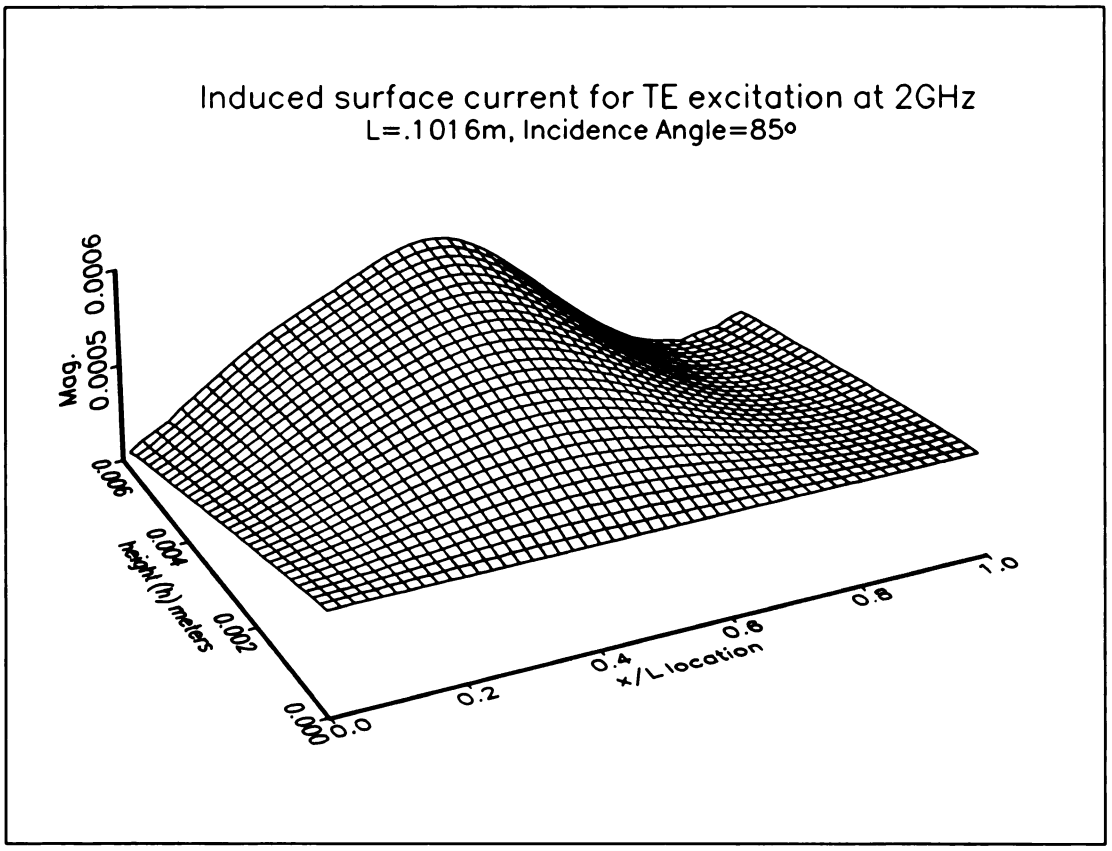

Figure 3.7 Dependence of currents induced on a PEC sinusoid for TE excitation for various surface heights.

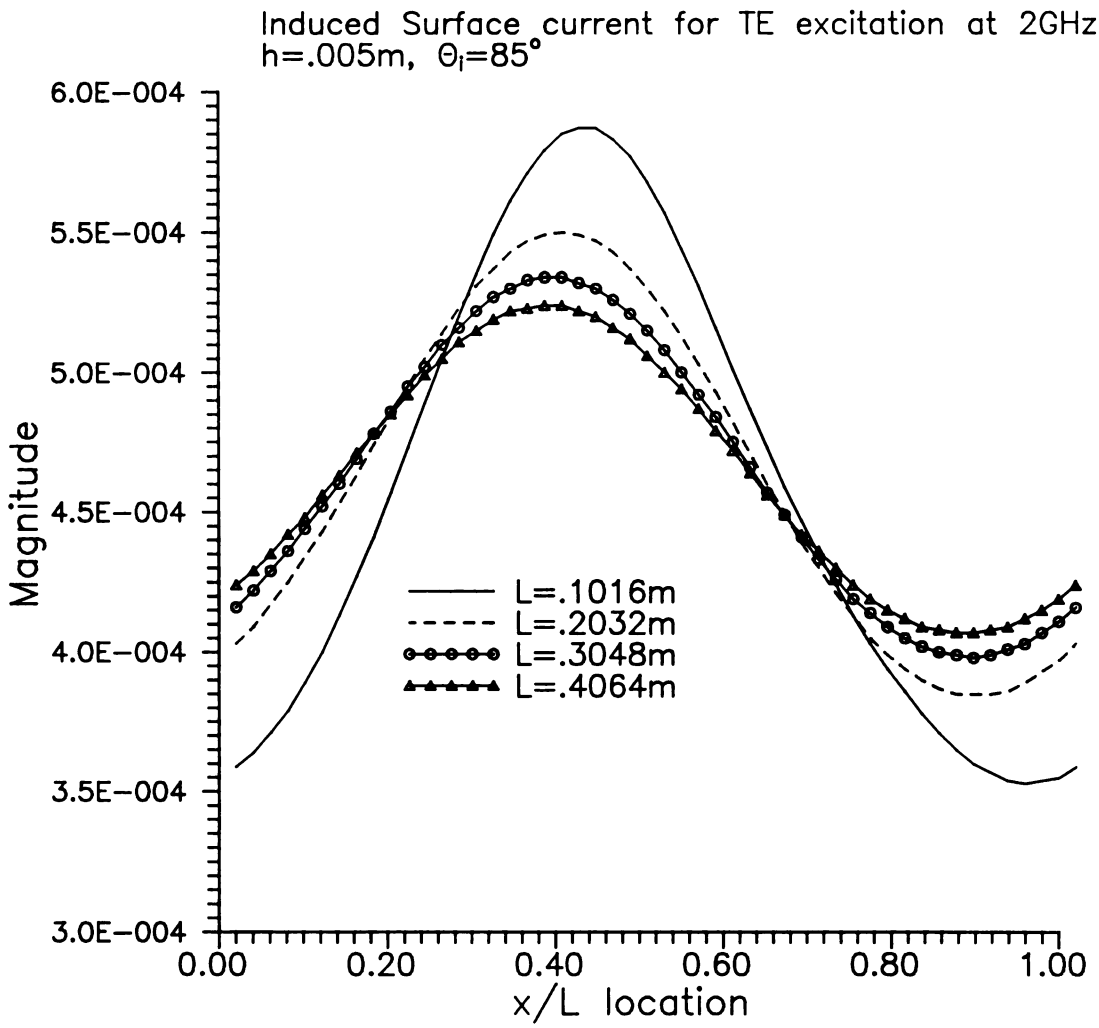

Figure 3.8 Dependence of currents induced on a PEC sinusoid for TE excitation for various surface period lengths (L).

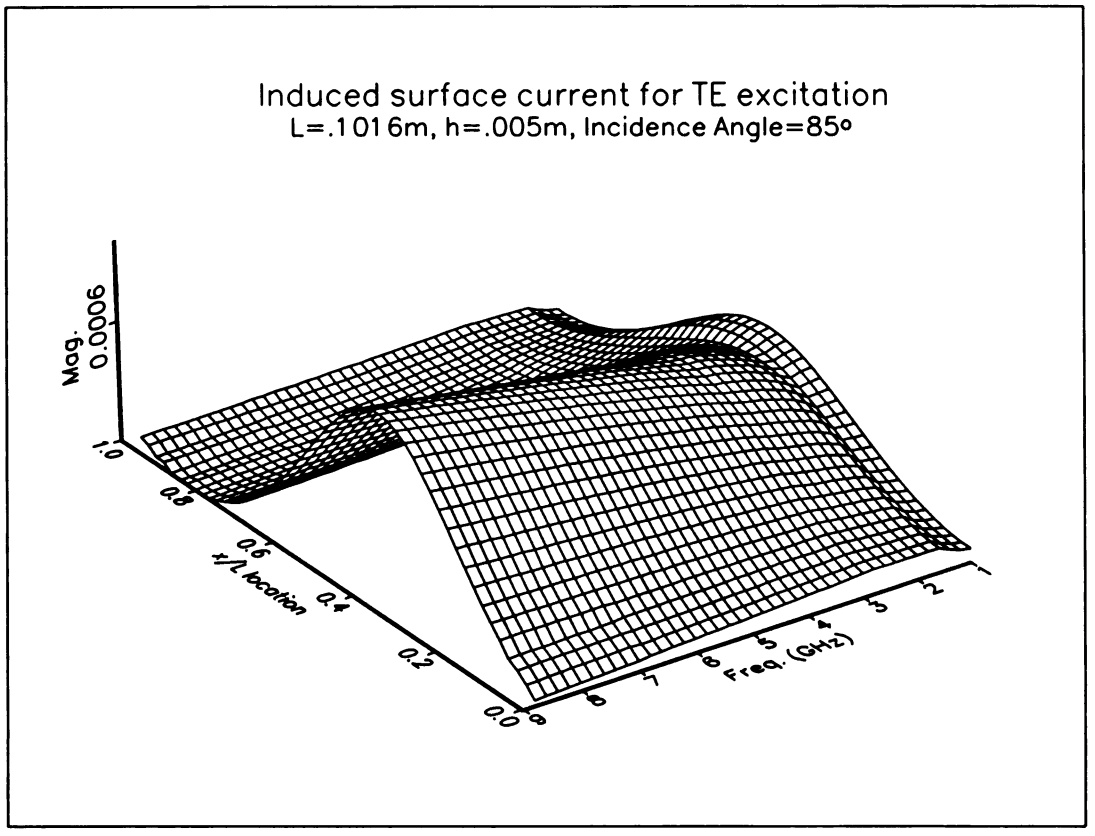

Figure 3.9 Dependence of currents induced on a PEC sinusoid for various TE excitation frequencies.

3.2.3 TE Scattering from a finite conducting surface.

This section is devoted to briefly describe the techniques used to find the scattered fields from a finite-sized, two-dimensional PEC surface. There are no restrictions to the surface curvature (i.e. no slope limitations); the physical size of the scatterer is limited only by numerical consequences (memory, and cpu time). This is due to the fact that the entire surface must be partitioned not just one period as in the PGF case.

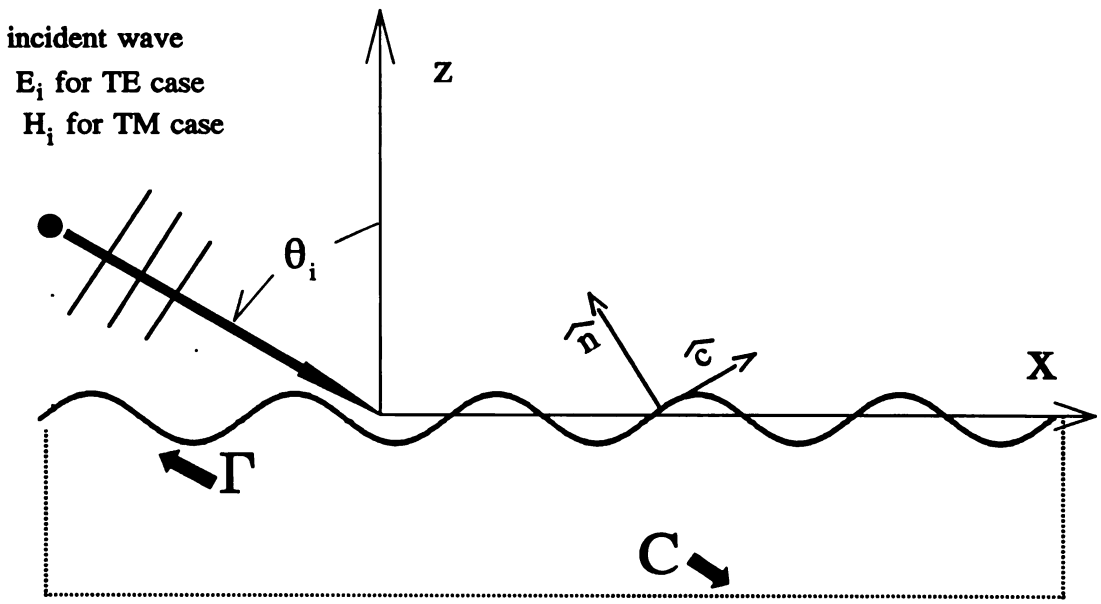

Figure 3.10 Finite, conducting sinusoidal surface scattering geometry.

The general approach is very similar to the infinite-surface case, in that an IE for the induced surface current must be solved prior to the typical determination of the scattered field using the 2-D free space Green's function.

The configuration and the nomenclature is the same as the infinite case except that the surface is truncated (See Figure 3.10). Since the E-field is polarized transversely, the induced surface current is also only transversely directed as $\vec{K}(x,z) = \hat{y}K_y(x,z)$. This current then can be used to find the scattered E-field,

$$E_s(x,z) = -\hat{y}\frac{\omega\mu_o}{4}\int_\Gamma K_y(x',z')H_o^{(2)}(k\,|\,\vec{\rho}-\vec{\rho}'\,|)dl' \tag{3.38}$$

where $\vec{\rho}$ is the position vector in the x-z plane, Γ describes the contour of the surface, and $H_o^{(2)}$ is the second kind Hankel function of order zero.

To obtain an integral equation for the currents, the boundary condition on the electric field is applied at the conductor surface. Substituting the scattered field into boundary condition yields the integral equation for the unknown surface current distribution $K_y(x,z)$ as

$$\int_\Gamma K_y(x',z')\ H_o^{(2)}(k\,|\,\vec{\rho}-\vec{\rho}'\,|)dl' = \frac{4}{k\eta}A_o e^{-j\beta x}e^{-jqz} \tag{3.39}$$

A MoM numerical solution is then implemented to solve the above integral equation. The current is expanded in a set of pulse basis functions and point matching is implemented. This results in a square matrix equation for the unknown current coefficients. In typical fashion the scattered field (3.38) can be determined numerically subsequent to evaluating the induced currents. For a far-zone scattered field, the asymptotic form of the Hankel function can be used to simplify the numerical integration [48]. Results comparing the infinite surface scattered fields with the finite surface response are provided, and in addition direct comparisons with experimental results can be made, because the finite surface is physically realizable.

3.2.4 Preliminary results of TE finite case.

The induced current for a finite PEC sinusoid is compared to the current induced on an infinite sinusoid. In Figure 3.11 the currents induced on a 5 period sinusoid, a 3 period sinusoid an the current for one period of an infinite sinusoid are seen to agree quite well. The effects of the edge of the finite surface are also evident (note that the incident wave is coming from the left). This result helps to establish the idea that the response from a periodic finite surface would match that of an infinite surface provided there is a sufficient number of periods for the finite model. This idea is used extensively

for the scattered field responses, which are obtained experimentally from a finite surface and are compared favorably to the responses from an infinite surface.

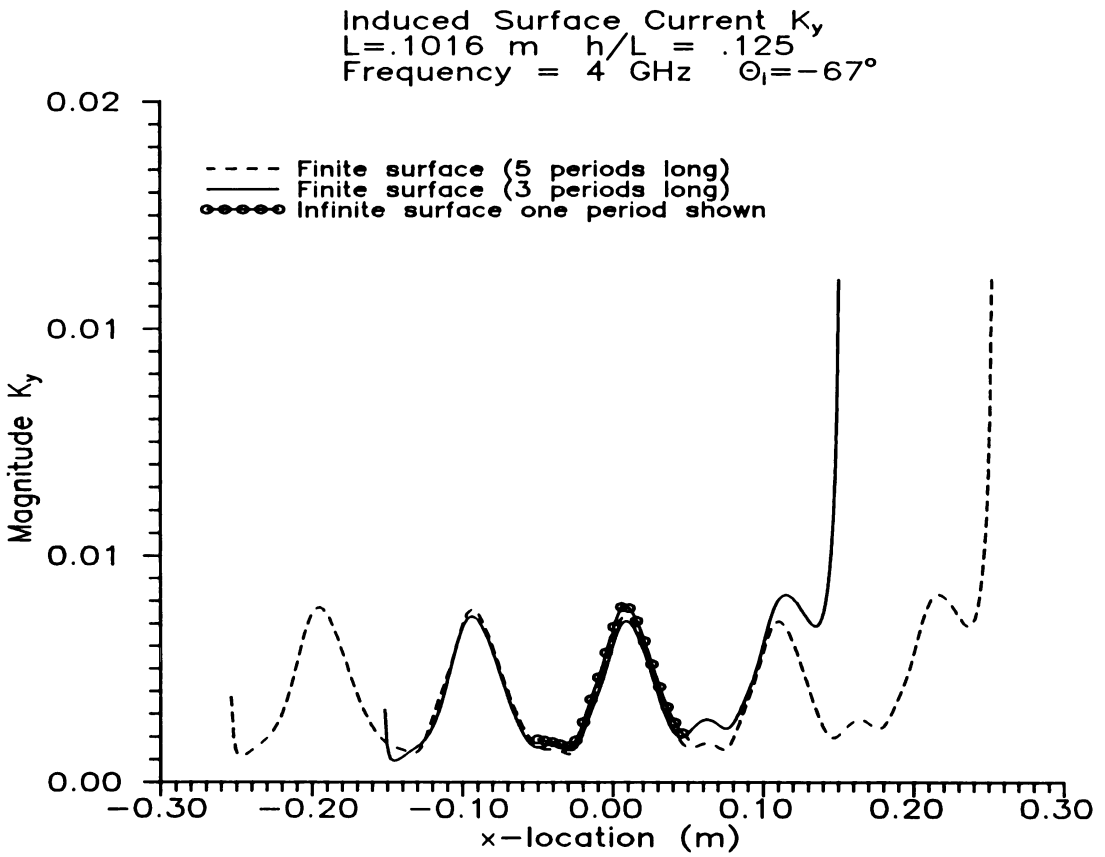

Figure 3.11 Comparison of induced surface currents on finite and infinite surfaces for TE excitation.

3.3 TM polarization

To complete the theoretical analysis, the other orthogonal polarization state is required. The scattering of a TM incident plane from a PEC sinusoidal is considered.

3.3.1 Infinite Surface

The surface configuration for this polarization state is the same as previously (see Figure 3.1) except the H-field is now directed transversely as $\vec{H}(x,z) = \hat{y}H_y(x,z)$ with the E-field parallel to the plane of incidence. Therefore by using $H_y(x,z)$ as the generating function in the same fashion as $E_y(x,z)$ was used for the TE polarization, similar analysis techniques may be employed. The electric field components can be found simply utilizing Maxwell's equations for this two-dimensional problem. The infinite PEC surface will be considered first, and once again it is possible to utilize the Rayleigh hypothesis for an adequately shallow sinusoidal surface, while a magnetic field integral equation (MFIE) will be developed for the infinite case.

Method I) Floquet Mode Matching\Rayleigh Hypothesis Analysis

Letting $\psi(x,z)$ represent the generating wave function ($H_y(x,z)$), an identical set of steps can be followed as in the TE development ((3.1) to (3.10)). That is, the total magnetic field is subjected to the 2-D Helmholtz equation and the Rayleigh hypothesis is invoked.

The total field is decomposed into the superposition of incident and scattered components as

$$\psi(x,z) = \psi_i(x,z) + \psi_s(x,z) = \text{incident wave} + \text{scattered wave} \qquad (3.40)$$

where the incident plane wave takes the form

$$\psi_i(x,z) = A_0 e^{-j\vec{k}\cdot\vec{r}} = A_0 e^{-j(k_x x + k_y y)} = A_0 e^{-j\beta x} e^{jqz} \qquad (3.41)$$

and the scattered magnetic field (via Rayleigh hypothesis)

$$\psi_s(x,z) = \sum_{n=-\infty}^{\infty} B_n e^{-j\beta_n x} e^{-jq_n z} \tag{3.42}$$

with identical definitions of β, q, β_n, q_n *and* k as the TE case.

The difference between the TE and TM polarization is manifested in the boundary condition (Neumann). The tangential electric field must vanish at the conductor, and this condition is satisfied if the normal derivative of the magnetic field vanishes at the conducting surface, therefore, the boundary condition at the ocean surface requires

$$\frac{\partial \psi}{\partial n} = \hat{n} \cdot \nabla(\psi_i + \psi_s) = 0 \quad \text{... at the sea surface } z = \rho \ . \tag{3.43}$$

The normal vector $\hat{n}$ to the ocean surface can be constructed in the following manner. Consider the 2-D scalar field $\Phi(x,z) = z - \rho(x)$, then $\Phi = 0$ defines the surface $z = \rho(x)$. The required surface normal is consequently

$$\hat{n} = \frac{\nabla\Phi}{|\nabla\Phi|} = \frac{\hat{z} - \hat{x}\dfrac{\partial\rho}{\partial x}}{\sqrt{1 + \left(\dfrac{\partial\rho}{\partial x}\right)^2}} \tag{3.44}$$

and satisfaction of boundary condition (3.43) consequently requires

$$-\frac{\partial\rho}{\partial x}\frac{\partial}{\partial x}(\psi_i + \psi_s) + \frac{\partial}{\partial z}(\psi_i + \psi_s) = 0 \ . \tag{3.45}$$

Combining (3.41) and (3.42) leads to

$$\psi_i + \psi_s = A_0 e^{-j\beta x} e^{jqz} + \sum_{n=-\infty}^{\infty} B_n e^{-j\beta_n x} e^{-jq_n z} \tag{3.46}$$

so condition (3.45) requires

$$\begin{aligned} -\frac{\partial\rho}{\partial x}\left(-j\beta A_0 e^{-j\beta x} e^{jqz} + \sum_{n=-\infty}^{\infty} -j\beta_n B_n e^{-j\beta_n x} e^{-jq_n z} \right) \\ + \left(jqA_0 e^{-j\beta x} e^{jqz} + \sum_{-\infty}^{\infty} -jq_n B_n e^{-j\beta_n x} e^{-jq_n z} \right) = 0 \end{aligned} \tag{3.47}$$

Since $\beta_n = \beta + 2n\pi/L$, then (3.47) carries a common factor of $\exp(-j\beta x)$, and implementing the boundary condition at $z = \rho = -h\cos(2\pi x/L)$ provides

$$\sum_{n=-\infty}^{\infty} B_n\left(\beta_n\frac{\partial\rho}{\partial x} - q_n\right)e^{-j2n\pi x/L}e^{-jq_n\rho} = -A_0\left(\beta\frac{\partial\rho}{\partial x} + q\right)e^{jq\rho} \tag{3.48}$$

The factor $\exp(-jq_n\rho)$ in (3.48) destroys the orthogonality of the $\exp(-j2n\pi x/L)$. Galerkin's method is therefore applied with the testing operator (3.12) leading to

$$\begin{aligned}\sum_{n=-\infty}^{\infty} B_n\int_0^L\left(\beta_n\frac{\partial\rho}{\partial x} - q_n\right)e^{j2\pi(m-n)x/L}e^{-jq_n\rho}\,dx \\ = -A_0\int_0^L\left(\beta\frac{\partial\rho}{\partial x} + q\right)e^{j2\pi mx/L}e^{jq\rho}\,dx\end{aligned} \tag{3.49}$$

This result is an infinite matrix equation for the unknown B_n, and can be written as

$$\sum_{n=-\infty}^{\infty} H_{mn}B_n = A_0D_m \quad \ldots\ \forall\ 0\le|m|<\infty \tag{3.50}$$

where the various coefficients are defined by

$$H_{mn} = \frac{j}{L}\int_0^L\left[\beta_n\frac{\partial\rho}{\partial x} - q_n\right]e^{j2\pi(m-n)x/L}e^{-jq_n\rho}\,dx \tag{3.51}$$

$$D_m = -\frac{j}{L}\int_0^L\left[\beta\frac{\partial\rho}{\partial x} + q\right]e^{j2\pi mx/L}e^{jq\rho}\,dx \tag{3.52}$$

The integrals in the definitions of coefficients (3.51) and (3.52) can be evaluated in closed form to obtain

$$\begin{aligned}H_{mn} = \frac{\pi h\beta_n}{l}\left[j^{|m-n+1|}J_{|m-n+1|}(q_nh) - j^{|m-n-1|}J_{|m-n-1|}(q_nh)\right] \\ -jq_n\,j^{|m-n|}J_{|m-n|}(q_nh)\end{aligned} \tag{3.53}$$

$$\begin{aligned}D_m = -\frac{\pi h\beta}{L}\left[j^{-|m+1|}J_{|m+1|}(qh) - j^{-|m-1|}J_{|m-1|}(qh)\right] \\ -jq\,j^{-|m|}J_{|m|}(qh)\end{aligned} \tag{3.54}$$

The infinite matrix equation (3.50) can be truncated to obtain an approximate solution for the complex amplitudes of the spatial harmonics. Convergence of the harmonic series must be tested numerically, and depends upon the relative height and period of the ocean surface normalized to the wavelength of the incident radiation.

Method II) MFIE-MoM Analysis

The scattering of TM polarized plane waves by a perfectly conducting, periodic surface can also be analyzed using an integral-operator-based method. The governing integral equation is in terms of the unknown H-field at the PEC surface, and the kernel consists of the normal derivative of the periodic Green's function

$$\frac{H(x,z)}{2} - PV\int_{C_p} H(x',z')\frac{\partial G(x,z|x',z')}{\partial n'}dl' = H_i(x,z) \qquad ...\forall \ \{x,z\} \in C_p \quad (3.55)$$

where the PGF $G(x,z|x',z')$ is given by (3.24), and $H_i(x,z)$ is the incident plane wave. The notation PV indicates that the integral must be evaluated in the principal-value sense. The integration path C_p is one period of the surface, because the PGF accounts for the inherent periodicity of the solution. Refer to Appendix C for the details on obtaining the above integral equation.

Subsequent to solution of MFIE (3.55) for surface field ψ, the far-zone scattered field can be calculated as

$$H_y^s(x,z) = \lim_{z\to\infty}\int_{C_p} \psi(\vec{\rho}')\frac{\partial G(\vec{\rho}\,|\,\vec{\rho}')}{\partial n'}dl' . \quad (3.56)$$

A MoM numerical solution to MFIE (3.55) is implemented by expanding the unknown surface magnetic field H in basis set $\{f_q\}$ as

$$H(x,z) = \sum_{q=1}^{N} a_q f_q(x,z) \quad (3.57)$$

and point matching the MFIE (3.55) at N points (x_p,y_p) on the first ocean-surface period C_p, leading to the matrix equation

$$\sum_{q=1}^{N} A_{pq} a_q = F_p \quad \cdots \; p = 1,2,\cdots,N \tag{3.58}$$

where the matrix elements are given by

$$A_{pq} = \frac{f_q(x_p,z_p)}{2} - PV\int_{C_p} f_q(x',z') \frac{\partial G(x_p,z_p|x',z')}{\partial n'} dl' \tag{3.59}$$

and the forcing vector is

$$F_p = H_0 e^{-j\beta x_p} e^{jqz_p} \tag{3.60}$$

A pulse-function basis set was used to implement the numerical solution. The first period $0 \le x \le L$ of the ocean surface is partitioned into N segments, each of length $\Delta x = L/N$, between end points $x_q = (q-1)\Delta x$ for $q = 1,2,\cdots,N+1$. Corresponding points on the surface are located by $z_q = \rho(x_q)$. The pulse functions are then defined by (3.33). The partitioning scheme is the same as was used for the TE case and can be visualized in Figure 3.3.

For the purpose of evaluating the integrals in matrix elements (3.59), the ocean surface is modelled as piecewise linear between partition end points x_q with slope $m_q = (z_{q+1} - z_q)/\Delta x$. An element of displacement along the ocean surface is $dl = S(x)dx$ with $S(x) = \sqrt{1 + (dz/dx)^2}$ such that within the q'th partition $dl' = S_q dx'$ with $S_q = \sqrt{1 + m_q^2}$. The matching points are located by $\bar{x}_p = x_p + \Delta x/2$, $\bar{z}_p = z_p + m_p \Delta x/2$. Matrix elements (3.59) are consequently calculated from

$$A_{pq} = \frac{f_q(\bar{x}_p,\bar{z}_p)}{2} - S_q PV\int_{x_q}^{x_q+\Delta x} \frac{\partial G(\bar{x}_p,\bar{z}_p|x',z')}{\partial n'} dx' \quad . \tag{3.61}$$

The normal derivative of the periodic Green's function can be evaluated as

$$\frac{\partial G}{\partial n'} = \frac{1}{2LS(x')} \sum_{n=-\infty}^{\infty} \left[-\frac{\beta_n \rho'(x')}{q_n} + sgn(z - z') \right] e^{-j\beta_n(x-x')} e^{-jq_n|z-z'|} \tag{3.62}$$

and expression (3.61) leads to

$$A_{pq} = \frac{\delta_{pq}}{2} - \frac{1}{2L}\sum_{n=-\infty}^{\infty} e^{-j\beta_n \bar{x}_p} \int_{x_q}^{x_q+\Delta x} \left[-\frac{\beta_n m_q}{q_n} + sgn(\bar{z}_p - z') \right] e^{j\beta_n x'} e^{-jq_n|\bar{z}_p - z'|} dx' \qquad (3.63)$$

where $z' = z_q + m_q(x' - x_q)$ for $x_q \le x' \le (x_q + \Delta x)$.

Finally, the integrals in (3.63) can be evaluated in closed form, leading to:

CASE 1: $\bar{z}_p \neq \bar{z}_q$, $\alpha_{nq} = \beta_n + sgn(\bar{z}_p - \bar{z}_q) q_n m_q$

$$A_{pq} = \frac{\delta_{pq}}{2} - \frac{1}{L}\sum_{n=-\infty}^{\infty} \left[-\frac{\beta_n m_q}{q_n} + sgn(\bar{z}_p - \bar{z}_q) \right] e^{-j\beta_n(\bar{x}_p - \bar{x}_q)} e^{-jq_n|\bar{z}_p - \bar{z}_q|} \frac{\sin(\alpha_{nq}\Delta x/2)}{\alpha_{nq}} \qquad (3.64)$$

CASE 2: $\bar{z}_p = \bar{z}_q$, $|\bar{z}_p - z'| = \bar{m}_q |x' - \bar{x}_q|$ with $\bar{m}_q = |m_q|$

$$\begin{aligned} A_{pq} = \frac{\delta_{pq}}{2} + \frac{sgn(m_q)}{L} \sum_{n=-\infty}^{\infty} \frac{e^{-j\beta_n(\bar{x}_p - \bar{x}_q)}}{\beta_n^2 - (q_n \bar{m}_q)^2} \Bigg[& j\beta_n(\bar{m}_q^2 + 1) \\ & + \left(\frac{\beta_n^2}{q_n} + q_n \right) \bar{m}_q e^{-jq_n \bar{m}_q \Delta x/2} \sin\left(\frac{\beta_n \Delta x}{2} \right) \\ & - j\beta_n(\bar{m}_q^2 + 1) e^{-jq_n \bar{m}_q \Delta x/2} \cos\left(\frac{\beta_n \Delta x}{2} \right) \Bigg] \end{aligned} \qquad (3.65)$$

The infinite series in case 2 consists of the sum of three terms, the first of which has no exponential decay and is therefore very slowly convergent. It is consequently necessary to accelerate the convergence of the series associated with that term. The summand of that first term is

$$f_n = \frac{sgn(m_q)}{L} \frac{e^{-j\beta_n(\bar{x}_p - \bar{x}_q)}}{\beta_n^2 - (q_n \bar{m}_q)^2} j\beta_n(\bar{m}_q^2 + 1) \qquad (3.66)$$

which for large $|n|$ has the asymptotic form

$$f_n^a = \frac{j\,sgn(m_q)}{2\pi} \frac{e^{-j2\pi n(\bar{x}_p - \bar{x}_q)/L}}{n} \qquad (3.67)$$

and decays only as n^{-1}. The convergence of the first term in the series of (3.65) can be accelerated by subtracting and adding (for $n \neq 0$) the asymptotic form (3.67) in its

summand. The subtracted term renders the resulting series rapidly convergent, while the series involving the added term can be summed in closed form. Combining the terms arising from $+n$ and $-n$ leads to

$$\sum_{n=1}^{\infty}\left(f_n^c + f_{-n}^c\right) = \frac{sgn(m_q)}{\pi}\sum_{n=1}^{\infty}\frac{\sin[2\pi n(\bar{x}_p - \bar{x}_q)/L]}{n} = sgn(m_q)\,\frac{\pi - |\psi|}{2\pi}\,sgn(\psi) \tag{3.68}$$

where $\psi = 2\pi(\bar{x}_p - \bar{x}_q)/L$, and use has been made of the summed series

$$\sum_{k=1}^{\infty}\frac{\sin(kx)}{k} = \frac{\pi - x}{2} \quad \text{... for } 0 \le x \le 2\pi \ . \tag{3.69}$$

Subsequent to solution of MoM matrix equation (3.57) for the a_q, the scattered field at points above the ocean surface can be obtained from expression (3.56) as

$$H_y^s(x,z) = \frac{1}{L}\sum_{q=1}^{N} a_q \sum_{n=-\infty}^{\infty}\left(-\frac{\beta_n m_q}{q_n} + 1\right) e^{-j\beta_n(x-\bar{x}_q)} e^{-jq_n(z-\bar{z}_q)}\,\frac{\sin[(\beta_n + q_n m_q)\Delta x/2]}{\beta_n + q_n m_q} \tag{3.70}$$

The backscattered field is obtained from (3.70) by restricting the sum over n to include only those Floquet modes which are propagating (q_n real) in the -x direction ($\beta_n < 0$).

3.3.2 Preliminary results for the TM infinite case

Preliminary results for the surface fields induced on a PEC infinite sinusoid for a TM incident plane wave are given below. These results are analogous to the TE results in 3.2.2. The comparison of the Floquet mode-matching and MFIE methods are shown back in Figure 3.5. The magnitude of the induced surface currents can be seen to match for both of the analytical methods. This serves as check for the numerical implementation of the methods and as a confirmation of the theory. It should be noted that currents induced by a TM incident plane wave will have both x- and z-components. This is because $\vec{K} = \hat{n} \times \hat{y}H_y$, which is a vector tangential to the sinusoidal surface. A vector $\hat{c}$ is defined as $\hat{n} \times \hat{y}$ and is the direction of the induced current (K_c). The following plots are all of the magnitude of K_c or equivalently H.

In Figure 3.12 the induced currents dependence on incidence angle is shown. Once again as the incidence angle is increased the side of the illuminated sinusoid has a maximal current distribution. There is also an interesting effect due to the Floquet mode resonances. Just as the propagating Floquet modes can be turned on and off as the frequency is swept (See Figure 3.15) the same phenomena occurs for the incidence angles. Therefore a Floquet mode must be located around 30°, which explains the increased magnitude.

The effect of increasing the sinusoidal surface height is shown in Figure 3.13. In the limit of zero height (flat surface) the magnitude of the H-field should be double the incident field at PEC surface. This fact is observed in the figure for the smallest heights, where the unit incident field is doubled to a strength of 2.0. As the heights increase the familiar distribution is seen, with the shadow region becoming more defined.

In Figure 3.14 the sinusoidal surface period lengths (L) are varied. The results are rather intuitive in that as L is increased the surface appears to become flatter, which results in a current distribution tending towards a constant 2.0. For the shorter surface period lengths an opposite effect occurs and shadowing becomes more noticeable.

As alluded to earlier the effect of varying the frequency of incident TM field are shown in Figure 3.15. The Floquet mode resonances are more apparent and have a more dramatic effect on the induced current. Those modes occur at frequencies of 1.5, 2.95 and 4.4 GHz (See Table 3.1 on page 66).

These preliminary results once again give us confidence in the theoretical developments of the preceding sections.

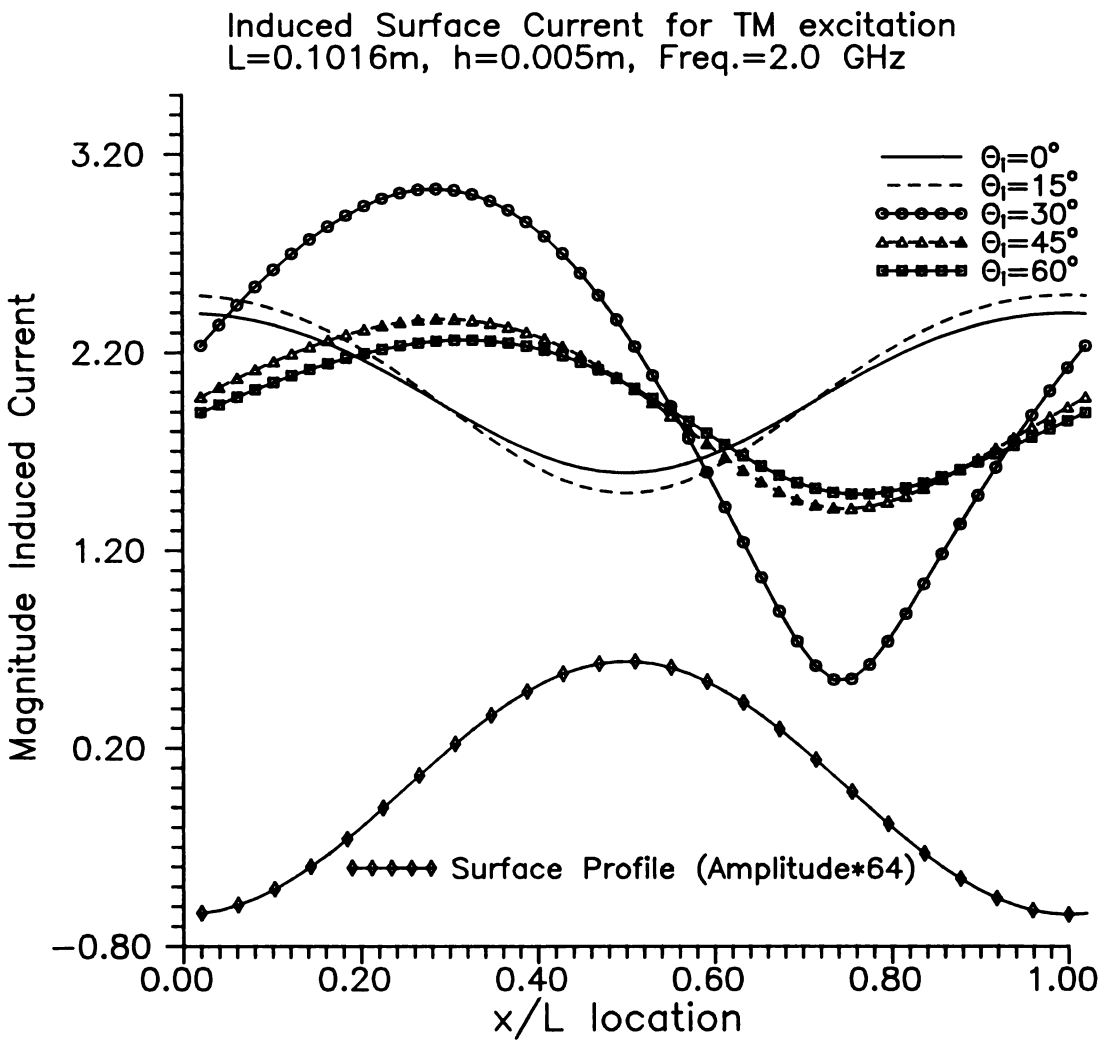

Figure 3.12 Dependence of currents induced on a PEC sinusoid for TM excitation for various incidence angles.

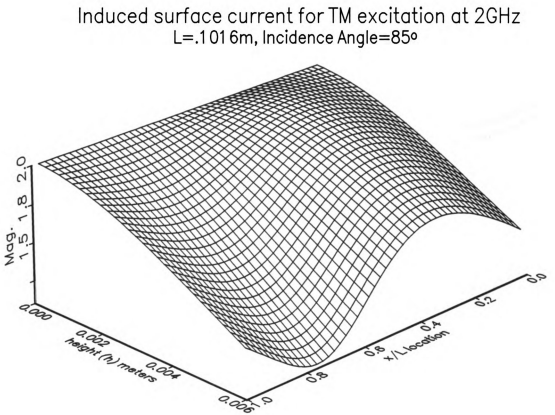

Figure 3.13 Dependence of currents induced on a PEC sinusoid for TM excitation for various surface heights.

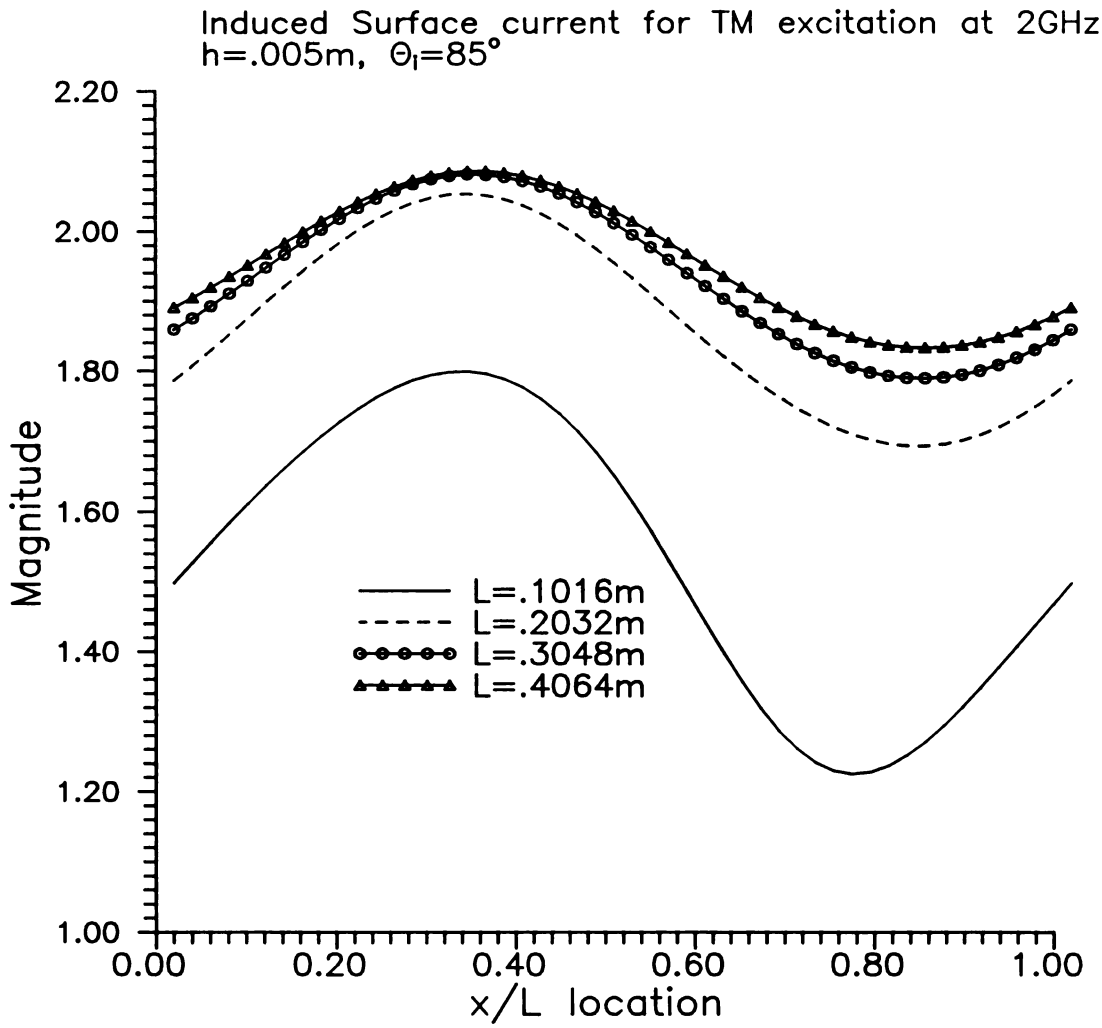

Figure 3.14 Dependence of currents induced on a PEC sinusoid for TM excitation for various surface period lengths (L).

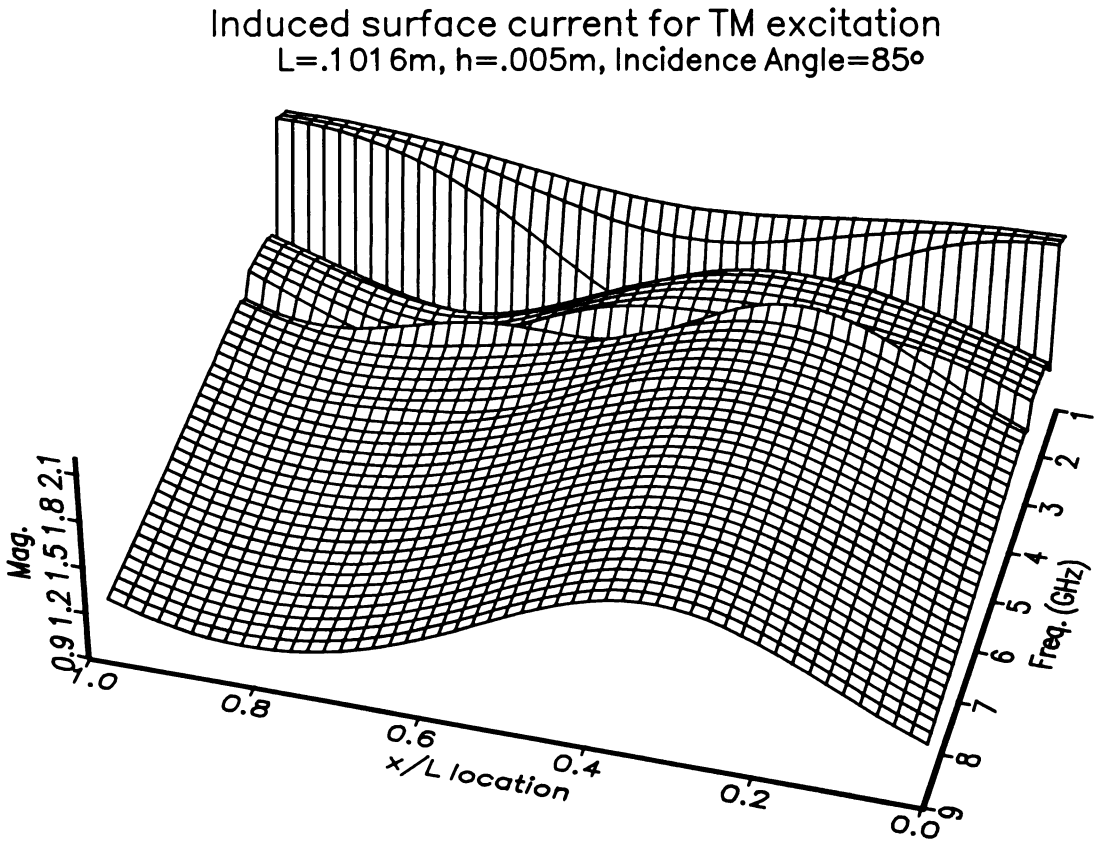

Figure 3.15 Dependence of currents induced on a PEC sinusoid for various TM excitation frequencies.

3.3.3 TM finite surface scattering

The analysis for the TM plane wave scattering from a finite PEC sinusoidal surface follows closely to techniques employed for the other integral-operator methods. Considering the geometry in Figure 3.10 with an incident H-field in the transverse direction, the scattered H-field can be determined, if the induced surface fields are known,

$$H_s(x,z) = \frac{j}{4}\int_{C+\Gamma}\vec{K}_s(x',z')\times\nabla H_o^{(2)}(kR)\,dc' \tag{3.71}$$

The contour needed for the MFIE is a closed contour and is denoted by $C+\Gamma$, and $\hat{c}$ is the unit vector tangential to the surface. The induced surface current $\vec{K}_s(x,z)$ can be rewritten as $\hat{c}(x,z)K_c(x,z)$ and the gradient of the second kind Hankel function can be evaluated (note R is distance between source and observation points) yielding,

$$H_s(x,z) = \frac{jk}{4}\int_{C+\Gamma}K_c(x',z')\,H_1^{(2)}(kR)\,[\hat{c}'\times\hat{R}]\,dc' \tag{3.72}$$

In order to determine the induced current a MFIE is implicated of the form

$$\frac{K_c(x,z)}{2} + \frac{jk}{4}PV\int_{C+\Gamma}K_c(x',z')\,H_1^{(2)}(kR)\,[\hat{c}(x',z')\times\hat{R}]\,dc' = H_i(x,z) \qquad \ldots\forall\,(x,z)\in C+\Gamma \tag{3.73}$$

Where the boundary condition on the tangential H-field has been applied.

A MoM numerical solution is then implemented to solve the above integral equation. The current is expanded in a set of pulse basis functions and point matching is implemented. This results in a square matrix equation for the unknown current coefficients. The scattered fields (3.71) can numerically be determined subsequent to performing the MoM numerical solution for the induced surface currents.

3.3.4 Preliminary results for the TM finite case

A comparison of the induced surface currents on a finite PEC sinusoid and an infinite PEC sinusoid are shown in Figure 3.16. The agreement is remarkable given the

construction of the finite surface. In order to create a MFIE for the finite surface a closed contour was required. This contour is shown in the figure. The edge effect of the finite surface is minimized by putting a curved endcap on the finite surface. The good agreement will serve as an argument for using the infinite surface responses in comparison to the experimentally obtained responses from a finite surface.

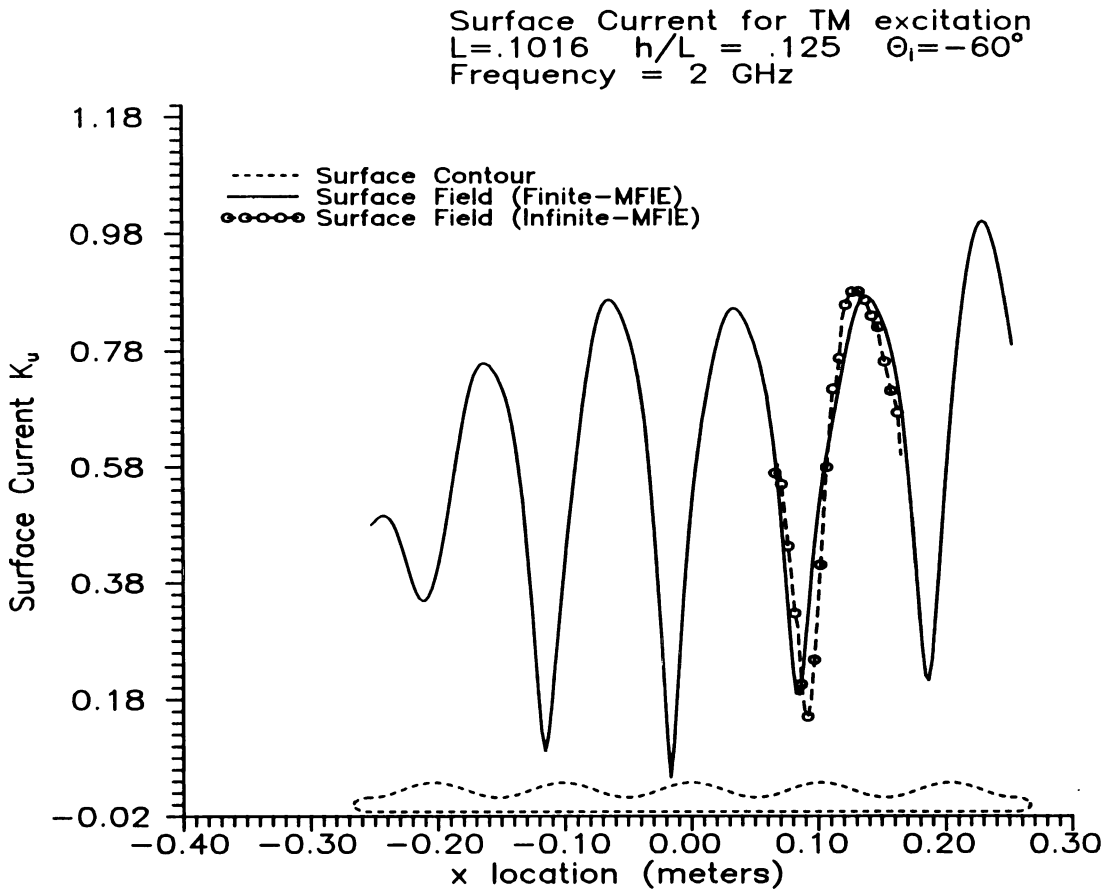

Figure 3.16 Comparison of induced surface currents on finite and infinite surfaces for TM excitation.

3.4 Cut-off frequency phenomena

As alluded to in the previous sections, an interesting cut-off phenomenon is associated with the scattered fields of the infinite periodic surface. The scattered Floquet modes from the infinite surface become evanescent in nature if $|\beta_n| > k$; there will be no real power flow away from the surface for such modes. This results in a cut-off frequency for each Floquet mode given as

$$(f_c)_n = \frac{|n|c}{L(1+\sin\theta_i)} \tag{3.74}$$

The n=0 mode (the specular reflection) has no low frequency cutoff, but all the other Floquet modes will exhibit a low frequency cut-off. As more Floquet modes begin to propagate and carry real power, an interference pattern is generated in the spectrum.

Also associated with the cut-off frequency is a maximal frequency for backscattered waves. For a Floquet mode to propagate backwards (-x direction) $\beta_n < 0$, and also the mode must be above cut-off frequency. Therefore, there exists a range of frequencies in which backward travelling Floquet modes can propagate. The maximal frequency is given by

$$(f_{max})_n = \frac{|n|c}{L\sin\theta_i} \tag{3.75}$$

Of note in the above equations is the lack of dependence on surface shape or height, only the period of the surface and incidence angle are involved. For L=0.1016 m, and an incidence angle of 85° a table of maximal and cut-off frequency for the backward travelling Floquet modes has been provided, in Table 3.1. A similar table (Table 3.2) is also provided for the case of a 67° incident angle.

Table 3.1 Low frequency cutoff and maximal frequency of backward Floquet modes. L=0.1016m, 85° incidence angle.

n	$(f_c)_n$ GHz	$(f_{max})_n$ GHz
-1	1.479	2.964
-2	2.958	5.928
-3	4.438	8.892
-4	5.916	11.86
-5	7.395	14.82

Table 3.2 Low frequency cutoff and maximal frequency of backward Floquet modes. L=0.1016m, 67° incidence angle.

n	$(f_c)_n$ GHz	$(f_{max})_n$ GHz
-1	1.537	3.117
-2	3.075	6.235
-3	4.613	9.526
-4	5.126	11.60
-5	9.226	19.25

3.5 Results and Experimental Confirmation

The primary interest is in the transient scattered field response of a sinusoidal surface. This can be obtained via a Fourier synthesis of the frequency domain results from the previous sections. Much physical insight is provided in the time domain that is not available in the frequency domain.

The goal of this chapter is to not only understand the transient scattering from infinite and finite sinusoidal surfaces, but to make a connection between the two. In the preliminary results a basis for this connection was established with the favorable surface current comparisons. This connection will serve as link between the experimental results for the finite surface and the hypothetical experimental results from an infinite surface. The theoretical finite surface scattering and the experimental finite surface results can be directly compared, then the theoretical finite and infinite surfaces can be compared in order to establish this link.

3.5.1 Infinite surface results

Two methods of analysis were employed for the infinite surface, the Floquet mode-matching and the integral equation (IE) method. As stated in the previous sections these methods have overlapping regimes of validity. The Floquet mode regime is limited by the surface slope being less than 0.448, meaning fairly smooth surfaces. This restriction should be strictly enforced for the near-zone fields, however we have noted that the far-zone fields are less affected by this restriction. Extending the Rayleigh hypothesis regime is not the subject of this thesis so we will stay within the strict limit. The IE method has no theoretical limits on surface slope or period length, but there are computational limits, such as matrix size, and matrix ill-conditioning.

The induced surface currents have been examined in the preliminary result sections. These currents give rise to the scattered fields, which are the primary interest of this thesis. These scattered fields are what an actual UWB/SP radar would receive. Both spectral and transient scattered field responses are examined and are interconnected.

This combination of time and frequency information is one of the strong points of UWB/SP radar.

The spectral domain scattered fields from a conducting sinusoidal surface (L=0.1016m, h/L =0.03565) generated by a TE plane wave with an incidence angle of 85° are calculated at an off-surface field point (x/L =0, z/L= 20) as a function of frequency over the bandwidth of 1-7 GHz. The spectral amplitudes of the total scattered field are computed by summing all the Floquet modes and the result is shown in Figure 3.17. The spectral amplitude of the backscattered field is computed by summing all Floquet modes propagating in the negative x-direction, and the result is shown in Figure 3.18. There are some interesting phenomena in these results. First, there are the cut-off and band-pass phenomena for the backscattered field as discussed in section 3.4. Also of note are the apparent nulls in the frequency domain of the total scattered field, demonstrating the frequency selectivity of the surface. The results shown in figures are produced by the Floquet mode-matching and IE methods, and they give almost identical results.

To find the time-domain, transient scattered field from the conducting sinusoidal surface created by a short pulse, the spectral results of the scattered field are inversely Fourier transformed. The short pulse used in this study is synthesized by inverting a uniform spectral response over a bandwidth of 1-7 GHz with a 1/8 cosine taper or Gaussian Modulated Cosine (GMC) windowings. The shapes of these two short pulses are shown in Figure 3.19. Consequently, the time-domain, transient scattered fields created by the short pulse can be obtained by inversely Fourier transforming the spectral results for the scattered field shown in Figure 3.17 and Figure 3.18 with the same weighting. The total scattered transient field created by a short pulse consists of large specular reflection followed by a small non-specular reflection after a time delay, as shown in Figure 3.20. For various incidence angles this time delay has been seen to change (see Figure 3.21). The non-specular reflections are stationary for the various

incidence angles. This is because the reflections all originate from directly below the field point and are in fact backscatter. The specular reflection is similar to that generated by a flat surface, although not all the energy is reflected.

The backscattered, transient field created by a short pulse, which is of major interest in this study, is shown in Figure 3.22. It is observed in this figure that the backscatttered response of a short pulse exhibits an expected periodic nature with the period correlating to the two-way transit time of the reflected wave between two crests of the sinusoidal surface. This response is dominated by the reflections of the short pulse from crests of the sinusoidal surface.

In Figure 3.23 is a close up of the non-specular reflection, referred to in the total scatter discussion regarding Figure 3.21, and is seen to actually be backscatter. Very interesting is the noticeable change in return pulse periods; this can be explained geometrically by examining the path lengths to the crests nearest to the field point that are contributing to the backscatter. By increasing the height of the sinusoid the backscattered field is enhanced as expected and shown in Figure 3.24. In addition, for the larger height sinusoids noticeable pulses are seen within the main crest pulses. This can be explained by the Rayleigh hypothesis. As these sinusoids are outside of the regime of validity, there must be multiple reflections occurring in the trough. Therefore additional reflections can be seen. It is worth noting that the nature of the total scattered field and the backscattered field are entirely different but they are consistent with physical intuition.

The dependence on surface period length is examined in Figure 3.25, where the transient backscattered fields from two surfaces of differing periods (L=.2032m and L=.4064m) and equal crest heights are compared. The separation distance between neighboring return pulses corresponds to the period length, but differing observation heights (z/L) lead to the unexpected return pulse period. Although the two surfaces have equal crest heights, it is interesting that the shorter period surface creates larger

amplitude return pulses. This phenomena can also be observed in the frequency domain (not shown). The difference in surface slopes lead to a physical explanation. The backscattered field is enhanced with the increased surface slopes, also there are noticeable multiple reflections on the shorter period surface.

Similar results are obtained for the TM excitation, including the Floquet modes cut-off frequencies, and the frequency selectivity. The total scattered magnetic field at a point located at z/L=20 is shown in Figure 3.26. The corresponding synthesized transient response for a GMC incident pulse is shown in Figure 3.27. The backscattered field for the same case as shown in Figure 3.28 (spectrum) and Figure 3.29 (synthesized transient response). The same phenomena as discussed for the TE excitation is observable for TM excitation. There will be more significant difference between the TE and TM cases when the sea-surface model is extended to be imperfectly conducting. This case is considered in the next chapter.

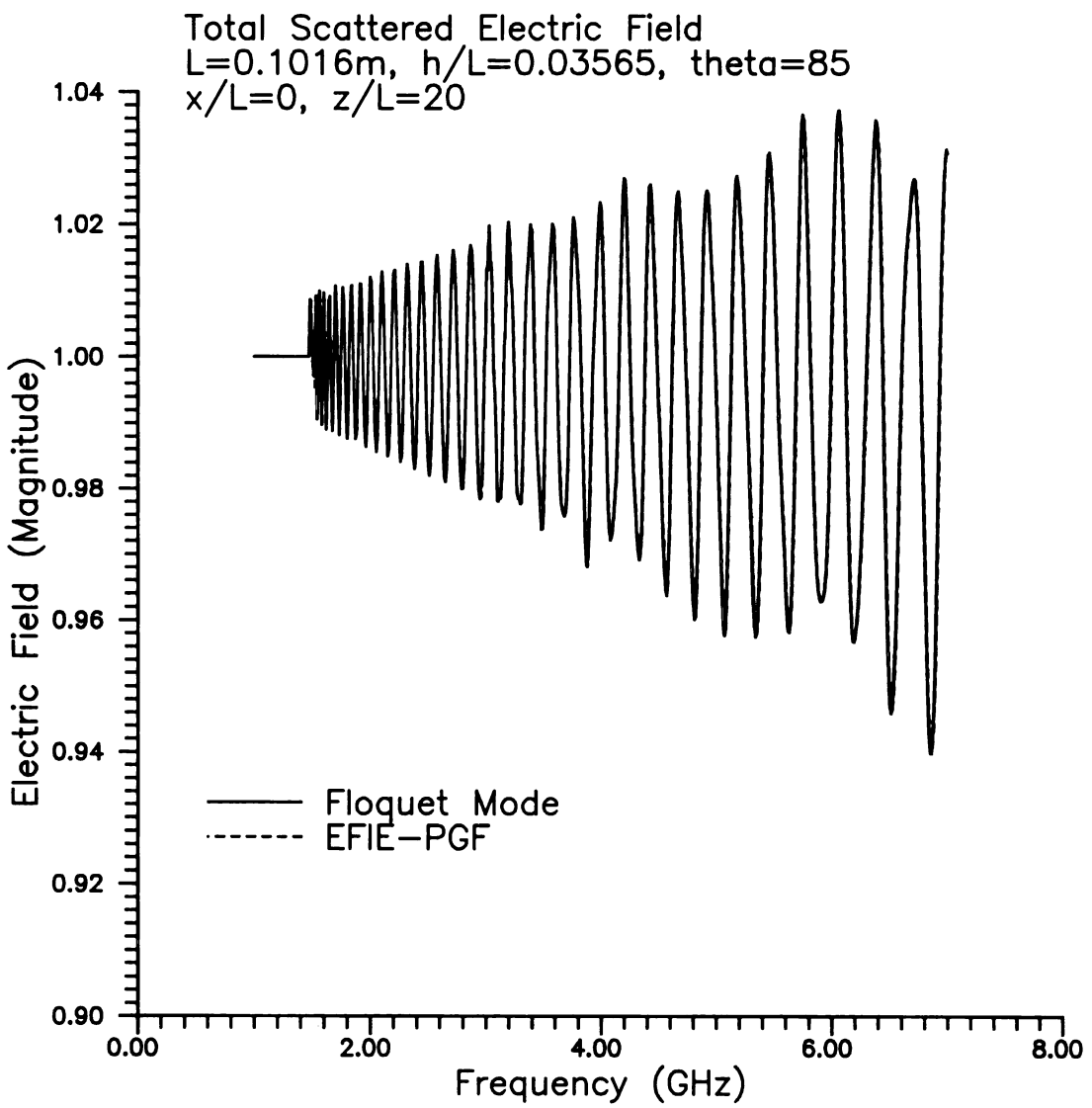

Figure 3.17 Magnitude of total scattered electric field from infinite, conducting sinusoidal surface as a function of frequency for TE excitation.

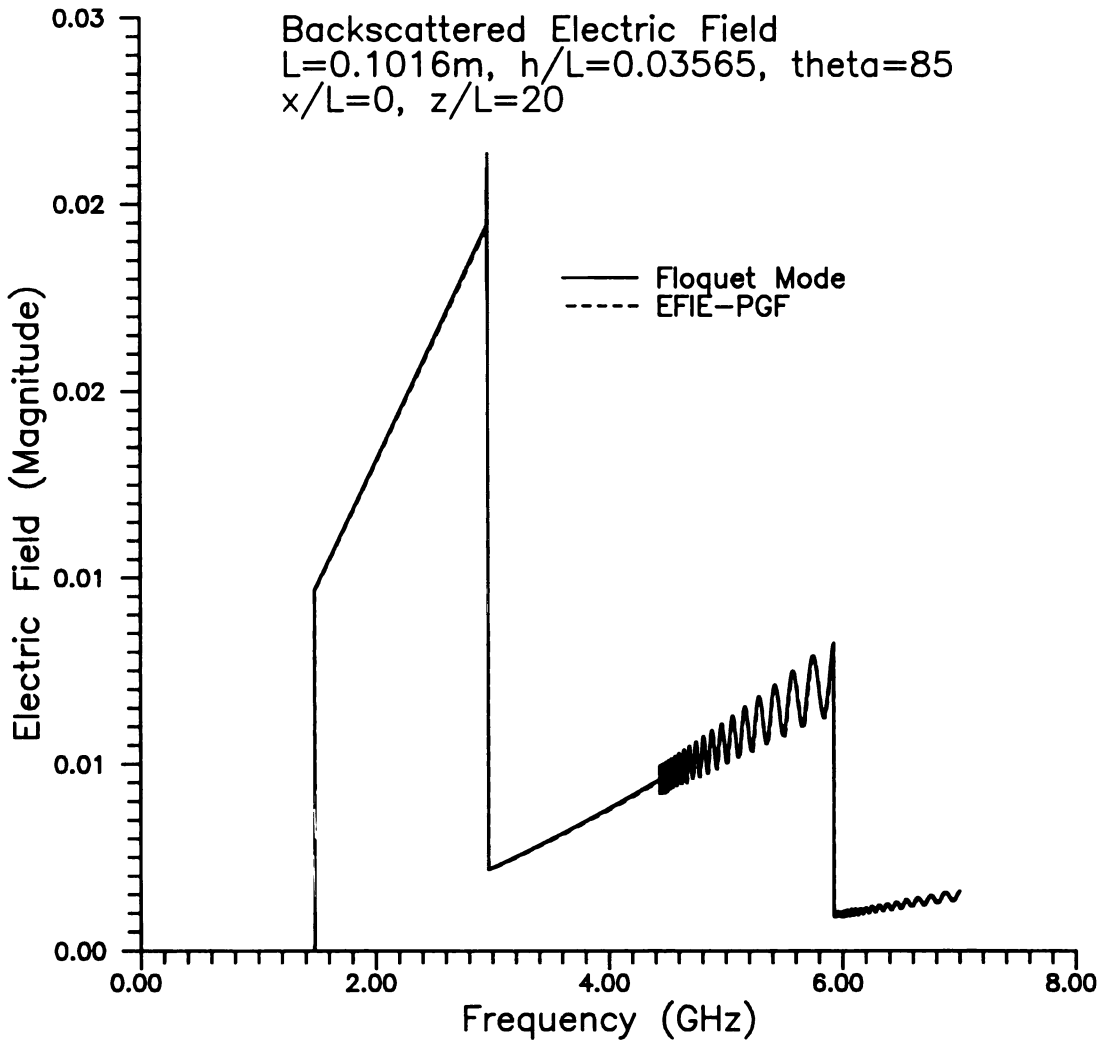

Figure 3.18 Magnitude of backscattered electric field from infinite, conducting sinusoidal surface for TE excitation as a function of frequency.

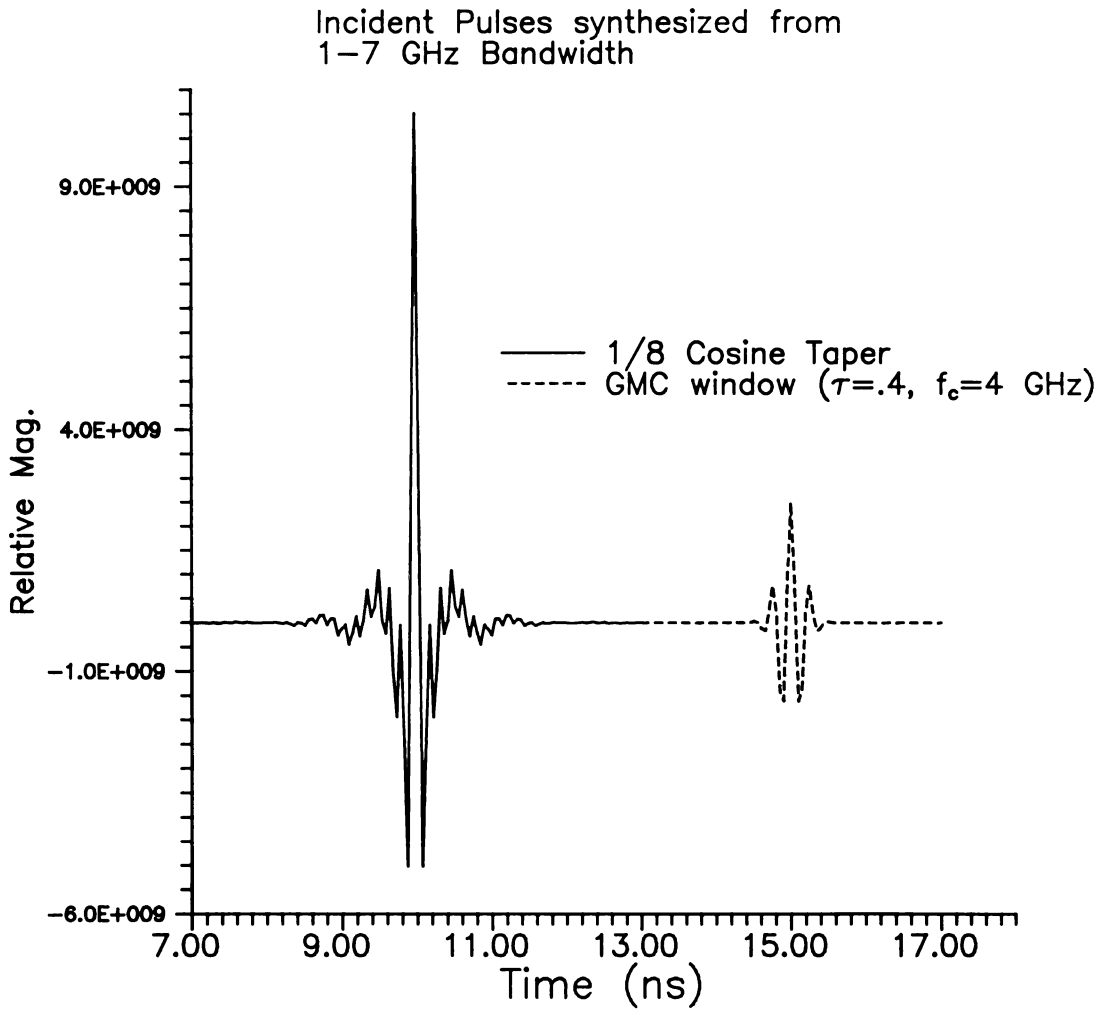

Figure 3.19 Synthesized pulses used for interrogation of conducting sinusoidal surfaces.

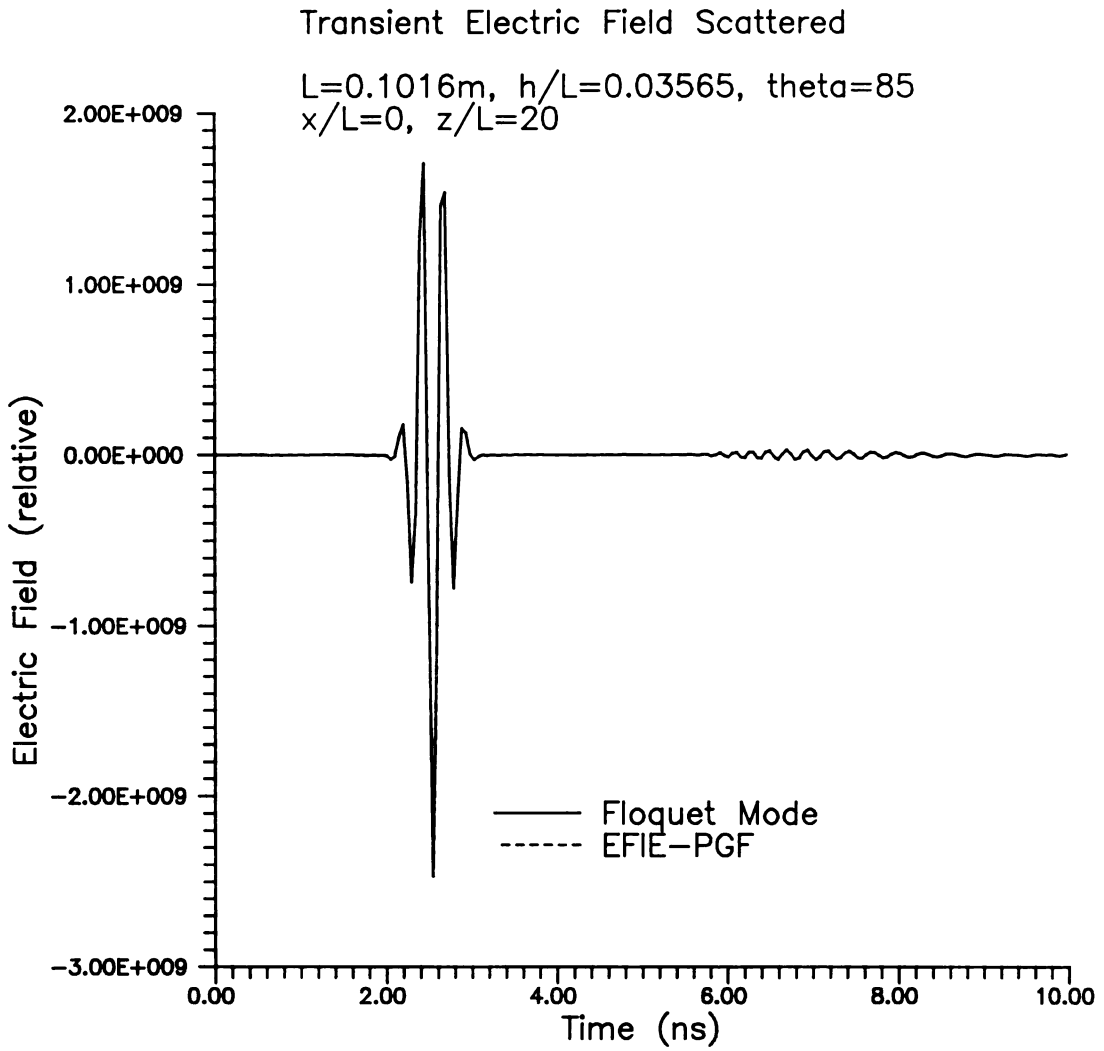

Figure 3.20 Total scattered electric field created by a GMC pulse from infinite, conducting sinusoidal surface for TE excitation.

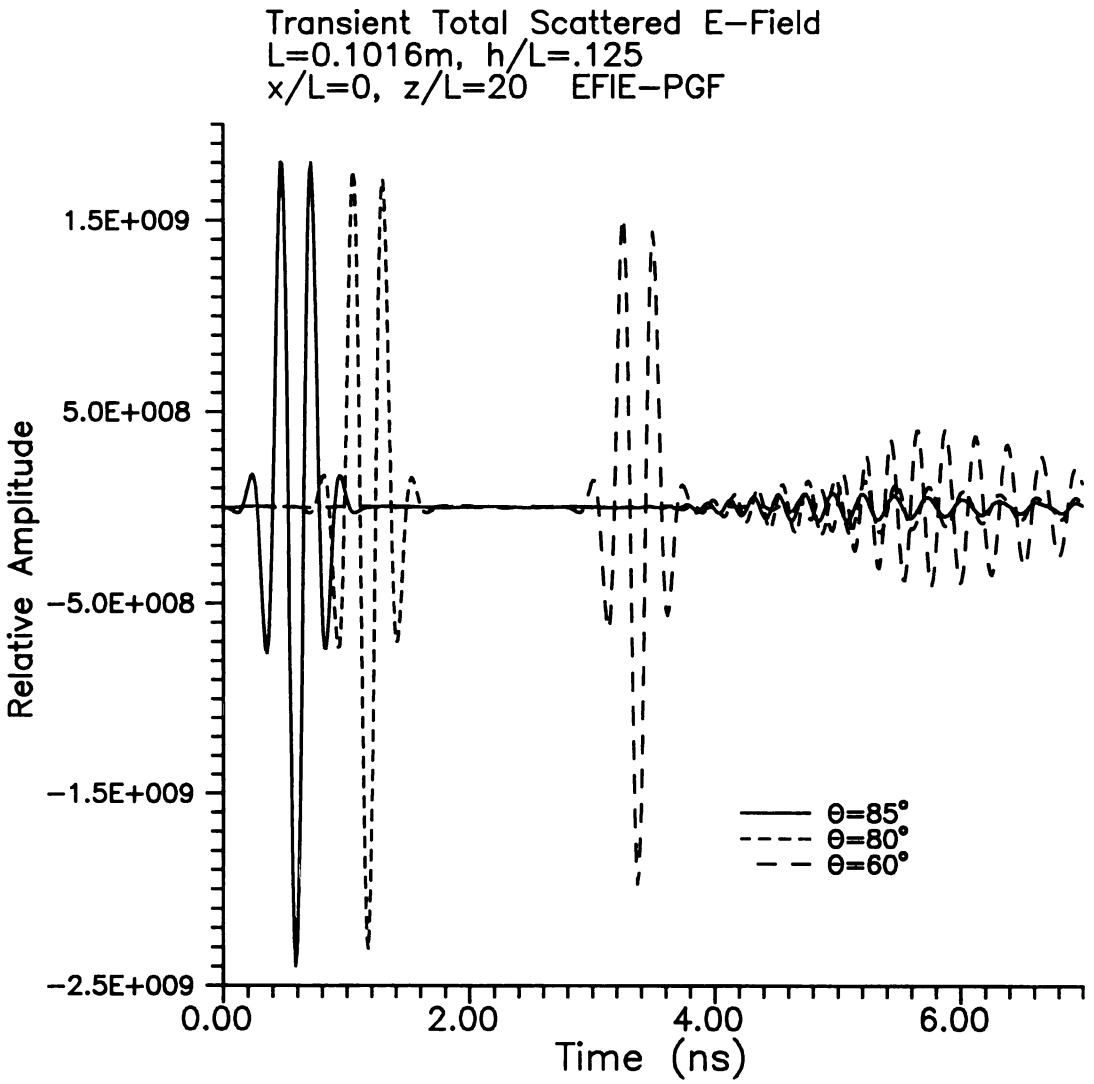

Figure 3.21 Comparison of transient total scattered electric fields created by a GMC pulse for various incidence angles upon an infinite sinusoidal surface for TE excitation.

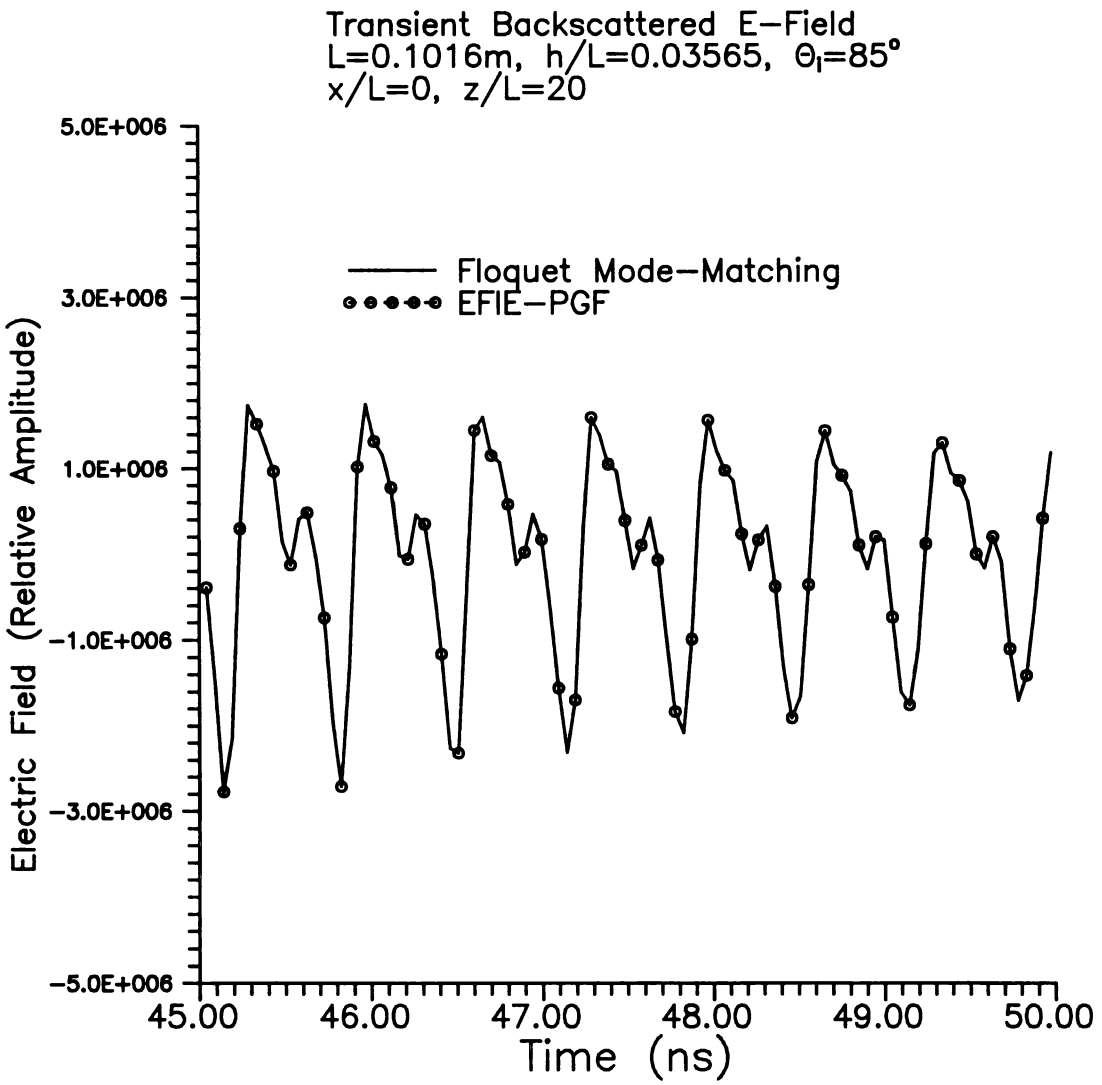

Figure 3.22 Transient backscattered electric field created by a 1/8 cosine pulse from infinite, conducting sinusoidal surface for TE excitation.

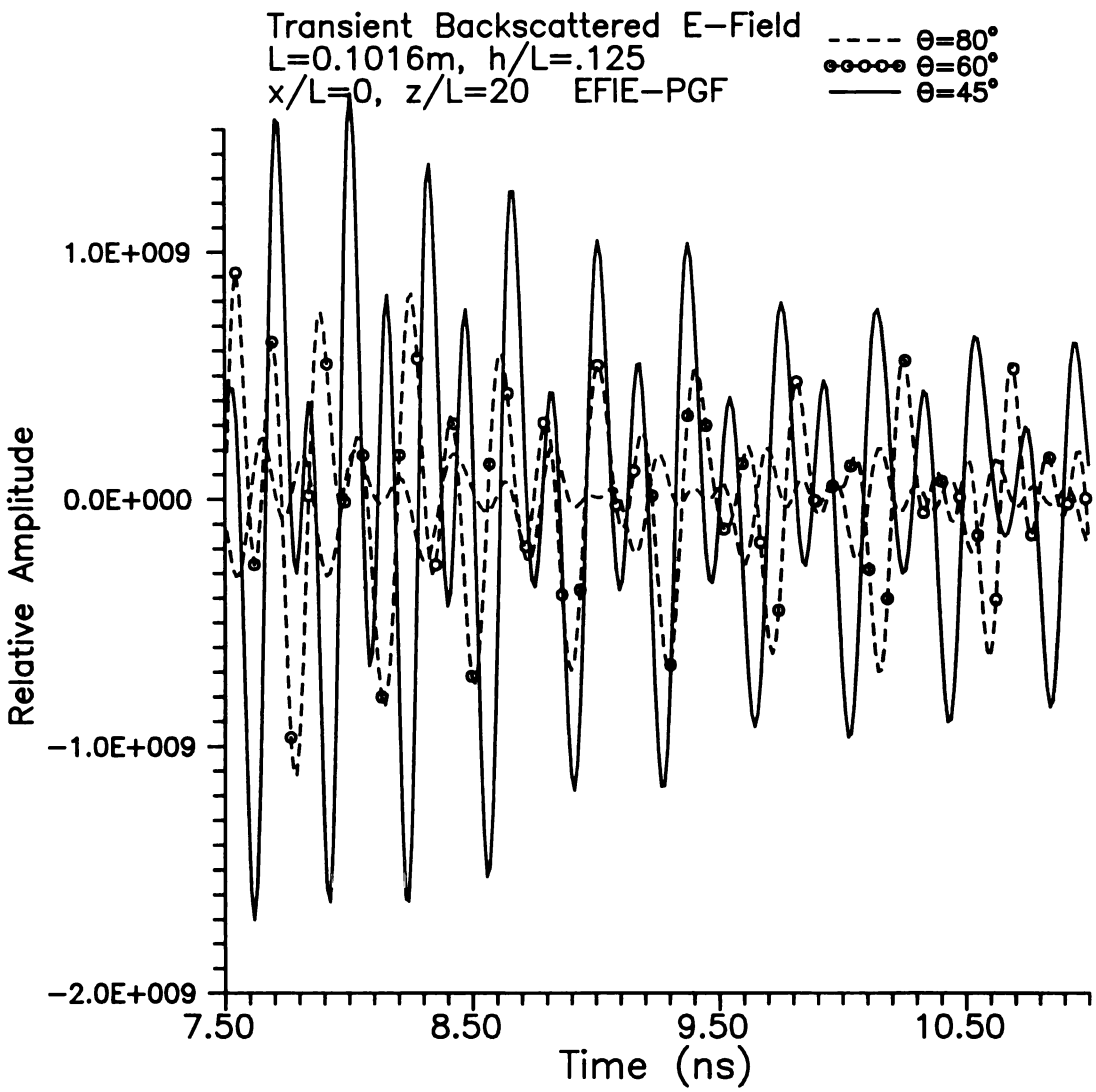

Figure 3.23 Comparison of transient backscattered electric fields created by a short pulse of various incidence angles upon an infinite sinusoidal surface for TE excitation.

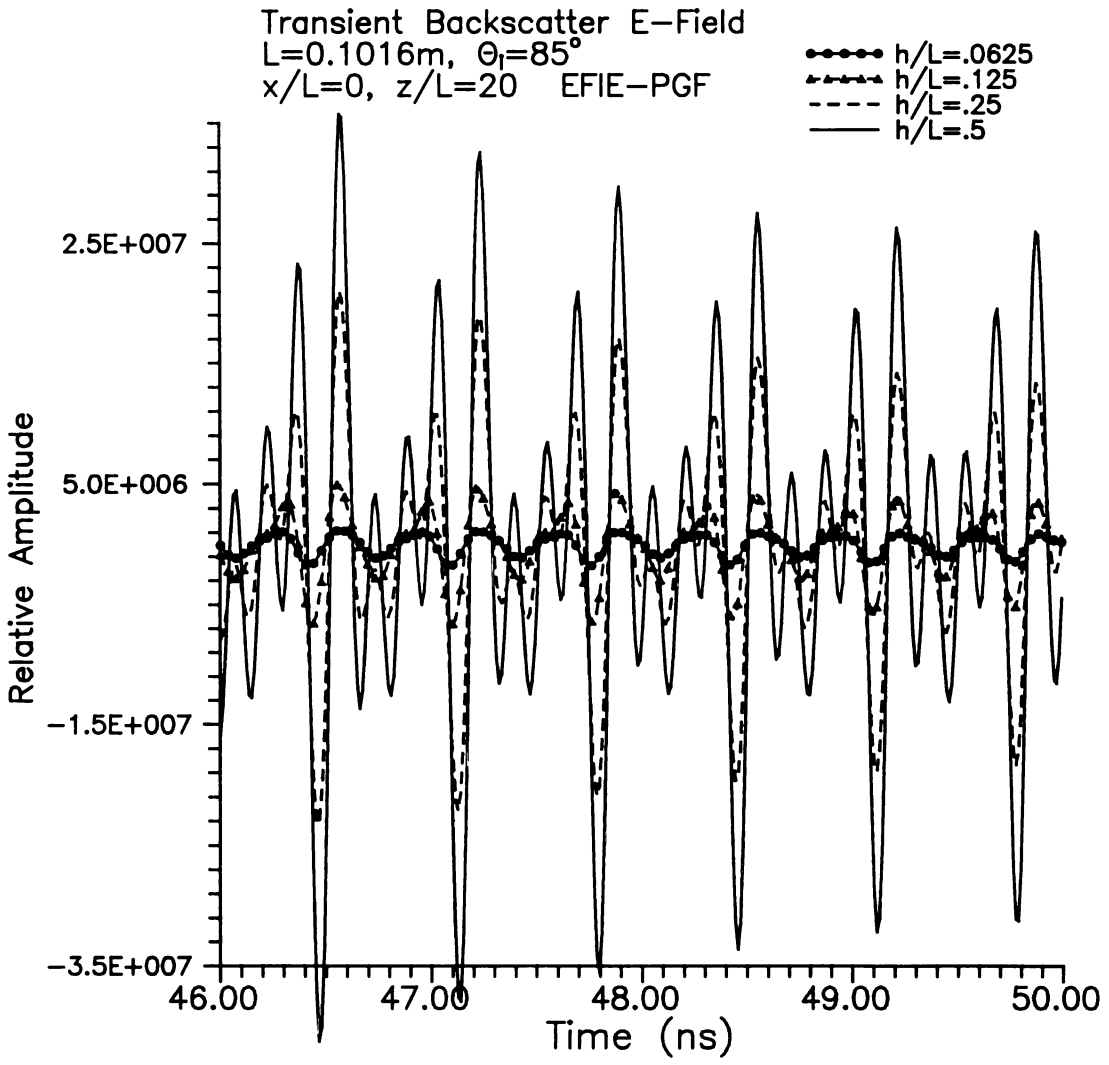

Figure 3.24 Comparison of transient backscaterred electric fields created by a short pulse from various height infinite sinusoidal surfaces for TE excitation.

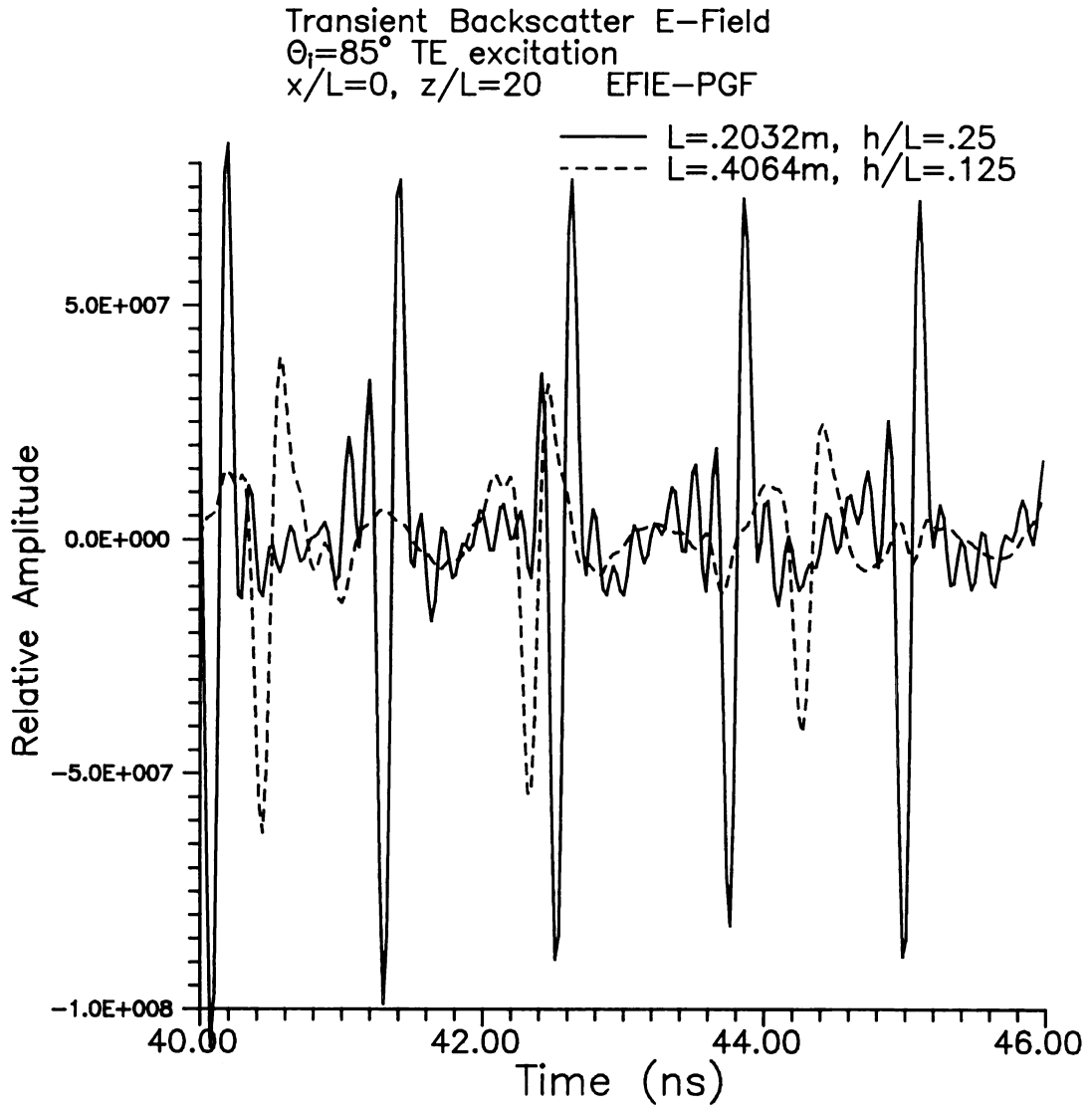

Figure 3.25 Comparison of transient backscattered electric fields created by a short TE pulse from infinite sinusoidal surfaces of differing periods.

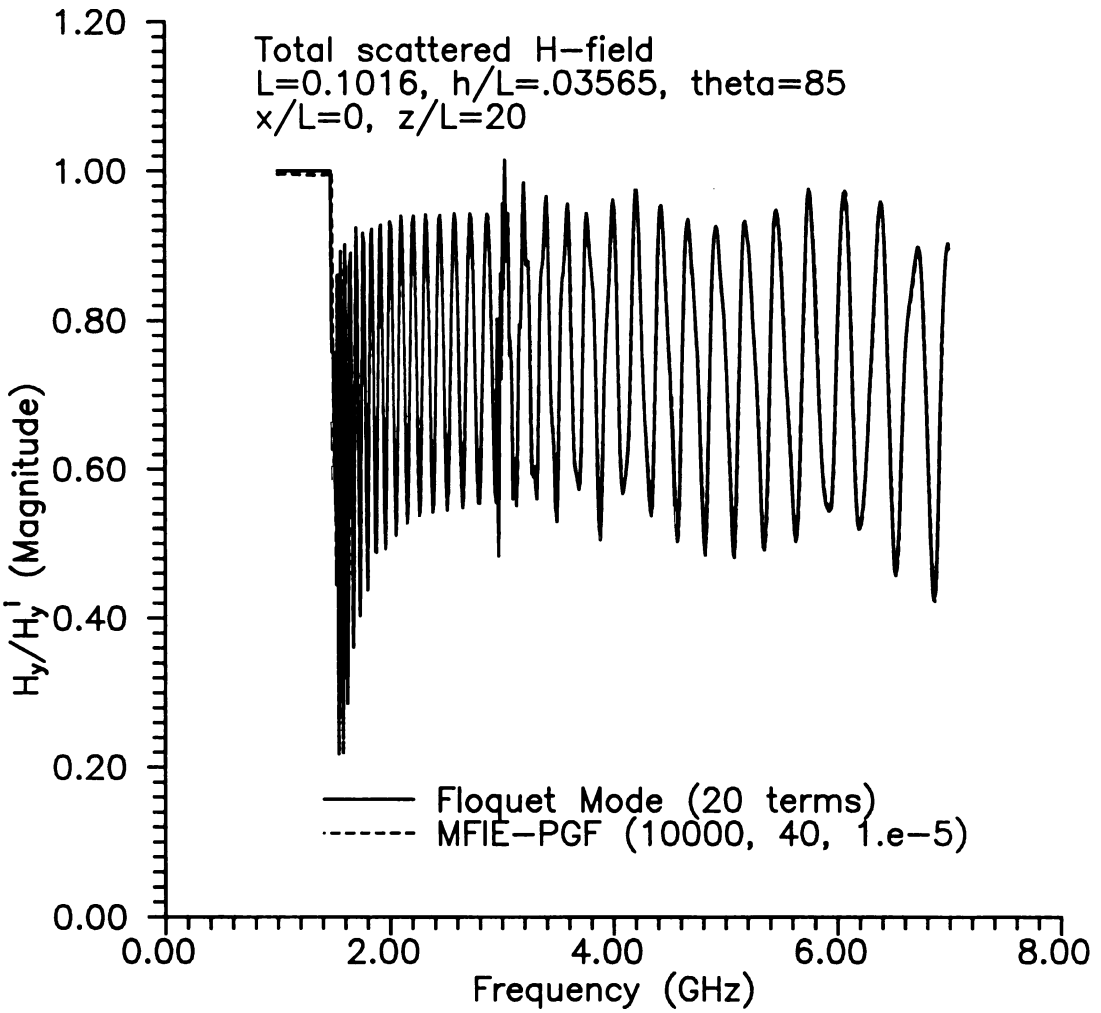

Figure 3.26 Total scattered magnetic field for TM excitation of a PEC sinusoid.

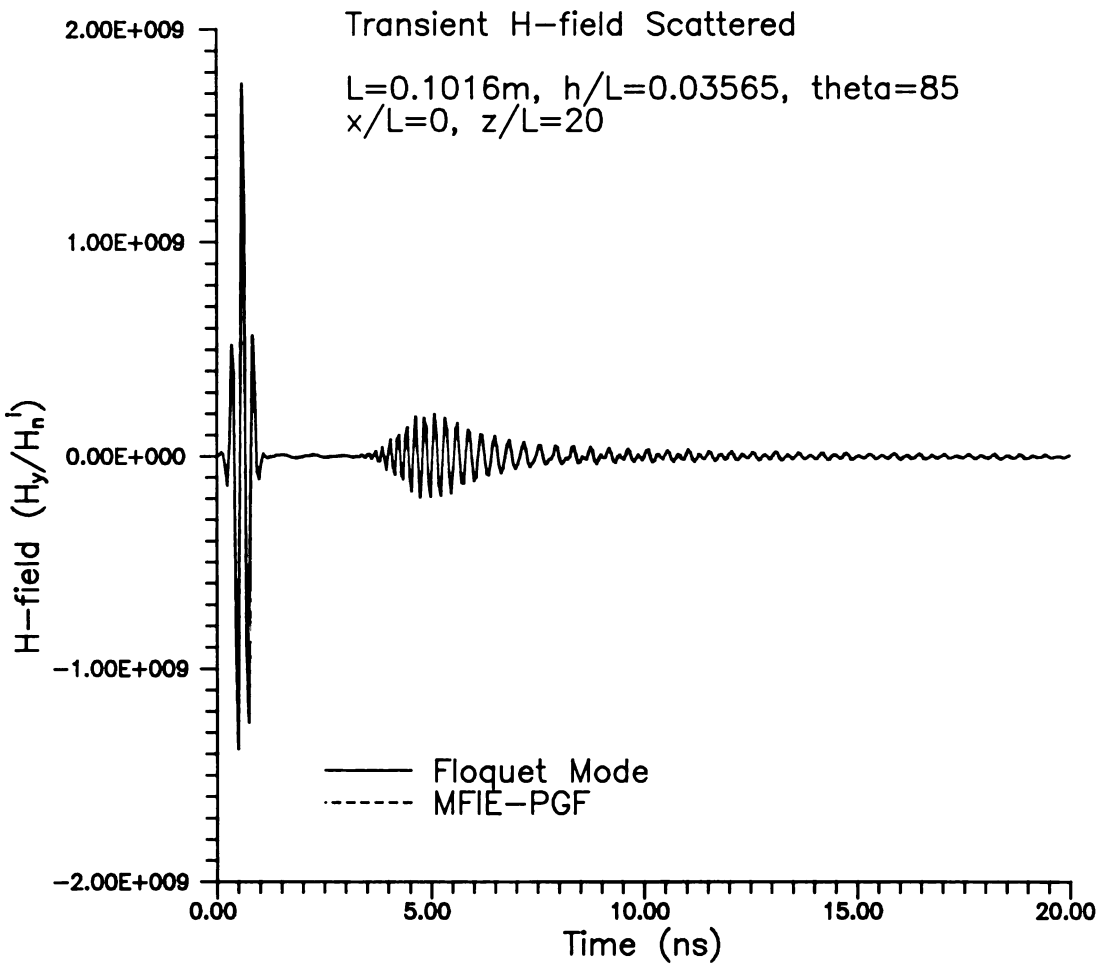

Figure 3.27 Total scattered magnetic field created by a GMC pulse from infinite, conducting sinusoidal surface for TM excitation.

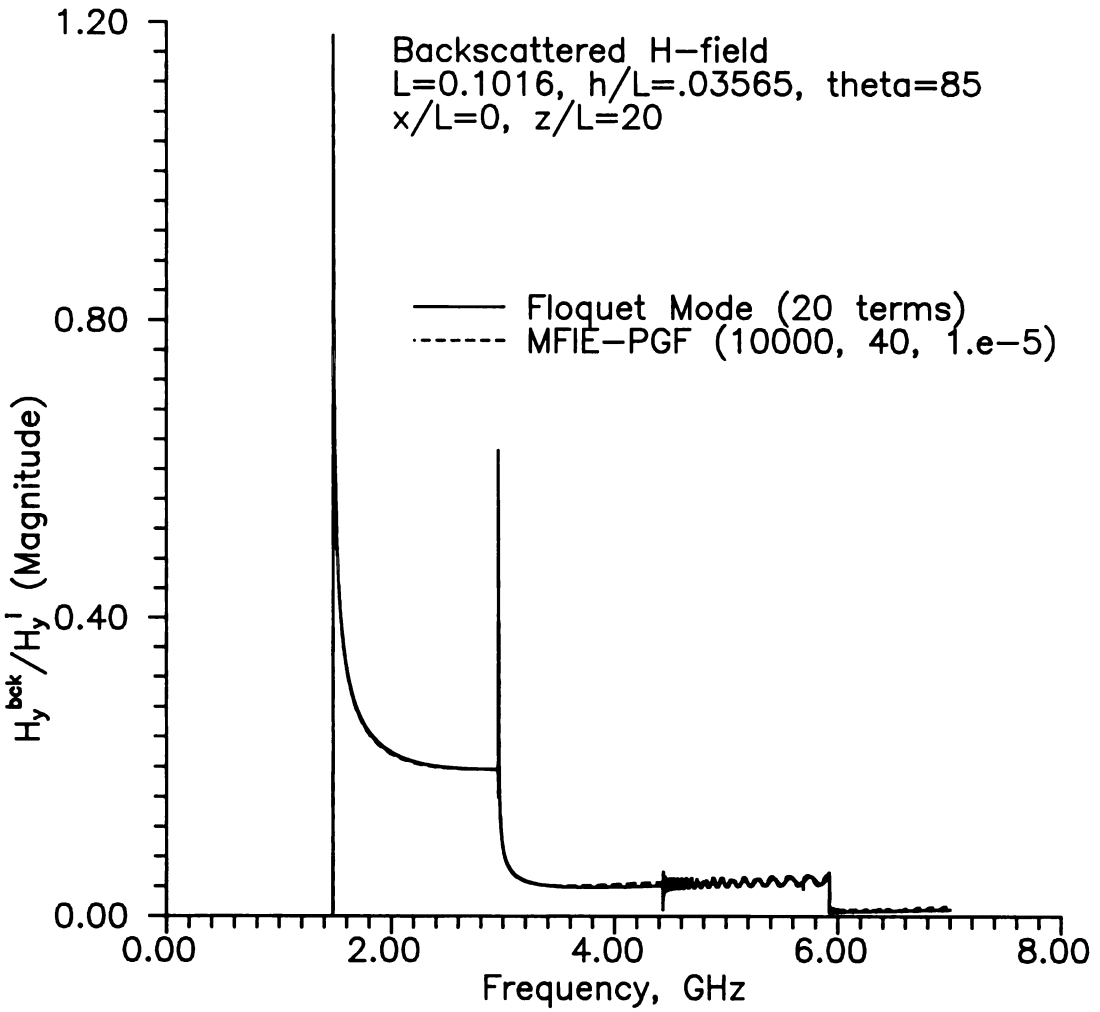

Figure 3.28 Backscattered magnetic field for TM excitation of a PEC sinusoid.

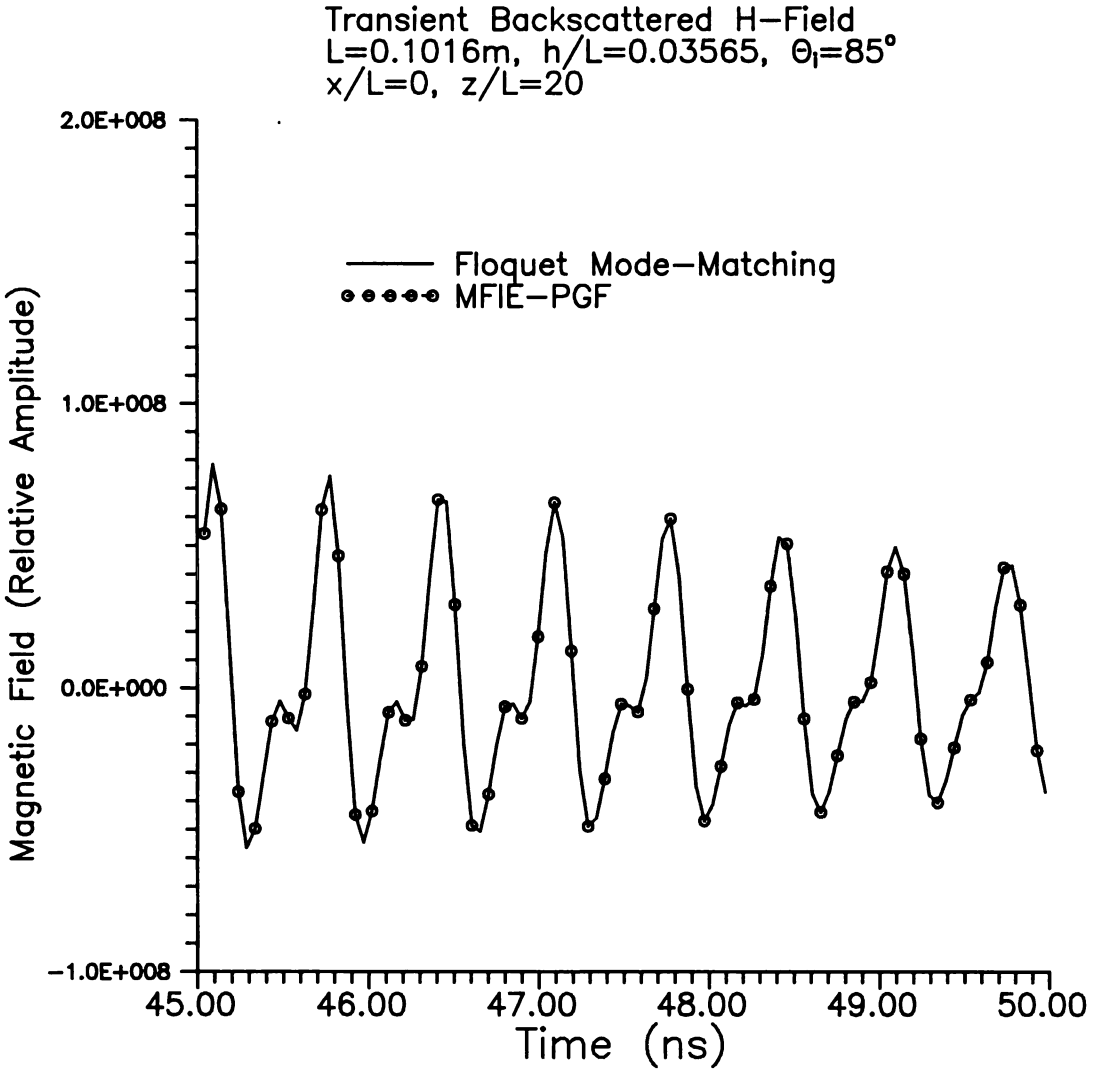

Figure 3.29 Transient backscattered magnetic field created by a 1/8 cosine pulse from infinite, conducting sinusoidal surface for TM excitation.

3.5.2 Finite surface results

The theory developed for the scattering of a plane wave from a finite sea surface is included primarily as a verification of experimental measurements. This is because the sea surfaces used in the experimental measurements are finite. The PEC sinusoid sea-surface model was constructed by adhering aluminum foil to a sinusoidally machined piece of styrofoam. This setup can be visualized in the figure below.

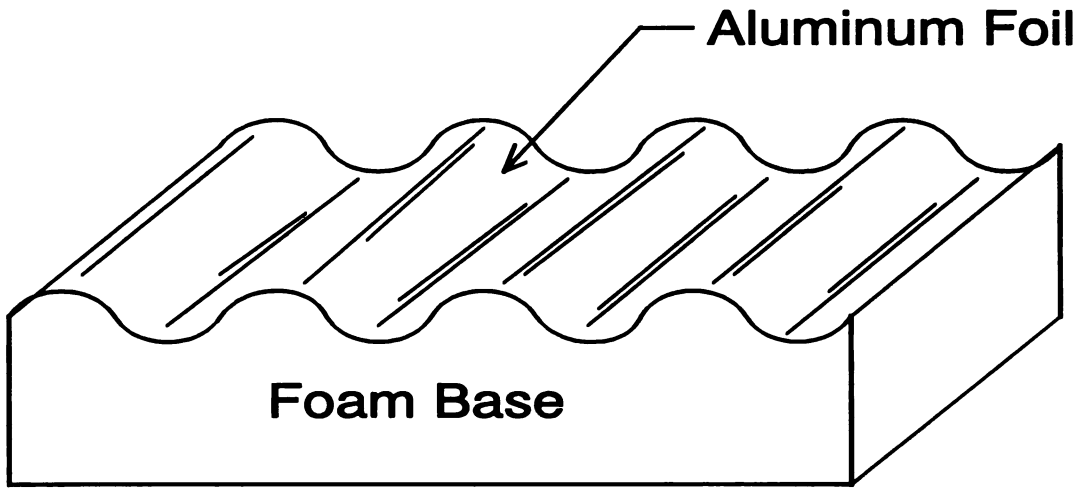

Figure 3.30 Construction of sinusoidal sea-surface model.

The period (L) of the surface is 0.1016m (4 inches) and the amplitude (h) is 1.27cm (0.5 inches). These dimensions where chosen to allow a reasonable number of periods (6 and 11) to be placed on the surface. The surface was limited in size by the measurement system characteristics (See Chapter 2).

The frequency domain synthesis technique in the anechoic chamber was used to measure the PEC sinusoid model. A bandwidth of 1-7 GHz was used to create the synthesized incident pulse. A qualitative look at the experimentally measured backscattered fields is shown in Figure 3.31.

Both the spectral and synthesized transient responses are shown for TE incident plane waves that vary from normally incident (0^{o}) to grazing (90^{o}). In the top plot the spectral response is shown and the striking feature is the Floquet mode spikes. These

spikes occur at the Floquet mode cut-off frequencies (See section 3.4). The dependence of these spikes on the incidence angle is evident and is predicted by equations (3.74) and (3.75). The cut-off frequencies were a by-product of the infinite surface theory and yet the finite surface still exhibits these.

The synthesized transient responses are shown in bottom plot of Figure 3.31. These returns were GMC windowed before transformation and then were individually normalized. Normalization was required because the near grazing returns had far less energy than the normally incident responses. This phenomenon was explained in the preliminary results section and was worsened by the edge condition. The returns exhibit a nice periodic spacing that corresponds to scattering from all the sinusoid crests.

These results indicate the high quality of the measurement system. A more detailed examination of individual incidence angles will follow.

The spectral amplitudes of theoretical and experimental backscattered electric fields generated by a TE plane wave at an incidence angle of 67° from finite sinusoidal surfaces are shown in Figure 3.32. The finite sinusoidal surface used in the experiment has 6.25 periods while that used in the theoretical calculations has only 5 periods. Theoretical and experimental results agree quite well, especially at the locations of frequency spikes. When the spectral results of Figure 3.32 are inversely Fourier transformed with 1/8 cosine windowing, the time domain, transient responses of theoretical and experimental backscattered electric fields created by a short pulse are obtained as shown in Figure 3.33. The backscattered response of a short pulse from a finite sinusoidal surface is a number of peaks representing the specular reflections of the pulse from the crests of the surface. Theory and experiment agrees very well except in the number of peaks; theory has 5 and experiment has 6.25.

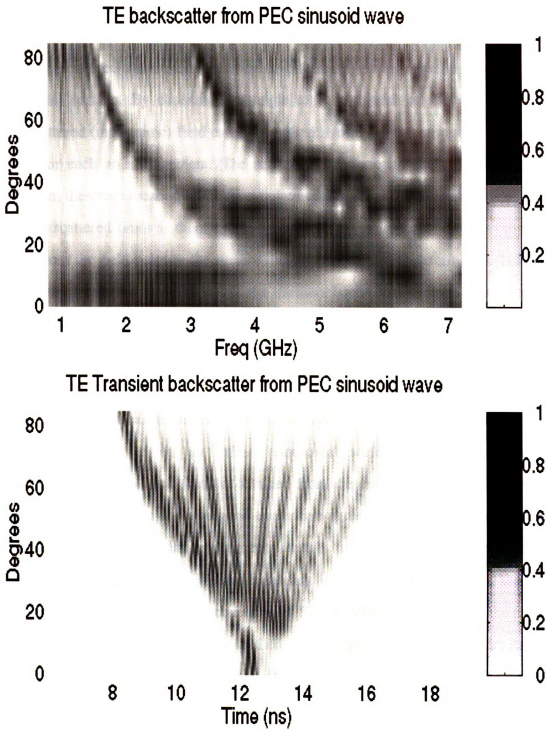

Figure 3.31 Experimental measurements of a PEC sinusoid with TE excitation. The measured spectral response and the synthesized transient returns are shown for numerous incidence angles.

To seek a link between experimental results from a finite sinusoidal surface and theoretical results based on an infinite sinusoidal surface, an enlarged experimental model of a sinusoidal surface with 11 periods was constructed. There is also a problem in the definition of backscatter from the finite and infinite surfaces. For the finite surface the far-zone scattered fields can be calculated for any given angle in reference to the sinusoidal surface. By choosing this angle to be the same as the incidence angle a backscattered (monostatic) field can be specified. However, the infinite surface does not allow for such an arrangement. The scattered fields are infinitely periodic in the x-direction, therefore location of the field point is unimportant. What allows us to compare the backscattered fields is their transient nature. By geometrically choosing the correct angle from the field point to the surface the path length can be determined. This in turn can be thought of as a time-delay. If the transient backscattered fields from the infinite surface are time shifted by the correct amount a strong agreement should exist. Since this method will only work for one point in space, there will be noticeable differences in the periods of the return pulses.

The theoretical results on the backscattered electric field in spectral domain and time domain derived on an infinite sinusoidal surface are compared with the corresponding experimental results obtained from the enlarged experimental surface in Figure 3.34 and Figure 3.35. A good qualitative agreement between theoretical results from an infinite surface and experimental results from a finite surface is observed in these figures. In Figure 3.34 the frequency spikes observed both in theory and experiment occur at the cut-off frequencies of the Floquet modes signifying the excitation of those modes. In Figure 3.35 both theory and experiment predict the backscattered response of a short pulse from a sinusoidal surface to be a series of peaks representing the specular reflections of the pulse from the crests of the sinusoidal surface. To further make a connection between the results of an infinite surface and a finite surface, the computed, transient backscattered electric fields from those two surfaces are compared

in Figure 3.36. The locations of the peaks are completely matched while a minor discrepancy on the shape of the response is observed.

For completeness, the results for the TM excitation are also included. In Figure 3.37 the frequency-domain backscattered magnetic fields, obtained from the theory for an infinite surface and the experiment on a finite surface, are compared. Figure 3.38 shows the comparison of the transient backscattered magnetic fields created by a short pulse obtained from the theory on an infinite surface and the experiment on an enlarged finite surface. Finally, theoretical, transient backscattered magnetic fields created by a short pulse from an infinite surface and a finite surface are compared in Figure 3.39. From the results there is generally good agreement between experimental and theoretical results from an infinite surface and a finite surface. It is noted that the MFIE employed in the analysis of a finite surface requires a closed surface contour. This may degrade the accuracy of the results on a finite surface by TM excitation.

3.6 Conclusions

Much has been learned regarding the nature of transient scattering of a short EM pulse from a conducting sinusoidal surface. In this chapter, theoretical analyses were conducted for an infinite sinusoidal surface and a finite sinusoidal surface for both TE and TM excitations. A series of experiments was also conducted on a finite surface model to verify the theory. There are some interesting observations due to the cut-off and band-pass phenomena of the Floquet modes excited by the periodic sinusoidal surface. It is shown theoretically and experimentally that the backscattered response of a short pulse from a conducting sinusoidal surface is a series of peaks representing the reflections of the pulse from the crests of the surface. A link between the finite and infinite surfaces was established. An argument for the validity of the Rayleigh hypothesis was made by observing the multiple scattering by the higher height sinusoids.

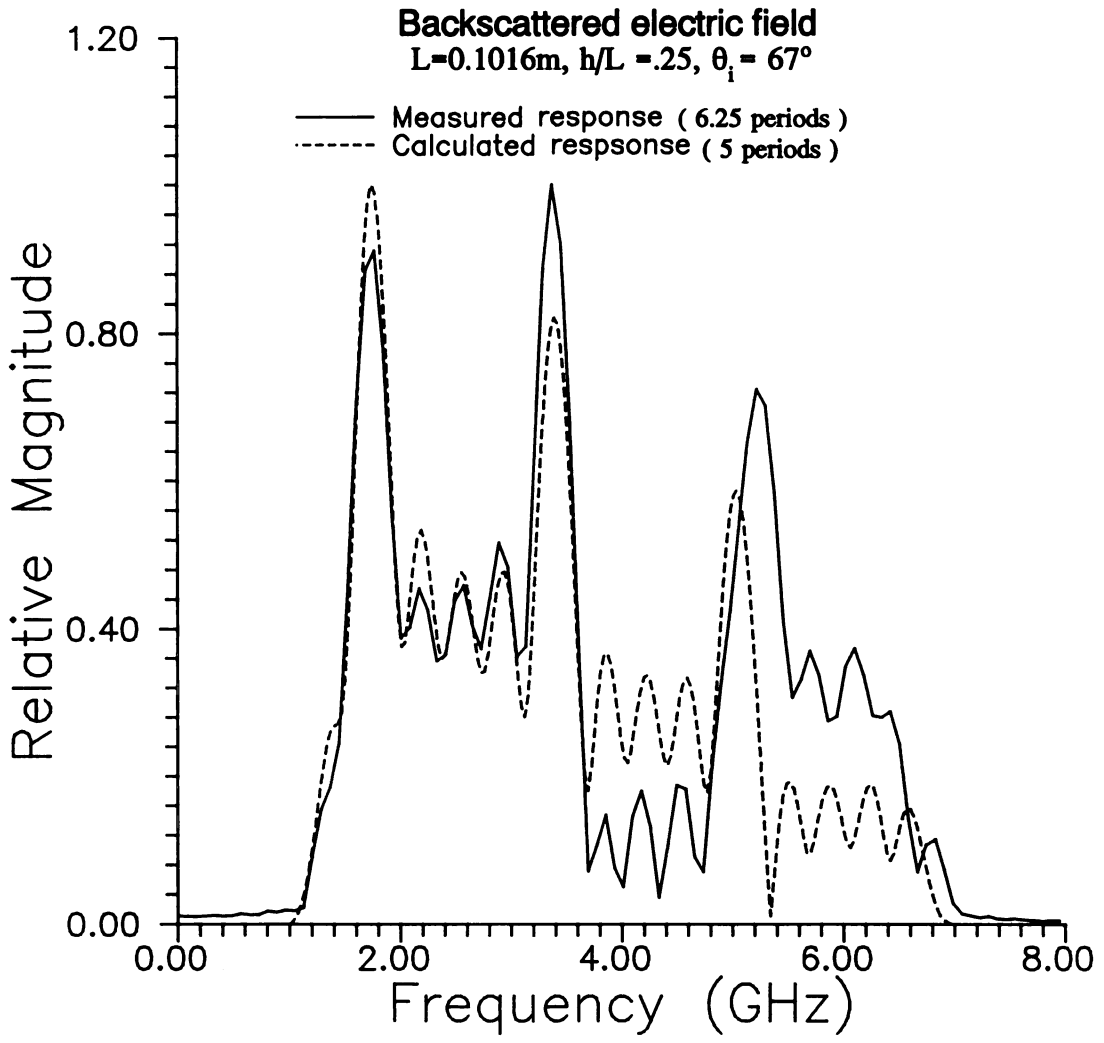

Figure 3.32 Spectral amplitudes of theoretical and experimental backscattered electric fields from a finite surface for TE excitation.

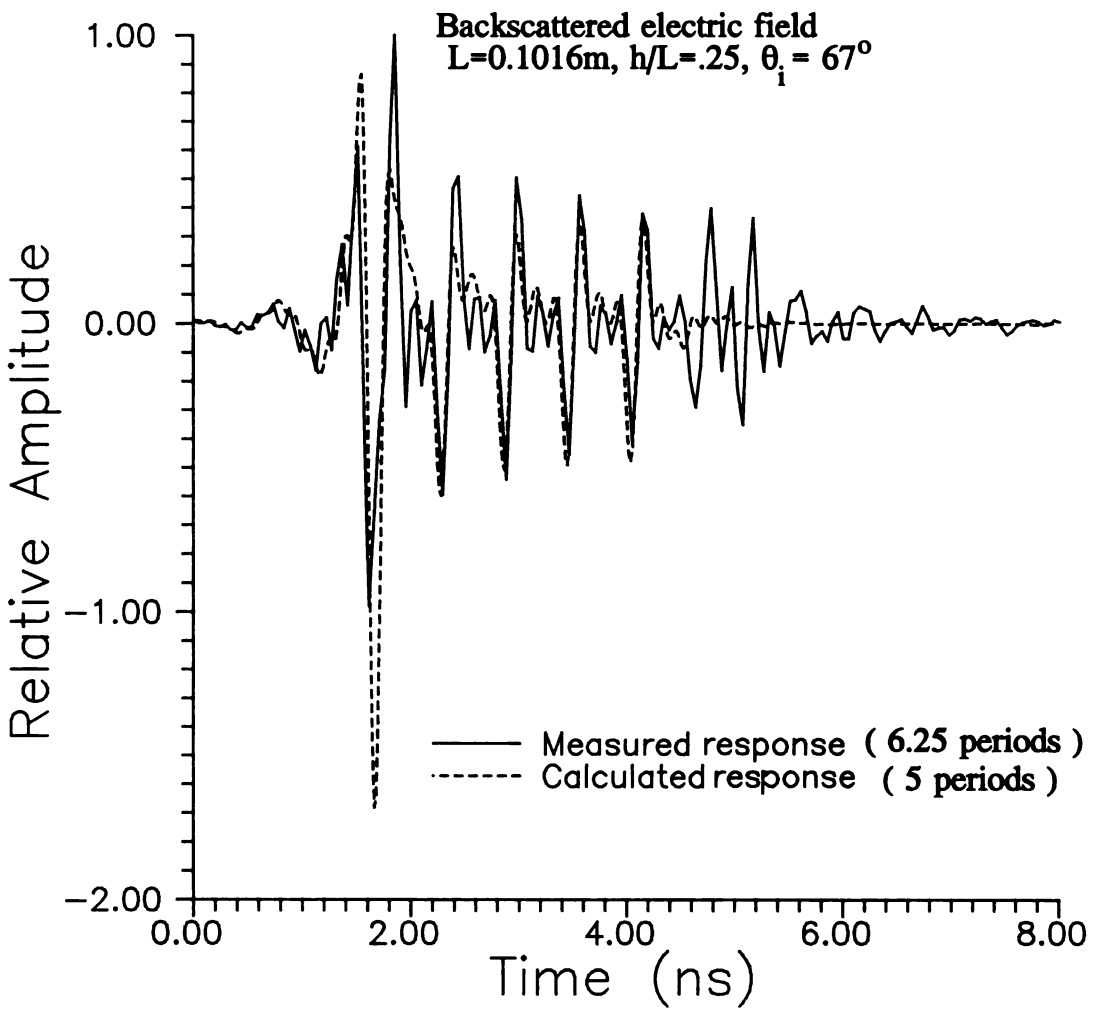

Figure 3.33 Theoretical and experimental transient backscattered electric fields created by a short pulse from a finite surface for TE excitation.

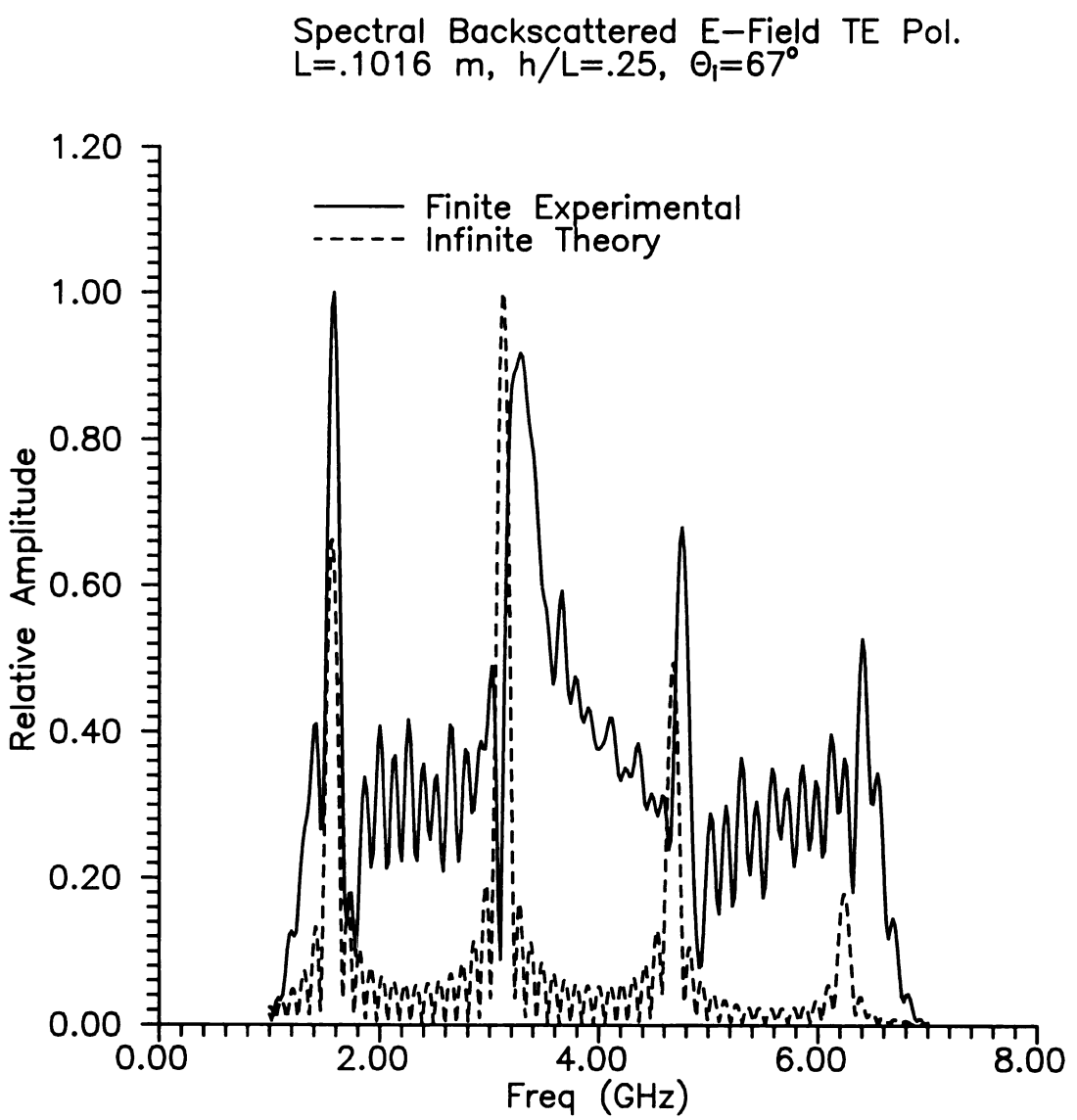

Figure 3.34 Comparison of experimental backscatter (finite surface) results to theoretical backscatter from an infinite surface for TE excitation.

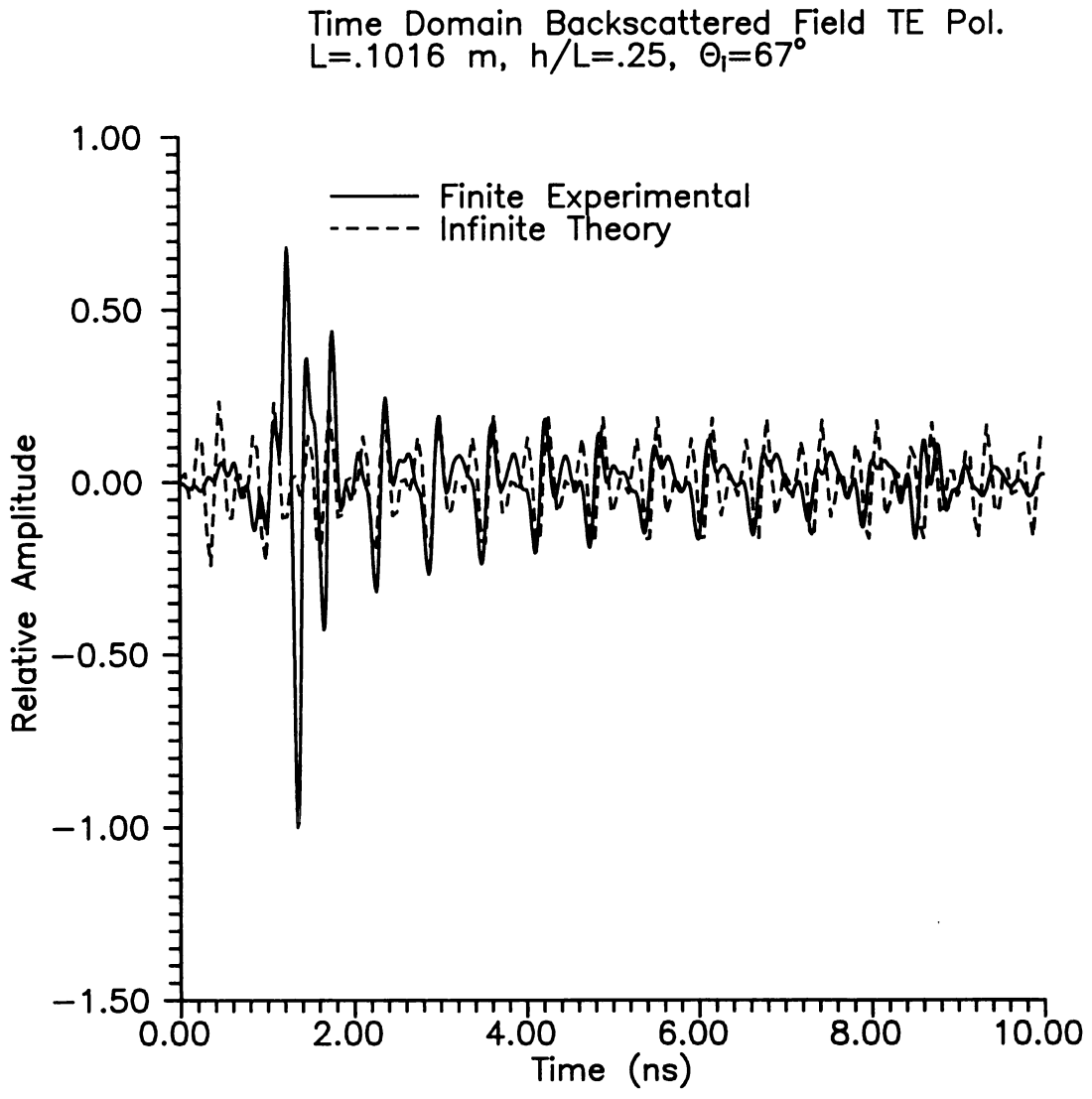

Figure 3.35 Comparison of transient backscatter created by a short pulse from an infinite surface (theoretical) and a finite surface (experimental) for TE excitation.

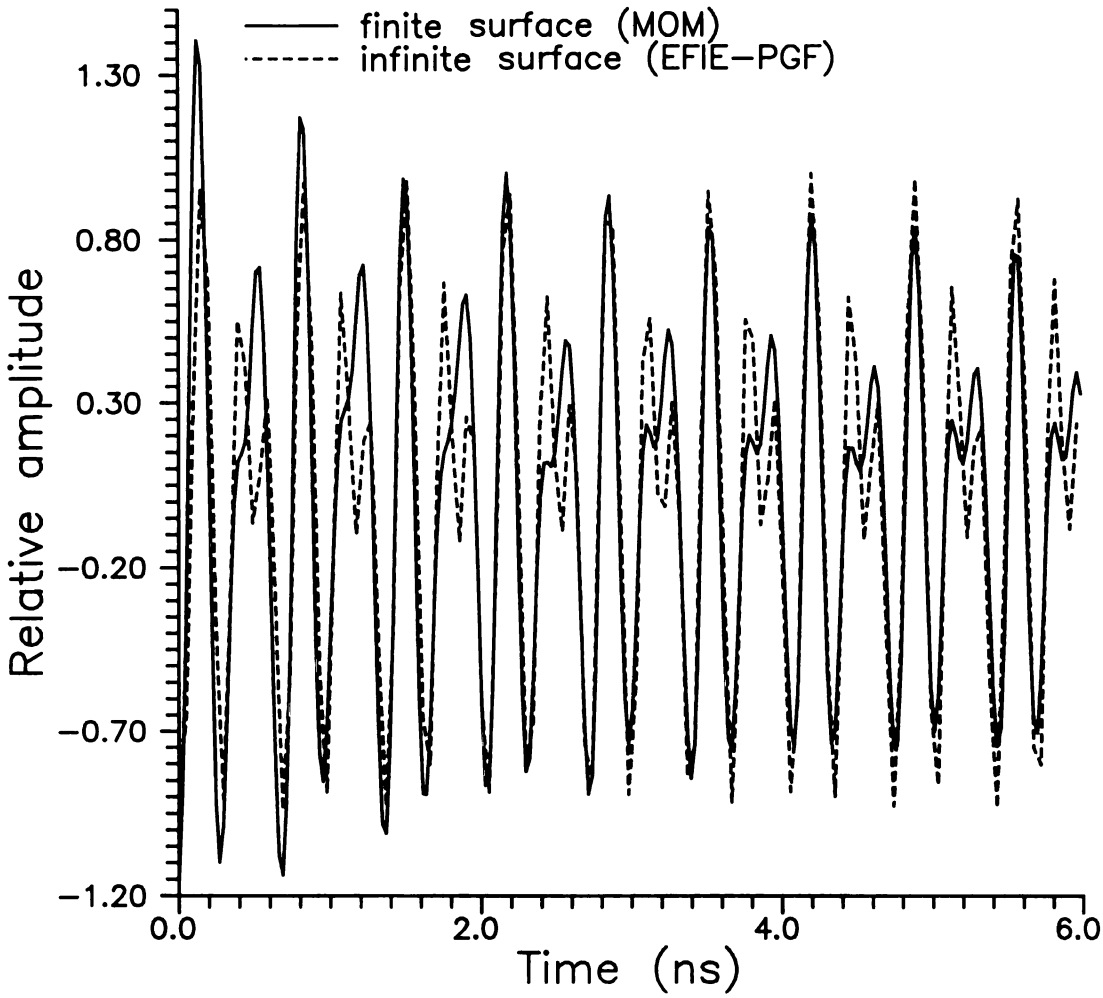

Figure 3.36 Comparison of transient backscattered electric field created by a short pulse from an infinite and finite surface for TE excitation.

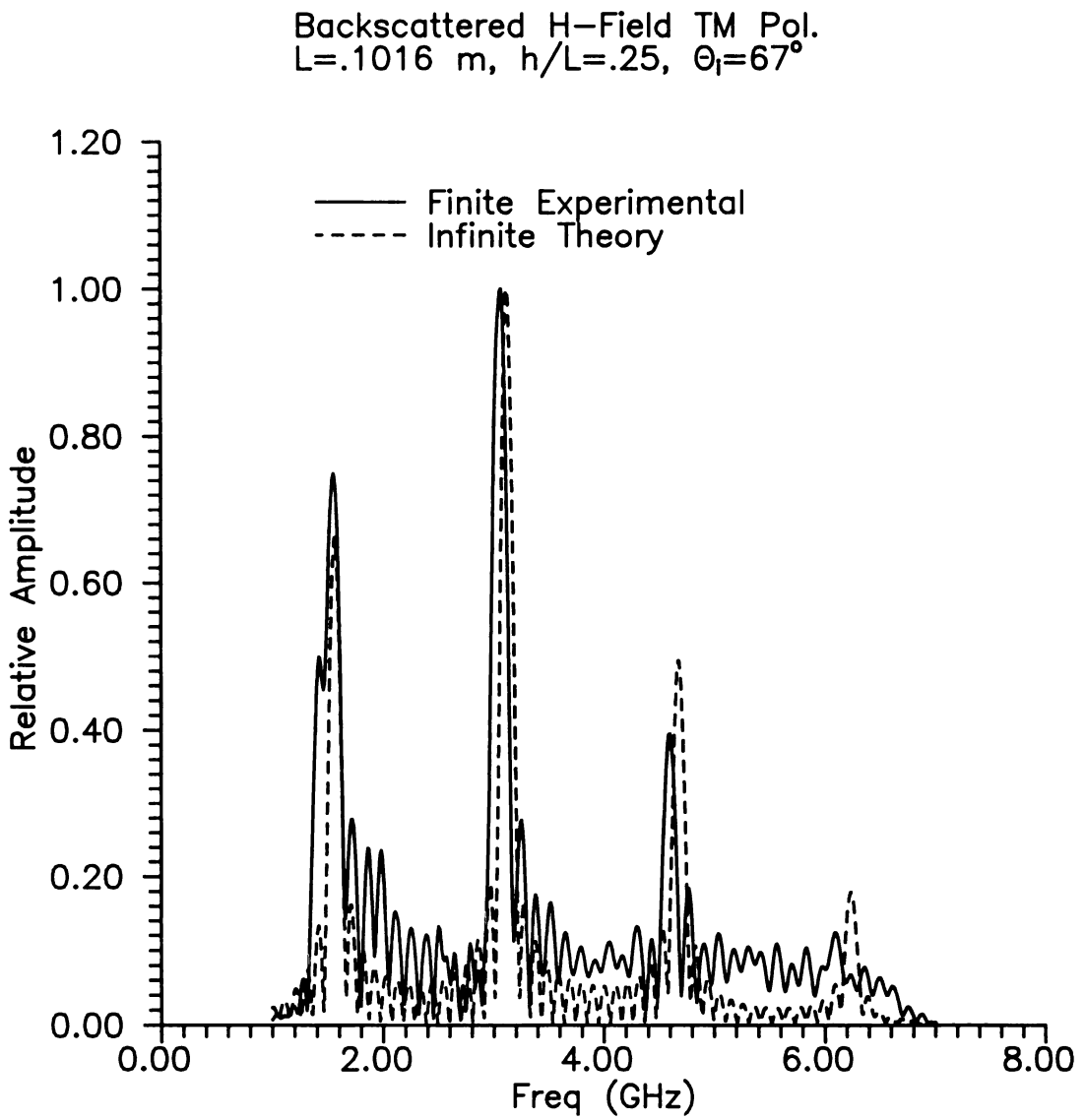

Figure 3.37 Comparison of spectral domain backscattered magnetic field from an infinite surface (theory) and a finite surface (experiment) for TM excitation.

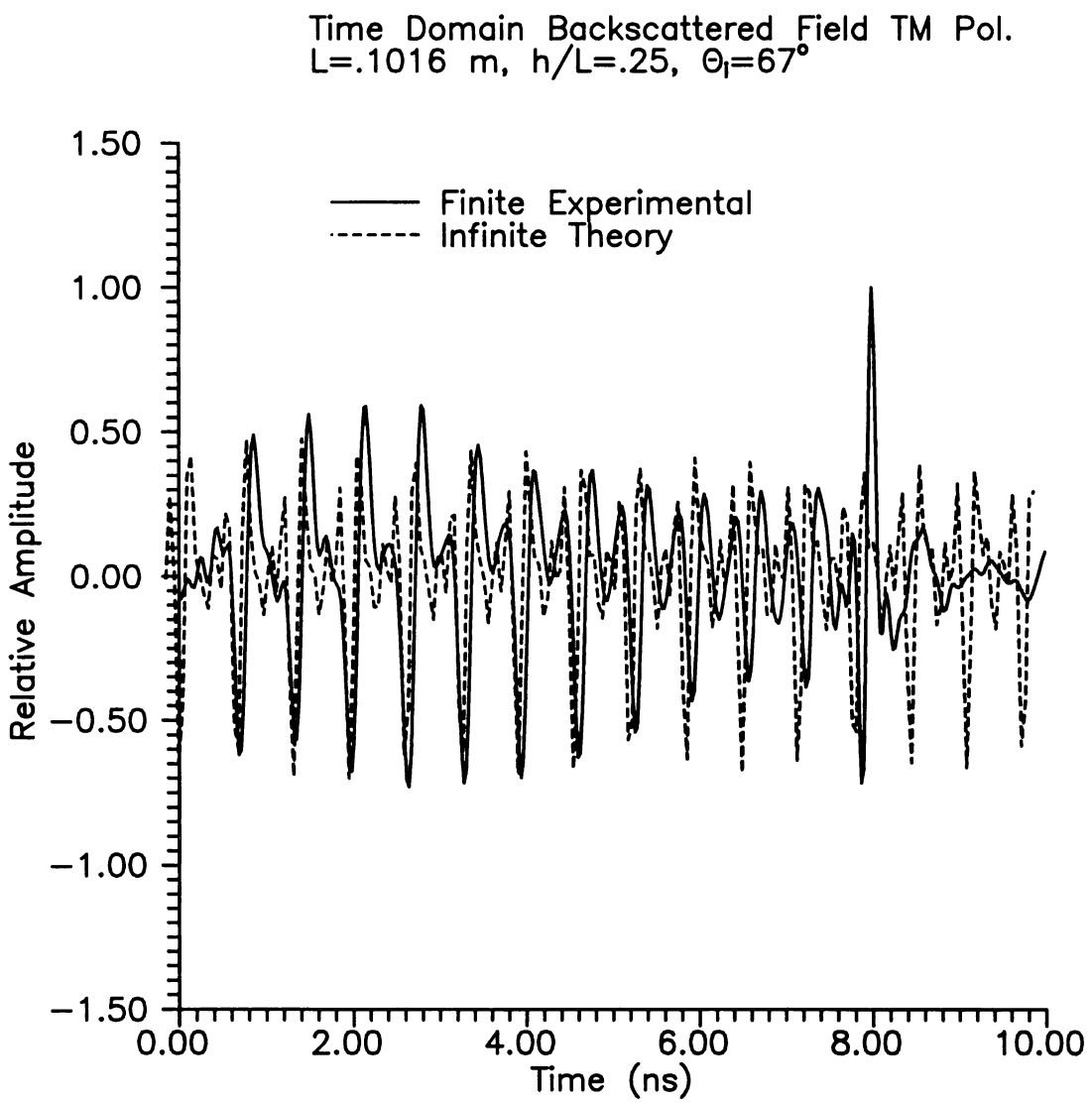

Figure 3.38 Comparison of transient backscattered magnetic field created by a short pulse from an infinite surface (theory) and a finite surface (experiment) for TM excitation.

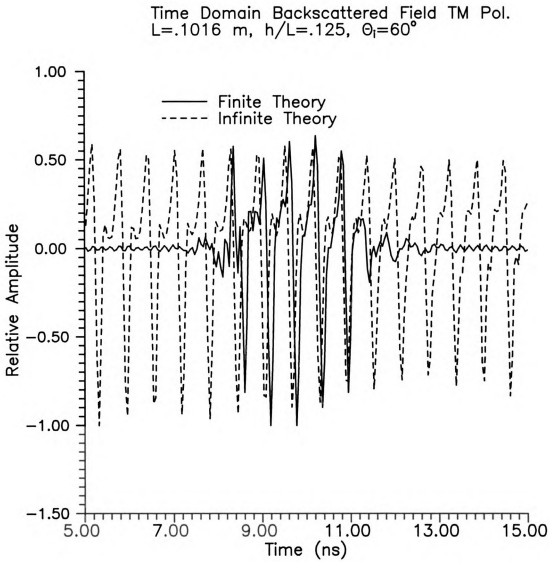

Figure 3.39 Theoretical transient backscattered magnetic field created by a short pulse from an infinite surface and a finite surface for TM excitation.

Chapter 4

Transient Scattering from an Imperfectly Conducting Sinusoidal Surface

4.1 Introduction

In this chapter the ocean model is improved by replacing the perfectly conducting sinusoidal surface by an imperfectly conducting one. The ocean model now consists of two general layers (media) separated by a sinusoidal interface. The effects of the finite conductivity will be examined and the possibility of a Brewster's angle phenomenon will be addressed. It is well known that a TM plane wave incident upon a flat dielectric material will exhibit a Brewster angle, therefore only the TM case will be fully examined for the sinusoidal surface. Both the Floquet-mode-matching and the Integral-Equation (IE-PGF) methods are extended to this two-media case. The Floquet-mode-matching method is once again limited to the Rayleigh hypothesis regime. However, it does provide a verification for the rigorous IE-PGF method for the two-media case.

The numerical solutions for the two-media case use more computer resources, both CPU time and memory, than the PEC case. This is due to the transmitted wave, which is now present in the second medium. The modal amplitudes of the transmitted wave and the scattered waves can be found through mode matching. However, the transmitted wave introduces another unknown to the governing equations, which implies that another set of equations is needed to specify the amplitudes. This additional equation is established by another boundary condition. Therefore there is a set of coupled equations created by satisfying the two boundary conditions at the interface of the media.

The goal of this chapter is to not only improve the ocean model, but to draw comparisons between the PEC model and the two-media model. This comparison will be

made theoretically as well as through experimental measurements. The experimental findings will also provide validation of the scattering theory. The experimental setup physically requires a finite surface but the theory for the finite two-media case is not presented and is not compared. The previous chapter established the link between the finite and infinite cases and those ideas will be applied in this chapter.

4.2 Floquet-Mode Matching Analysis

The classical mode-matching formulation [12] for scattering from an imperfectly conducting periodic ocean surface is considered.

The Rayleigh hypothesis allows simplification of the scattered and transmitted fields, thereby reducing the computation time involved in finding a numerical solution.

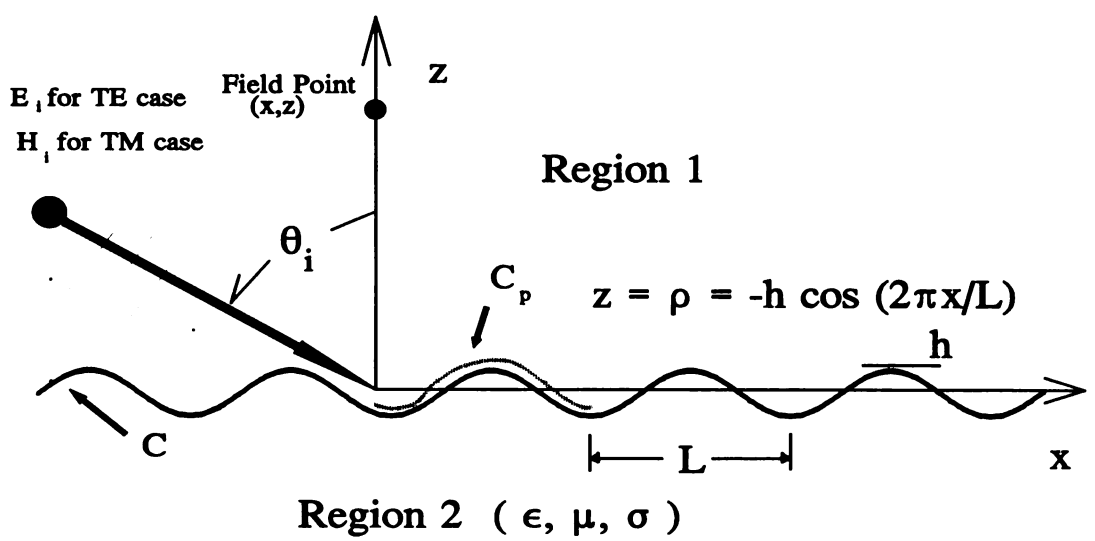

Figure 4.1 Geometry for two media scattering problem.

A TM polarized plane wave is incident at an angle θ_i upon a sinusoidally periodic ocean surface. The region above the ocean surface is assumed to be free space, with wavenumber k_1 and the region below the air-ocean interface is ocean-water with the nominal parameters (σ=4 *S/m*, ϵ_r=80) and with wavenumber k_2. The geometry is shown in Figure 4.1.

For TM excitation $H_y(x,z)$ is the generating field component, which satisfies the 2-D Helmholtz equation

$$\nabla_t^2 H_{yi}(x,z) + k_i^2 H_{yi}(x,z) = 0 \tag{4.1}$$

$$\vec{E}_i(x,z) = \frac{j}{\omega \epsilon_i} \hat{y} \times \nabla_t H_{yi}(x,z) \tag{4.2}$$

where $\nabla_t = \hat{x}\partial/\partial x + \hat{z}\partial/\partial z$ is a 2-D transverse differential operator and i is the space region (1 or 2). The boundary conditions require tangential magnetic and electric fields to be continuous at the interface, thus (applying (4.2))

$$H_{y2} = H_{y1} \quad , \quad \frac{\partial H_{y2}}{\partial n} = \frac{\epsilon_2}{\epsilon_1} \frac{\partial H_{y1}}{\partial n} \tag{4.3}$$

Since the magnetic field has only a y-component, and the fields in region (1) are composed only of incident and scattered waves, and the fields in region (2) are only composed of transmitted waves, the subscripts $y1$ and $y2$ are be dropped. The incident magnetic field is assumed to be of a plane wave nature. Therefore,

$$H_i(x,z) = H_0 e^{-j\beta x} e^{jqz} \tag{4.4}$$

where $\beta = k_{x1} = k_1 \sin\theta_i$, and $q = -k_{z1} = k_1 \cos\theta_i$.

By Floquet's theorem the scattered (i=1) and transmitted (i=2) magnetic fields can be modeled as

$$H_s(x,z) = \sum_{n=-\infty}^{\infty} e^{-j\beta_n x} f_n(z) \tag{4.5}$$

$$H_t(x,z) = \sum_{n=-\infty}^{\infty} e^{-j\beta_n x} f_{tn}(z) \tag{4.6}$$

where $\beta_n = \beta + \frac{2n\pi}{L}$, and $\beta = k_{x1} = k_1 \sin\theta_i$ is necessary to match the phases of the incident wave and the n=0 scattered and transmitted waves at the interface.

Both the scattered and transmitted magnetic fields obey the 2-D Helmholtz equation (4.1). Therefore substituting (4.5) and (4.6) into (4.1), gives

$$\sum_{n=-\infty}^{\infty}\left[\frac{\partial^2 f_n}{\partial z^2}+(-\beta_n^2+k_1^2)f_n\right]e^{-j\beta_n x}=0 \tag{4.7}$$

$$\sum_{n=-\infty}^{\infty}\left[\frac{\partial^2 f_{tn}}{\partial z^2}+(-\beta_n^2+k_2^2)f_{tn}\right]e^{-j\beta_n x}=0 \tag{4.8}$$

where the partial derivatives with respect to x have been performed.

Due to orthogonality the $e^{-j\beta_n x}$, the above equations are satisfied when

$$\frac{\partial^2 f_n}{\partial z^2}+q_n^2 f_n=0 \tag{4.9}$$

$$\frac{\partial^2 f_{tn}}{\partial z^2}+q_{tn}^2 f_{tn}=0 \tag{4.10}$$

where $q_n^2=k_1^2-\beta_n^2$, and $q_{tn}^2=k_2^2-\beta_n^2$ with branch cuts requiring $Im\{q_n\}<0$ and $Im\{q_{tn}\}<0$.

The branch cuts are chosen to accommodate the physics of the problem by requiring exponential decay of the non-propagating scattered and transmitted fields. These branch cuts once again introduce the cut-off and turn-on frequencies associated with the Floquet modes. This was discussed in chapter 3.

The general solutions to equations (4.9) and (4.10) are

$$f_n(z)=B_n e^{-jq_n z}+C_n e^{jq_n z} \tag{4.11}$$

$$f_{tn}(z)=B_{tn} e^{-jq_{tn} z}+C_{tn} e^{jq_{tn} z} \tag{4.12}$$

The Rayleigh hypothesis (see chapter 3) states that the scattered field can be approximated by summing only the space harmonics that are travelling upward away from the air-ocean interface, and the transmitted field can be approximated by summing the space harmonics that are travelling downward away from the air-ocean interface.

Therefore, C_n=0 and B_{tn}=0 which results in a simplified representation of the scattered and transmitted magnetic fields

$$H_s(x,z) = \sum_{n=-\infty}^{\infty} B_n e^{-j\beta_n x} e^{-jq_n z} \tag{4.13}$$

$$H_t(x,z) = \sum_{n=-\infty}^{\infty} C_{tn} e^{-j\beta_n x} e^{jq_{tn} z} \tag{4.14}$$

The first boundary condition at the air-ocean interface requires

$$H_i + H_s = H_t \qquad \text{... at} \quad z=\rho \tag{4.15}$$

where, $\rho = -h\cos(\frac{2\pi x}{L})$ for a sinusoidal ocean surface. Substituting the values from (4.4), (4.13), and (4.14) into (4.15) yields

$$H_0 e^{jq\rho} = -\sum_{n=-\infty}^{\infty} B_n e^{-jq_n\rho} e^{\frac{-j2\pi nx}{L}} + \sum_{n=-\infty}^{\infty} C_{tn} e^{jq_{tn}\rho} e^{\frac{-j2\pi nx}{L}} \tag{4.16}$$

where the common factor $e^{-j\beta x}$ has been eliminated.

The factors $\exp(-jq_n\rho)$ and $\exp(-jq_{tn}\rho)$ in (4.16) destroy the orthogonality of the $\exp(-j2\pi nx/L)$. Galerkin's method is therefore applied, using the testing operator

$$\int_0^L e^{j2m\pi x/L}\{...\}\,dx \tag{4.17}$$

leading to

$$H_0\int_0^L e^{j2\pi mx/L} e^{jq\rho} dx = \sum_{n=-\infty}^{\infty} -B_n \int_0^L e^{-jq_n\rho} e^{j2(m-n)\pi x/L} dx + \sum_{n=-\infty}^{\infty} C_{tn}\int_0^L e^{jq_{tn}\rho} e^{j2\pi(m-n)x/L} \tag{4.18}$$

To simplify the notation the integrals can be referenced as

$$A_m = \int_0^L e^{j2\pi mx/L} e^{jq\rho} dx \tag{4.19}$$

$$K_{mn} = -\int_0^L e^{j2\pi(m-n)x/L} e^{-jq_n\rho} dx \tag{4.20}$$

$$K_{mnt} = -\int_0^L e^{j2\pi(m-n)x/L} e^{jq_{tn}\rho} dx \tag{4.21}$$

Therefore

$$H_o A_m = \sum_{n=-\infty}^{\infty} K_{mn} B_n + \sum_{n=-\infty}^{\infty} K_{mnt} C_{tn} \tag{4.22}$$

For all three integrals (4.19), (4.20) and (4.21) let $u=2\pi x/L \rightarrow du=\frac{2\pi}{L}dx$ then

$$A_m = \frac{L}{2\pi}\int_0^{2\pi} e^{jmu} e^{-jqh\cos(u)} du \tag{4.23}$$

Using Euler's identity, and the fact that cos(x) is an even function and sin(x) is and odd function, (4.23) reduces to

$$A_m = \frac{L}{\pi}\int_0^{2\pi} \cos|mu| e^{jqh\cos(u)} du \tag{4.24}$$

which has the closed form solution

$$A_m = Lj^{|m|} J_{|m|}(qh) \tag{4.25}$$

because $\pi j^n J_n(z) = \int_0^{\pi} \cos n(u) e^{jz\cos(u)} du$.

In a similar manner (4.20) and (4.21) have the following closed form solution

$$K_{mn} = -Lj^{|m-n|} J_{|m-n|}(q_n h) \tag{4.26}$$

$$K_{mnt} = Lj^{-|m-n|} J_{|m-n|}(q_{tn} h) \tag{4.27}$$

The second boundary condition at the air-ocean interface requires

$$\hat{n}\cdot\nabla_t (H_i + H_s) = \frac{\epsilon_1}{\epsilon_2}\hat{n}\cdot\nabla_t H_t \quad \ldots \quad at \quad z=\rho \tag{4.28}$$

where $\hat{n} = (\hat{z} - \hat{x}\frac{\partial\rho}{\partial x})/\sqrt{1+(\frac{\partial\rho}{\partial x})^2}$. Performing the dot product on the expanded gradient results in

$$-\frac{\partial \rho}{\partial x}\frac{\partial}{\partial x}(H_i+H_s)+\frac{\partial}{\partial z}(H_i+H_s)=\frac{\epsilon_1}{\epsilon_2}\left[-\frac{\partial \rho}{\partial x}\frac{\partial H_t}{\partial x}+\frac{\partial H_t}{\partial z}\right] \tag{4.29}$$

Substituting the values from (4.4), (4.13), and (4.14) into (4.29) and performing the partial differentiations, yields

$$\begin{aligned} -H_0(\beta\frac{\partial \rho}{\partial x}+q)e^{jq\rho} &= \sum_{n=-\infty}^{\infty} B_n(\beta_n\frac{\partial \rho}{\partial x}-q_n)e^{-jq_n\rho}e^{-j2n\pi x/L} \\ &-\frac{\epsilon_1}{\epsilon_2}\sum_{n=-\infty}^{\infty} C_{tn}(\beta_n\frac{\partial \rho}{\partial x}+q_{tn})e^{jq_{tn}\rho}e^{-j2\pi nx/L} \end{aligned} \tag{4.30}$$

where the common factor $e^{-j\beta x}$ has been eliminated. The factors $\exp(-jq_n\rho)$ and $\exp(-jq_{tn}\rho)$ in (4.30) destroy the orthogonality of the $\exp(-j2\pi nx/L)$. Galerkin's method is therefore applied, using the testing operator (4.17) leading to

$$\begin{aligned} -H_0\int_0^L(\beta\frac{\partial \rho}{\partial x}+q)e^{j2\pi mx/L}e^{jq\rho}dx &= \sum_{n=-\infty}^{\infty} B_n\int_0^L(\beta_n\frac{\partial \rho}{\partial x}-q_n)e^{-jq_n\rho}e^{j2(m-n)\pi x/L}dx \\ &-\frac{\epsilon_1}{\epsilon_2}\sum_{n=-\infty}^{\infty} C_{tn}\int_0^L(\beta_n\frac{\partial \rho}{\partial x}+q_{tn})e^{jq_{tn}\rho}e^{j2\pi(m-n)x/L}dx \end{aligned} \tag{4.31}$$

Using a form similar to the first boundary condition evaluation (4.22) gives

$$H_0D_m=\sum_{n=-\infty}^{\infty} L_{mn}B_n-\frac{\epsilon_1}{\epsilon_2}\sum_{n=-\infty}^{\infty} L_{mnt}C_{tn} \tag{4.32}$$

where

$$L_{mn}=\beta_nI_{mn}^{(1)}-q_nI_{mn}^{(2)} \tag{4.33}$$

$$L_{mnt}=\beta_nI_{mnt}^{(3)}+q_{tn}I_{mnt}^{(4)} \tag{4.34}$$

$$D_m=-\beta I_m^{(5)}-qI_m^{(6)} \tag{4.35}$$

and

$$I_{mn}^{(1)} = \int_0^L \frac{\partial \rho}{\partial x} e^{j2\pi(m-n)x/L} e^{-jq_n\rho} dx \tag{4.36}$$

$$I_{mn}^{(2)} = \int_0^L e^{j2\pi(m-n)x/L} e^{-jq_n\rho} dx \tag{4.37}$$

$$I_{mnt}^{(3)} = \int_0^L \frac{\partial \rho}{\partial x} e^{j2\pi(m-n)x/L} e^{jq_{tn}\rho} dx \tag{4.38}$$

$$I_{mnt}^{(4)} = \int_0^L e^{j2\pi(m-n)x/L} e^{jq_{tn}\rho} dx \tag{4.39}$$

$$I_m^{(5)} = \int_0^L \frac{\partial \rho}{\partial x} e^{j2\pi mx/L} e^{jq\rho} dx \tag{4.40}$$

$$I_m^{(6)} = \int_0^L e^{j2\pi mx/L} e^{jq\rho} dx \tag{4.41}$$

These six integrals (4.36)-(4.41) can be evaluated to produce closed form solutions. Note that (4.37),(4.39), and (4.41) are in the same form as (4.20),(4.21), and (4.19) respectively, and have the following closed form solutions

$$I_{mn}^{(2)} = Lj^{|m-n|} J_{|m-n|}(q_n h) \tag{4.42}$$

$$I_{mnt}^{(4)} = Lj^{-|m-n|} J_{|m-n|}(q_{tn} h) \tag{4.43}$$

$$I_m^{(6)} = Lj^{-|m|} J_{|m|}(qh) \tag{4.44}$$

The remaining three integrals can be evaluated after the $\partial\rho/\partial x$ term is expanded. This gives

$$I_{mn}^{(1)} = -j\pi h \left[j^{|m-n+1|} J_{|m-n+1|}(q_n h) - j^{|m-n-1|} J_{|m-n-1|}(q_n h) \right] \tag{4.45}$$

$$I_{mnt}^{(3)} = -j\pi h\left[j^{-|m-n+1|}J_{|m-n+1|}(q_{tn}h) - j^{-|m-n-1|}J_{|m-n-1|}(q_{tn}h)\right] \tag{4.46}$$

$$I_{m}^{(5)} = -j\pi h\left[j^{|m+1|}J_{|m+1|}(qh) - j^{|m-1|}J_{|m-1|}(qh)\right] \tag{4.47}$$

The two boundary conditions (4.3) yield a system of equations, which can be solved using matrix operations. This system can be written as

$$\begin{bmatrix} L_{mn} & -L_{mnt}\epsilon_1/\epsilon_2 \\ K_{mn} & K_{mnt} \end{bmatrix}\begin{bmatrix} B_n \\ C_{tn} \end{bmatrix} = \begin{bmatrix} D_m \\ A_m \end{bmatrix} \tag{4.48}$$

where $L_{mn}, L_{mnt}, K_{mn}, K_{mnt}$ are $M \times N$ matrices, and B_n, C_{tn} are N element vectors, and A_m, D_m are also N element vectors. The number N is related to the number of propagating modes and is chosen to insure convergence of the series and is discussed in chapter 3 and in [12].

Subsequent to determination of B_n and C_{tn} from the matrix in (4.48). The scattered and transmitted fields can be evaluated with (4.13) and (4.14) as

$$H_s(x,z) = \sum_{n=-N_-}^{N_+} B_n e^{-j\beta_n x} e^{-jq_n z} \tag{4.49}$$

$$H_t(x,z) = \sum_{n=-N_-}^{N_+} C_{tn} e^{-j\beta_n x} e^{jq_{tn} z} \tag{4.50}$$

Where the summation range N_-, N_+ corresponds to the matrix in (4.48), such that $N = (N_- + N_+ + 1)$.

The above analysis based on eqns. (4.15) to (4.48) was specialized to a sinusoidal interface. A non-sinusoidal interface could have been specified, but would require numerical integration to determine the matrix entries. The case of a non-sinusoidal interface will be considered in the next chapter.

4.3 Integral Equation Formulation

The two-media problem can also be formulated using an integral-operator technique. This method is rigorous an overcomes any limitations set by the Rayleigh-hypothesis method. The transverse magnetic (TM) scattering problem is of greatest interest, due to the absence of specular reflections at the Brewster's incidence angle, so only a formulation for that polarization state is presented here, although the TE problem can be studied similarly.

The two-medium scattering problem consists of space and ocean-water regions separated by a periodic ocean surface and illuminated by a plane wave incident from the space region, as indicated in Figure 4.1. It is assumed that region (1) is located above ocean-surface contour C, with permittivity $\epsilon_1 = \epsilon_0$. The ocean water is region (2), located below ocean-surface contour C, with complex permittivity ϵ_2. Wavenumbers in the two regions are $k_i = \omega\sqrt{\mu_0\epsilon_i}$ for $i = 1,2$. Unit normal vectors to the interface contour C are chosen as $\hat{n}_1$ directed outward from region (1) and $\hat{n}_2$ directed outward from region (2) such that $\hat{n}_2 = -\hat{n}_1 = \hat{n}$.

For the TM polarization, all EM fields can be expressed in terms of the generating field $H_y(x,z)$, which satisfies the 2-D Helmholtz equation. Relevant field relations are

$$\nabla_t^2 H_{yi}(x,z) + k_i^2 H_{yi}(x,z) = -\hat{y}\cdot\nabla_t \times \vec{J}(x,z) \quad \text{... for } i = 1,2 \tag{4.51}$$

and

$$\vec{E}_i(x,z) = \frac{j}{\omega\epsilon_i}\,\hat{y}\times\nabla_t H_{yi}(x,z) \tag{4.52}$$

where $\nabla_t = \hat{x}\,\partial/\partial x + \hat{z}\,\partial/\partial z$ is a 2-D transverse differential operator.

The boundary conditions requiring continuity of tangential $\vec{H}$ and $\vec{E}$ (applying Eq. (4.52)) lead to

$$H_{y2} = H_{y1} \quad , \qquad \frac{\partial H_{y2}}{\partial n} = \frac{\epsilon_2}{\epsilon_1} \frac{\partial H_{y1}}{\partial n} \tag{4.53}$$

at points along the ocean-surface interface contour C. To simplify the notation, the magnetic field is identified with a wave function such that $H_{yi}(x,z) = \psi_i(x,z)$.

The scattered field ψ_1^s in region (1) can be expressed in terms of the surface values of ψ_1 and $\partial\psi_1/\partial n$ at points along the interface contour C. It is consequently desired to obtain a pair of simultaneous integral equations for the latter surface-field quantities. Wave function ψ_1 is the field in region (1) and at points approaching interface contour C from the region (1) side. Similarly, wave function ψ_2 is the field in region (2) and at points approaching the interface contour C from the region (2) side. The required integral equations implicate two-dimensional (2-D) Green's functions for unbounded homogeneous media having wavenumbers k_1 and k_2. They include both the aperiodic 2-D Green's function

$$\tilde{G}_i(\vec{\rho}\,|\,\vec{\rho}\,') = \frac{-j}{4} H_0^{(2)}(k_i|\vec{\rho} - \vec{\rho}\,'|) \tag{4.54}$$

and the periodic Greens's function (see Appendix A)

$$G_i(\vec{\rho}\,|\,\vec{\rho}\,') = -\frac{j}{2L} \sum_{n=-\infty}^{\infty} \frac{e^{-j\beta_n(x-x')} e^{-jq_{in}|z-z'|}}{q_{in}} \tag{4.55}$$

for $i = 1,2$, where $\vec{\rho} = \hat{x}x + \hat{z}z$ is the 2-D position vector, $\beta_n = \beta + 2n\pi/L$ and $q_{in}^2 = k_i^2 - \beta_n^2$ so $q_{in} = -j\sqrt{\beta_n^2 - k_i^2}$ with the branch cuts chosen such that $Im\{q_{in}\} < 0$.

For the purpose of calculating the field in region (1), region (2) is replaced by equivalent polarization currents $\vec{J}_{eq}^{(2)} = j\omega(\epsilon_2 - \epsilon_1)\vec{E}_2$ immersed, along with primary current $\vec{J}$, in a homogeneous medium having wavenumber k_1. The polarization currents in region (2) are then replaced by equivalent surface sources over contour C. Applying the 2-D Green's theorem, the definitions for Green's functions (4.54) and (4.55), and eqn. (4.51) leads to (See Appendix C)

$$\psi_1(\vec{\rho}) = \psi_1^i(\vec{\rho}) + \int_{C_p} \left[\psi_1(\vec{\rho}') \frac{\partial G_1(\vec{\rho}\,|\,\vec{\rho}')}{\partial n'} - G_1(\vec{\rho}\,|\,\vec{\rho}') \frac{\partial \psi_1(\vec{\rho}')}{\partial n'} \right] dl' \qquad (4.56)$$

where C_p is the ocean-surface contour in its first period for $0 \le x \le L$, and ψ_1^i is the impressed field maintained by primary impressed current as

$$\psi_1^i(\vec{\rho}) = \int_{CS} \left[\hat{y} \cdot \nabla_t' \times \vec{J}(\vec{\rho}') \right] \tilde{G}_1(\vec{\rho}\,|\,\vec{\rho}')\, dS' \quad . \qquad (4.57)$$

For remote source currents, the incident field can be modelled as the plane wave

$$\psi_1^i(\vec{\rho}) = H_0 e^{-j\beta x} e^{jqz} \qquad (4.58)$$

where $\beta = k_1 \sin\theta_i$ and $q = k_1 \cos\theta_i$.

Initially, the integral equation (4.56) domain was infinite and implicated the use of the aperiodic Green's function $\tilde{G}_1$. The periodic Green's function, however, allows for the reduction of the integration domain to a single period of the sinusoidal surface. This was discussed in chapter 3 and is the key step in creating a tractable problem.

When $\vec{\rho}$ is a point on C, accommodating the source-point singularity leads to

$$\frac{\psi_1(\vec{\rho})}{2} = \psi_1^i(\vec{\rho}) + PV \int_{C_p} \left[\psi_1(\vec{\rho}') \frac{\partial G_1(\vec{\rho}\,|\,\vec{\rho}')}{\partial n'} - G_1(\vec{\rho}\,|\,\vec{\rho}') \frac{\partial \psi_1(\vec{\rho}')}{\partial n'} \right] dl' \qquad (4.59)$$

where PV indicates that the integral must be evaluated in a principal value sense by excluding a small neighborhood centered at field point $\vec{\rho}' = \vec{\rho}$.

Following a similar procedure, the field in region (2) is obtained by replacing region (1) with equivalent polarization currents $\vec{J}_{eq}^{(1)} = j\omega(\epsilon_1 - \epsilon_2)\vec{E}_1$ immersed in a homogeneous medium having wavenumber k_2. The primary and polarization currents in region (1) are then replaced by equivalent surface sources over interface contour C. Applying the 2-D Green's theorem, the homogeneous specialization of (4.51) and the definitions for Green's functions (4.54) and (4.55) leads, for field points $\vec{\rho} \in C$, to

$$\frac{\psi_2(\vec{\rho})}{2} = -PV\int_{C_P}\left[\psi_2(\vec{\rho}')\frac{\partial G_2(\vec{\rho}\,|\,\vec{\rho}')}{\partial n'} - G_2(\vec{\rho}\,|\,\vec{\rho}')\frac{\partial \psi_2(\vec{\rho}')}{\partial n'}\right]dl' \quad . \tag{4.60}$$

Boundary conditions (4.53) require

$$\psi_2 = \psi_1 = \psi \quad , \qquad \frac{\partial \psi_2}{\partial n} = \frac{\epsilon_2}{\epsilon_1}\frac{\partial \psi_1}{\partial n} = \frac{\epsilon_2}{\epsilon_1}\frac{\partial \psi}{\partial n} \tag{4.61}$$

along contour C, where ψ and $\partial\psi/\partial n$ are regarded as unknown. Implementing these boundary conditions in (4.59) and (4.60) leads to

$$\frac{\psi(\vec{\rho})}{2} - PV\int_{C_P}\left[\psi(\vec{\rho}')\frac{\partial G_1(\vec{\rho}\,|\,\vec{\rho}')}{\partial n'} - \frac{\partial \psi(\vec{\rho}')}{\partial n'}G_1(\vec{\rho}\,|\,\vec{\rho}')\right]dl' = \psi_1^i(\vec{\rho}) \tag{4.62}$$

$$\frac{\psi(\vec{\rho})}{2} + PV\int_{C_P}\left[\psi(\vec{\rho}')\frac{\partial G_2(\vec{\rho}\,|\,\vec{\rho}')}{\partial n'} - \frac{\epsilon_2}{\epsilon_1}\frac{\partial \psi(\vec{\rho}')}{\partial n'}G_2(\vec{\rho}\,|\,\vec{\rho}')\right]dl' = 0 \tag{4.63}$$

for all points $\vec{\rho}\in C_P$. These are a pair of coupled integral equations (IE's) for the unknown wave function and its normal derivative. Subsequent to obtaining a solution, the scattered field in region (1) is obtained from Eq. (4.56) as

$$\psi_1^s(\vec{\rho}) = \int_{C_P}\left[\psi(\vec{\rho}')\frac{\partial G_1(\vec{\rho}\,|\,\vec{\rho}')}{\partial n'} - \frac{\partial \psi(\vec{\rho}')}{\partial n'}G_1(\vec{\rho}\,|\,\vec{\rho}')\right]dl' \quad . \tag{4.64}$$

The formulation for TM wave scattering from a perfectly-conducting, periodic ocean surface is obtained as a special case of IE's (4.62) and (4.63). For a perfectly-conducting ocean, $\epsilon_2/\epsilon_1 \to -j\infty$ such that IE (4.63) requires $\partial\psi/\partial n' = 0$ and IE (4.62) subsequently becomes independent in wave function ψ as

$$\frac{\psi(\vec{\rho})}{2} - PV\int_{C_P}\psi(\vec{\rho}')\frac{\partial G_1(\vec{\rho}\,|\,\vec{\rho}')}{\partial n'}dl' = \psi_1^i(\vec{\rho}) \quad . \tag{4.65}$$

Integral equation (4.65) is identical to the result obtained in chapter 3.

The two-medium ocean scattering problem is studied through solutions to integral equations (4.62) and (4.63). Based upon experience gained from the integral-equation (with periodic Green's function) formulation for the conducting ocean-surface model, moment-method numerical solutions are obtained for the unknown surface field quantities. The forward and backward scattered waves maintained by those surface fields are subsequently calculated, leading to the various transfer functions required to calculate the forward and backward scattered fields.

4.3.1 Moment-Method Numerical Solution

In the previous section the field on the ocean-surface satisfied the pair of simultaneous integral equations (4.62) and (4.63). A method-of-moments numerical solution can be implemented by expanding the unknown field $\psi(x,z)$ and its normal derivative $\frac{\partial\psi(x,z)}{\partial n}$ in basis sets $\{f_q\}$ and $\{g_q\}$, respectively, as

$$\psi(x,z) = \sum_{q=1}^{N} a_q f_q(x,z) \tag{4.66}$$

$$\frac{\partial\psi(x,z)}{\partial n} = \sum_{q=1}^{N} b_q g_q(x,z) \tag{4.67}$$

A pulse-function basis set is used to implement the numerical solution. The integral path for the first period of the ocean surface is divided into N parts where $\Delta x = \frac{L}{N}$, $x_q = (q-1)\Delta x$ and $z_q = -h\cos(\frac{2\pi x_q}{L})$. The partitioning scheme is identical to that used in chapter 3 (e.g. Figure 3.3).

Point matching the integral equations at N points $(\bar{x}_p,\bar{z}_p)$ on the first ocean surface period C_p, leads to the matrix equation

$$\begin{bmatrix} A & b \\ C & D \end{bmatrix} \begin{bmatrix} a \\ b \end{bmatrix} = \begin{bmatrix} F \\ 0 \end{bmatrix} \tag{4.68}$$

where A,B,C,D are $N\times N$ matrices, and a,b,F are vectors with N elements. The matrix elements are given by

$$A_{pq} = \frac{1}{2}\delta_{pq} - PV \int_{\bar{x}_q - \frac{\Delta x}{2}}^{\bar{x}_q + \frac{\Delta x}{2}} \frac{\partial G_1(\bar{x}_p, \bar{z}_p | x', z')}{\partial n'} S_q dx' \tag{4.69}$$

$$B_{pq} = PV \int_{\bar{x}_q - \frac{\Delta x}{2}}^{\bar{x}_q + \frac{\Delta x}{2}} G_1(\bar{x}_p, \bar{z}_p | x', z') S_q dx' \tag{4.70}$$

$$C_{pq} = \frac{1}{2}\delta_{pq} + PV \int_{\bar{x}_q - \frac{\Delta x}{2}}^{\bar{x}_q + \frac{\Delta x}{2}} \frac{\partial G_2(\bar{x}_p, \bar{z}_p | x', z')}{\partial n'} S_q dx' \tag{4.71}$$

$$D_{pq} = -\frac{\epsilon_2}{\epsilon_1} PV \int_{\bar{x}_q - \frac{\Delta x}{2}}^{\bar{x}_q + \frac{\Delta x}{2}} G_2(\bar{x}_p, \bar{z}_p | x', z') S_q dx' \tag{4.72}$$

where $\delta_{pq} = \begin{cases} 1 & p=q \\ 0 & otherwise \end{cases}$. The forcing vector is

$$F_p = H_o e^{-j\beta \bar{x}_p + jq_0 \bar{z}_p} \tag{4.73}$$

Exchanging the implied summation of the PGF and then performing the principal value integration results in the following

$$A_{pq} = \frac{1}{2}\delta_{pq} - \frac{1}{2L}\sum_{n=-\infty}^{\infty} \left[f_{1pq_n} + \frac{\beta_n m_q}{q_{1n}} g_{1pq_n} \right] \tag{4.74}$$

$$B_{pq} = j\frac{S_q}{2L}\sum_{n=-\infty}^{\infty} \left[\frac{g_{1pq_n}}{q_{1n}} \right] \tag{4.75}$$

$$C_{pq} = \frac{1}{2}\delta_{pq} + \frac{1}{2L}\sum_{n=-\infty}^{\infty} \left[f_{2pq_n} + \frac{\beta_n m_q}{q_{2n}} g_{2pq_n} \right] \tag{4.76}$$

$$D_{pq} = \frac{\epsilon_2}{\epsilon_1}\frac{jS_q}{2L}\sum_{n=-\infty}^{\infty} \left[\frac{g_{2pq_n}}{q_{2n}} \right] \tag{4.77}$$

There are three cases for f_{ipq_n} and g_{ipq_n}.

CASE I $(\bar{z}_p > \bar{z}_q)$

$$g_{ipq_n} = f_{ipq_n} = e^{-j\beta_n(\bar{x}_p - \bar{x}_q) - jq_{in}(\bar{z}_p - \bar{z}_q)} \frac{2\sinh[j(\beta_n + q_{in}m_q)\frac{\Delta x}{2}]}{j(\beta_n + q_{in}m_q)} \tag{4.78}$$

CASE II $(\bar{z}_p < \bar{z}_q)$

$$g_{ipq_n} = -f_{ipq_n} = e^{-j\beta_n(\bar{x}_p - \bar{x}_q) - jq_{in}(\bar{z}_q - \bar{z}_p)} \frac{2\sinh[j(\beta_n - q_{in}m_q)\frac{\Delta x}{2}]}{j(\beta_n - q_{in}m_q)} \tag{4.79}$$

CASE III $(\bar{z}_p = \bar{z}_q)$

$$g_{ipq_n} = \frac{2e^{-j\beta_n(\bar{x}_p - \bar{x}_q)}}{\beta_n^2 - q_{in}^2 m_q^2}\{jq_{in}|m_q| + e^{-jq_{in}|m_q|\frac{\Delta x}{2}}[\beta_n \sin(\beta_n \frac{\Delta x}{2}) - jq_{in}|m_q|\cos(\beta_n \frac{\Delta x}{2})]\} \tag{4.80}$$

$$f_{ipq_n} = \frac{-2jsgn(m_q)e^{-j\beta_n(\bar{x}_p - \bar{x}_q)}}{\beta_n^2 - q_{in}^2 m_q^2}\{\beta_n - e^{-jq_{in}|m_q|\frac{\Delta x}{2}}[\beta_n \cos(\beta_n \frac{\Delta x}{2}) + jq_{in}|m_q|\sin(\beta_n \frac{\Delta x}{2})]\} \tag{4.81}$$

where $i=1,2$, and $sgn(x) = \begin{cases} 1 & x>1 \\ 0 & x=0 \\ -1 & x<1 \end{cases}$.

4.3.2 Scattered fields

Once ψ and $\partial\psi/\partial n$ have been obtained, the scattered fields in both regions may be determined by

$$\psi_1^s(\vec{\rho}) = \int_{C_p}\left[\psi_1(\vec{\rho}\,')\frac{\partial G_1(\vec{\rho}\,|\,\vec{\rho}\,')}{\partial n'} - \frac{\partial \psi_1(\vec{\rho}\,')}{\partial n'}G_1(\vec{\rho}\,|\,\vec{\rho}\,')\right]dl' \tag{4.82}$$

$$\psi_2^s(\vec{\rho}) = -\int_{C_p}\left[\psi_1(\vec{\rho}\,')\frac{\partial G_2(\vec{\rho}\,|\,\vec{\rho}\,')}{\partial n'} - \frac{\epsilon_2}{\epsilon_1}\frac{\partial \psi_1(\vec{\rho}\,')}{\partial n'}G_2(\vec{\rho}\,|\,\vec{\rho}\,')\right]dl' \tag{4.83}$$

Exchanging the implied summation in the PGF and the principal value integration in (4.82) and (4.83) gives

$$H_{y1}^{s}(x,z) = \psi_1^{s}(x,z) = \sum_{n=-\infty}^{\infty} \gamma_n e^{-j\beta_n x} e^{-jq_{1n}z} \tag{4.84}$$

$$H_{y2}^{s}(x,z) = \psi_2^{s}(x,z) = \sum_{n=-\infty}^{\infty} \zeta_n e^{-j\beta_n x} e^{jq_{2n}z} \tag{4.85}$$

where

$$\gamma_n = \frac{1}{j2Lq_{1n}} \int_{C_p} \left[\psi_1(x',z') \frac{\partial g_{1n}(x',z')}{\partial n'} - g_{1n}(x',z') \frac{\partial \psi_1(x',z')}{\partial n'} \right] dl' \tag{4.86}$$

$$\zeta_n = -\frac{1}{j2Lq_{2n}} \int_{C_p} \left[\psi_1(x',z') \frac{\partial g_{2n}(x',z')}{\partial n'} - \frac{\epsilon_2}{\epsilon_1} g_{2n}(x',z') \frac{\partial \psi_1(x',z')}{\partial n'} \right] dl' \tag{4.87}$$

and $g_{1n}(x',z') = e^{j\beta_n x'} e^{jq_{1n}z'}$, $g_{2n}(x',z') = e^{j\beta_n x'} e^{-jq_{2n}z'}$.

The scattered field in region (1) is seen to be comprised of an infinite number of plane waves. Only a finite number of these carry power to the far field, and the rest are evanescent in nature. The modes that propagate must have a real q_{in}, *for* i=1,2. Therefore, in region (1) $|\beta_n| < k_1$, and in region (2) $|\beta_n| < k_2$.

Subsequent to the solution of the MoM matrix equation (4.68) for a_q, b_q, the scattered field in both regions off the ocean surface can be determined from (4.84) and (4.85). The backscattered field is obtained from by restricting the sum over n to include only those modes which are propagating in the $-x$ direction ($\beta_n < 0$).

4.4 Duality of TE and TM polarizations

The above analysis was performed assuming a monochromatic TM polarized incident plane wave. Through the use of the duality theorem [49] the TE polarization state can be analyzed. The incident magnetic field [H_{yi}] is replaced with an incident electric field [E_{yi}] and the constitutive parameters are also exchanged (μ, ϵ). The unknowns for TE case integral equations will be E_y and $\frac{\partial E_y}{\partial n}$. A table of the relationships between the TE and TM cases is shown below.

TM	ϵ	μ	H_y	E_x	E_z	$\partial H_y / \partial n$
TE	μ	ϵ	E_y	$-H_x$	$-H_z$	$\partial E_y / \partial n$

The resulting integral equations for the TE case are

$$\frac{\psi(\vec{\rho})}{2} - PV\int_{C_P}\left[\psi(\vec{\rho}')\frac{\partial G_1(\vec{\rho}\,|\,\vec{\rho}')}{\partial n'} - \frac{\partial \psi(\vec{\rho}')}{\partial n'}G_1(\vec{\rho}\,|\,\vec{\rho}')\right]dl' = \psi_1^i(\vec{\rho}) \qquad (4.88)$$

$$\frac{\psi(\vec{\rho})}{2} + PV\int_{C_P}\left[\psi(\vec{\rho}')\frac{\partial G_2(\vec{\rho}\,|\,\vec{\rho}')}{\partial n'} - \frac{\mu_2}{\mu_1}\frac{\partial \psi(\vec{\rho}')}{\partial n'}G_2(\vec{\rho}\,|\,\vec{\rho}')\right]dl' = 0 \qquad (4.89)$$

where ψ_i now represents the electric field [E_y] and the Green's functions remain the same. This set of coupled integral equations can also be solved by a similar MoM numerical method.

4.5 Numerical Examples

This section presents theoretical numerical results for several cases of interest. Where possible, the results from the PGF method are compared to the results of the Rayleigh mode-matching analysis. As a starting point, the parameters are chosen to match those of the experimental periodic surface discussed in Chapter 3. The spatial wavelength is chosen as L=0.1016m. The parameters of the lower medium are chosen as the nominal ocean parameters ϵ=80, σ=4.

The first set of results to be examined will be theoretical responses for TM excitation. The TM polarization state is of primary interest because of the possibility of a Brewster's-angle phenomenon. The manner in which the results are to be shown will mirror the chapter 3 treatment. The induced surface fields will be compared in order to confirm the theoretical methods and to build upon the phenomenological base started in chapter 3. Following the surface field results will be an examination of the Brewster's-

angle phenomenon. The theoretical transient scattered fields, which are the ultimate goal, are briefly examined before an in-depth treatment in section 4.6.

Figure 4.2 shows a comparison of the magnitude of the surface fields computed using the PGF and Rayleigh methods. It is clear that for smaller heights the two methods agree very well, while for larger heights the Rayleigh method does not match the predictions of the PGF method. This result lends strength to the numerical methods. The knowledge gained from the PEC case has also contributed to the confidence in the methods. Note, although not shown, there was also excellent agreement between the other unknown surface field quantity (the normal derivative of the magnetic field).

The effects of the various problem parameters on the surface fields are shown in the following figures. Many of the same features noted in the PEC case are also evident for the imperfectly conducting case. There are also some new findings that will be highlighted. In Figure 4.3 the frequency dependence of the surface fields for a TM incident wave are shown. The surface is an infinite sea-water sinusoid with L=0.1016m and h/L=.125. There is more variation with frequency as compared to the PEC case (Figure 3.15). This is due to the increased sinusoid height.

The dependence of sinusoid height is examined in Figure 4.4 and Figure 4.5. The higher amplitude surface (Figure 4.4) require the MFIE formulation and exhibit some interesting variation. The lower height sinusoids (Figure 4.5), which are all in the Rayleigh-hypothesis regime, do not exhibit a similar dependency. This is reasonable since there is multiple scattering in the troughs of the higher amplitude surfaces. These multiple scatters manifest themselves in the redistribution of the surface fields.

The effect of incidence angle, as shown in Figure 4.6, is very similar to the PEC case. The normal incidence has a symmetric distribution as expected and a shadowed region appears for the increasing incidence angles.

In Figure 4.7 the period length (L) of the sea-water sinusoidal surface is increased from 0.1016m to 0.4064m. The resultant induced surface fields reveal the same

tendencies as observed in the PEC case. The surface becomes relatively flatter since the amplitude (h) is not changed which results in less shadowing and a field distribution approaching a constant, which is expected for a flat surface.

The new feature with the two-media case is finite conductivity. The effects of conductivity on the surface fields, which lead directly to scattered fields (by Huygen's principle), are examined in Figure 4.8 and Figure 4.9. In Figure 4.8 the excitation frequency is 2 GHz and as conductivity is increased the magnitude of the surface fields is also increased. It is interesting that sea-water ($\sigma = 4S/m$) is closer to a perfect dielectric than a PEC. In Figure 4.9 the excitation frequency is increased to 6 GHz. The results indicate a more defined shadow region, and the conductivity effects are reduced. These phenomena are expected, as the frequency increases the imaginary part of the complex permittivity is reduced, thereby reducing the conductivity effects. Physically the polarization currents become dominant over the conduction currents. The effects on the TE case are similar but are not shown.

Information about the Brewster angle phenomenon can be extracted by varying the incidence angle and observing the forward scattered amplitudes. It is well known that a TM polarized plane wave incident upon an infinite planar dielectric will exhibit a Brewster's angle. From the classical theory the Brewster angle for a air-dielectric interface is given by $\theta_b = \tan^{-1}(\sqrt{\epsilon_r})$. If the dielectric had a relative permittivity of 80 then the Brewster's angle would be 83.6°. However, the problem that has been analysed deviates from the ideal planar/dielectric case. The interface is now sinusoidal and the lower medium can be lossy. The expectation is that there will no longer be a true Brewster's angle but possible a minimum in the same range of incidence angles. In Figure 4.10 a comparison of TE and TM forward scattered fields are shown for incidence angles around the expected Brewster's angle. The TM case does indeed exhibit a minimum and is also compared with the case of a lossy flat surface. This is a very

favorable result and gives hope that the TM incidence could be of great importance. A detailed examination of the TM case follows.

Figure 4.11 shows the variation of the forward scatted H-field vs incidence angle for various wave heights for a lossless dielectric (σ =0). It is clear for a flat surface that the forward scattered field is zero at the Brewster's angle (approximately 83.6°). As the wave height is increased, the forward scattered H-field no longer goes to zero, but instead has a minimum near the Brewster angle. For the lossy case, there is no true Brewster angle even for a perfectly flat surface. There is however, a well defined minimum as shown in Figure 4.12.

The frequency dependence of the Brewster's angle is shown in Figure 4.13. The lower frequencies, where there is only one propagating Floquet mode, exhibit a smooth variation and reveal the Brewster angle minimum. For the higher frequencies the location of the Brewster's angle minimum is less obvious. The additional propagating Floquet modes produce an interference pattern; the fundamental mode (specular) has the largest amplitude so there still remains the general minimum around the Brewster's angle.

The effects on the Brewster's angle minimum with respect to the sea-water surface height is shown in Figure 4.14. This figure is a different representation of Figure 4.12 and shows the variation of the minimum angle as the height is increased. The Brewster's angle minimum is seen to move from roughly 84° to around 78° as the sea-water height is increased. An explanation is found when the effective permittivity of the sea-water is considered. The increasing sinusoid amplitude results in more backscatter (Figure 4.15) and this would act like a change in effective permittivity. The increasing sinusoid height would reduce the effective permittivity and this would change the Brewster's angle correspondingly.

The scattered field dependence on field point location is shown in the next set of figures. The response for a TM incident plane wave at 85° upon an infinite sea-water sinusoid with L=0.1016m and h/L=.125 is shown. In Figure 4.16 the backscattered H-

field is shown for various locations of the field point along the x-axis. The expected periodic nature in the x-direction is noted as well the Floquet mode spikes. A variation of the field point along the z-axis is shown in Figure 4.17. For small values of z (near the surface) the effects of evanescent waves and the number of propagating Floquet modes are observable.

The forward scattered H-fields for the same cases as above are shown in Figure 4.18 and Figure 4.19. The Floquet mode locations are once again obvious and the periodic nature of the fields along the x-direction is also seen. The frequency dependence is quite interesting but there is little physical interpretation.

Next, the consistency of the two methods (MFIE and Floquet mode-matching) for calculation of the total scattered field is evaluated. The parameters chosen are h/L=0.0625, θ_i=85°, and the observation point is x/L=0, z/L=20. The field was computed for frequencies between 0 and 12 GHz. The two methods are seen to agree well in spectral magnitude as shown in Figure 4.20. The transient response was synthesized using the Floquet mode spectral response and is shown in Figure 4.21. Similar behavior was observed for the perfectly conducting results in chapter 3.

The backscattered field was also computed using both methods. The agreement between the methods is very good as shown in Figure 4.22. The backscattered field for the ocean surface behaves similarly to the perfectly conducting case shown in the previous chapter. The synthesized transient response was also computed. A small portion of the temporal response is shown in Figure 4.23. The two methods are seen to agree reasonably well in overall amplitude and waveshape.

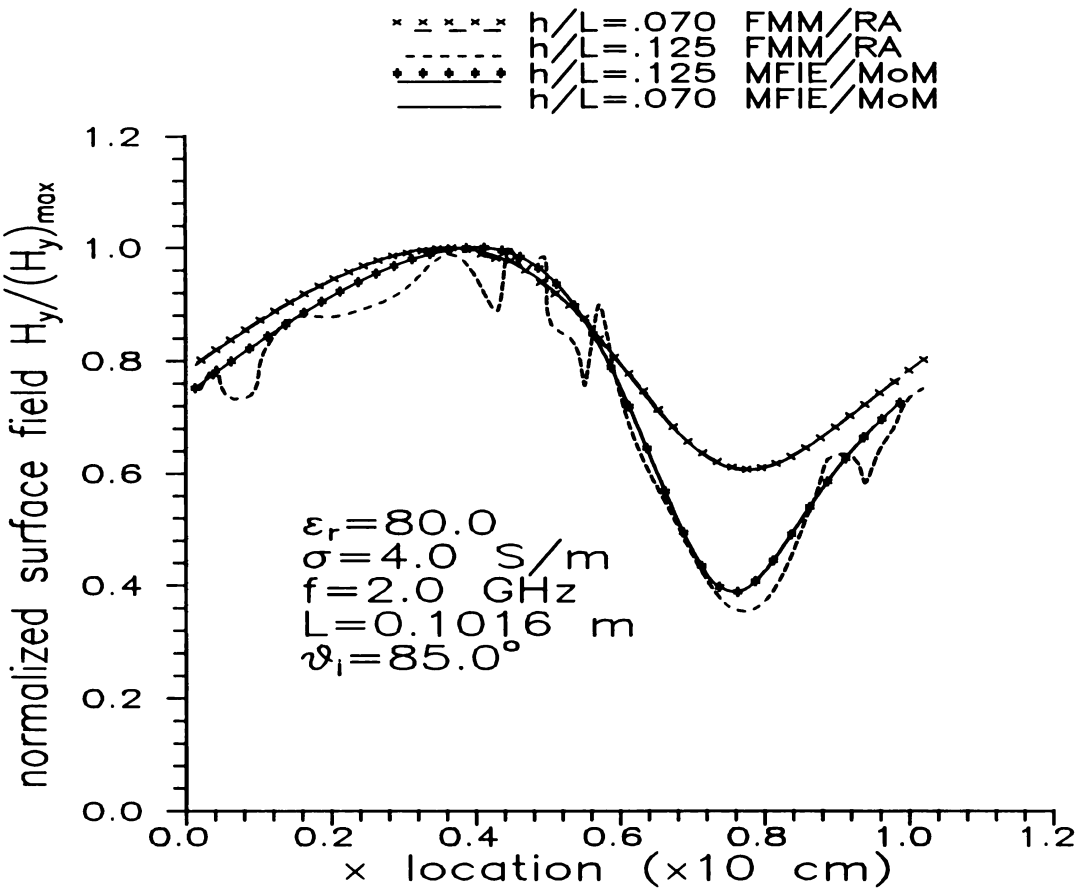

Figure 4.2 Surface field calculations using Rayleigh-mode-matching method compared to MFIE PGF method for various h/L ratios.

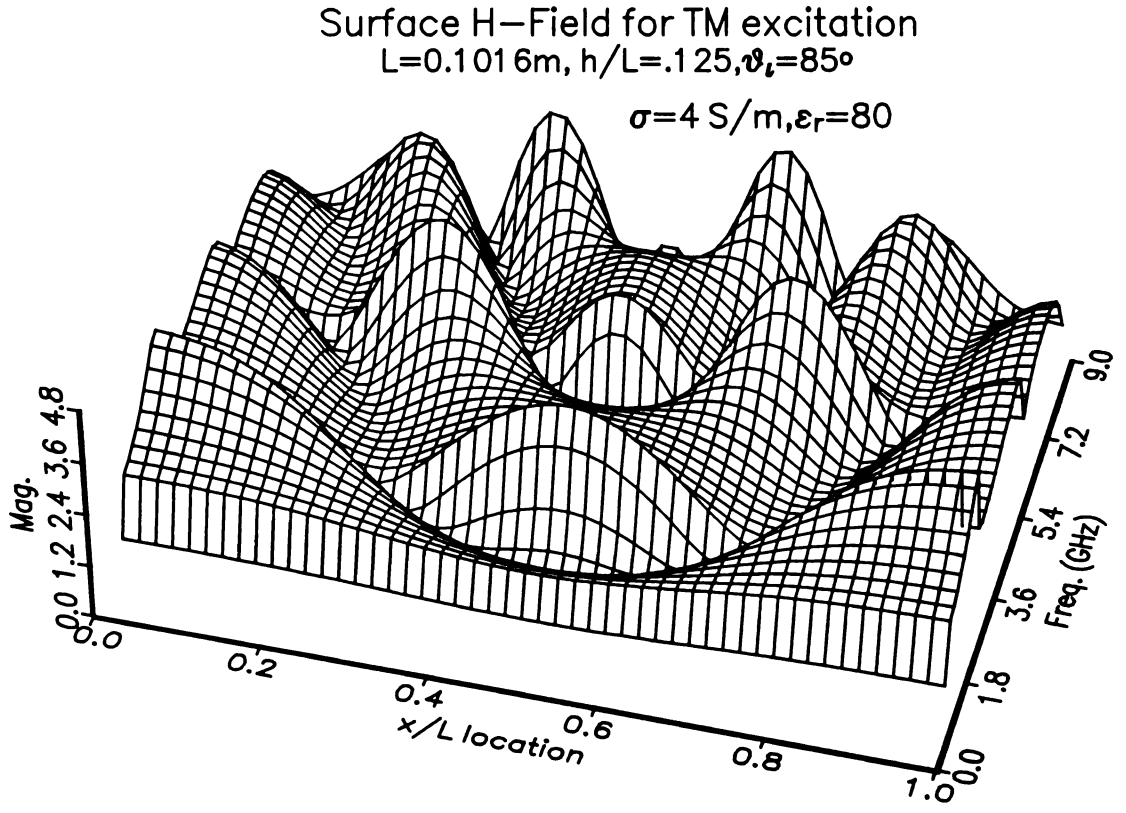

Figure 4.3 Surface H-fields on an infinite sea-water sinusoid for a TM incident plane wave. Excitation frequency dependence is shown.

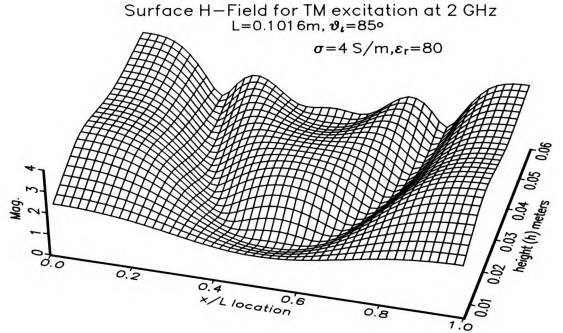

Figure 4.4 Surface H-fields on an infinite sea-water sinusoid due to TM excitation at 2 GHz. The dependence on sinusoid interface amplitude (h) is examined.

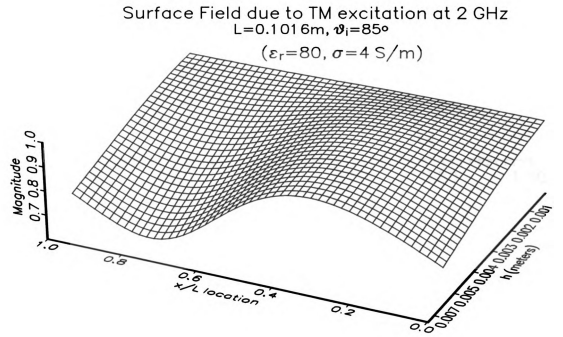

Figure 4.5 Surface H-fields on smaller height sea-water sinusoids.

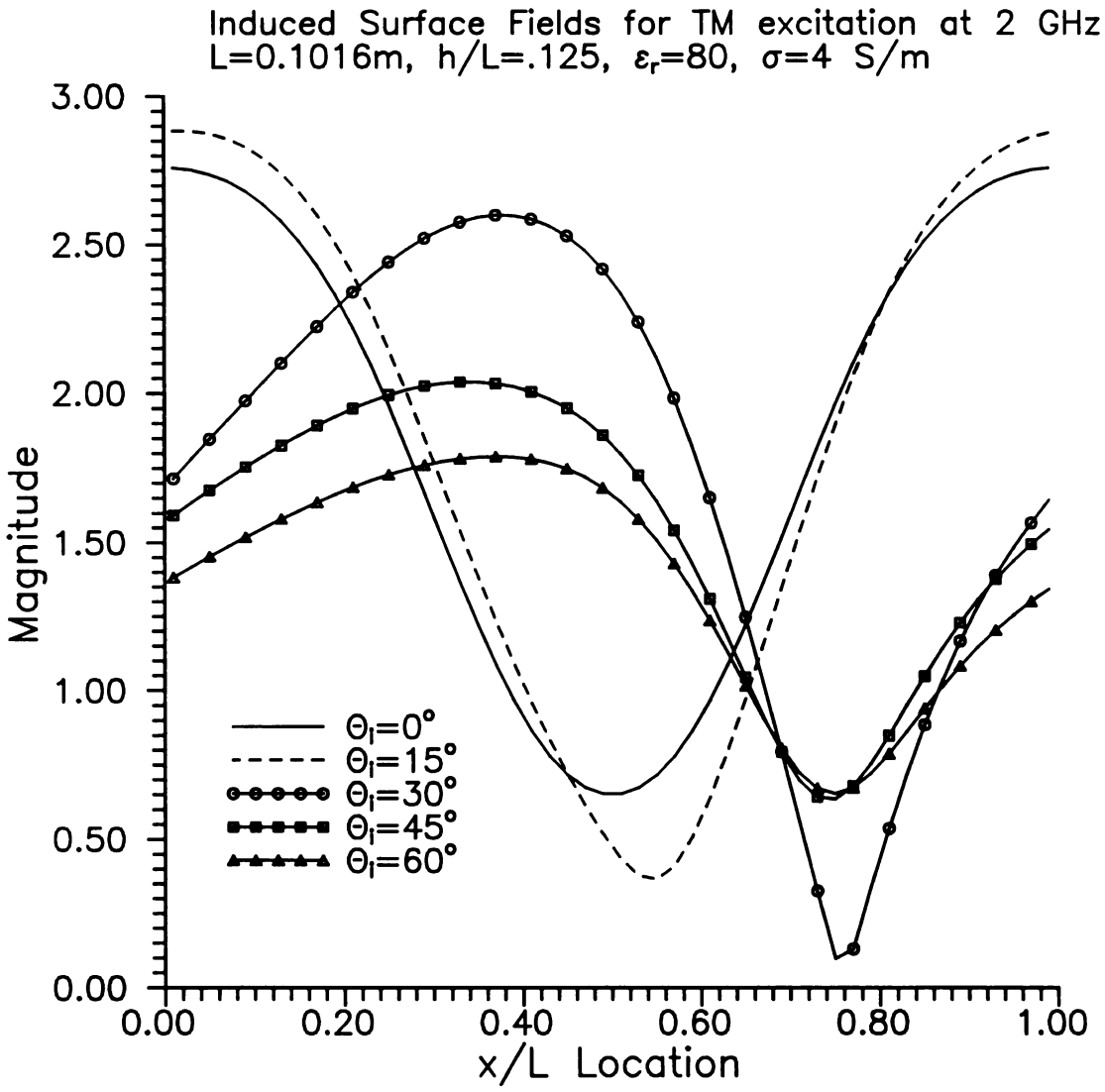

Figure 4.6 Surface H-fields on an infinite sinusoid for TM excitation at 2 GHz. The dependence on incidence angle is examined.

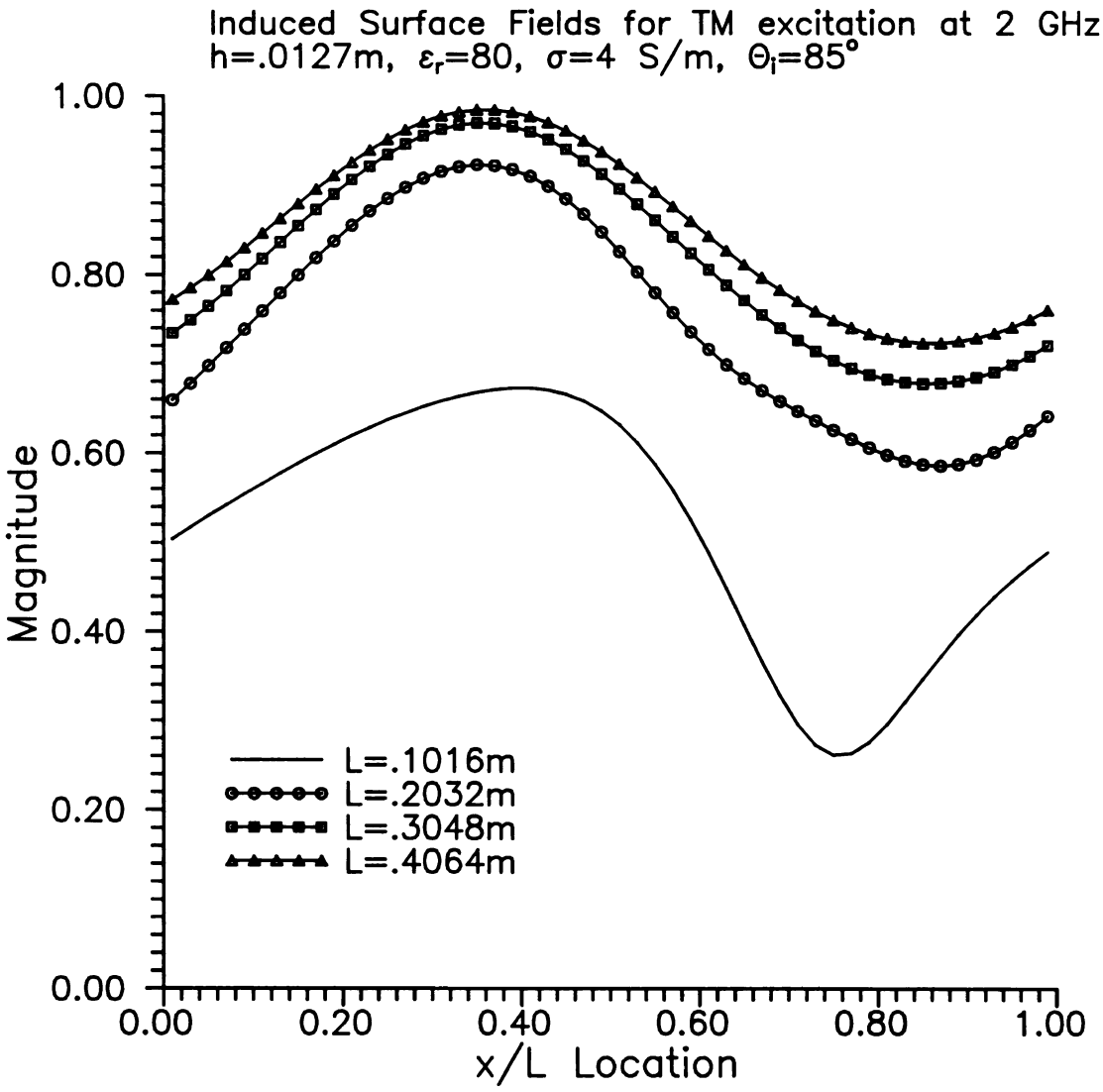

Figure 4.7 Surface H-fields on an infinite sea-water sinusoid due to TM excitation at 2 GHz. The dependence on sea-surface period is shown.

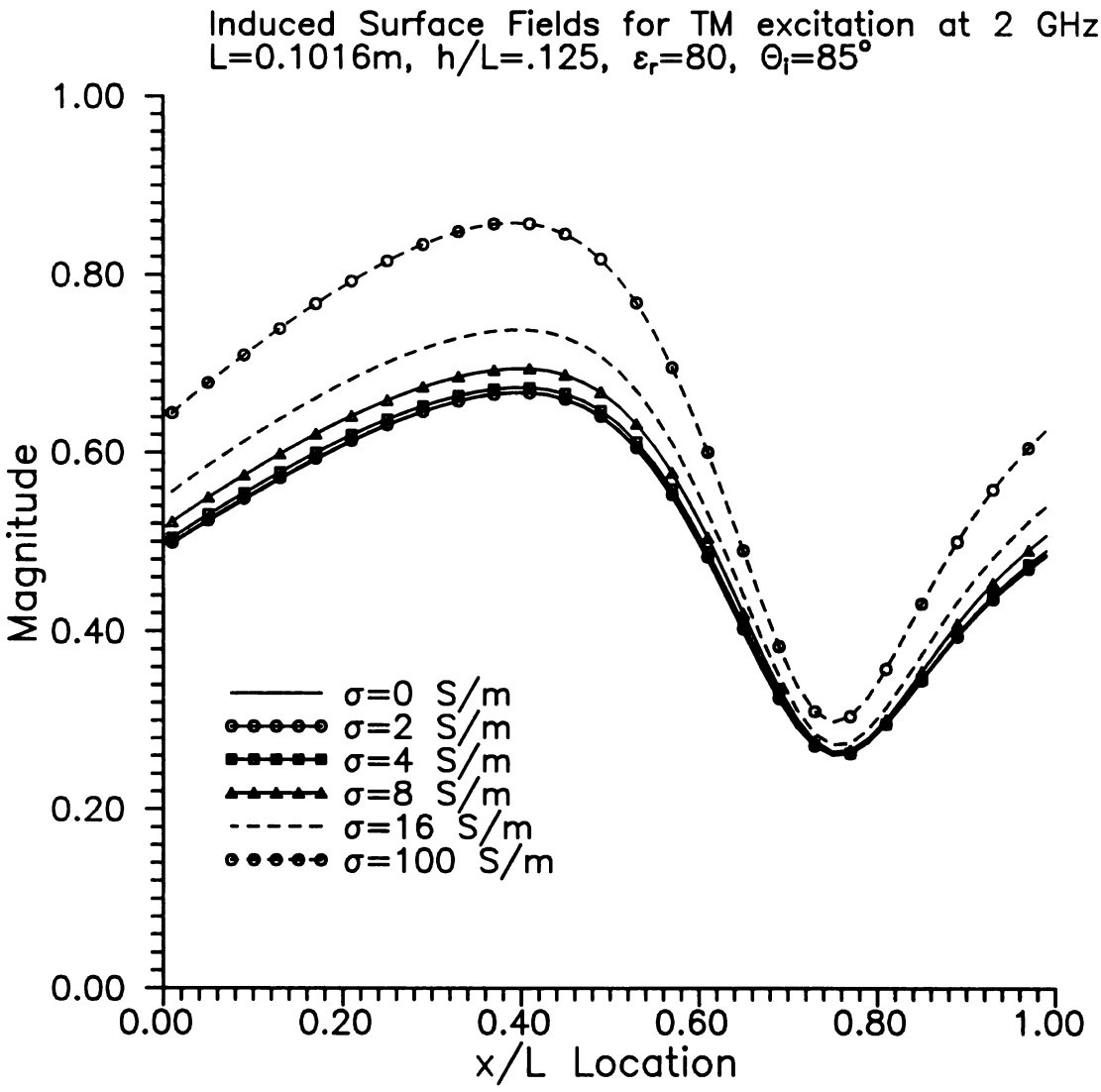

Figure 4.8 Surface H-fields on an infinite sinusoid due to TM excitation at 2 GHz. The effects of conductivity are shown.

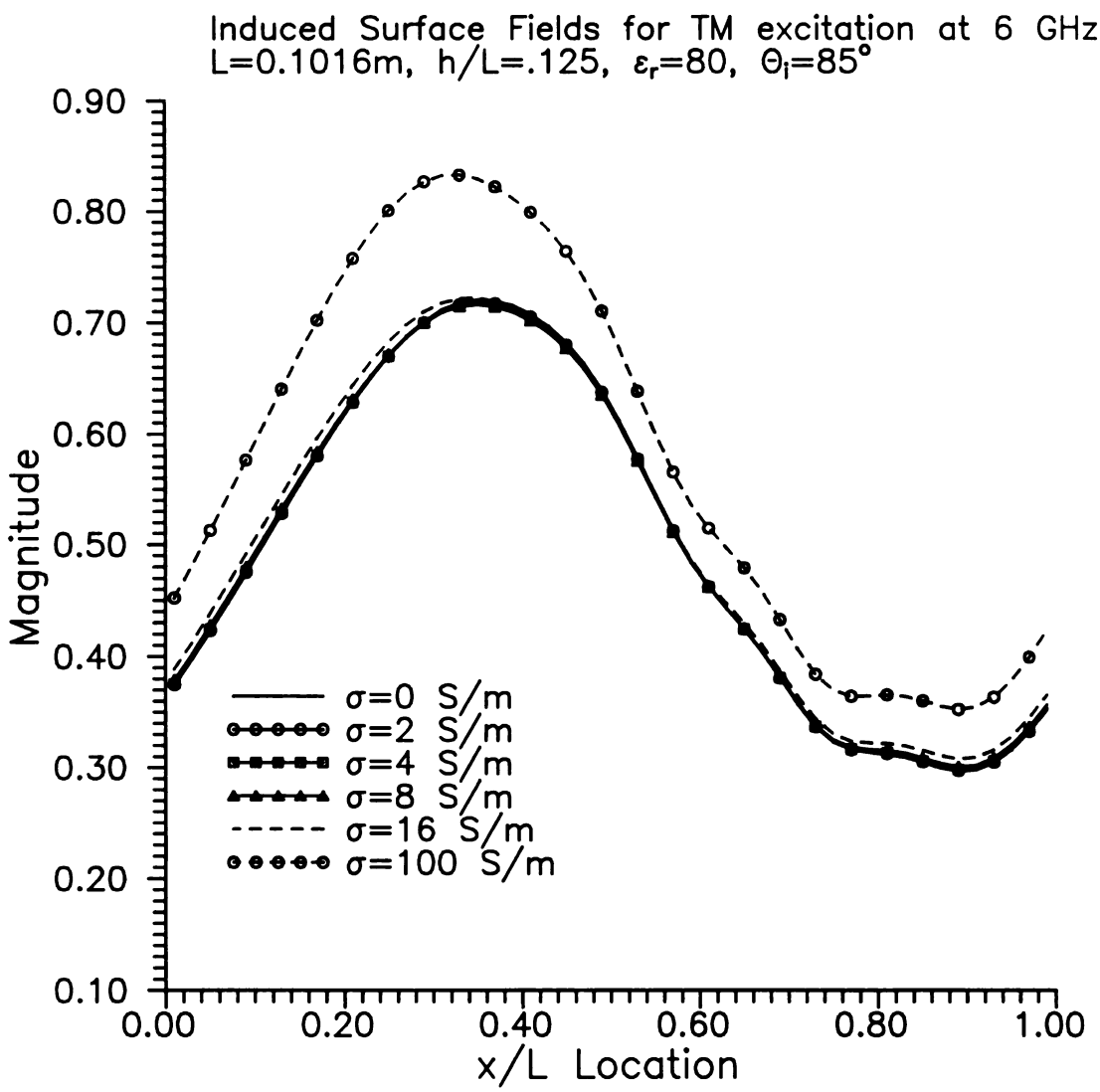

Figure 4.9 Surface H-fields on a infinite sinusoid excited by a 6 GHz TM wave. The effects of conductivity are shown.

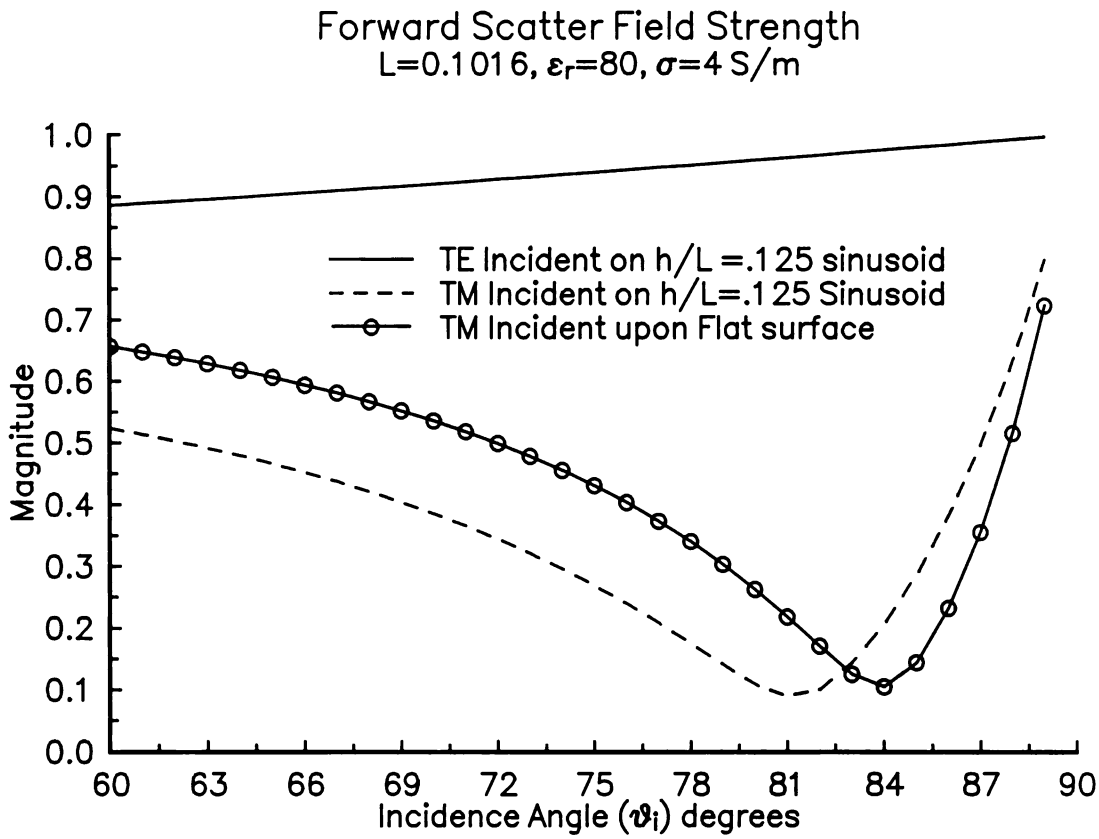

Figure 4.10 Identification of a Brewster angle for TM incidence. Comparison with TE excitation is shown.

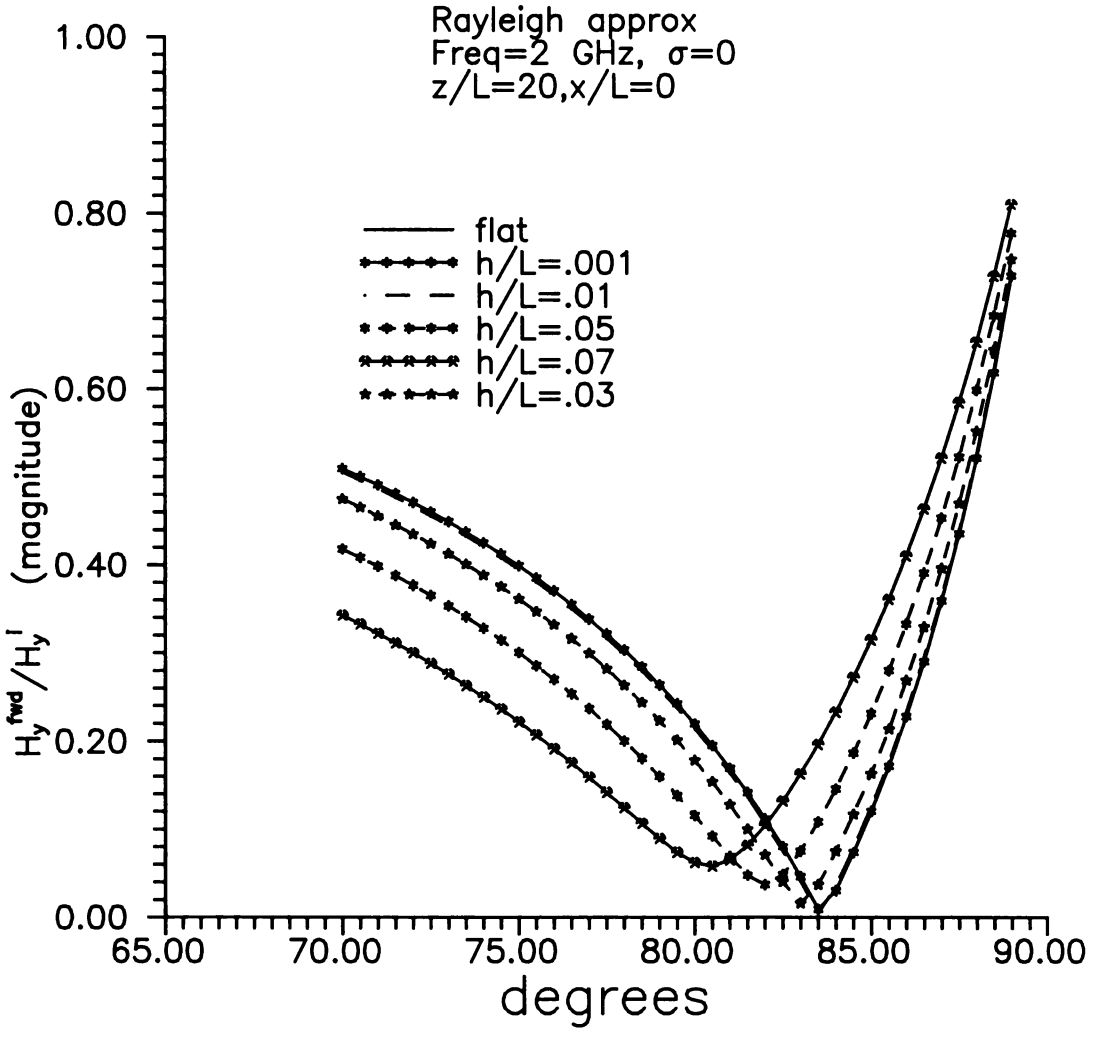

Figure 4.11 Identification of Brewster's angle for lossless dielectric (ϵ=80,σ=0) surface.

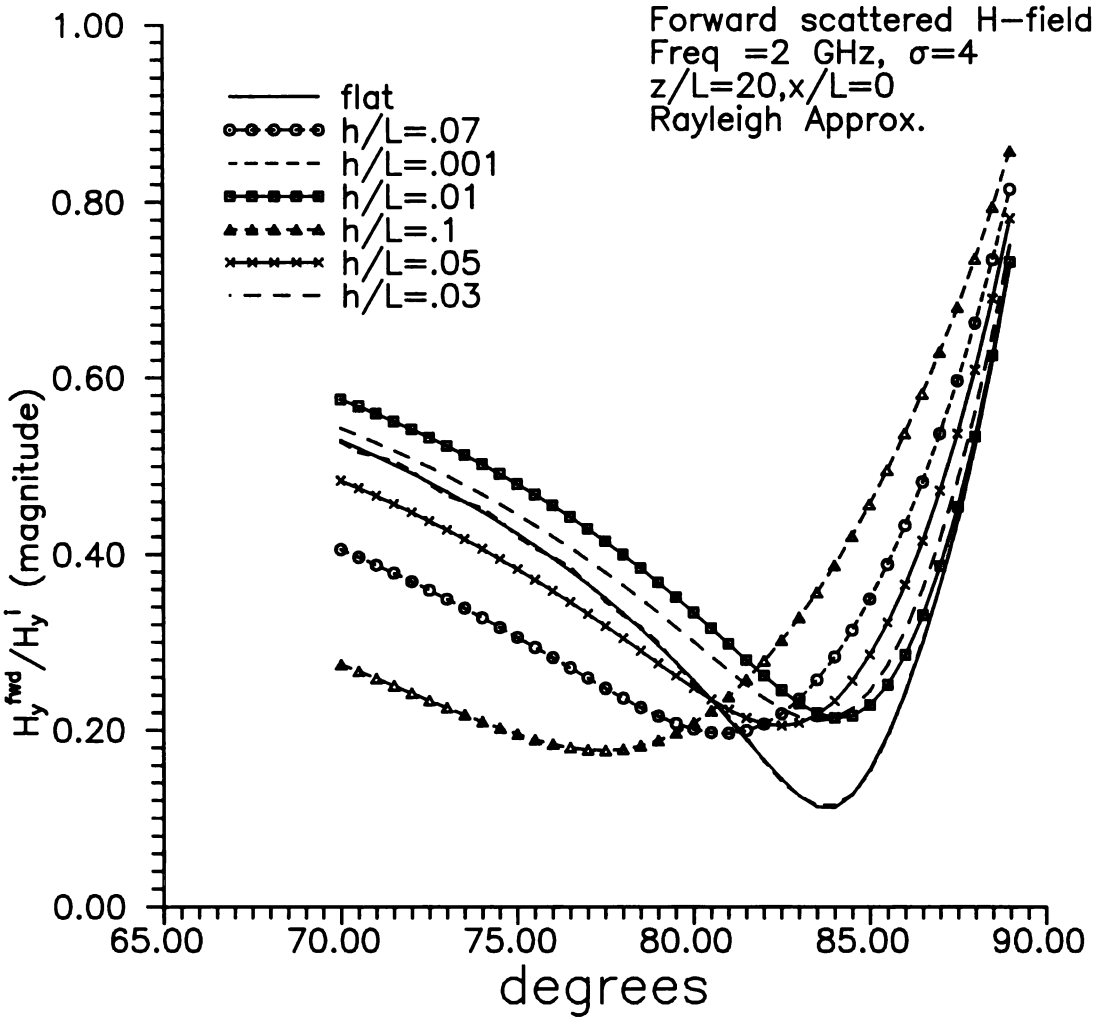

Figure 4.12 Identification of Brewster angle for lossy dielectric surface (ϵ=80,σ=4) for various h/L.

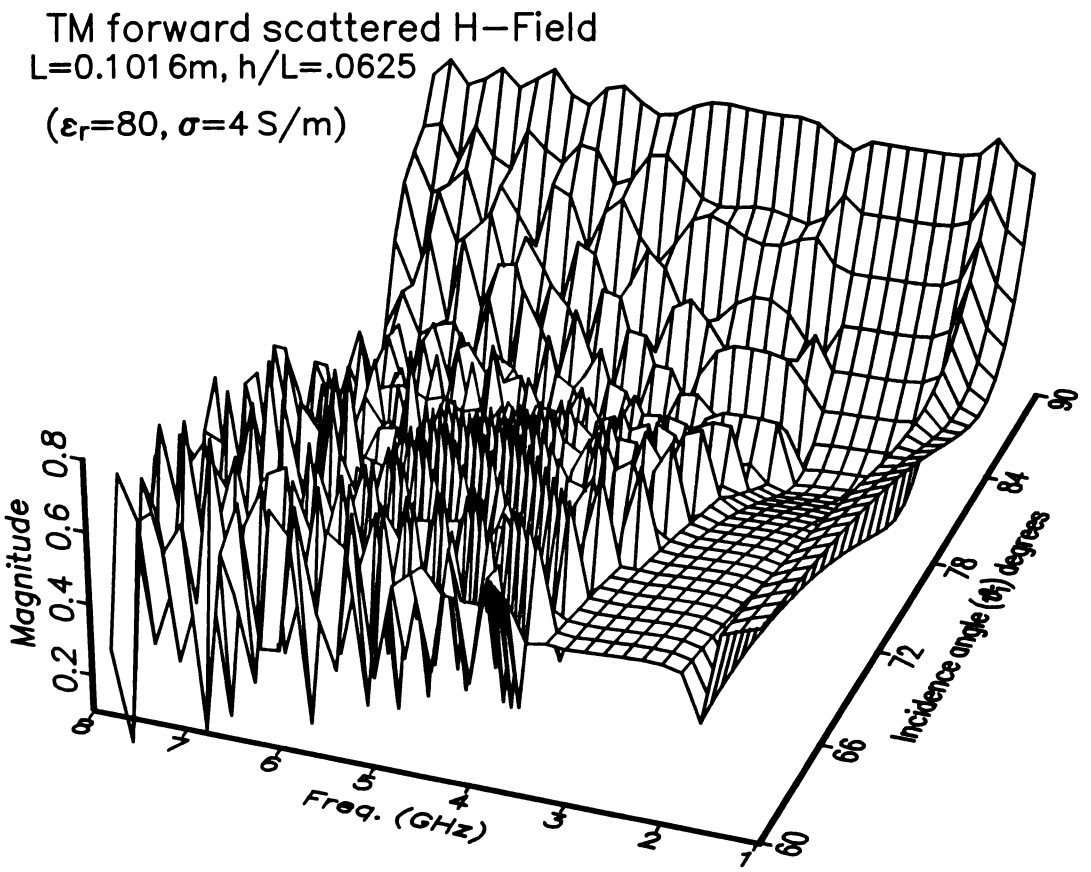

Figure 4.13 Identification of a Brewster angle for TM incidence. The effects of excitation frequency are shown.

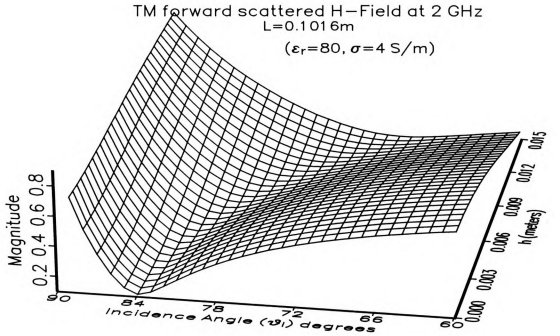

Figure 4.14 Identification of a Brewster angle for TM incidence. The effects of seawater sinusoid amplitude are examined.

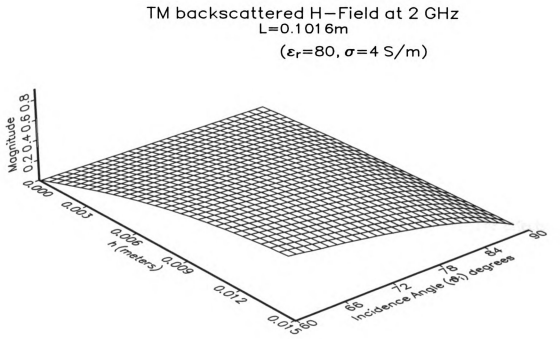

Figure 4.15 The backscattered H-field around the Brewster angle for TM incidence.

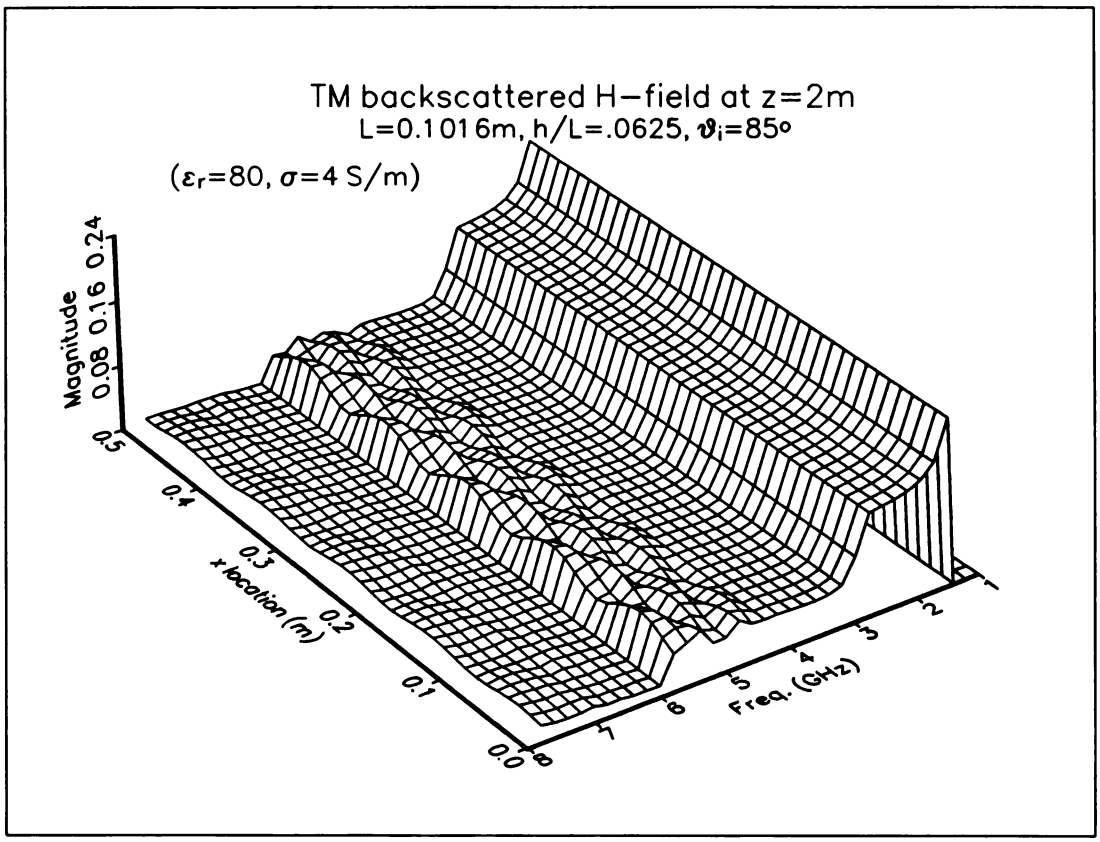

Figure 4.16 Backscattered H-field from an infinite sea-water sinusoid. The effects of field point location are examined.

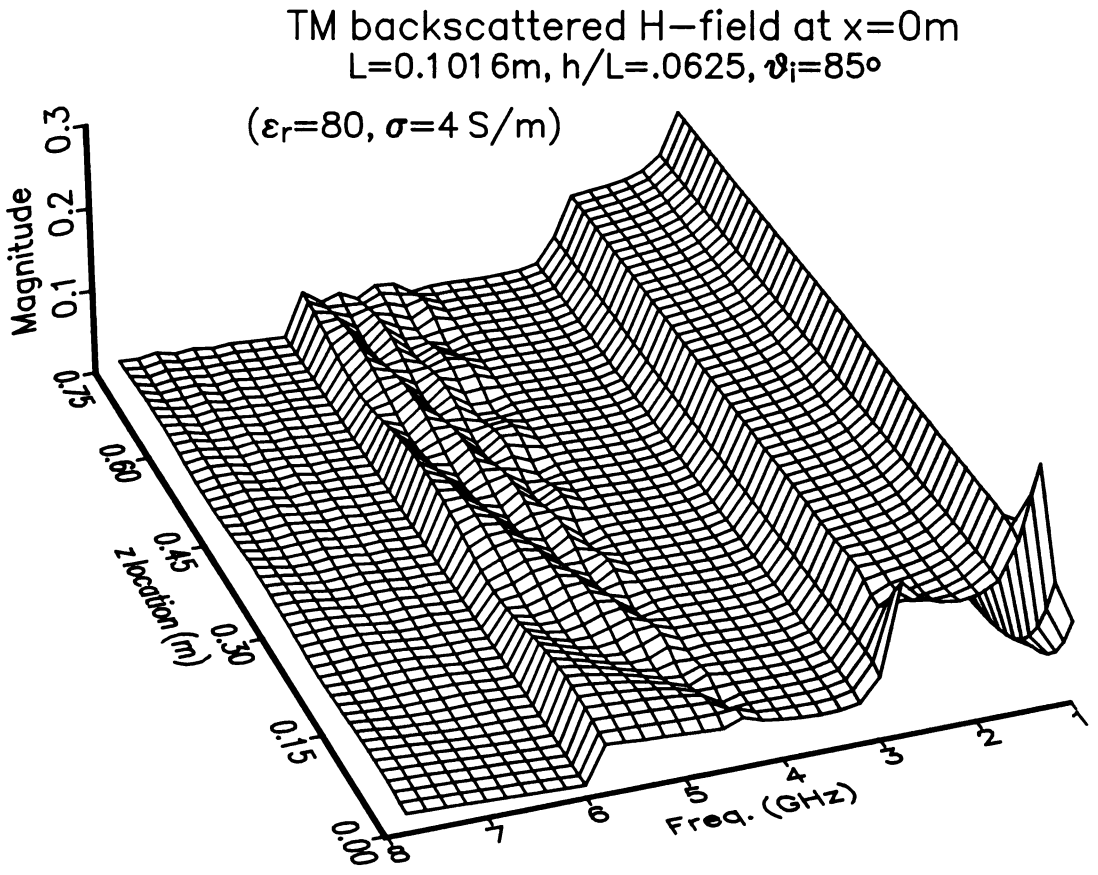

Figure 4.17 Backscattered H-field from an infinite sea-water sinusoid. The effects of field point location are examined.

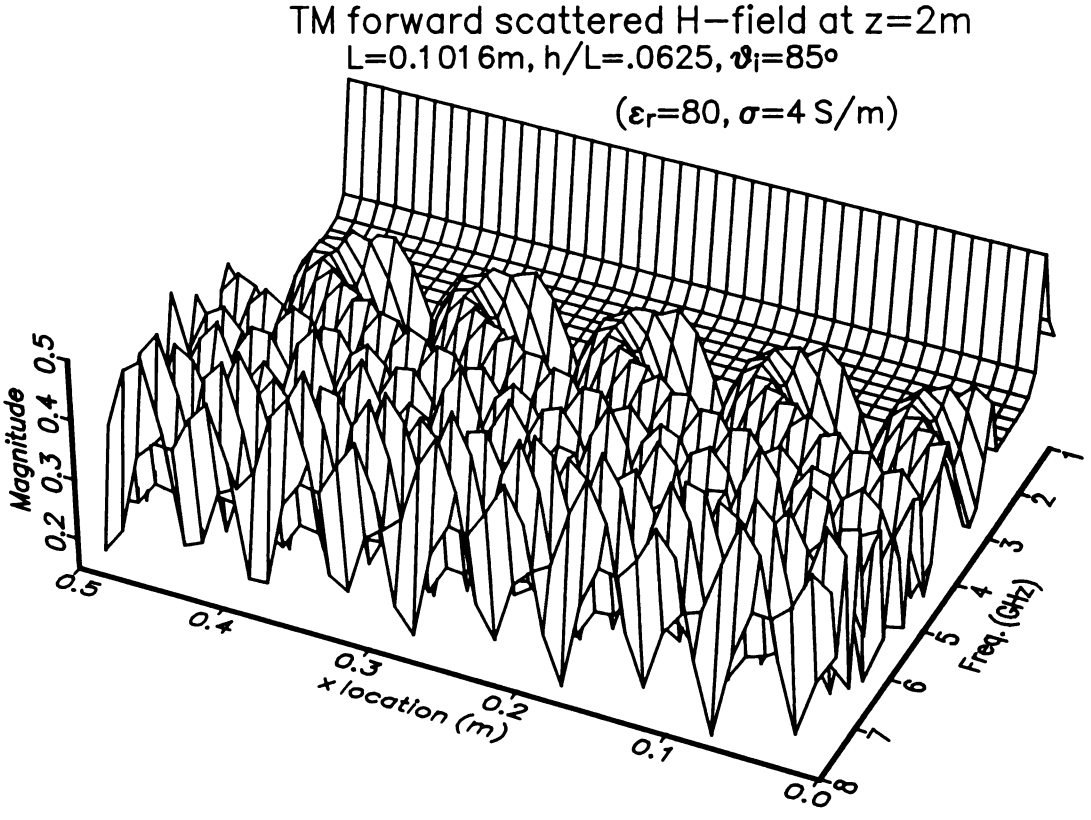

Figure 4.18 Forward scattered H-field from an infinite sea-water sinusoid. The effects of field point location are examined.

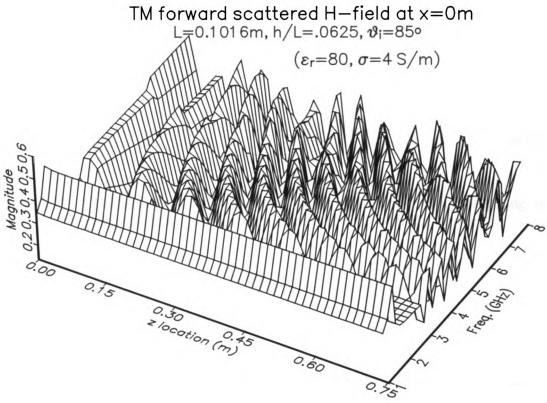

Figure 4.19 Forward scattered H-field from an infinite sea-water sinusoid. The effects of field point location are examined.

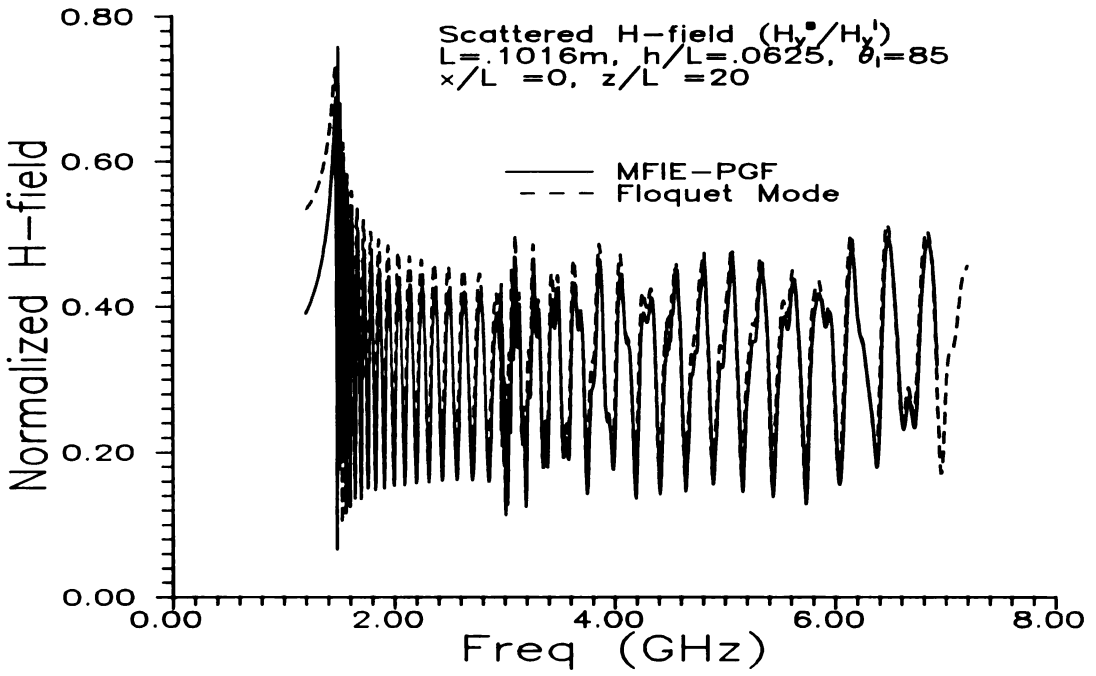

Figure 4.20 Comparison of Rayleigh and MFIE-PGF method for computing total scattered field spectrum from imperfectly conducting surface.

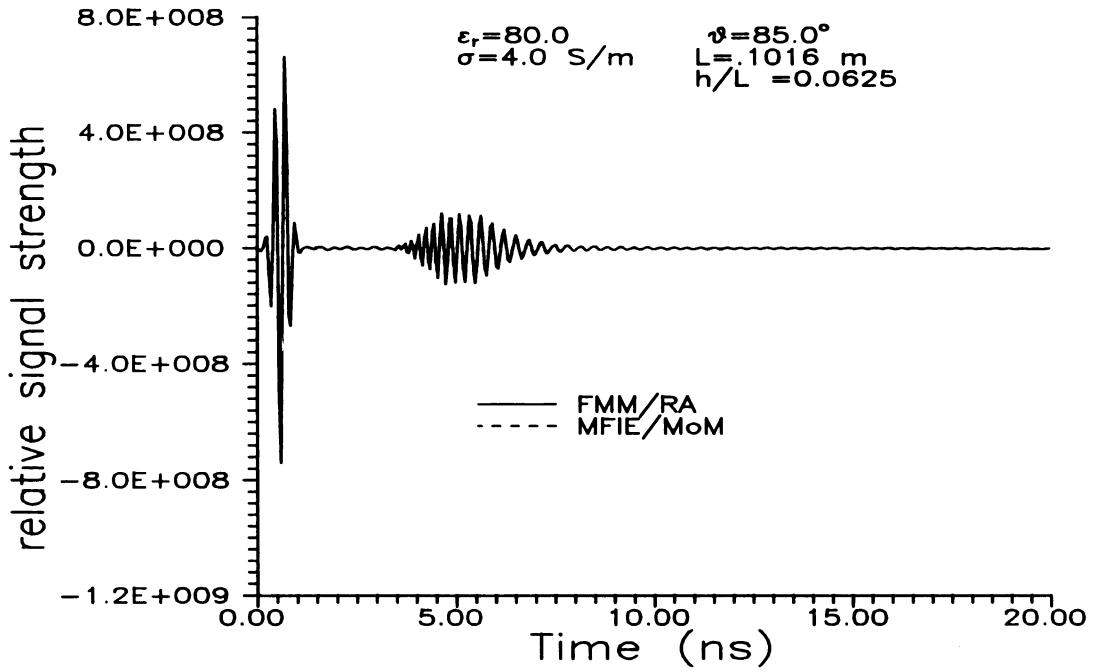

Figure 4.21 Transient TM response of imperfectly conducting sinusoidal surface.

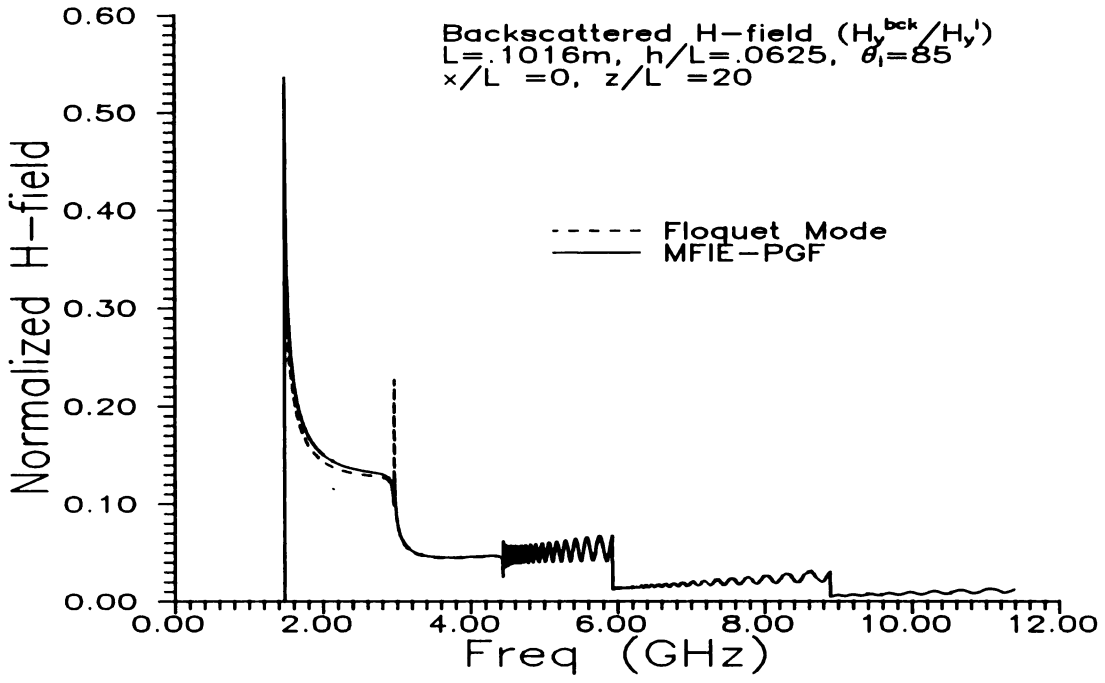

Figure 4.22 Comparison of Rayleigh and MFIE PGF methods for computing backscattered field spectrum for imperfectly conducting surface.

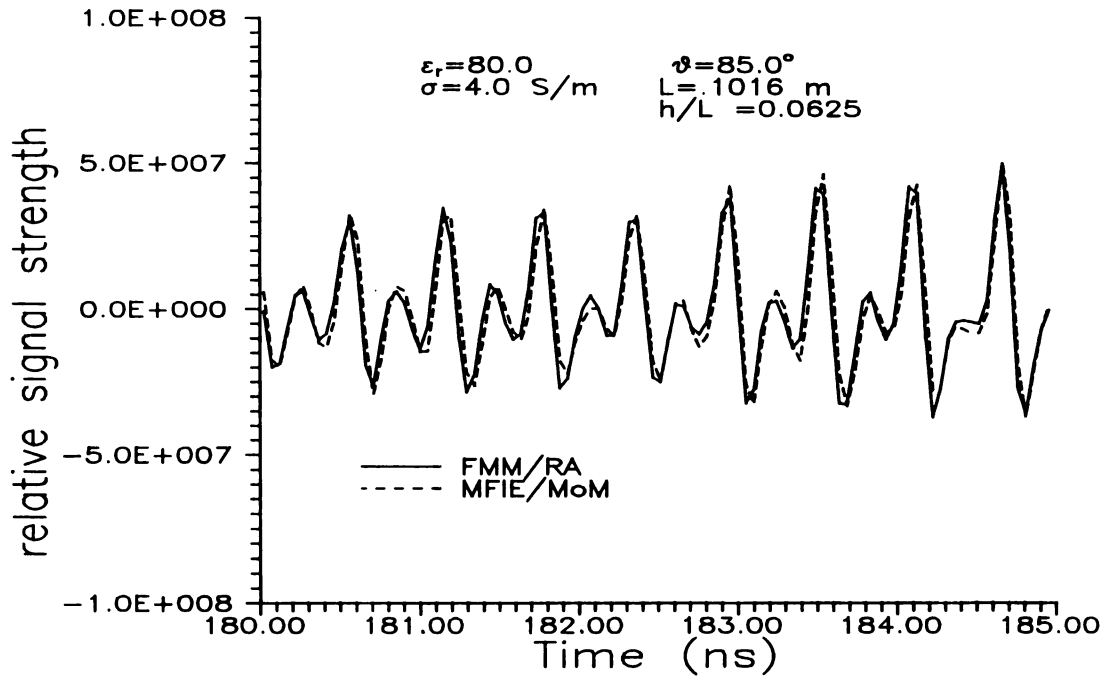

Figure 4.23 Backscattered transient response of imperfectly conducting surface.

4.6 Experimental Results

The measured responses of a sinusoidal sea-water wave are more difficult to obtain experimentally than the PEC sinusoid model. The construction of the sinusoidal wave, which must once again be finite, is not as straightforward as constructing a PEC sinusoid. The measurements must be performed using the arch range scattering system, which was described in chapter 2, because of the nature of the sea-water wave. The wave was constructed by creating a cavity in a block of expanded polystyrene ("styrofoam"). The cavity was made in order to hold the water and had one side machined as a sinusoid (11 crests) with L=0.1016m and h/L=.125. A diagram of this structure is shown in Figure 4.24.

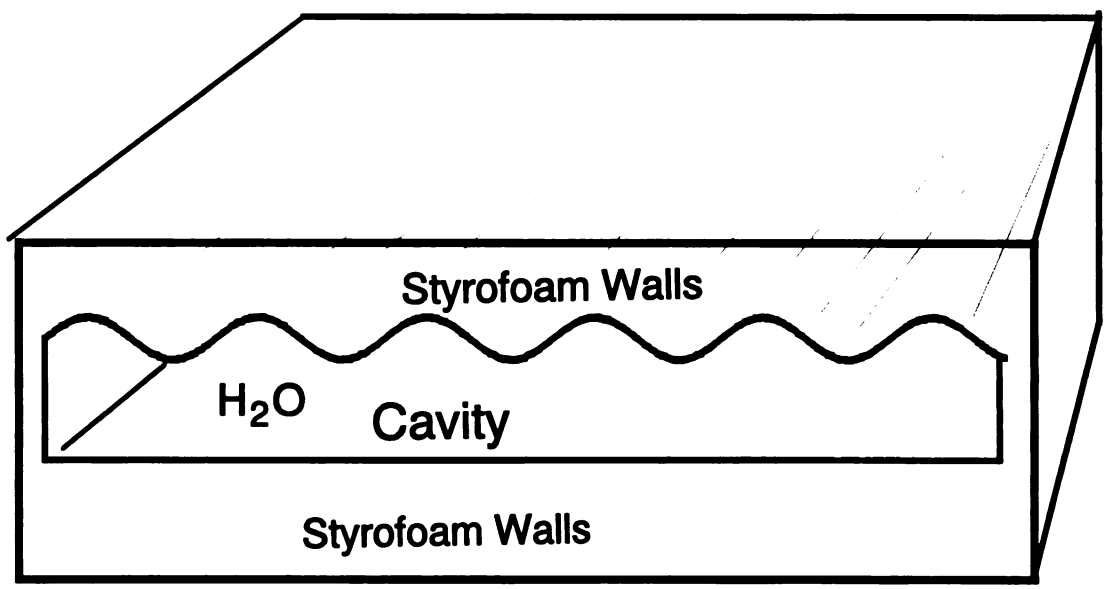

Figure 4.24 Configuration of sea-water sinusoid for experimental measurements.

The styrofoam cavity is placed vertically (cavity opening facing up) and filled with sea-water. The measurements are then performed in the arch range, which can produce backscatter and forward scatter responses.

There are a number of problems associated with the sea-water structure and the arch-range system. The styrofoam cavity leaked and therefore required a thin plastic lining. The thin lining had a negligible effect on the scattered fields. The finite depth of the sea-water holding structure could also be disregarded due to the decay of the transmitted fields inside the sea-water. There was an additional problem concerning the antenna patterns of the arch-range system. The antennas (and lenses) create a TEM plane wave, but it has a rather small footprint. The footprint is gaussian in nature and is physically smaller than the sea-water sinusoid. The effects of the antenna pattern is noticeable in the results.

The arch-range system operates in the same fashion as the anechoic chamber system that was used in the chapter 3 measurements of the PEC model. The frequency-domain synthesis technique is employed and calibration is performed with a sphere. The details of this method can be found in chapter 2.

The first set of measurements consisted of backscattered field responses from the sea-water model and also the PEC for comparison purposes. The wave models were interrogated with both TE and TM incident waves at roughly 60°.

The theoretical backscattered fields from both a PEC and a sea-water sinusoid are shown in Figure 4.25 for the TM polarization. In this figure an incidence angle of 60° was assumed and the surface parameters match the experimental model parameters. The results indicate that some of the energy is being transmitted into the sea-water. The spectral content however is nearly identical (other than magnitude). The synthesized transient response is shown in Figure 4.29 and will be discussed later.

The TE case is shown in Figure 4.26. The parameters and geometry are the same as the TM case. These results also reveal that the effects of the sea-water seem to only reduce the magnitude of the backscattered field. The synthesized transient response is shown in Figure 4.31.

When the incidence angle is increased (near grazing) it is expected that the TM case will exhibit some sort of Brewster's angle phenomenon. In Figure 4.27 the incidence angle is increased to 85° there is a noticeable change between the PEC and the sea-water models as compared to Figure 4.25 (60°). This is due to the Brewster's angle minimum. As a confirmation of this the TE case is also considered. In Figure 4.28 the theoretical backscattered responses for a PEC and sea-water surfaces are compared for TE incidence at 85°. The results in this figure when compared with the 60° (Figure 4.26) returns confirms the above assertion.

The measured synthesized transient responses of the PEC and sea-water surfaces are shown in Figure 4.30 for TM excitation at 60°. The effects of the edges (finite models) are seen and the limited footprint (gaussian beam) antenna pattern are also obvious. These results are compared with the theoretical synthesized transient results in Figure 4.29. Note that the theoretical results assume an infinite surface and an ideal plane wave. The results match quite well. This agreement solidifies many of the gray areas. Those gray areas include the effects of the lining, the effect of the finite surface (also discussed in chapter 3) and the gaussian beam illumination. It should be noted that a 1/8 cosine taper was utilized for all (TM and TE) the synthesized transient results.

The TE case was also measured with a similar degree of success. The synthesized transient responses for the PEC and sea-water sinusoids are compared in Figure 4.32 (measured) and Figure 4.31 (theoretical). There are increased difficulties with TE interrogation. The TE incident wave polarization is such that the edges and any wrinkles in the lining are excited. This injects unwanted pulses and noise, which can be seen in the returns.

The spectral responses, which are what is actually measured, are also compared. In Figure 4.33 and Figure 4.34 the theoretical and measured frequency-domain responses are shown. In Figure 4.33 the theoretical results for both the PEC and sea-water wave are shown for 60° incidence. The spectra were obtained by time gating the synthesized

transient responses and then transforming to the frequency domain. The portion of the transient response that was time gated is shown in Figure 4.29 and corresponds to an 11 crest wave. The actual measured backscatter response for the PEC and sea-water sinusoids is shown in Figure 4.34. The agreements between the measured and theoretical responses is excellent. The measured response does, however, contain the effects of the gaussian beam illumination. A direct comparison between the measured and theoretical backscatter response from a sea-water sinusoid is shown in Figure 4.37. The strong agreement between the measured and theoretical responses for both PEC and sea-water sinusoids is an excellent indicator of the correctness of both the theory and the measurement techniques.

The spectra for the TE case are shown in Figure 4.35 (theoretical) and Figure 4.36 (measured). As expected from the transient results there is good agreement between measured and theoretical results. The theoretical results have once again been time gated before transforming back to the frequency domain. The measured results exhibit a slight inconsistency in the lower frequencies. This is probably due to the problems associated with TE excitation explained above.

The arch-range system does allow for forward scatter measurements. The methods for properly calibrating these measurements has not been conceived. Therefore a rough method, which does not use a calibration will be implemented here.

The TM spectral and synthesized transient forward-scattered responses for the sea-water sinusoid (L=0.1016m and h/L=.125) are shown in Figure 4.38. In the upper plot the spectral returns between 4.8 and 6.2 GHz are shown for near-grazing angles. There is a wide minimum located between 75° and 80°. The minimum is migrating towards 82° as the frequency is increased. This minimum agrees with the theoretical prediction for h/L=.125 as shown in Figure 4.11. The bottom plot is the magnitude of the synthesized transient forward scatter for the same case as the top plot. This plot also shows the

Brewster's angle effect in the 75° to 82° area. These plots and the methods of the forward scattered measurement were quite rough and there is a need for further investigation.

4.7 Conclusions

In this chapter the sea model was improved to include the effects of an imperfectly conducting sea-surface. The results presented in this chapter, therefore, focused on the differences or likenesses of the transient scattering from PEC and lossy sinusoidal surfaces. One of the major findings was that there are very few differences in the scattering phenomenology between the PEC and lossy surfaces. The transient and spectral responses were nearly identical except for a scale factor. The scale factor was due to the portion of the incident wave that was transmitted by the lossy surface thereby reducing the scattered energy. This was shown both theoretically and experimentally.

The Brewster's-angle phenomenon, however, is a physical effect that was not predicted with the PEC case. The theoretical and experimental search for a possible Brewster's angle for the TM polarization was another main concern of this chapter. The results were fairly positive. It was shown rather conclusively with the theoretical results that indeed a Brewster's-type angle did exist for a lossy sinusoidal surface. The conclusion was that the angle is reduced (from 83.6° to 78°) when the surface is changed from flat to sinusoidal (h/L=.125). The forward scatter at the Brewster's angle is no longer zero, as in the flat lossless case, but a sharp minimum occurs for the sinusoidal (and/or lossy) case. The theoretical findings were substantiated with experimental measurements. The measurements were performed in the frequency domain using the arch-range system and provided a rough glimpse at the Brewster's angle phenomena.

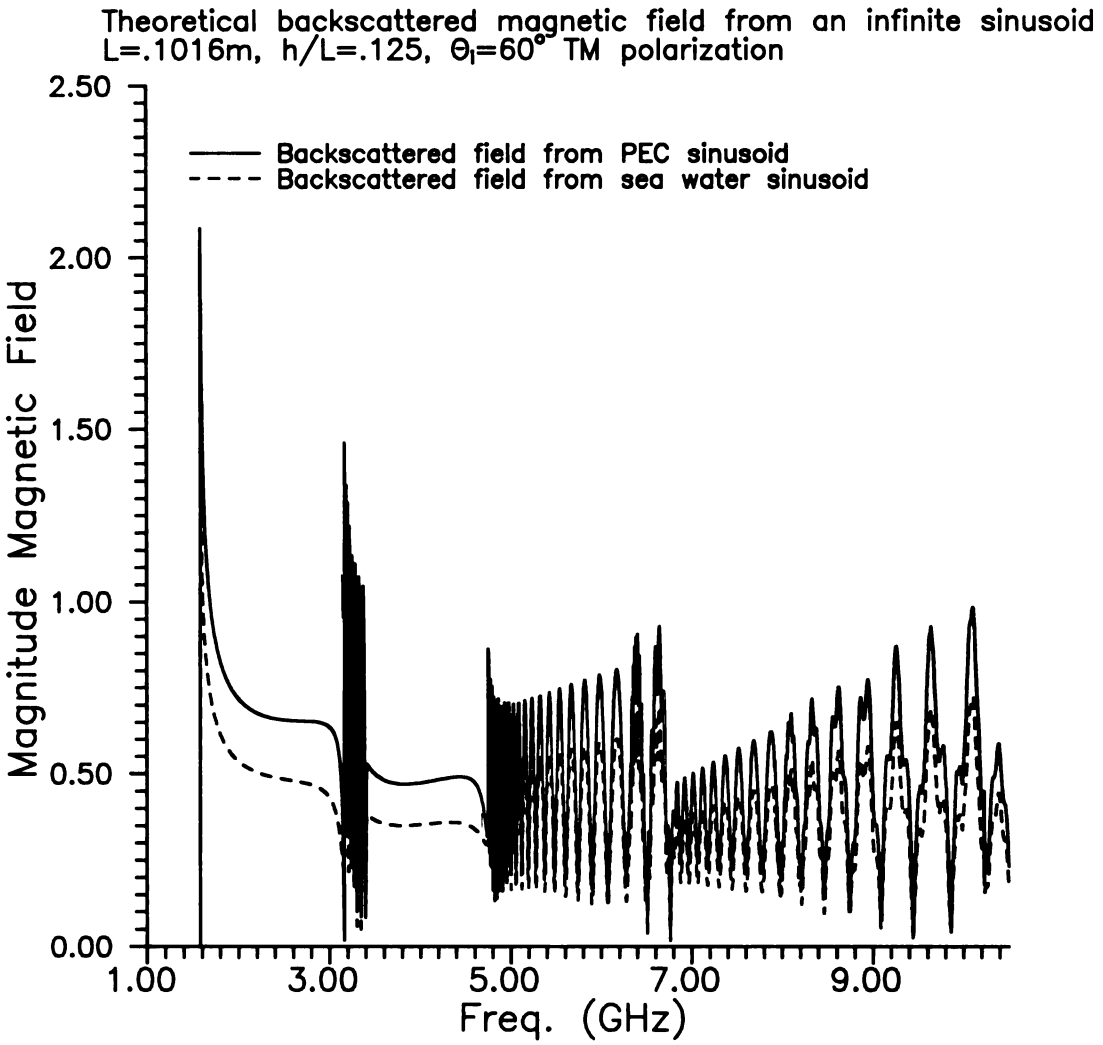

Figure 4.25 Theoretical backscattered H-field from an infinite sinusoid. Comparison of PEC and sea-water models for TM excitation at 60°.

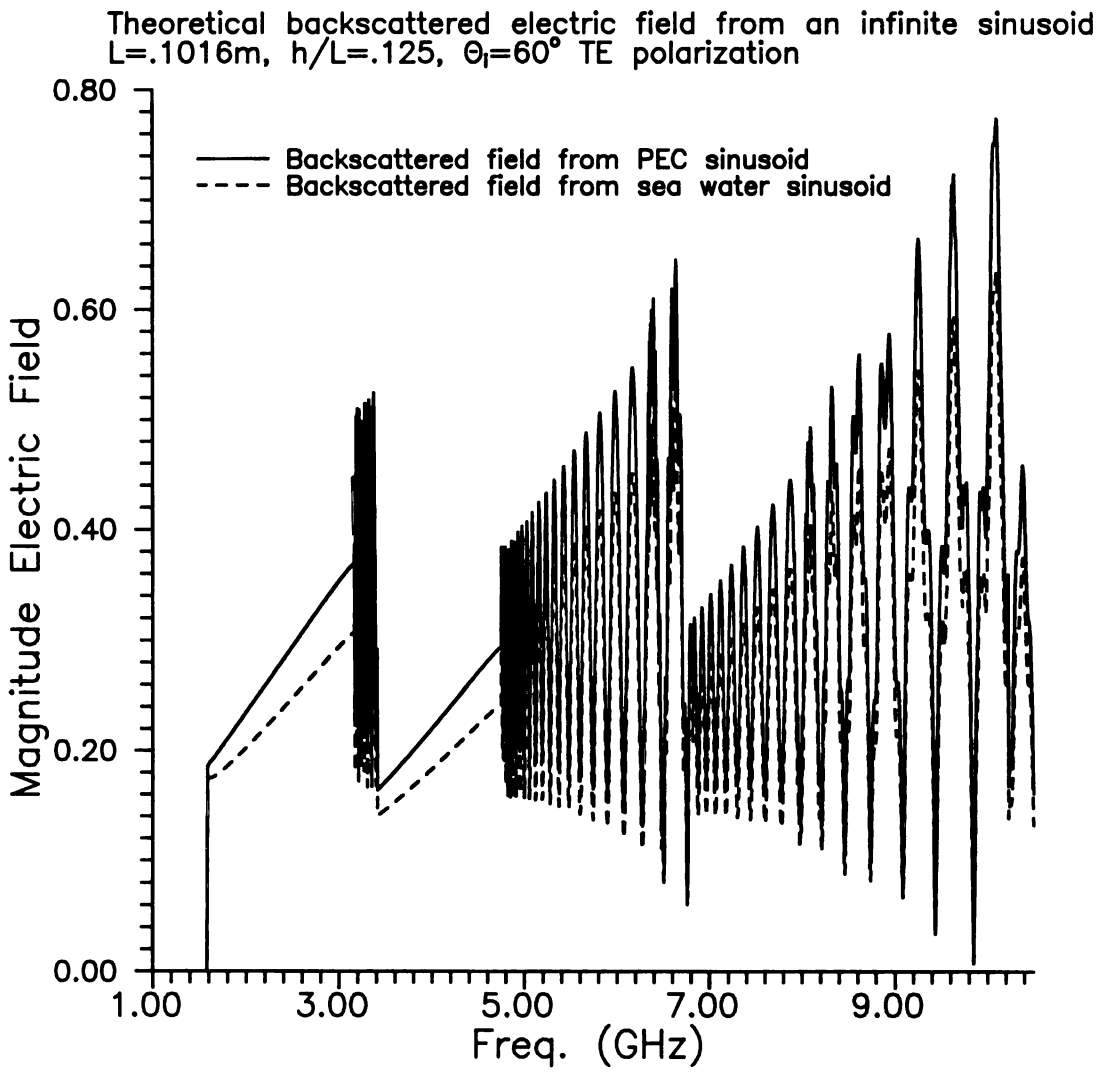

Figure 4.26 Theoretical backscattered E-field from an infinite sinusoid. Comparison of PEC and sea-water models for TE excitation at 60°.

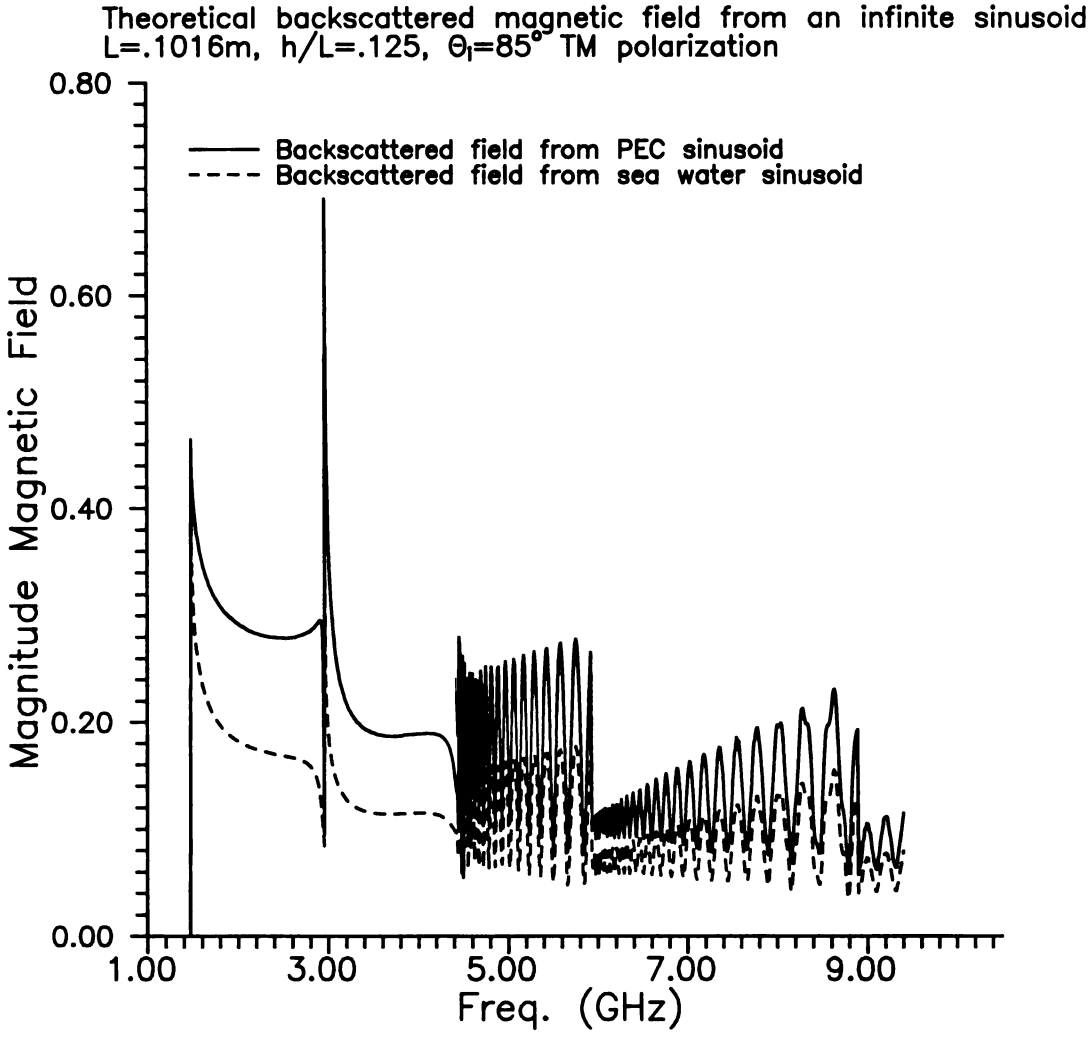

Figure 4.27 Theoretical backscattered H-field from an infinite sinusoid. Comparison of PEC and sea-water models for TM excitation at 85°.

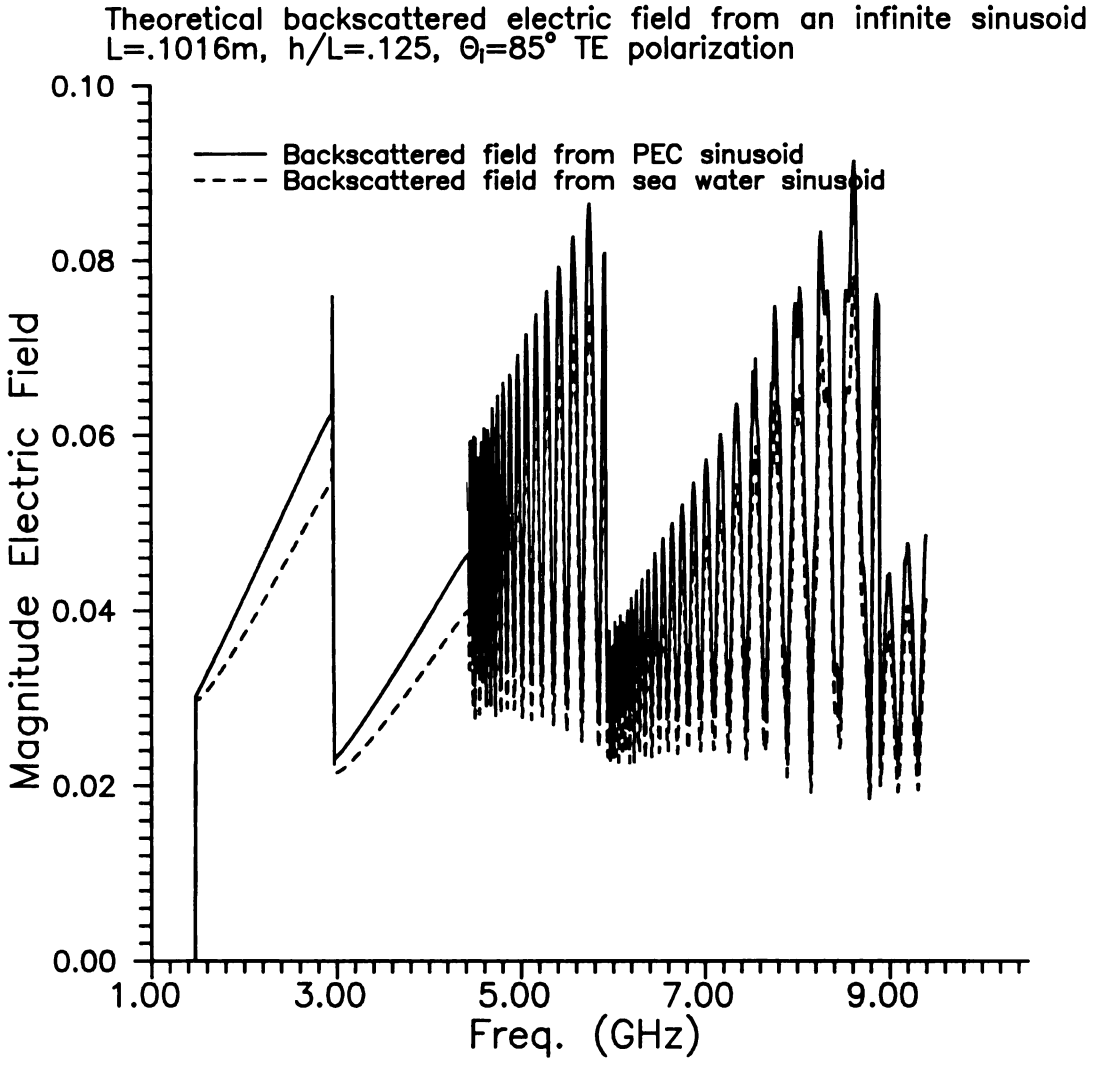

Figure 4.28 Theoretical backscattered E-field from an infinite sinusoid. Comparison of PEC and sea-water models for TE excitation at 85°.

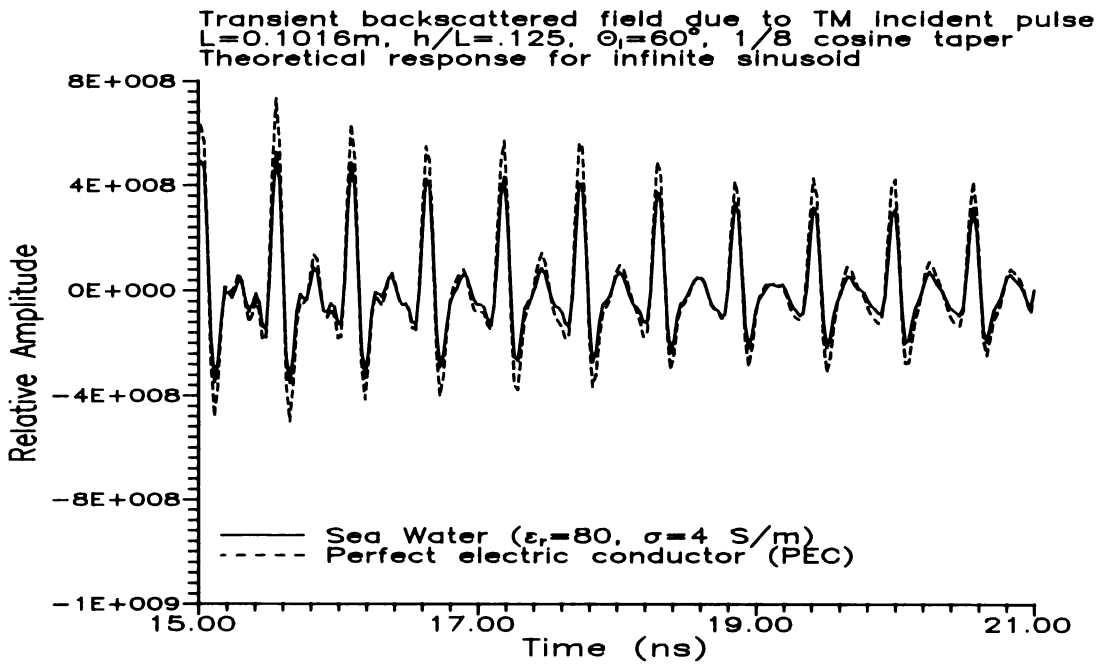

Figure 4.29 Theoretical transient backscatter for TM excitation.

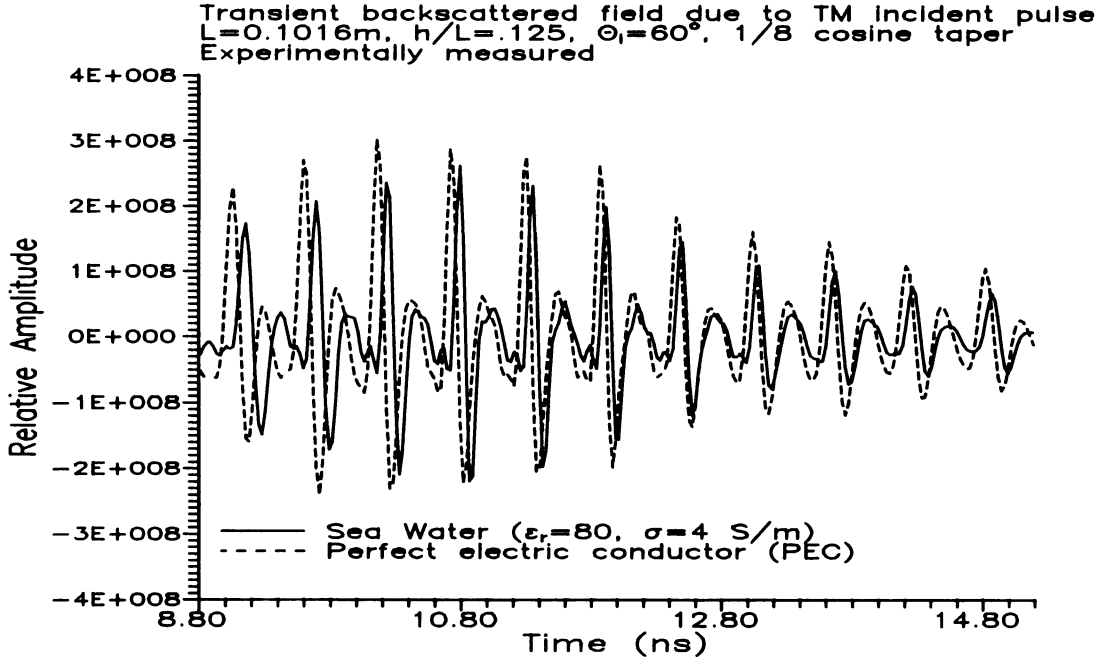

Figure 4.30 Experimentally measured transient backscatter for TM excitation.

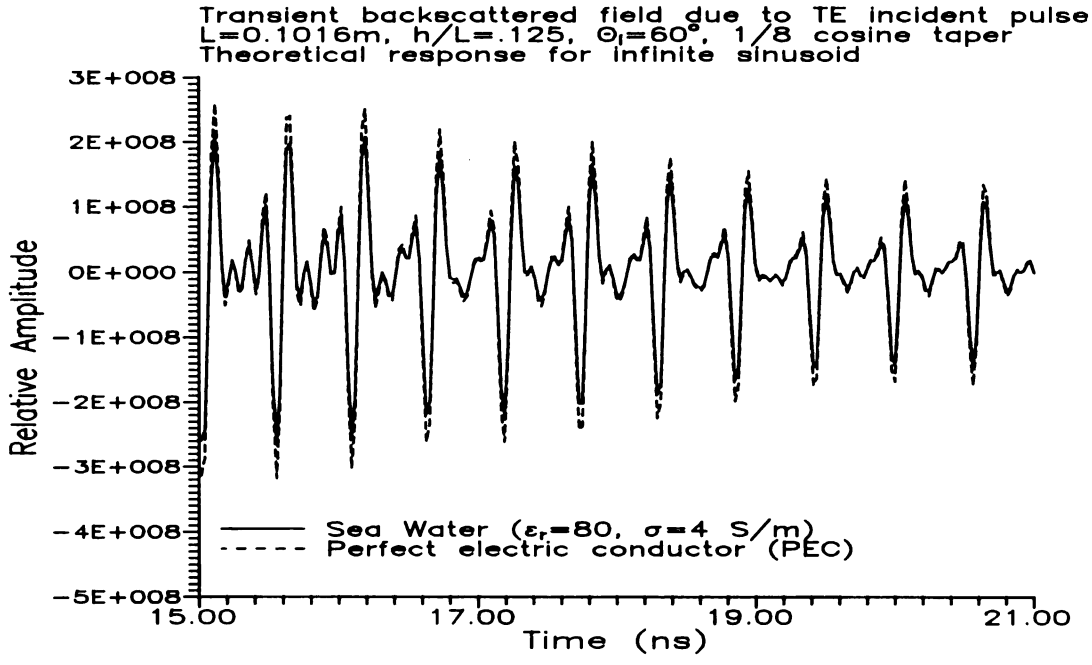

Figure 4.31 Theoretical transient backscatter for TE excitation.

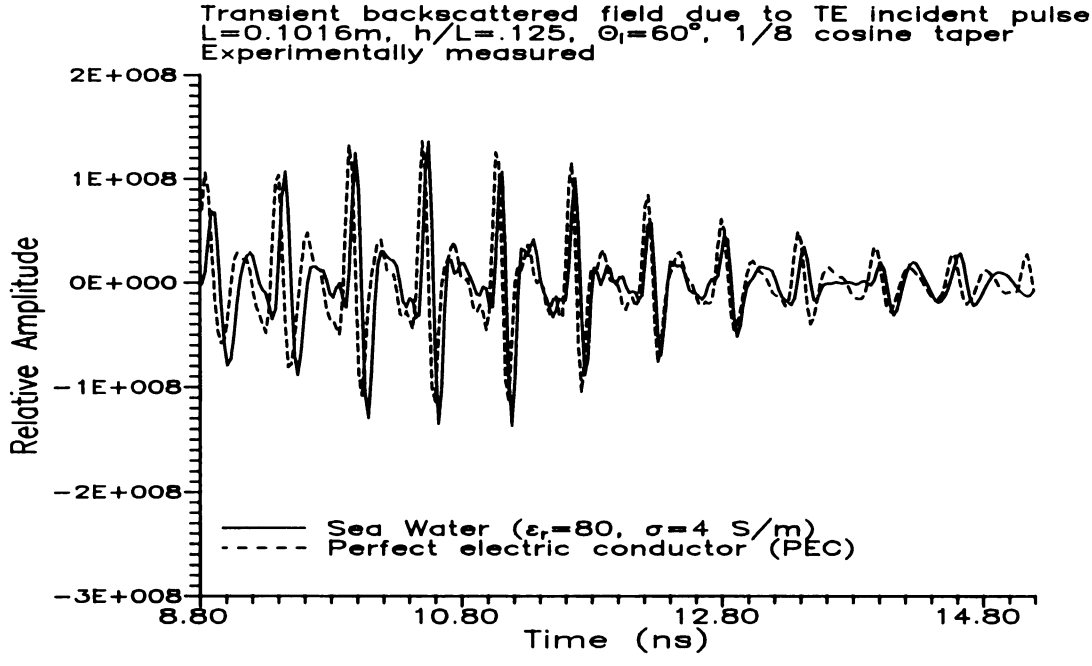

Figure 4.32 Experimentally measured transient backscatter for TE excitation.

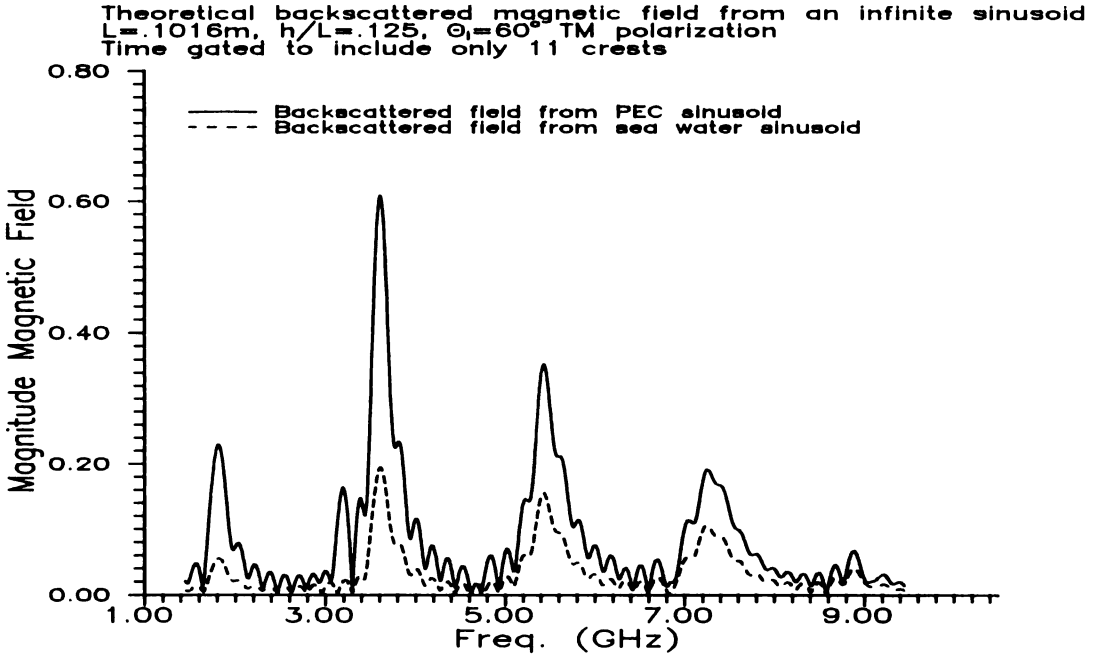

Figure 4.33 Theoretical time-gated backscatter for TM excitation.

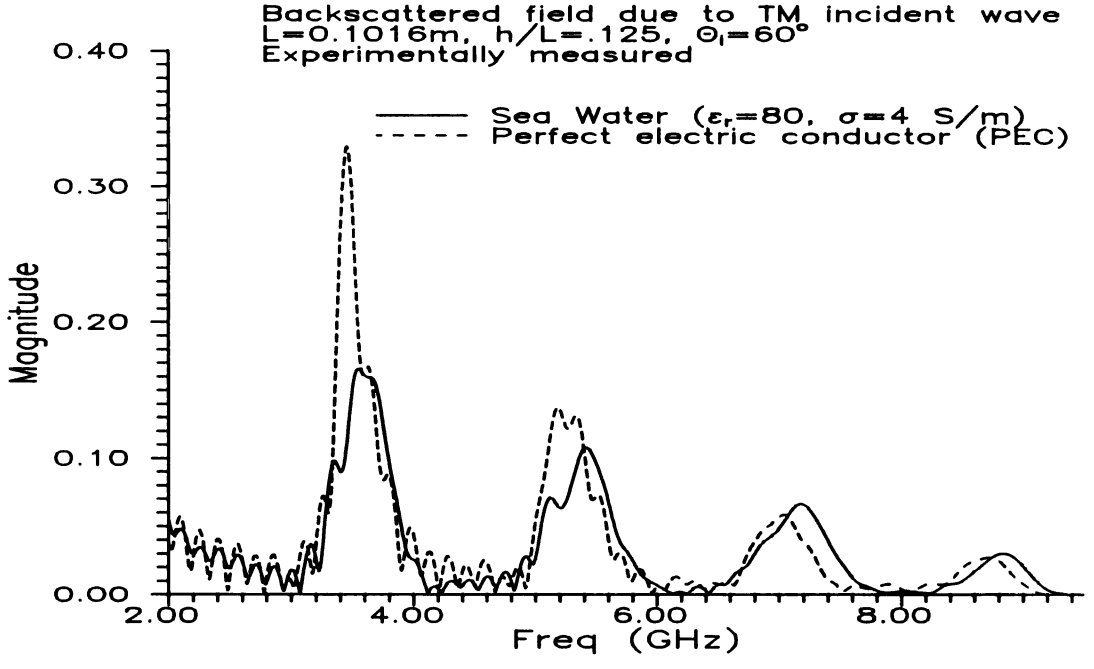

Figure 4.34 Experimentally measured backscatter for TM excitation.

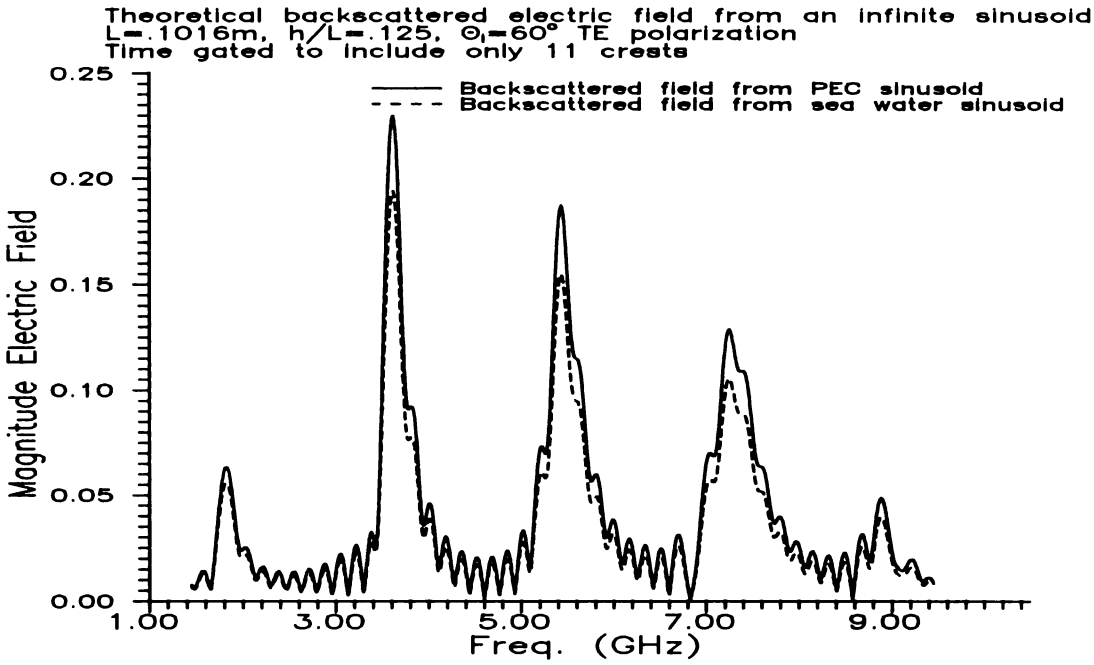

Figure 4.35 Theoretical time-gated backscatter for TE excitation.

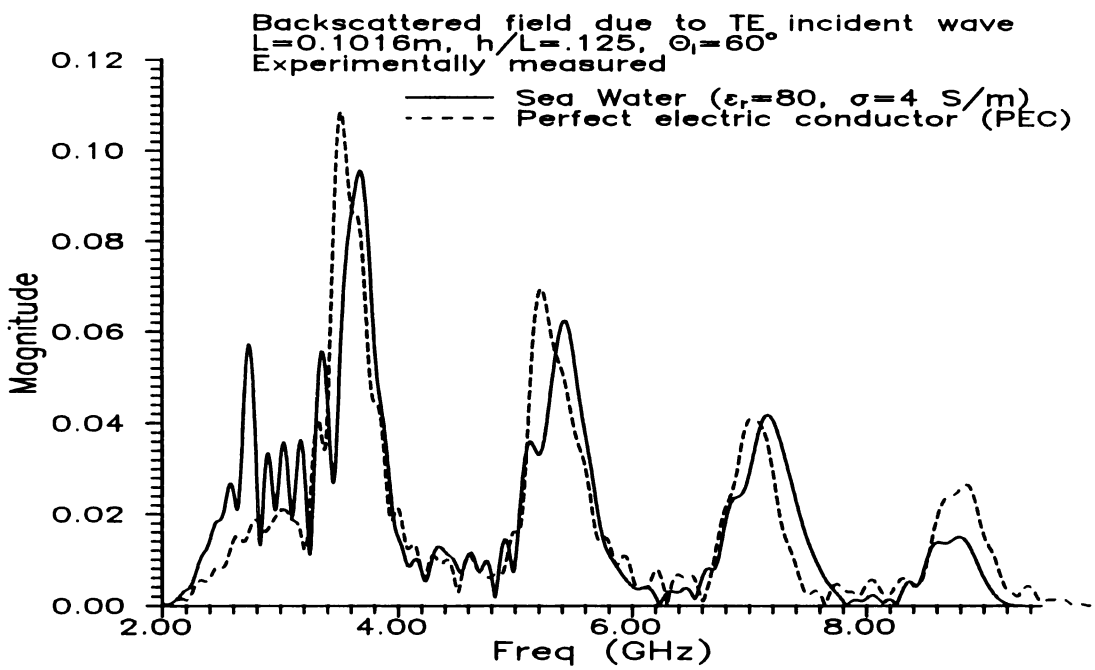

Figure 4.36 Experimentally measured backscatter for TE excitation.

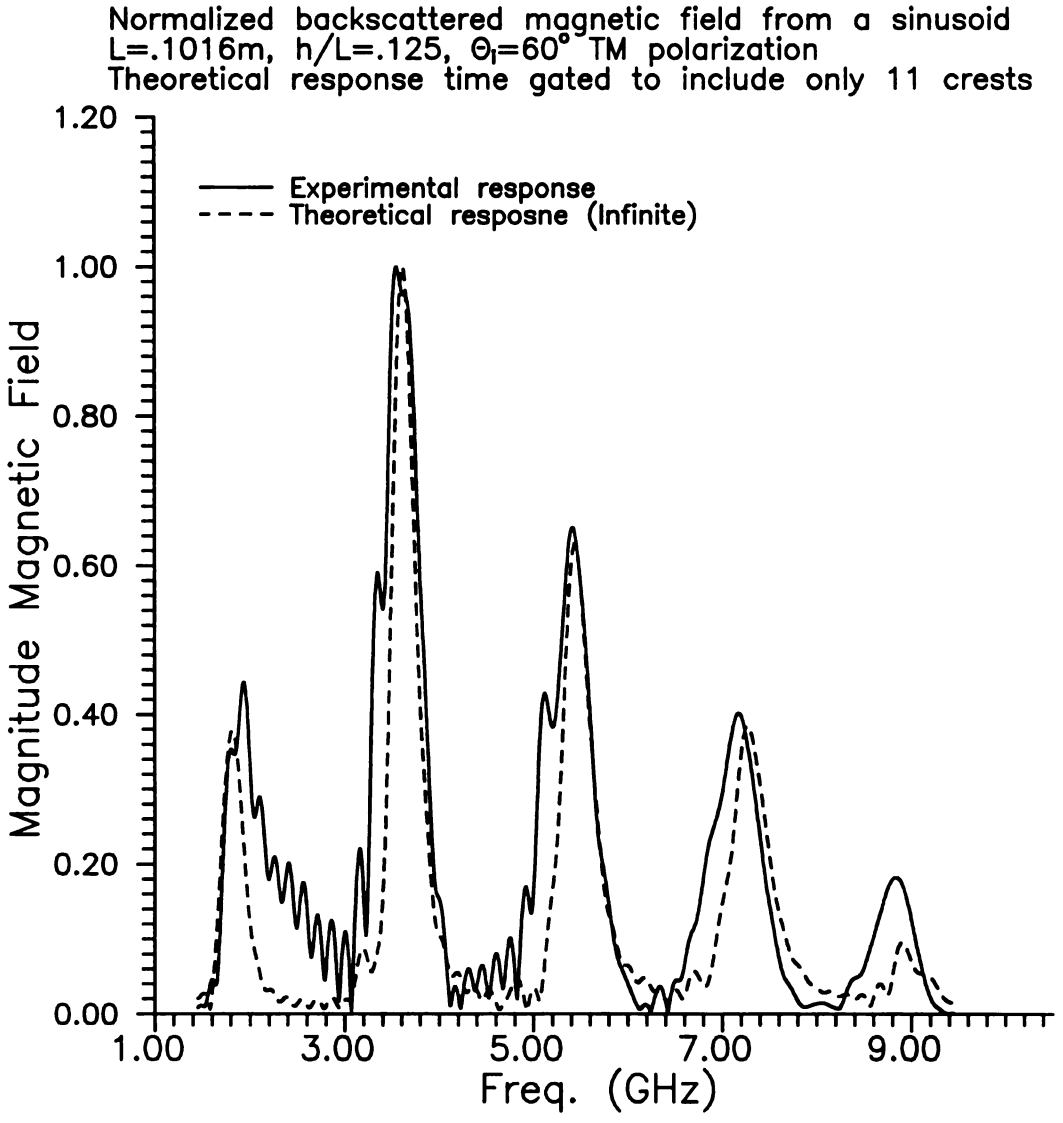

Figure 4.37 Comparison of theoretical and measured TM backscatter from a sea-water sinusoid.

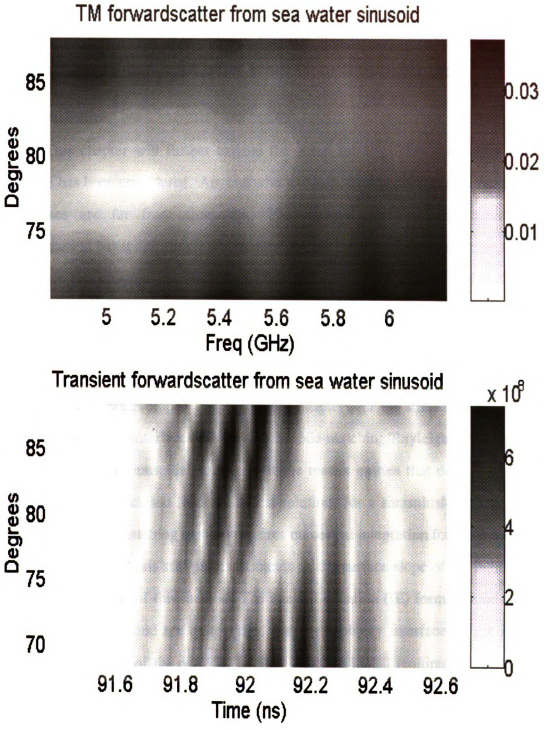

Figure 4.38 Experimentally measured forward scatter from a finite sea-water sinusoid. Both transient and spectral results are shown of a number of incidence angles.

Chapter 5
Transient Scattering from Non-Sinusoidal Surfaces

5.1 Introduction

This chapter will further expand the ocean models. Thus far only a sinusoidal interface has been considered. Anyone who has seen an ocean (or lake) would agree that the waves are far from sinusoidal. The sinusoidal surface was merely a first approximation but it did impart a considerable amount of useful information, which will be used in this chapter. The surface models that will be considered in this chapter will make an important step towards a realistic sea-surface. The clutter (or backscatter) from these non-sinusoidal surfaces greatly varies from the sinusoidal surface. It will provide an excellent showcase for the attributes of a UWB/SP radar system.

The theory developed in the previous chapters for the sinusoidal interface is not limited to sinusoidal interfaces. The Floquet-mode-matching/Rayleigh-hypothesis method is not limited to a sinusoidal surface, but the matrix entries that determine the modal amplitudes do have closed form analytical solutions for a sinusoidal surface. To extend the Floquet-mode-matching method requires numerical integration for the matrix entries. The Rayleigh hypothesis still places demands on the surface slope of the interface which limits the usefulness of this method. The integral-equation (IE) formulations are already numerical in nature and are quite suited for any arbitrary interface. If the interface is infinite then the use of the periodic Green's function is still required and constrains the non-sinusoidal surfaces to be periodic. The IE method does, however, suffer numerically when the sea-surfaces are highly oscillatory (rough). There are a number of techniques that have been developed to overcome the numeric difficulties of these rougher sea-surface realizations [50,51].

The knowledge gained in chapters 3 and 4 will be put to use in this chapter. This would include experimental methods that can now be applied to the non-sinusoidal surfaces, phenemonology associated with the short pulse scattering from periodic surfaces, and the effects of sea-water surface as compared to conducting surface. It was found in chapter 4 that the differences between PEC and imperfectly conducting surfaces was minimal (only the Brewster's angle phenomenon). Therefore, the results and experiments in this chapter will focus on PEC non-sinusoidal surfaces.

5.2 Extensions to theory to accommodate non-sinusoidal surface.

As alluded to in the introduction it was necessary to make a number of numerical adjustments to theory developed in chapters 3 and 4. These adjustments were needed to accommodate the non-sinusoidal interface.

5.2.1 Floquet mode-matching/Rayleigh Hypothesis

In the FMM/RH method the coefficients for the modal amplitudes are integrals arising from the application of Galerkin's method. As an example the TE case for the PEC interface has (3.17) as the coefficients for the scattered modal amplitudes. Note that the other integrals for the TM case and the two-media case are quite similar. That integral is rewritten here

$$\bar{K}_{mn} = \int_0^L e^{-jq_n\rho} e^{j2\pi(m-n)\frac{x}{L}} dx \tag{5.1}$$

where $\rho(x)$ is the functional description of the interface.

For the sinusoidal case this integral had a closed form solution consisting of a Bessel function. The specialization of $\rho(x)$ to be non-sinusoidal requires a numerical integration. This integration can be performed by standard numerical integration routines (Romberg, trapezoidal rule, etc..) or by treating the interface as piecewise linear. If the interface is partitioned to be piecewise linear that does introduce discontinuities in the

first derivative of the surface. The Rayleigh hypothesis is therefore violated, but the error can be minimized to an allowable tolerance by reducing partition lengths.

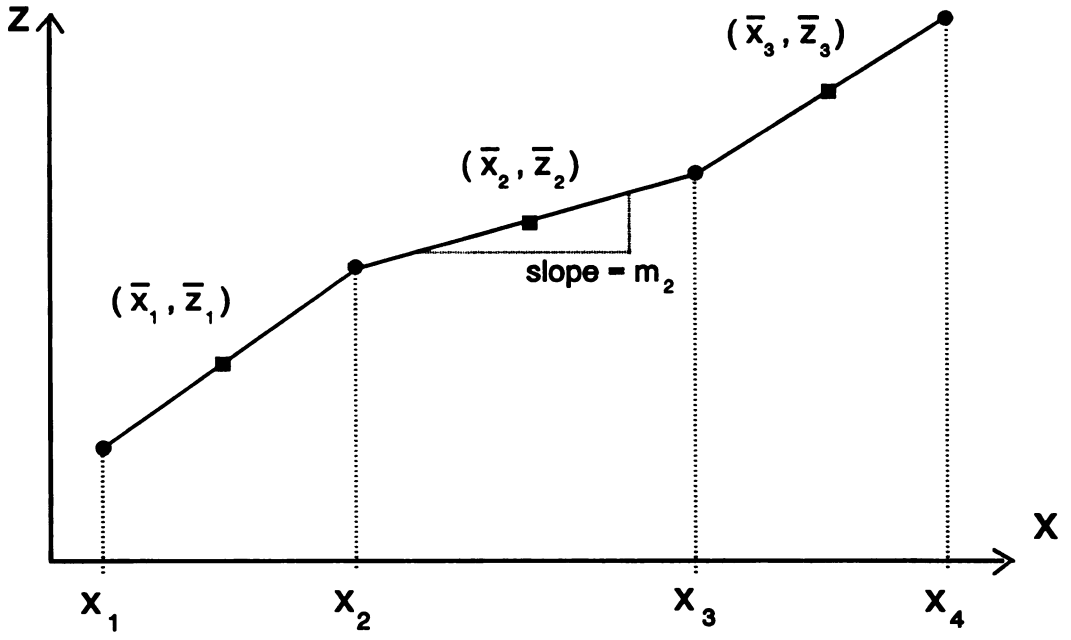

Figure 5.1 Partition scheme for sea-surface interface.

The partition scheme is identical to that used for the MoM solutions of the integral equations of chapters 3 and 4, and is shown in Figure 5.1. The interface is partitioned into N segments where the slope on the $q'th$ segment is m_q. With the piecewise linear interface shape the integral (5.1) can be rewritten as

$$\bar{K}_{mn} = \sum_{q=0}^{N-1} \int_{x_q}^{x_{q+1}} e^{-jq_n(z_q + m_q(x - x_q))} e^{j2\pi(m-n)\frac{x}{L}} dx \tag{5.2}$$

The integral over the $q'th$ partition can be evaluated to yield

$$\bar{K}_{mn} = \sum_{q=0}^{N-1} e^{-jq_n z_q} \left[e^{j\left(\frac{2\pi(m-n)}{L} x_{q+1} - q_n m_q \Delta x\right)} - e^{j\frac{2\pi(m-n)}{L} x_q} \right] \tag{5.3}$$

where $\Delta x = x_{q+1} - x_q$.

The matrix element integrals and the forcing vector integrals are the only changes that are needed for the non-sinusoidal surface. The scattered fields are found subsequent to determination of the modal amplitudes (matrix inversion).

5.2.2 Integral Equation Formulation

The integral equation methods are rigorous for non-sinusoidal surfaces and need no adjustments for any such surfaces. The numerical implementation of the MoM solution for the infinite (periodic) case is affected by non-sinusoidal surfaces. The rough surfaces create a problem with the convergence of the periodic Green's function.

In chapters 3 and 4 the MoM matrix entries were calculated by exchanging the implied summation of the PGF with the integration over a partition. The integral in this case can be computed in closed form. The resultant summation was then performed until a convergence criterion was met. If the surface becomes rough this summation is very slowly convergent for certain testing points. The convergence, however, can be accelerated.

The method of acceleration used in this thesis can be found in [44]. In this method the summation of the Green's function is performed first and then the integration over the partition is performed numerically. The alternate version of the PGF used in this acceleration method [44] is

$$G(x,z\,|\,x',z') = G_+ + G_- - \frac{j}{4}H_o^{(2)}\left(k\sqrt{(x-x')^2+(z-z')^2}\right) \tag{5.4}$$

where

$$G_\pm(x,z\,|\,x',z') = \frac{e^{-j(b_\pm s - t_\pm)}}{\pi}\int_0^\infty \frac{e^{-s(b_\pm+1)u^2}\cos\left(au\sqrt{u^2+2j}\right)}{(1-e^{-su^2}e^{jt_\pm})\sqrt{u^2+2j}}du \tag{5.5}$$

where

$$a = k(z-z')$$

$$b_+ = -b_- = -(x - x')/L$$

$$s = kL$$

$$t_+ = -L(k + \beta)$$

$$t_- = -L(k - \beta)$$

$$k = \omega\sqrt{\mu_o \epsilon_o}$$

The integrals in (5.5) can be evaluated numerically and converge rapidly for most cases. For the TE PEC case the MoM matrix entries are found by integrating G over a partition (see Figure 5.1). The integral (3.34) that utilizes G is of the form

$$A_{pq} = \int_{x_q}^{x_q+\Delta x} G(\bar{x}_p, \bar{z}_p \,|\, x', z')\, dx' \tag{5.6}$$

The MoM matrix entries (5.6) are numerically integrated. The numerical integration over the *q'th* partition requires the successive evaluation of G (see eq. (5.4)). This may seem to be a less effective method of determining the MoM matrix entries, but for the non-sinusoidal surfaces this method is vastly superior to the original method in chapter 3.

The TM case and the two-media problem require the normal derivative of the PGF ($\partial G/\partial n'$). If the interface is modelled as piecewise linear (as is the case) the normal derivative can be performed analytically under the integrals (5.5). This eliminates the need for numerical differentiation, which can be very noisy. The normal derivative of the PGF over the *q'th* partition (See Figure 5.1) is given by

$$\frac{\partial G}{\partial n'} = \hat{n}' \cdot \nabla' G = \frac{\hat{z} - \hat{x} m_q}{\sqrt{1 + m_q^2}} \cdot \nabla' G \tag{5.7}$$

Performing the dot product yields

$$\frac{\partial G}{\partial n'} = \frac{1}{\sqrt{1+m_q^2}}\left[\frac{\partial G}{\partial z'} - m_q \frac{\partial G}{\partial x'}\right] \tag{5.8}$$

The partial derivatives are taken inside the implied integration of G. The derivative on the argument of a Hankel function of order zero results in a first order Hankel function. The partial differentiations of G_+ and G_- are

$$\frac{\partial G_\pm}{\partial z'} = \frac{e^{j(b_\pm s - t_\pm)}}{\pi}\int_o^\infty \frac{e^{-s(b_\pm+1)u^2}\sin\left(au\sqrt{u^2+2j}\right)}{(1-e^{-su^2}e^{jt_\pm})} k_i u\, du \tag{5.9}$$

$$\frac{\partial G_\pm}{\partial x'} = \mp\frac{e^{-j(b_\pm s - t_\pm)}}{\pi}\int_o^\infty \frac{e^{-s(b_\pm+1)u^2}\cos\left(au\sqrt{u^2+2j}\right)}{(1-e^{-su^2}e^{jt_\pm})\sqrt{u^2+2j}} k_i (j+u^2)\, du \tag{5.10}$$

The integrals for the partial derivatives of $G_\pm$ are computed numerically. The MoM matrix entries, given by (3.61) for the TM PEC case, are of the form

$$A_{pq} = \int_{x_q}^{x_q+\Delta x} \frac{\partial G(\bar{x}_p,\bar{z}_p|x',z')}{\partial n'} dx' \tag{5.11}$$

still must be numerically integrated. Once again the numerical integration over the partition length requires successive evaluations of $\partial G / \partial n'$. It has also been found that this method is superior to the chapter 3 method for some troublesome cases.

The additional computational efficiency gained with the convergence accelerators, which were discussed above, allow for the rigorous IE formulation of non-sinusoidal rough (periodic) surfaces. The results for a number of non-sinusoidal surfaces will be shown in the following sections. These results will be accompanied by experimental findings that further confirm the theory developed.

5.3 Non-sinusoidal sea-surface models

The wave models have been chosen to test a number of scattering mechanisms. There is a Stokes-type wave [52], that has a very large slope (at the crest), and double sinusoid wave that simulates two-scale roughness, and a realistic aperiodic Donelan-

Pierson [53-56] wave. The Donelan-Pierson wave is constructed from actual ocean statistics and is a function of wind-speed, a periodic swell is superimposed upon the wind roughened waves. A comparison of the three wave models that will be used extensively in this chapter is shown in Figure 5.2. In Appendix B is further discussion regarding the development of these sea-surface models.

5.4 Preliminary numerical results

The effects of the change in surface shape will be considered with the examination of the induced surface currents. This was the starting point for the chapter 3 and 4 numerical results for the sinusoidal surfaces. The results for these more complex surfaces can be compared and contrasted with those of the sinusoidal surface. The IE method was used for the analytic results, due to the nature of sea-surface models.

In Figure 5.3 the induced surface currents on a sinusoid are compared to the currents on double-sinusoid models. The double sinusoids that are compared have increasing ripple height. The noticeable feature is the shadowing that occurs for each individual crest. As the secondary ripple height is increased deep nulls appear in the troughs. It is important to note the excitation frequency to surface wavelength ratio. If the frequency had been lower the effects of the ripple would be reduced. This effect will further examined in the analysis of the scattered fields.

The induced surface current of TE excitation of the Stokes wave (L=0.1778m) is shown in Figure 5.4 for an incidence angle of 85°. This figure displays the effects of the large surface slope of the Stokes wave model. At 2 GHz the Stokes wave could be fairly accurately described by a line source located at the crest of the wave. When the frequency is increased there is a noticeable change in the current distribution. This change could be attributable to the onset of multiple scattering or possibly a secondary scattering center. In the following sections the transient backscattered field response will further illuminate the possible scattering mechanisms.

In Figure 5.5 the currents induced on the double sinusoid model (L=0.1778) are displayed. The multiple shadow regions are obvious once again for the secondary ripples. A comparison of the currents induced on the double sinusoid model and the Stokes wave model is shown in Figure 5.6. The current is seen to be larger in magnitude for the Stokes wave model. The increased current is due to the surface slope of the stokes wave model. This effect will lead to enhanced backscattered fields for the larger-sloped waves.

The enhanced backscatter for both the Stokes and double sinusoid wave models can be observed in the frequency domain backscattered fields. In Figure 5.7 the theoretical backscattered fields from a sinusoidal and double sinusoidal wave are shown for an 85° TE incident wave. It is obvious that as the frequency is increased there is a stronger response from the double sinusoid model. This effect is due to a number of mechanisms. The surface slopes are greater for the double sinusoid model and also the secondary ripples are in resonance (Floquet mode). There is a similar enhancement for the Stokes wave model which is shown in Figure 5.8. For the Stokes wave the enhancement is due entirely to the increased surface slope. It is interesting to note that at the lower frequencies the sinusoid model is quite similar to the Stokes and double sinusoid models. This effect was briefly explained above, and is due to the frequency to surface wavelength ratio.

The synthesized transient field responses for the above spectral results are shown in Figure 5.9 and Figure 5.10. The results reflect the backscatter enhancement and also reveals the strength of the UWB/SP radar. The increased feature resolution can be seen with the double sinusoid response (Figure 5.9), where the secondary ripples are easily observable. The response from the Stokes wave model seems to indicate multiple scattering centers on the high peaked crest (Figure 5.10).

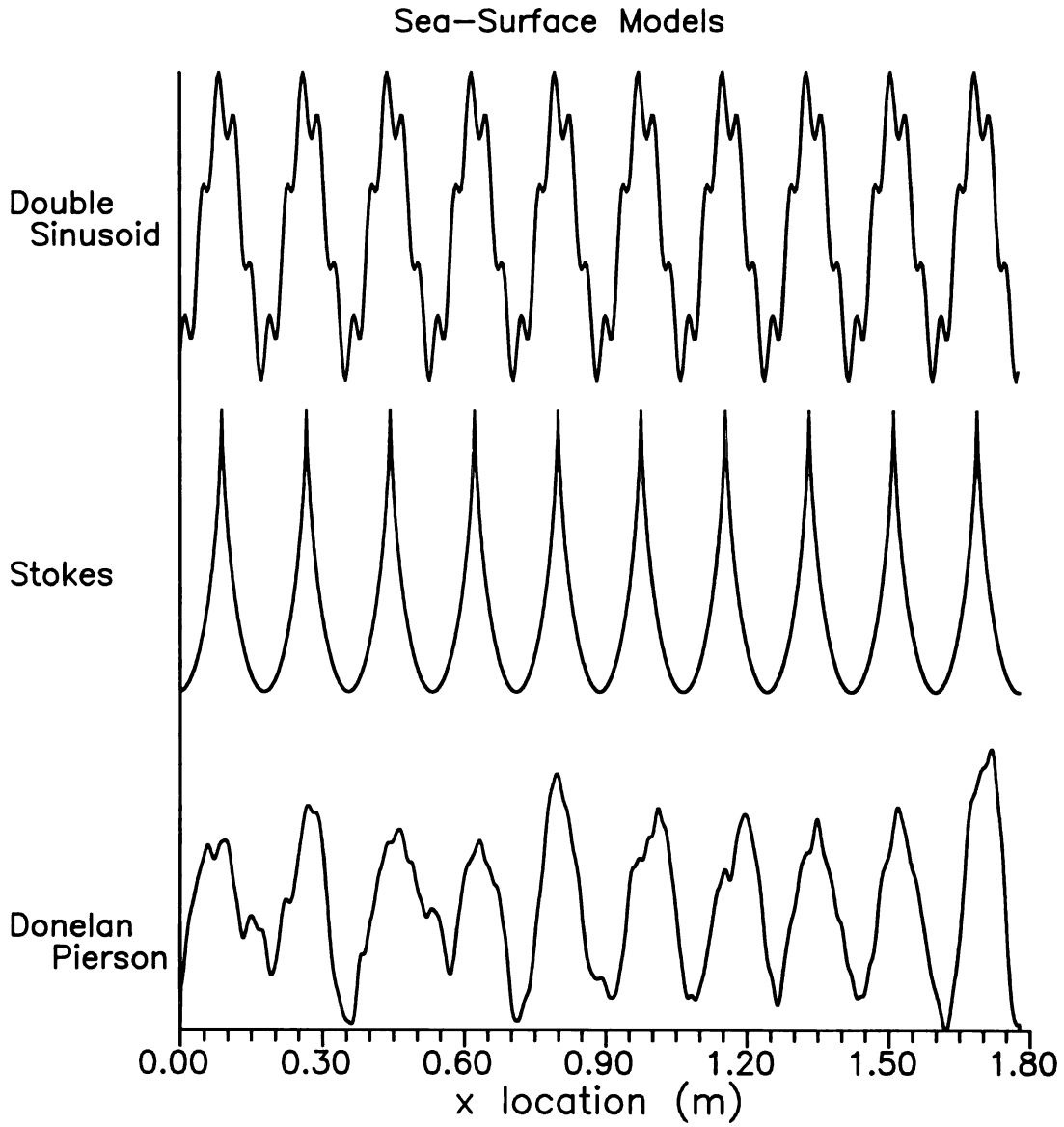

Figure 5.2 Comparison of sea-surface models.

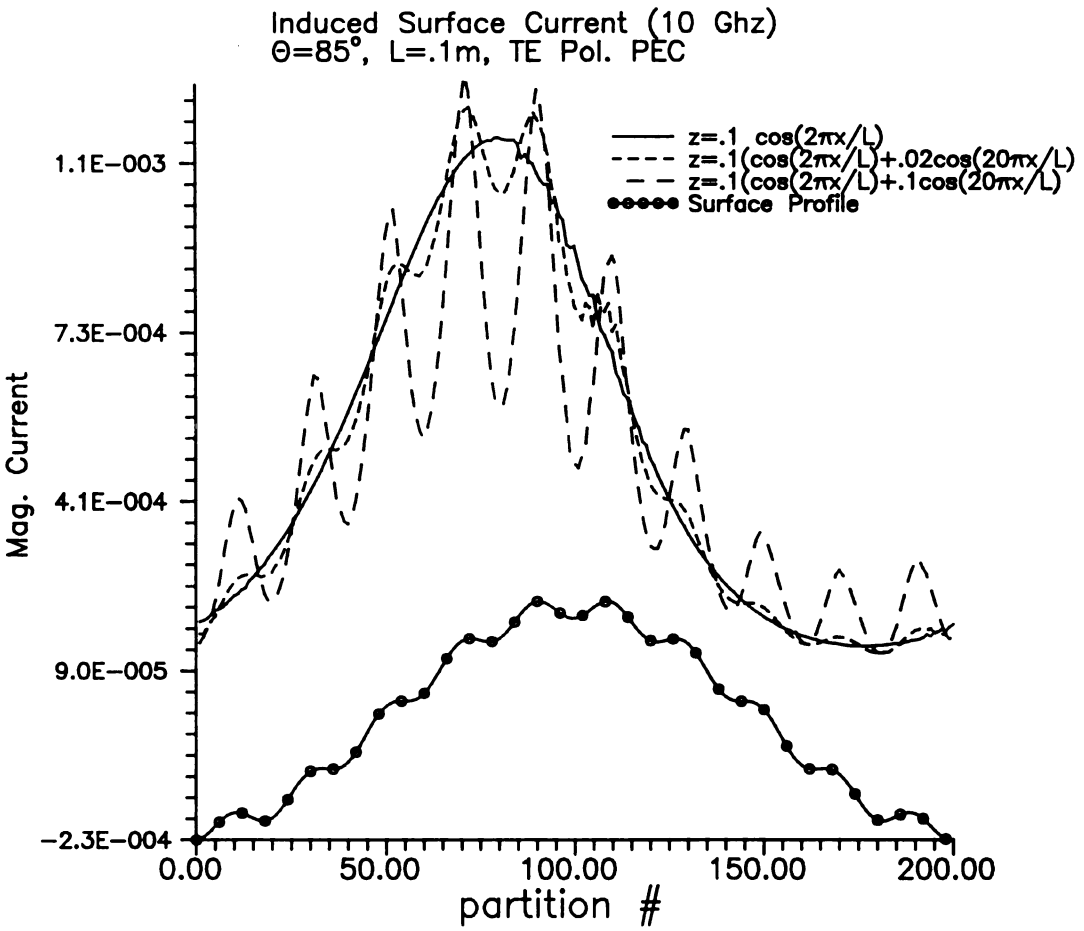

Figure 5.3 Surface current on PEC double sinusoid with increasing ripple height.

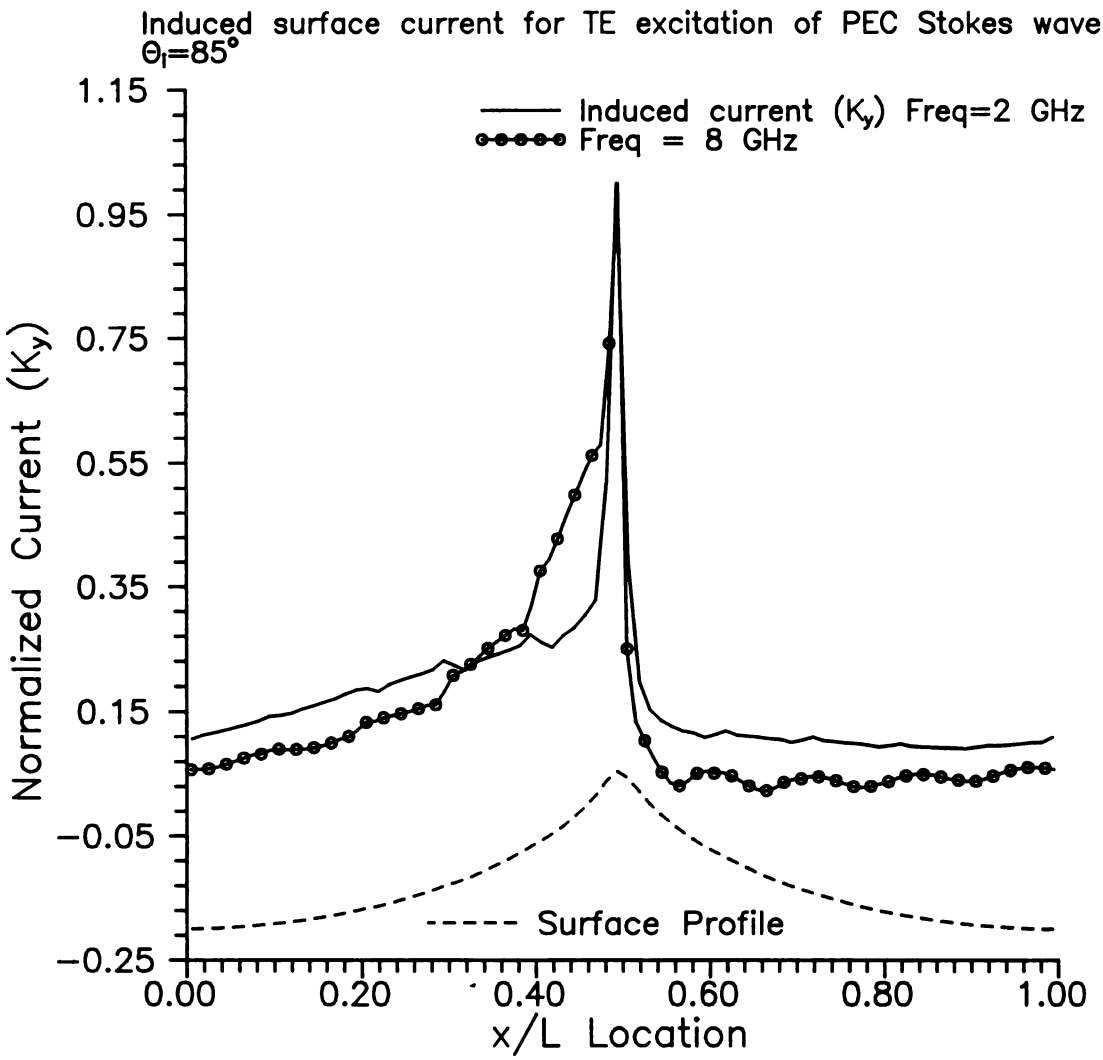

Figure 5.4 Surface current induced on the Stokes wave model for a TE incident plane wave at 85° with frequency of 2 GHz.

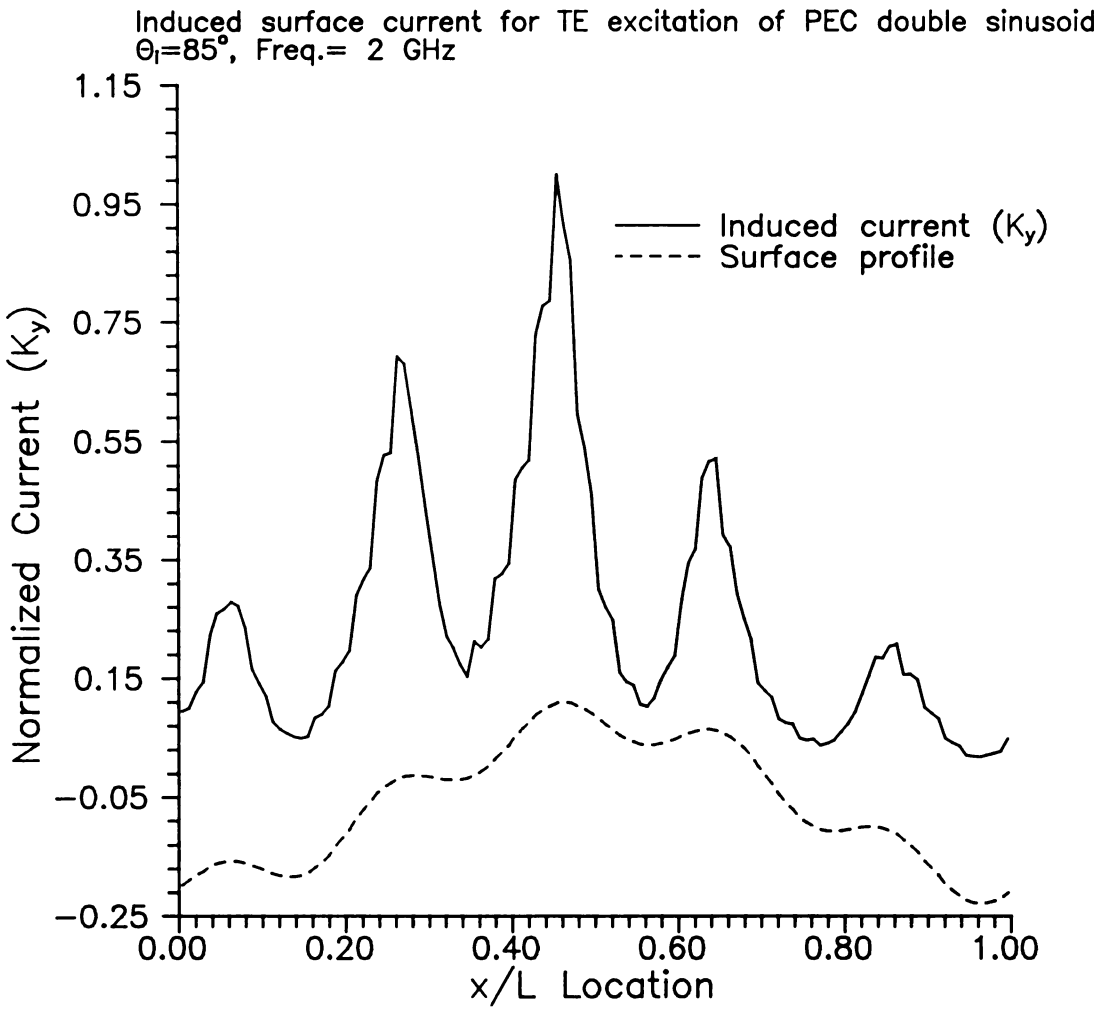

Figure 5.5 Surface current induced on the double sinusoid wave model for a TE incident plane wave at 85° with frequency of 2 GHz.

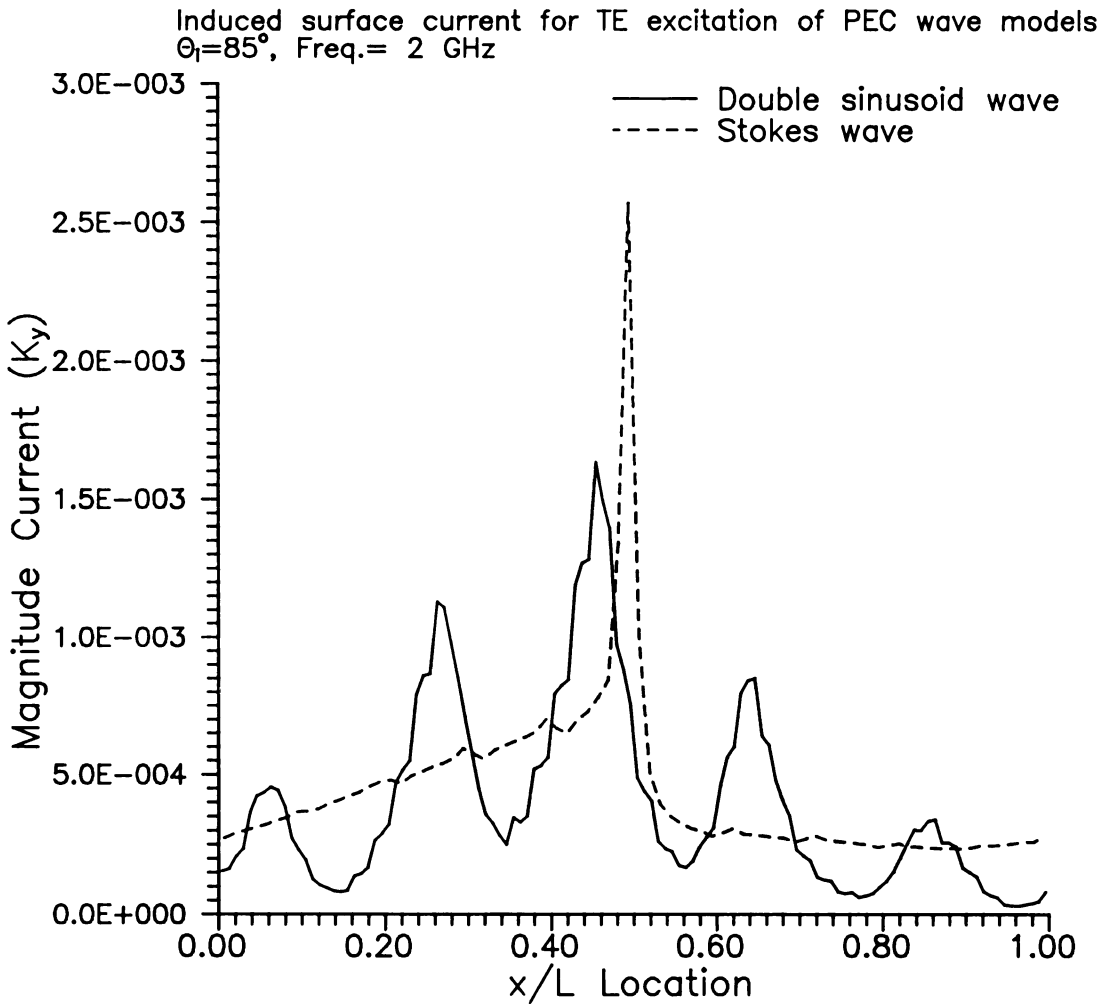

Figure 5.6 Comparison of induce surface currents on the Stokes and double sinusoid wave models.

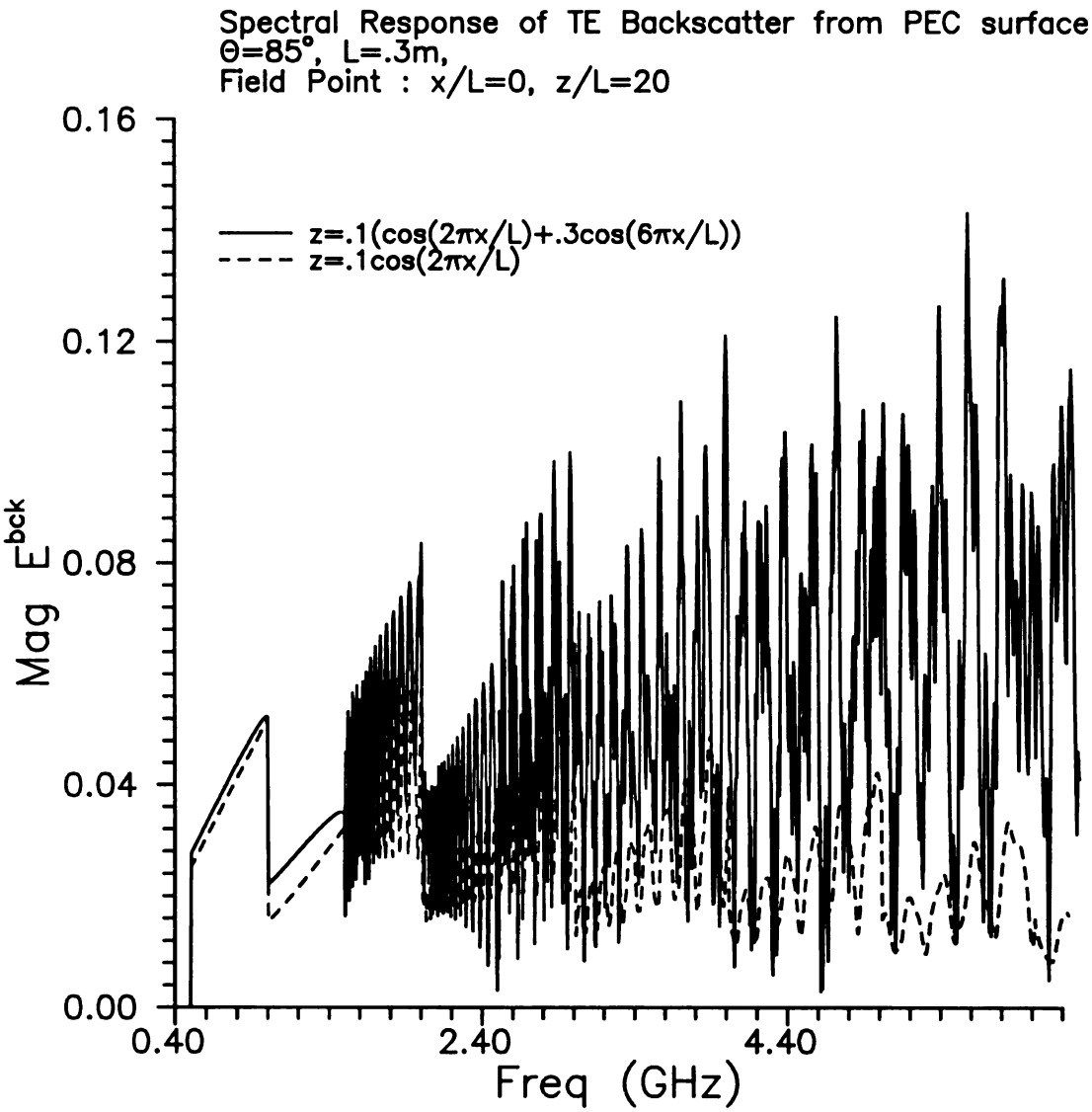

Figure 5.7 Spectrum of backscatter for TE incident wave at 85°, L=.3m at field point x/L=0, z/L=20

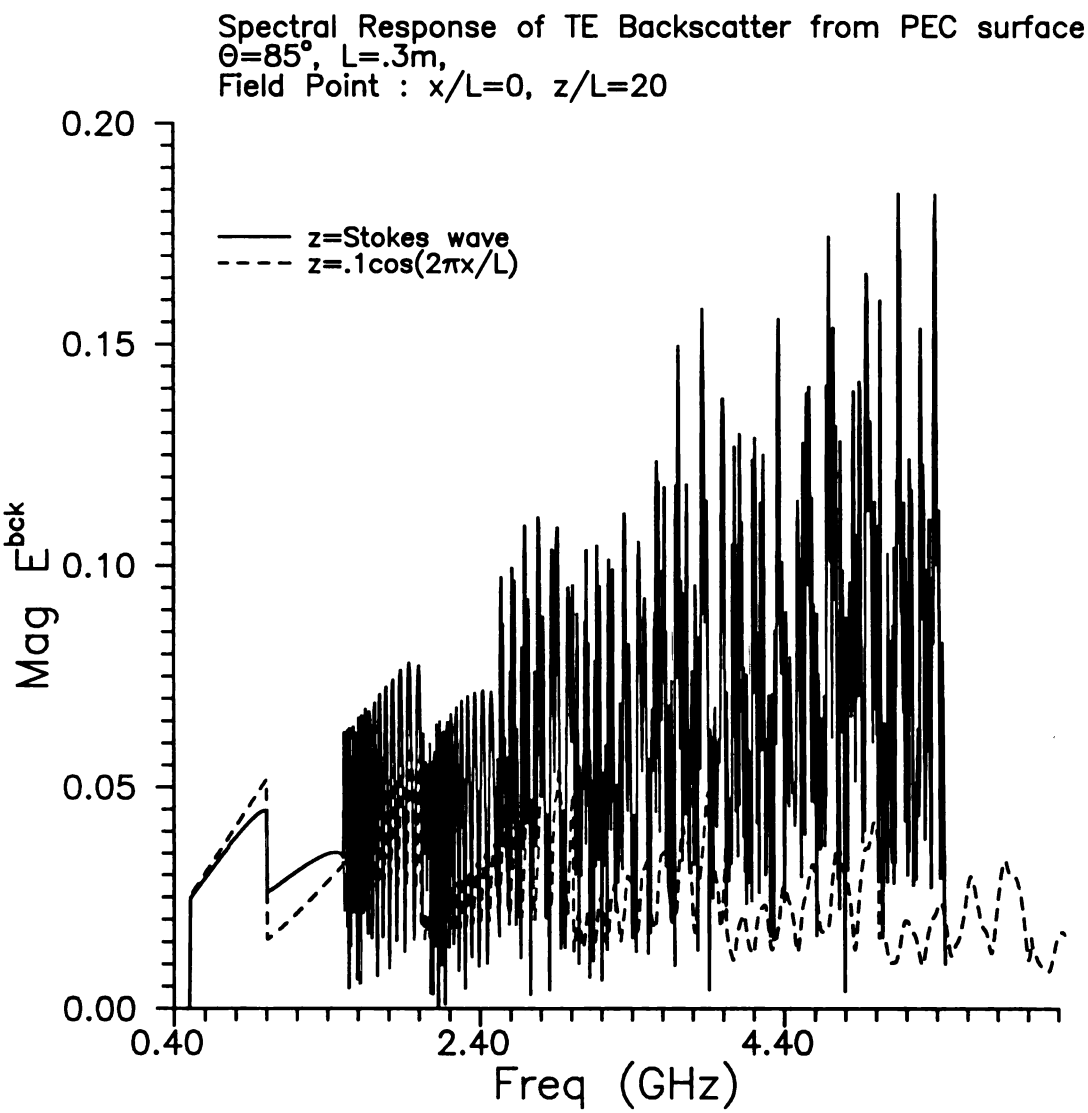

Figure 5.8 Spectrum of backscatter for TE incident wave at 85°, L=.3m at field point x/L=0, z/L=20

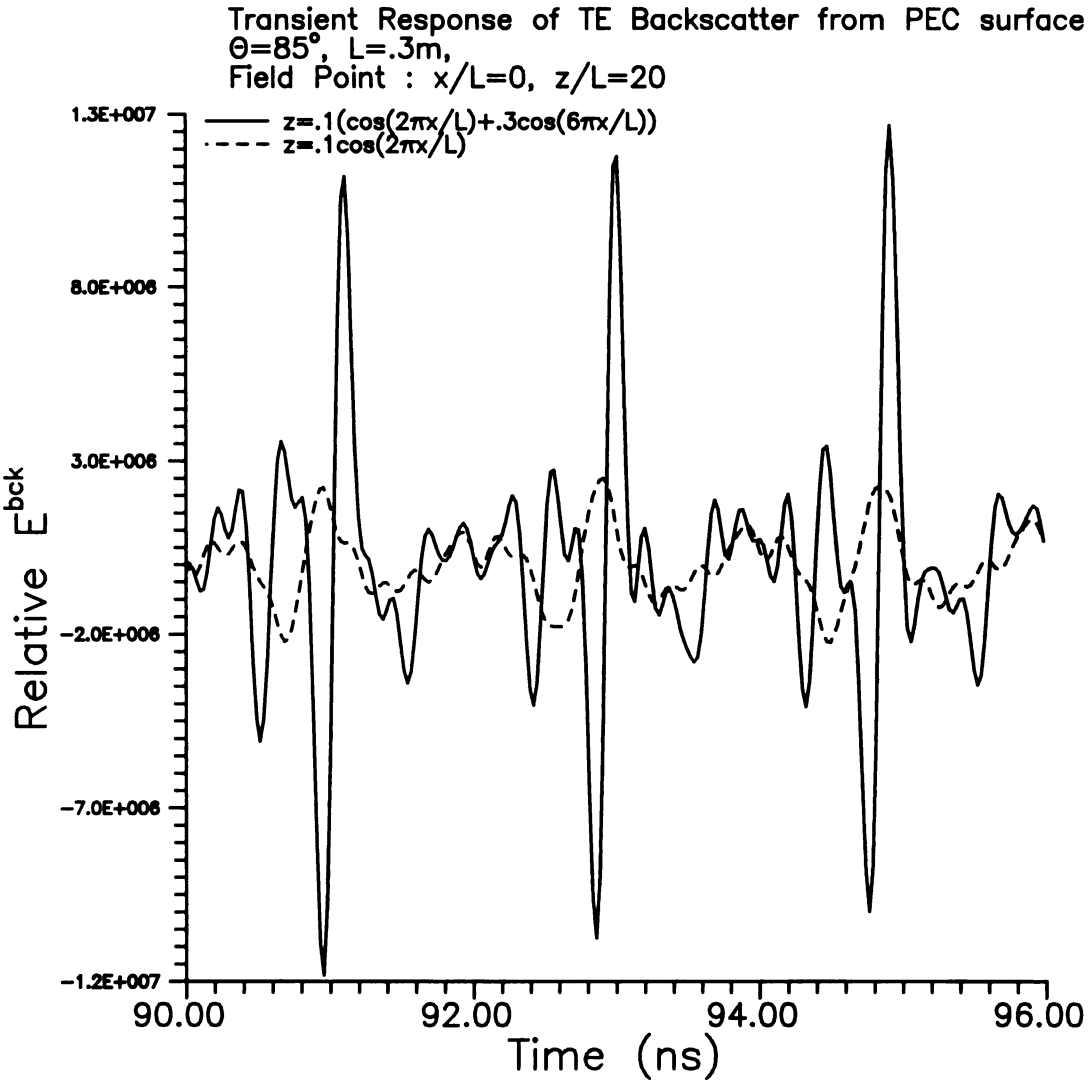

Figure 5.9 Transient backscatter from PEC surface with TE incident wave at 85°, L=0.3m, x/L=0, z/L=20

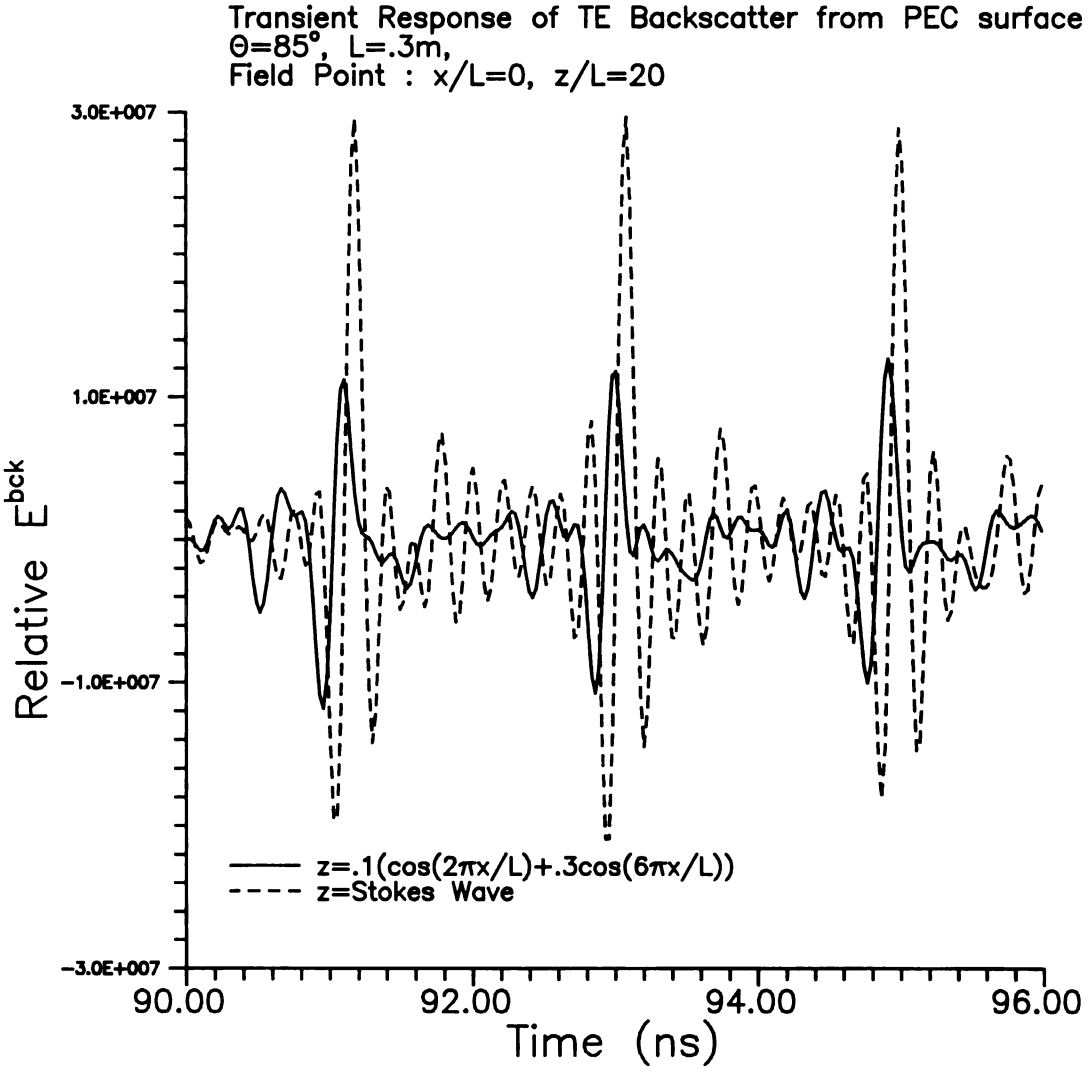

Figure 5.10 Transient backscatter from PEC surface with TE incident wave at 85°, L=0.3m, x/L=0, z/L=20

5.5 Scattering from PEC surfaces for TM excitation

In general there was very good agreement between the theoretical and measured transient backscattered fields from all three sea-surface models. It will be shown later that the theoretical backscattered fields from the infinite surface are in excellent agreement with the measured results, and in fact results are better than theoretical ones with the finite surface. This unexpected result can be attributed to the far-field approximation made in calculating the backscattered field from the finite surface. This approximation could have been lifted at greater numerical costs. The theory for the infinite surface did not contain any such approximations and therefore could better model the cylindrical scattered waves and the relative path length variation along the surface, which manifested itself in the spreading of the Floquet mode spikes.

The experimental measurements consist of true time-domain interrogation with a high voltage PPL pulse generator, and of synthesized frequency domain excitation (via a HP 8720B Network Analyzer). The frequency domain synthesis method allows for a much wider bandwidth and a larger dynamic range, resulting in higher quality measurements. These experimental measurements will be examined in the time and frequency domains and will be compared to theoretical models previously developed.

There are a number of scattering mechanisms present in the non-sinusoidal models that will be closely examined. These mechanisms include the effect of large surface slopes, rougher two-scale surfaces, the aperiodicity of the Donelan-Pierson wave and the onset of multiple scattering. It is hoped that the combination of experimental and theoretical results will encourage the use of UWB/SP radar.

5.5.1 Experimental Results for TM Excitation

The measurements were performed in the anechoic chamber at Michigan State University (MSU). The measurement techniques were described in chapter 2. Specific applications of the frequency domain synthesis technique were provided in chapters 3 and 4. The frequency domain synthesis measurements of the non-sinusoidal surfaces were

performed in an identical manner as in chapters 3 and 4. The true time-domain short-pulse measurements were also performed in the chamber as described in chapter 2.

The wave models for the experimental measurements were constructed by adhering aluminum foil to precision machined polystyrene. The physical size of the three wave models is 1.78m by 0.91m. The Stokes wave consisted of 10 periods with period length (L) of 17.8cm and height of 5.5cm.

The Stokes wave is cycloidal in nature with a large surface slope at the crest of the wave. It is the large slope that is of primary interest; this slope is expected to enhance the backscattered field, and create multiple scattering within a trough.

The double sinusoid has 10 periods (L=17.8cm) with a shorter wavelength (L=3.6cm) superimposed. The height of the large swell is 5.5cm, while the smaller wave is 1.1cm. The double sinusoid model simulates a two-scale roughness ocean model; the finer structure should be resolved by the UWB/SP radar.

The Donelan-Pierson wave was constructed with 10 swells having an aperiodic wind-driven wave superimposed, therefore the DP surface is not periodic. The Donelan-Pierson model is the most realistic, and is constructed from actual ocean statistics, where the wind was assumed to be 10 m/s. This model contains two-scale roughness and large surface slopes, which will provide a stringent test of the UWB/SP radar.

The first results to be considered (somewhat qualitative) investigate the angular dependence of the scattered fields, which were measured via the frequency-domain synthesis technique. The normalized synthesized transient TM backscatter from the Stokes wave model is shown in the bottom plot of Figure 5.11 for incidence angles ranging from near grazing (θ_i = 90°) to normal incidence (θ_i = 0°). Normalization was required to enhance the near grazing backscatter, which contained far less energy than the normally incident backscatter. Observable in the bottom plot are the time-domain backscatter from each individual peak of the wave, and the change in the two-way transit time versus the incidence angle. The finer structure, such as multiple scattering, are hard

to discern in this plot. The remaining transient results provide a better glimpse at individual incidence angles.

Accompanying the transient results are the corresponding spectral returns (actual measurements). In the top plot of Figure 5.11 the Floquet-mode spikes are evident, and the interference patterns for higher frequencies can be seen. Of great interest is the location and movement of the Floquet-mode spikes as the incidence angle is rotated from near grazing to normal incidence. This phenomenon is expected and attributable to the periodic nature of the surface, as discussed in previous chapters. The clarity of the modes indicate the high quality of both the measurement system, and the sea surface construction.

There are similar results for the other wave models. In Figure 5.12 the experimentally measured response from double sinusoid wave is shown. The spectral returns (upper plot) look remarkable similar to the Stokes wave, this is due to periodicity of the wave. The differences between the two wave models can be seen the transient response, which is of primary interest. The synthesized TM transient response, shown in the bottom plot, reveals the non-shadowed ripples on the double sinusoid model.

The response from the Donelan Pierson surface is shown in Figure 5.13 and Figure 5.14. The Donelan Pierson model is aperiodic, therefore it is not expected to produce the Floquet mode spikes. Thus, the spectral returns (upper plots) are quite amazing, and actually reveal a Floquet mode type pattern for the lower frequencies. This is due to the periodic swell that what superimposed upon the wind-driven surface waves. The transient results (lower plots) also show the effects of the aperiodicity. Due to the variance in the wave crest heights there is a strong shadowing effect evident at the near grazing angles. In Figure 5.2 the Donelan Pierson wave is shown and the highest peaks in the wave are quite visible in the transient response. The smaller wave crests are only visible for the angles nearing normal incidence.

The TM scattering from the three waves at an incidence angle (θ_i) of 80° are compared in Figure 5.15, where the measured frequency-domain results are compared. The large spikes in the spectral returns are due to periodicity of the surfaces and are called Floquet-mode spikes. These spikes are dependent upon the incidence angle and the spatial period of the sea surface. Note that the Donelan Pierson surface lacks these highly defined spikes due to the aperiodic nature of the surface. The overall strength of the returns at this incidence angle are greatest for the Stokes wave, because of the large slope near the crest of the wave.

The short-pulse transient response can be obtained by performing an IFFT on the frequency-domain responses. The short-pulse interrogation of the three wave models for the incidence angle of 70° is shown in Figure 5.16. These waveforms represent the returns an actual UWB/SP radar would produce if it was endowed with the bandwidth of the corresponding spectral responses (Figure 5.15). The differences between the three wave models is quite evident in the transient response. The double-sinusoid and Stokes wave models produce a periodic set of return pulses, while the response from the Donelan-Pierson model is erratic. The additional surface features of the double-sinusoid and the Donelan-Pierson models produce the multiple-scattering-center return pulses. These transient responses were weighted with a $\frac{1}{8}$ cosine taper before transformation.

A further investigation continues in Figure 5.17 and Figure 5.18. The TM backscattered response for two incidence angles is shown for the Stokes (Figure 5.17) and double sinusoid (Figure 5.18) wave models. When the incidence angle is lowered to 60° there are visible changes in the spectral responses. The well-defined single Floquet mode spike is no longer present at the higher frequencies, where the spectra become erratic. This indicates that small structures are nearing resonance, or that multiple scattering is occurring.

The corresponding synthesized transient responses are shown in the following figures. The differences in the responses between the three wave models is of primary

interest for describing the underlying physics. The TM transient response from the Stokes wave model for 80° and 60° incidence is shown in Figure 5.19. The periodic return of pulses is expected because of periodic nature of the wave. The effects of multiple scattering, which was predicted from the spectral returns, is more pronounced for the 60° case. This is due to the erratic high frequency content observable in the frequency domain.

The transient response for the double sinusoid model is shown in Figure 5.20. The major difference (with the Stokes wave) is the additional return pulses from the smaller scale sinusoids. This was also predicted by the spectral returns. Another interesting feature is the amplitude differences between the two incidence angles. There is a much greater difference for the double sinusoid case. The cause for this effect is the surface slope. The Stokes wave has a much larger surface slope, therefore the near grazing angles still produce a large backscatter.

The response from the Donelan-Pierson model shows the shadowing effect produced by the first crest of the surface as indicated in Figure 5.21. The first crest is by far the largest (see Figure 5.2 and note that the wave was actually measured from the right) and creates the easily observable shadowing of the remaining wave crests. Note that the transient responses were normalized and the 60° incidence response was actually much larger (as expected) than the 80° return.

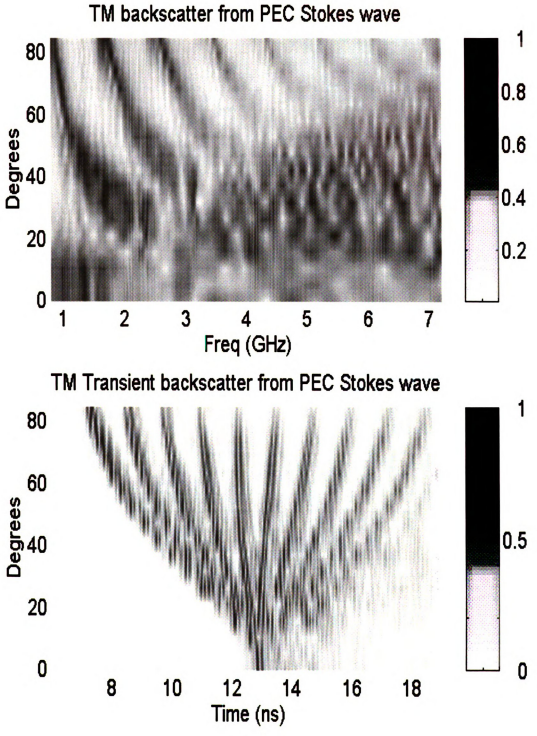

Figure 5.11 Angular dependence of TM scattered fields of the Stokes wave model.

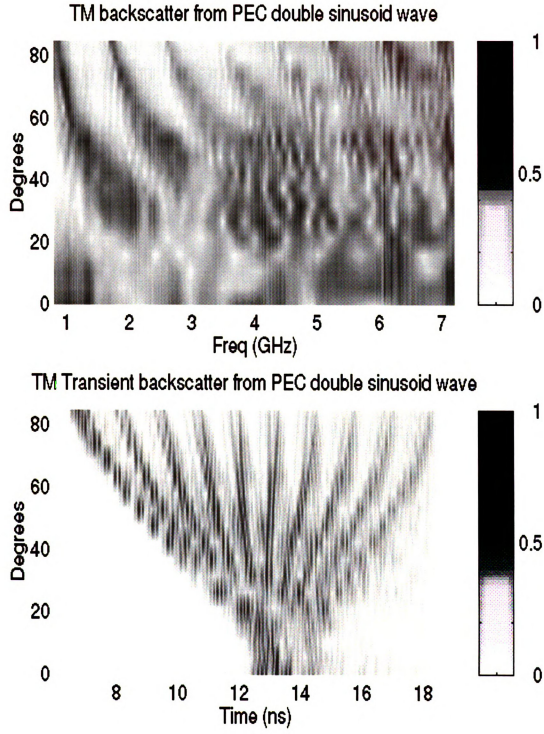

Figure 5.12 Angular dependence of TM scattered fields of the double sinusoid wave model.

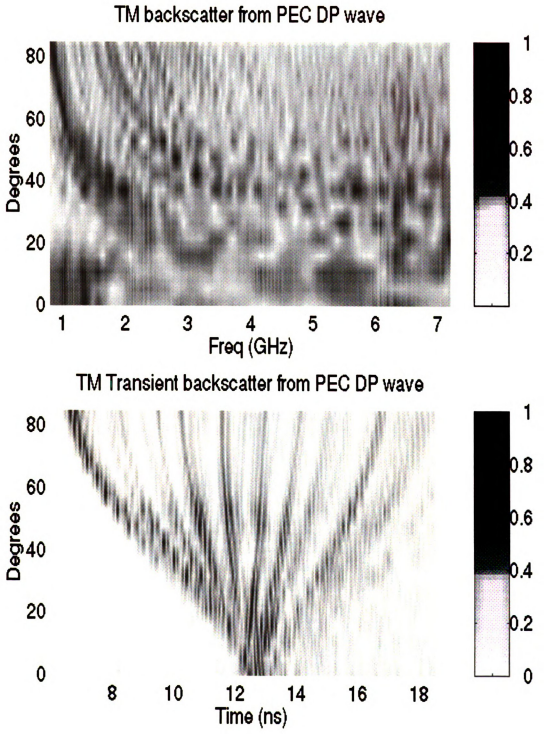

Figure 5.13 Angular dependence of TM scattered fields of the Donelan Pierson wave model.

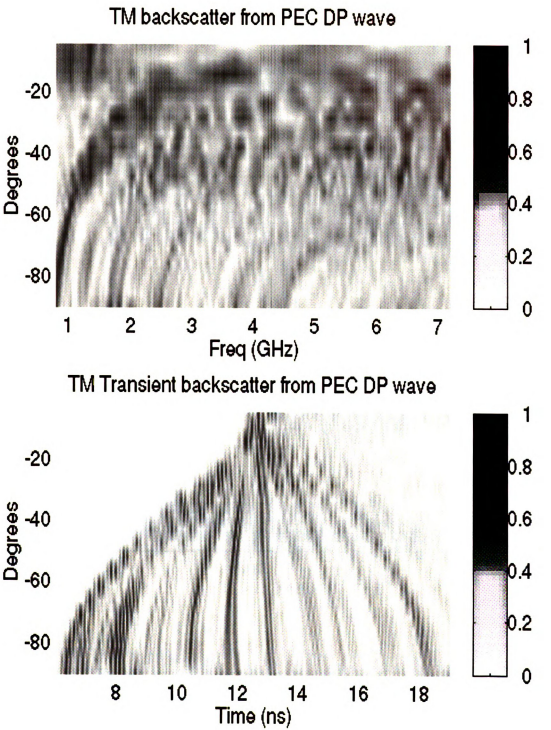

Figure 5.14 Angular dependence of TM scattered fields of the Donelan Pierson wave model.

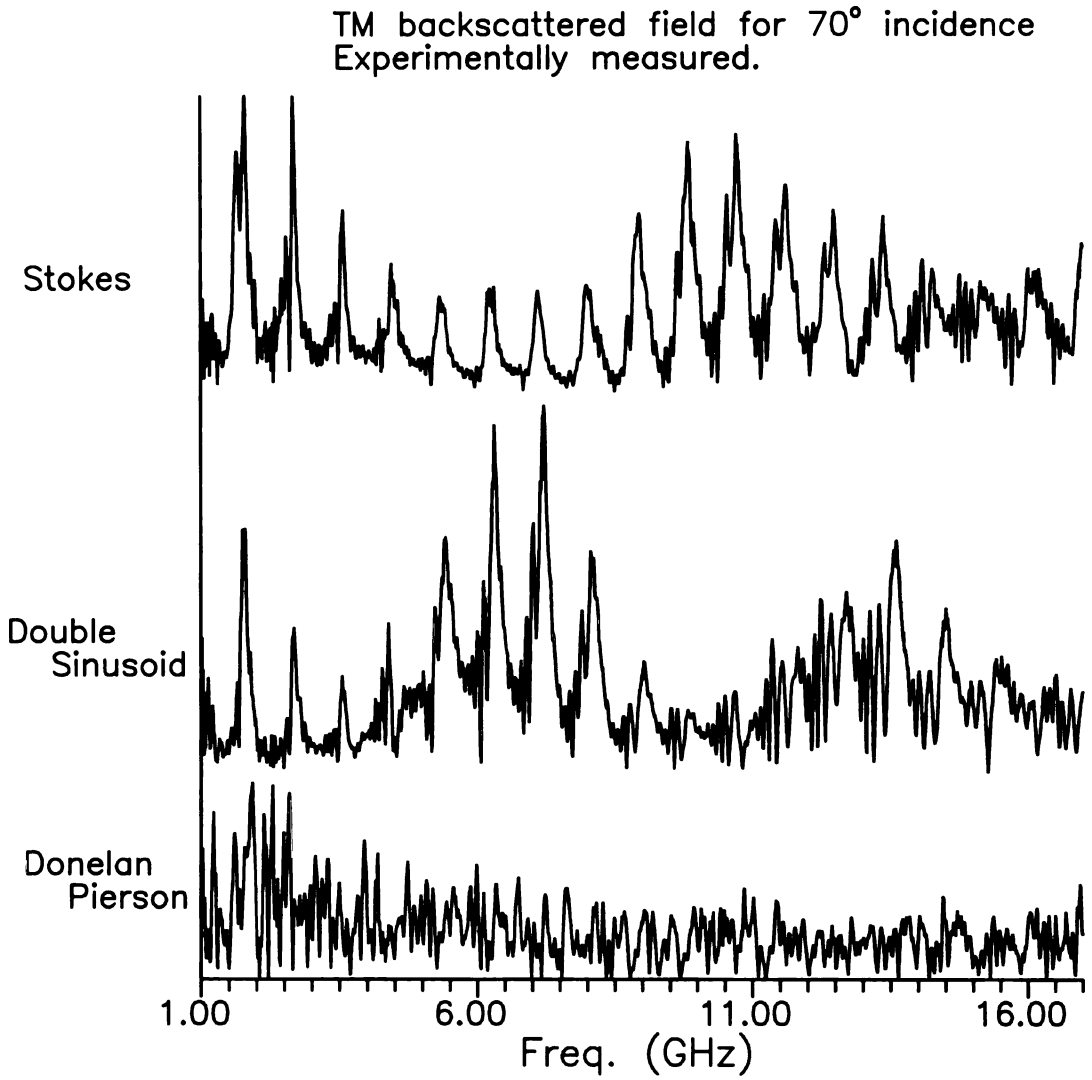

Figure 5.15 Experimental TM scattering from various wave models for an incidence angle of 70°.

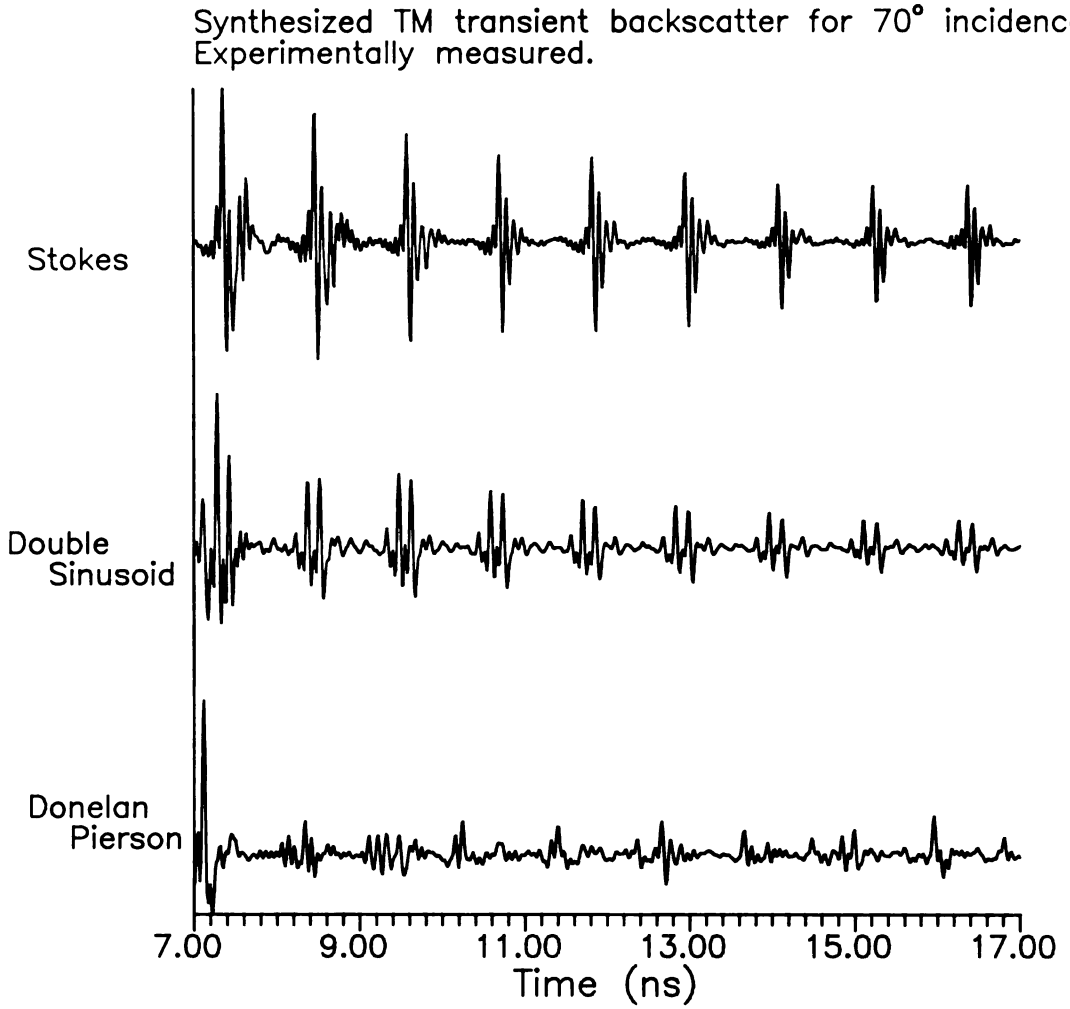

Figure 5.16 Experimental TM transient scattering from various wave models for an incidence angle of 70°. Synthesized with a 1/8 cosine taper.

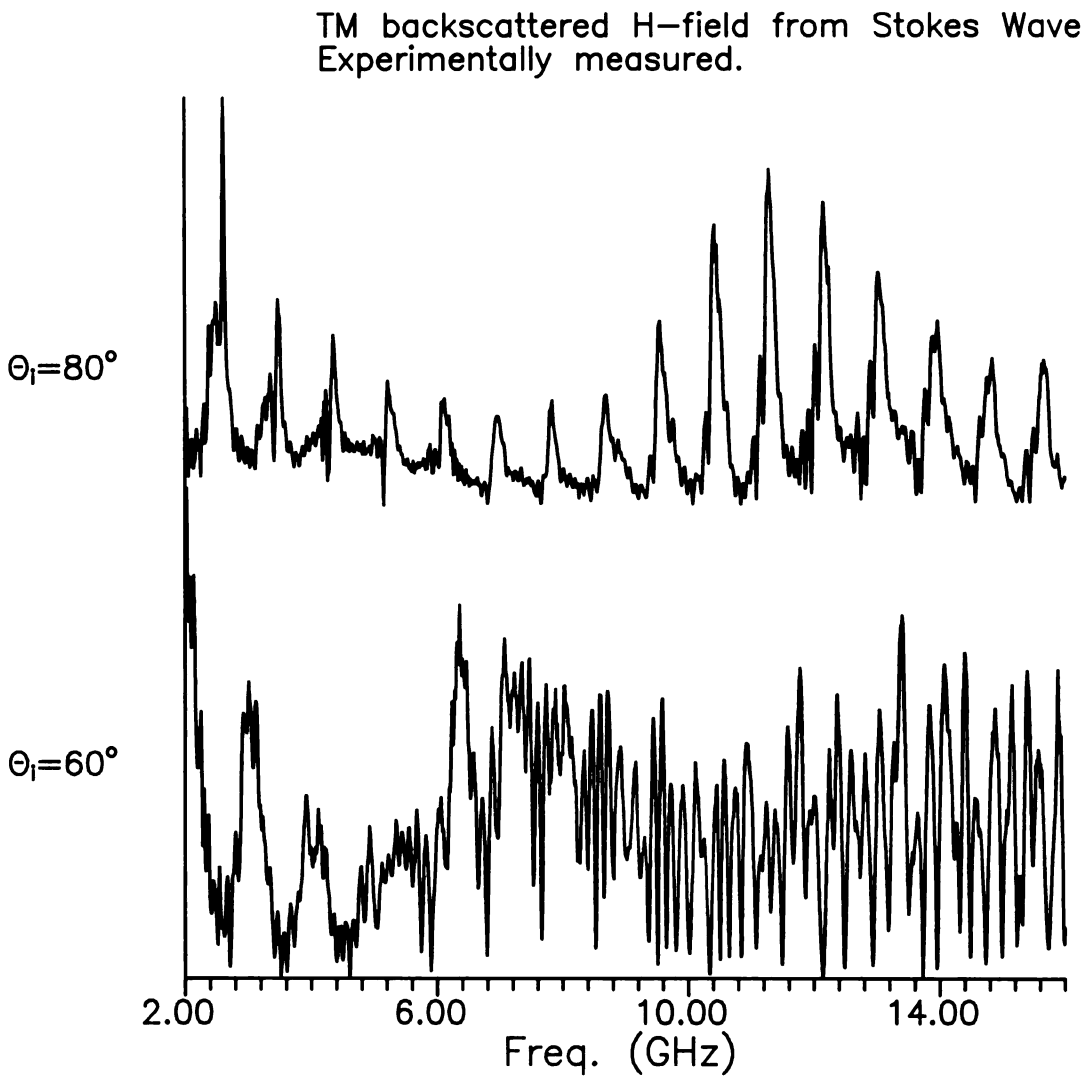

Figure 5.17 TM backscattered fields from the Stokes wave model. Experimentally measured response at 60° and 80°.

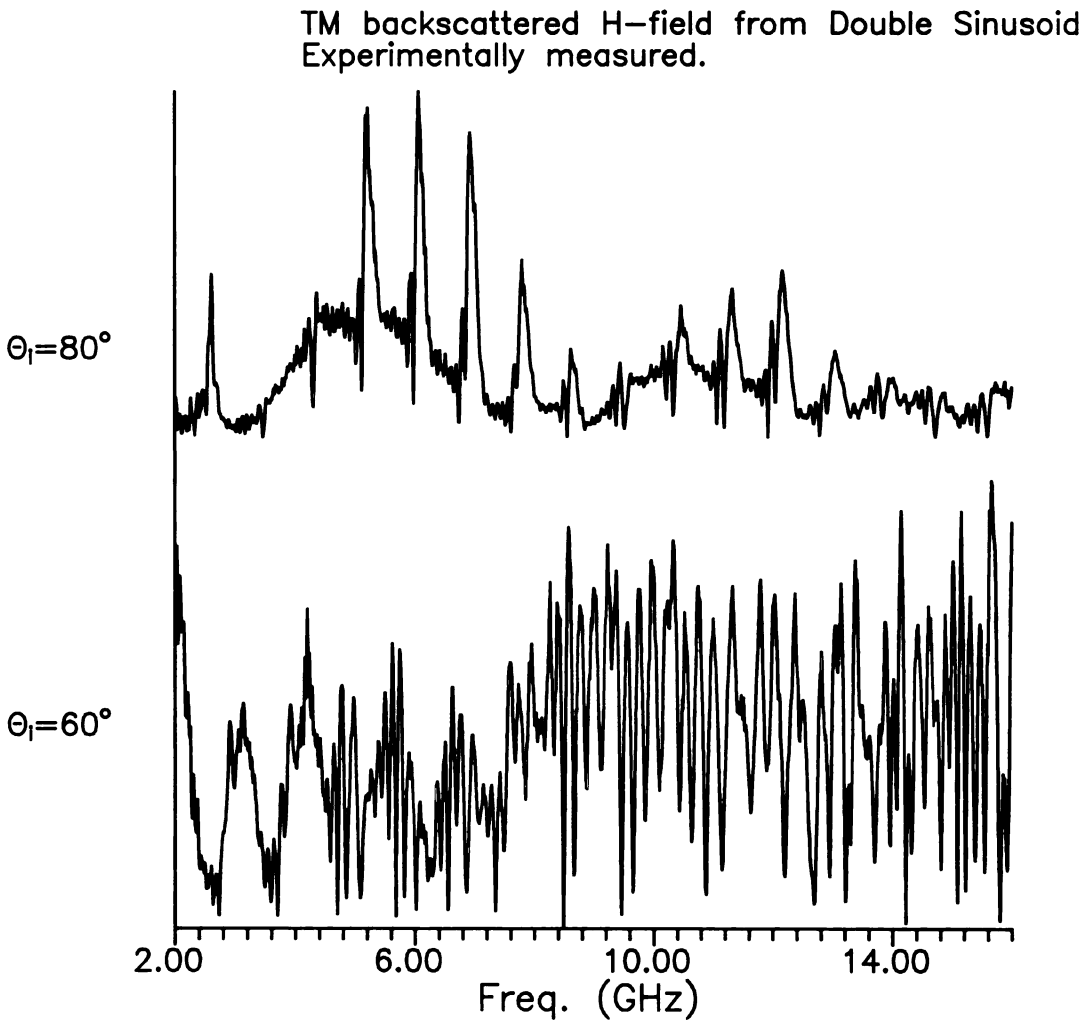

Figure 5.18 TM backscattered fields from the double sinusoid wave model. Experimentally measured response at 60° and 80°.

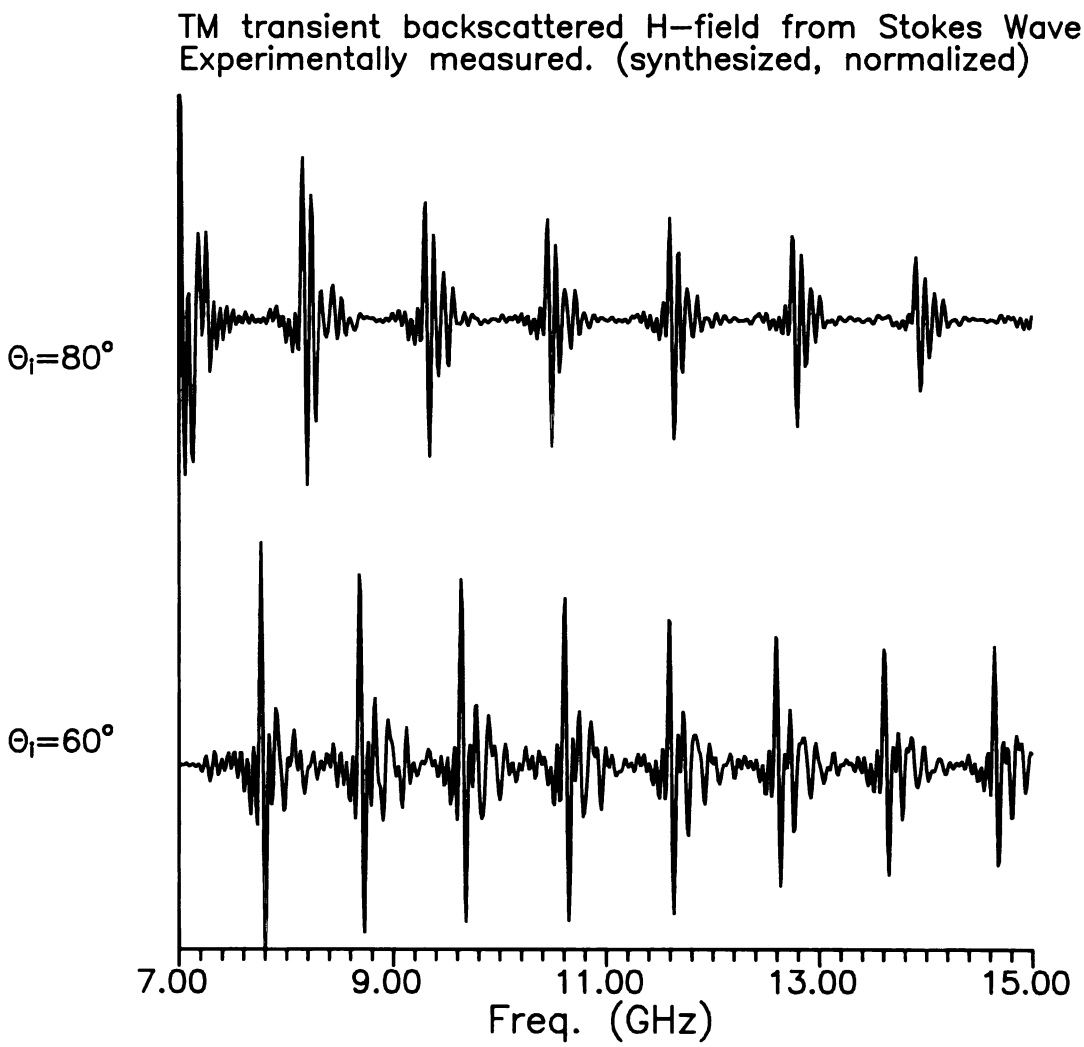

Figure 5.19 TM synthesized transient backscattered fields from the Stokes wave model. Experimentally measured response at 60° and 80°. Spectral returns were weighted with 1/8 cosine taper before IFFT.

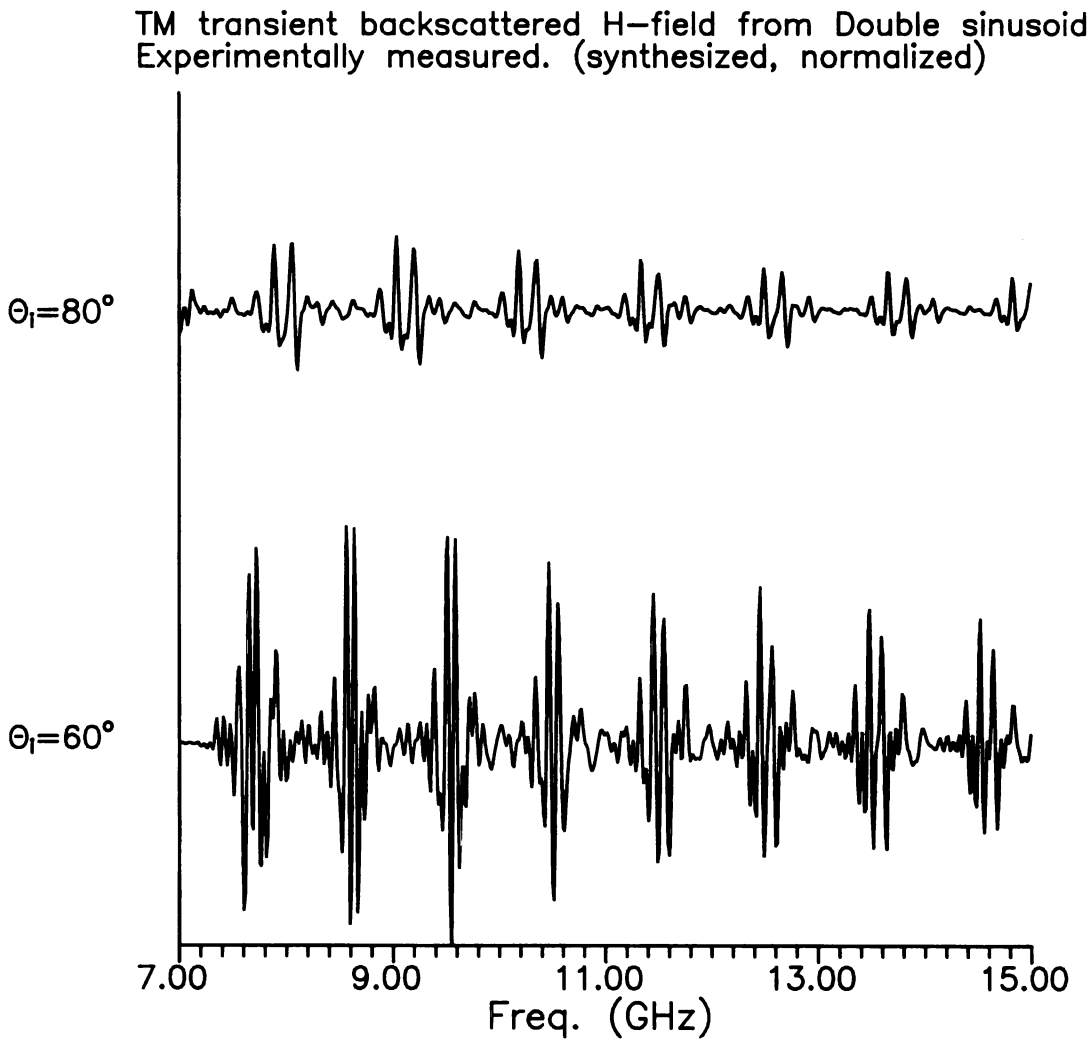

Figure 5.20 TM synthesized transient backscattered fields from the double sinusoid wave model. Experimentally measured response at 60° and 80°. Spectral returns were weighted with 1/8 cosine taper before IFFT.

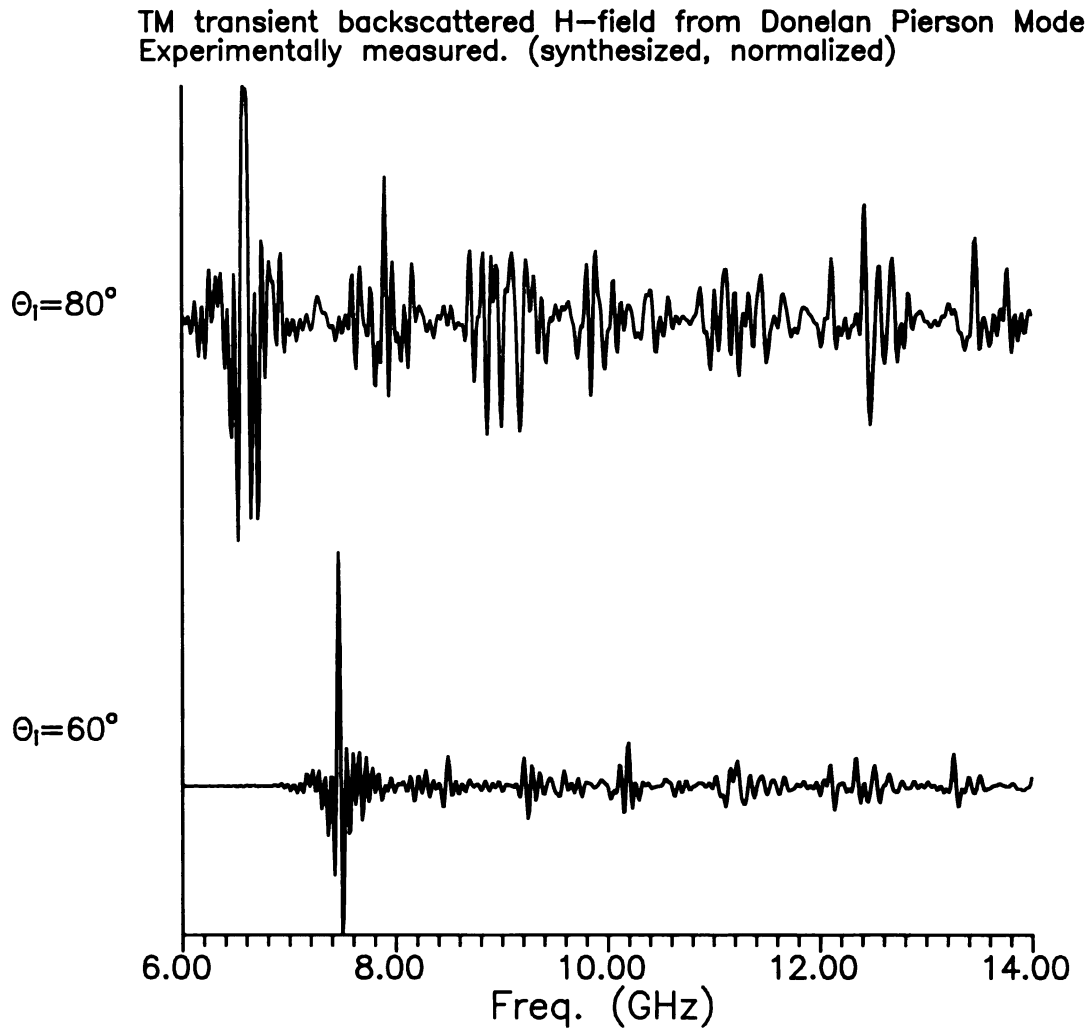

Figure 5.21 TM synthesized transient backscattered fields from the Donelan Pierson wave model. Experimentally measured response at 60° and 80°. Spectral returns were weighted with 1/8 cosine taper before IFFT.

5.5.1a TM Measurements performed in time domain

The experimental results up to this point have all been obtained through the frequency domain synthesis technique. An actual UWB/SP radar system would not operate in this fashion. Instead the UWB/SP radar would transmit and receive and an actual short-pulse. This near instantaneous interrogation method is the primary reason the ocean surface models can be treated as stationary. Therefore it is important to perform some true short-pulse measurements of the sea-surface models. The importance lies not only in establishing the feasibility of an UWB/SP radar system, but also as another verification of both the theoretical and the frequency-domain synthesis results.

The first set of results are the TM transient backscatter responses of the three wave models. The responses acquired via the frequency domain synthesis technique are composed of roughly the same effective spectral bandwidth as the true time-domain system. The true time-domain system produces a 1/2 ns pulse or a roughly 2 GHz bandwidth (baseband). In Figure 5.22, Figure 5.23, and Figure 5.24 a comparison of the two measurements techniques is shown for the Stokes, double sinusoid, and Donelan Pierson models, respectively. The agreement between the two methods is quite remarkable. The effect of the reduction in bandwidth is noticeable in the reduced resolution. It is difficult to determine the differences between the Stokes and double sinusoid transient responses. This is a direct consequence of the effective bandwidth of the measurement systems. The lower frequencies do not excite the small-scale features of the double sinusoid model and therefore only the fundamental frequency is seen. The Donelan Pierson response does differ from the others, as expected, because of the aperiodicity.

The spectral responses for the three models are considered next. The true time-domain measurements had to be transformed to the frequency domain to be compared with the actual measurements obtained by the frequency domain synthesis system. In Figure 5.25 the spectra generated by the two measurements techniques are compared.

There is an excellent agreement until roughly 2 GHz. The spectral limitations of the true time-domain measurement system can be seen beyond 2 GHz.

A comparison of the TM spectral backscatter from the Stokes and the double sinusoid in Figure 5.26 support the conclusion made above. That is, over this frequency band the two wave models are quite similar and therefore produce similar transient responses as shown above. This fact will also be shown in the theoretical results in the following section.

The favorable results of this section strengthen confidence in the frequency domain synthesis technique and have also illuminated some the phenomenology associated with transient scattering. The performance of the true time-domain system, which simulates an UWB/SP radar system, was also remarkable given the spectral limitations.

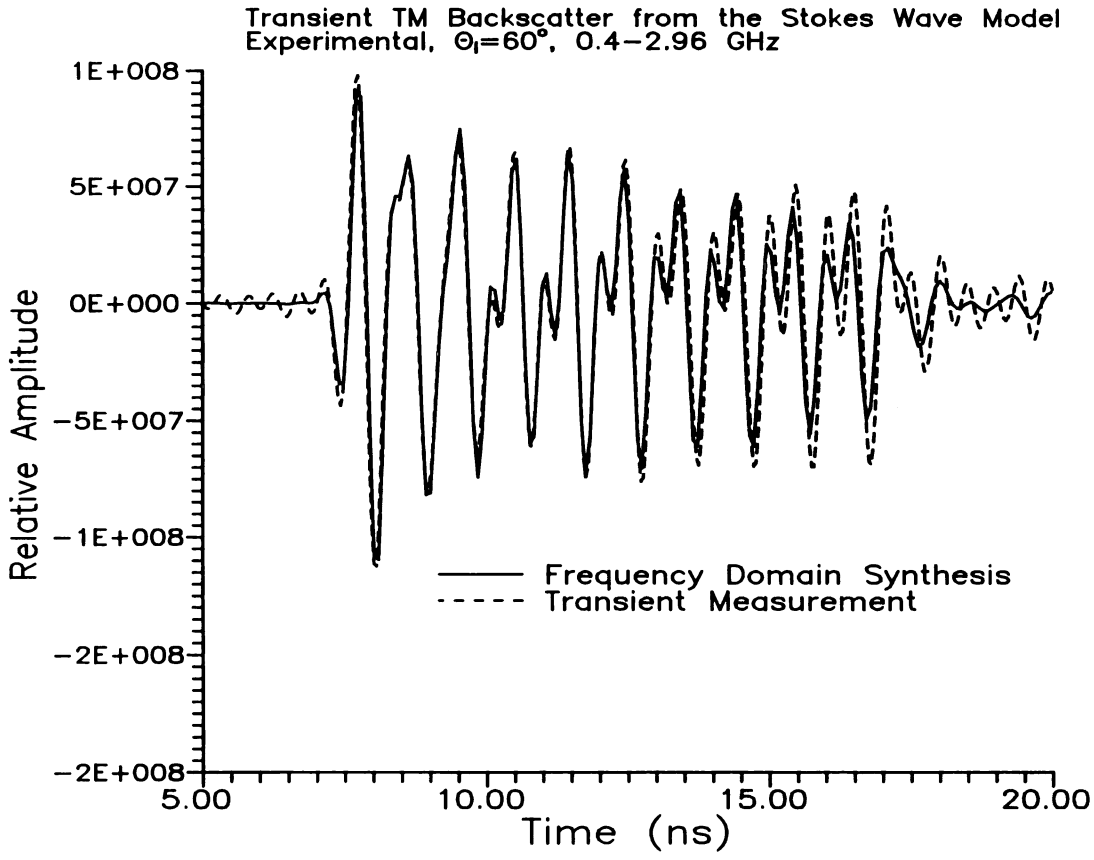

Figure 5.22 Transient TM backscatter response for the Stokes wave model. A comparison of frequency-domain synthesis and time-domain techniques.

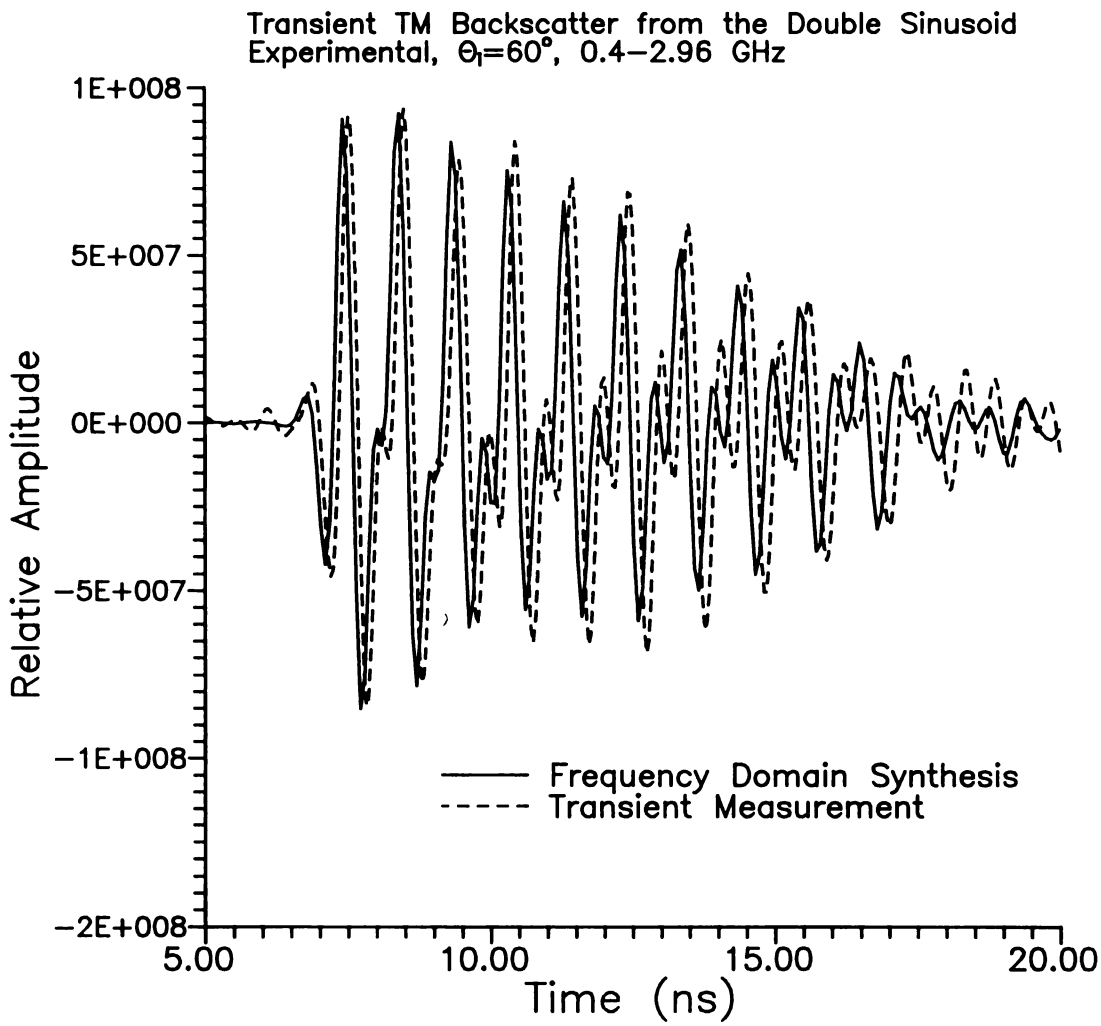

Figure 5.23 Transient TM backscatter response for the double sinusoid wave model. A comparison of frequency-domain synthesis technique and time-domain technique.

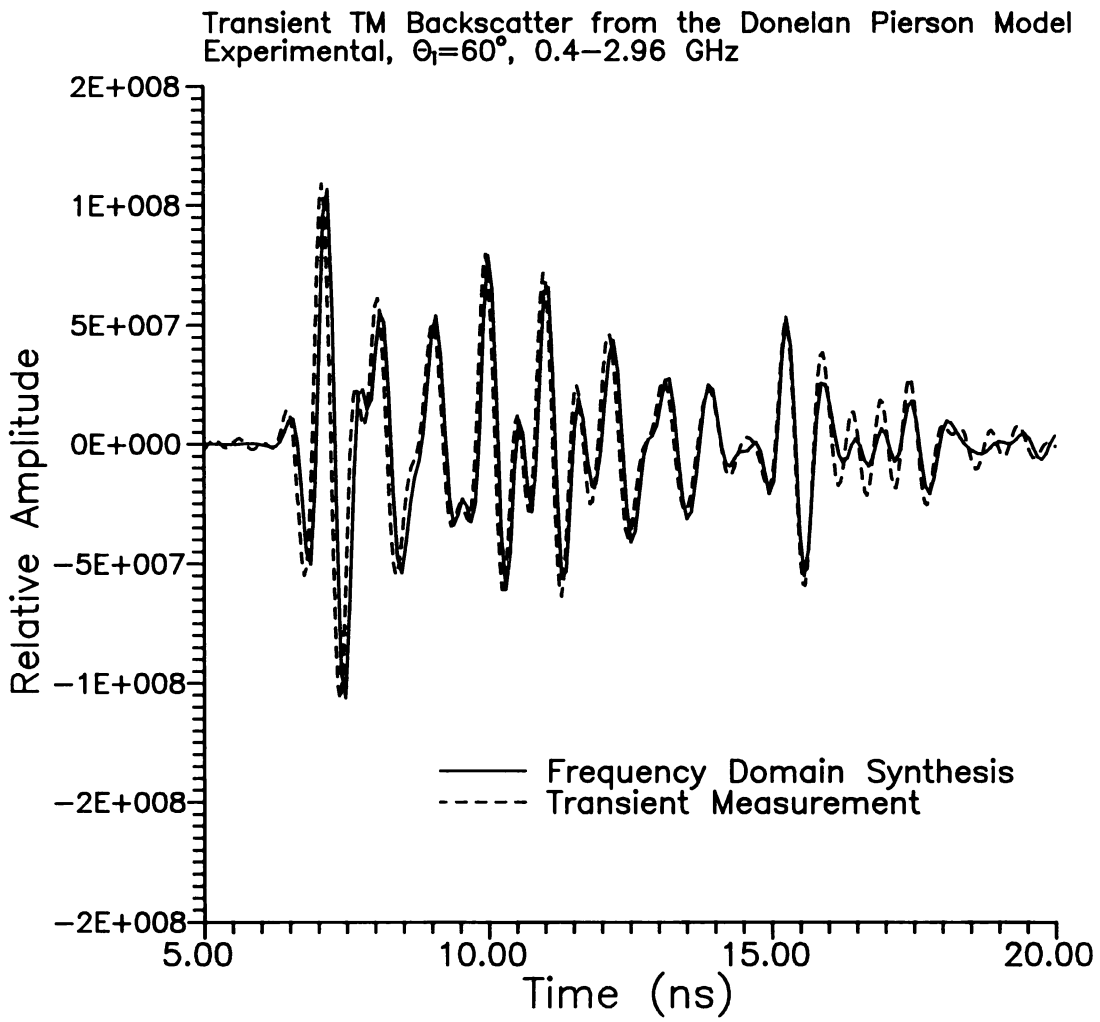

Figure 5.24 Transient TM backscatter response for the Donelan Pierson wave model. A comparison of frequency-domain synthesis technique and time-domain technique.

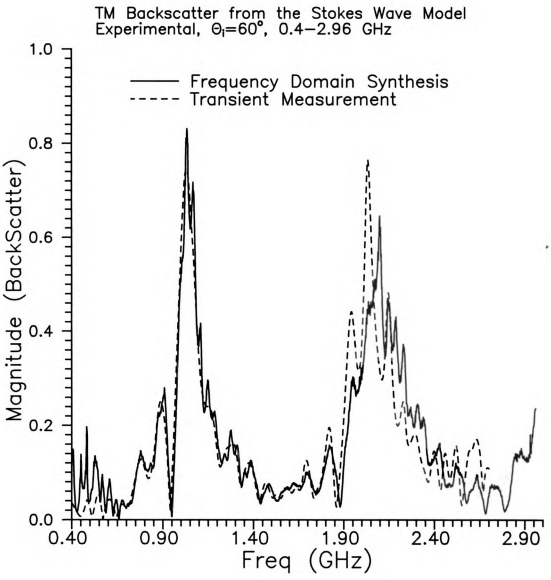

Figure 5.25 Spectrum of TM backscatter response for the Stokes wave model. A comparison of frequency-domain synthesis technique and time-domain technique.

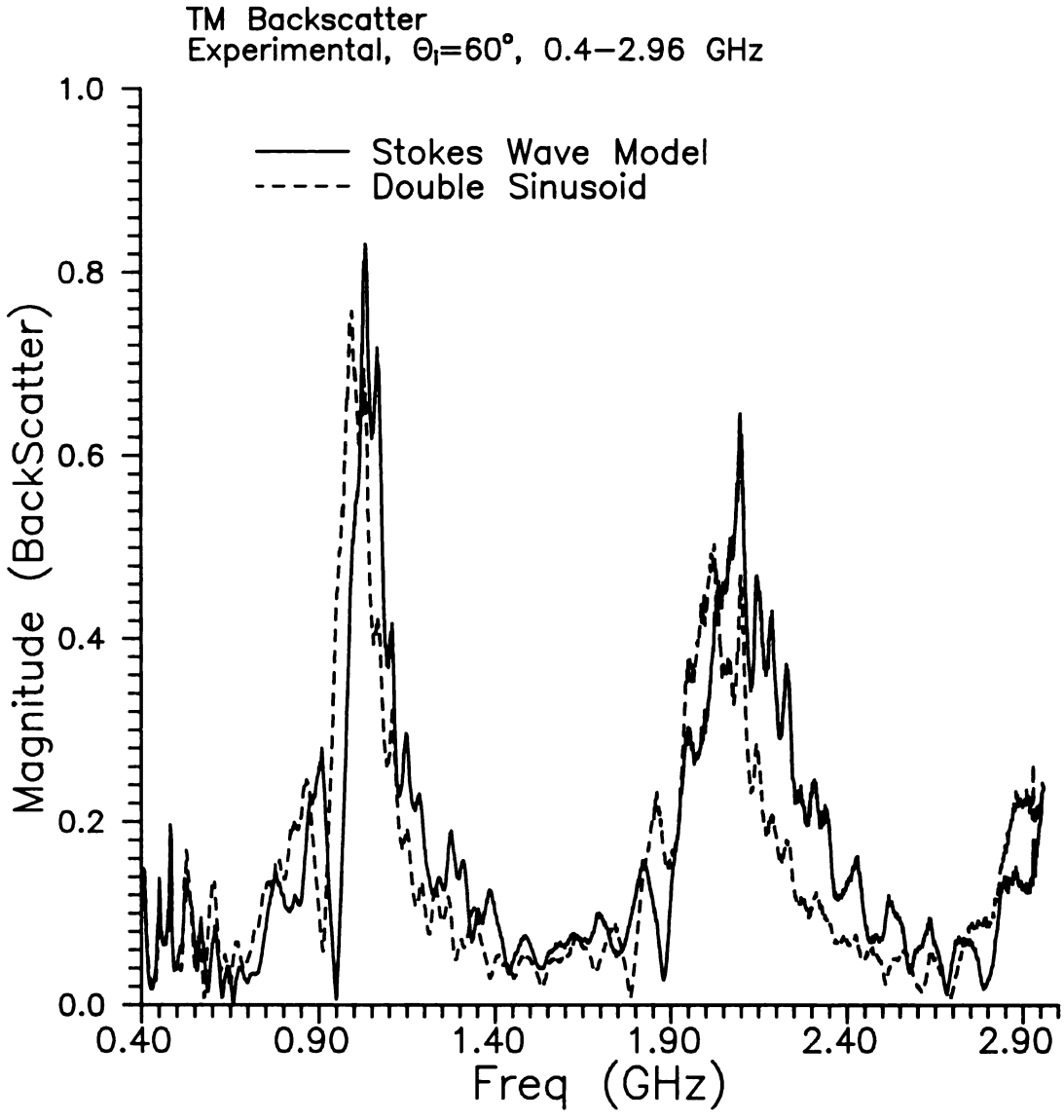

Figure 5.26 Spectra of TM backscatter response for the Stokes and double sinusoid wave models. Measurements were performed using the time-domain technique.

5.5.2 Theoretical Response for TM Excitation

The theoretical TM backscattered fields from the wave models that have been experimentally measured will be briefly examined. The comparison and validation of the theoretical and measured responses are included in the following section. The theoretical results were obtained using the IE formulation supplemented with the PGF acceleration technique described in section 5.2.2. The results are for infinite (periodic) PEC surfaces and therefore only the Stokes and double sinusoid waves are considered in this section.

In Figure 5.27 and Figure 5.28 are the spectral and synthesized transient responses for TM excitation of the Stokes wave. The figures compare the effect of incidence angle (θ_i) upon the backscattered fields. The spectral returns (Figure 5.27) illustrate the change in Floquet mode location with incidence angle. The synthesized transient response (Figure 5.28) produces many of the same effects that were observable in the experimental results. The periodic return of pulses from the single crest of the Stokes wave appears along with an additional multiple scatter as seen in the trough region. The effects of incidence angle on the transient response is difficult to discern.

The response from the double sinusoid model is shown in Figure 5.29 and Figure 5.30. The strength of the return is greater for the 60° aspect as seen in the spectral responses of Figure 5.29. This phenomenon has been explained in previous sections and is intuitively expected. The synthesized transient responses reveal the periodic nature of the wave and the resolution capabilities of the narrow interrogation pulse. The transient results are shown in Figure 5.30. The shadowing effect is also noticeable for the 85° incidence; this effect was seen the experimental results and will be compared in the following section.

The spectral returns for both the Stokes and double-sinusoid wave models have amazing similarities. This was also found with the experimental results and is therefore substantiated by these theoretical findings. The periodicity of the wave models is what causes the remarkable similarities in the spectra.

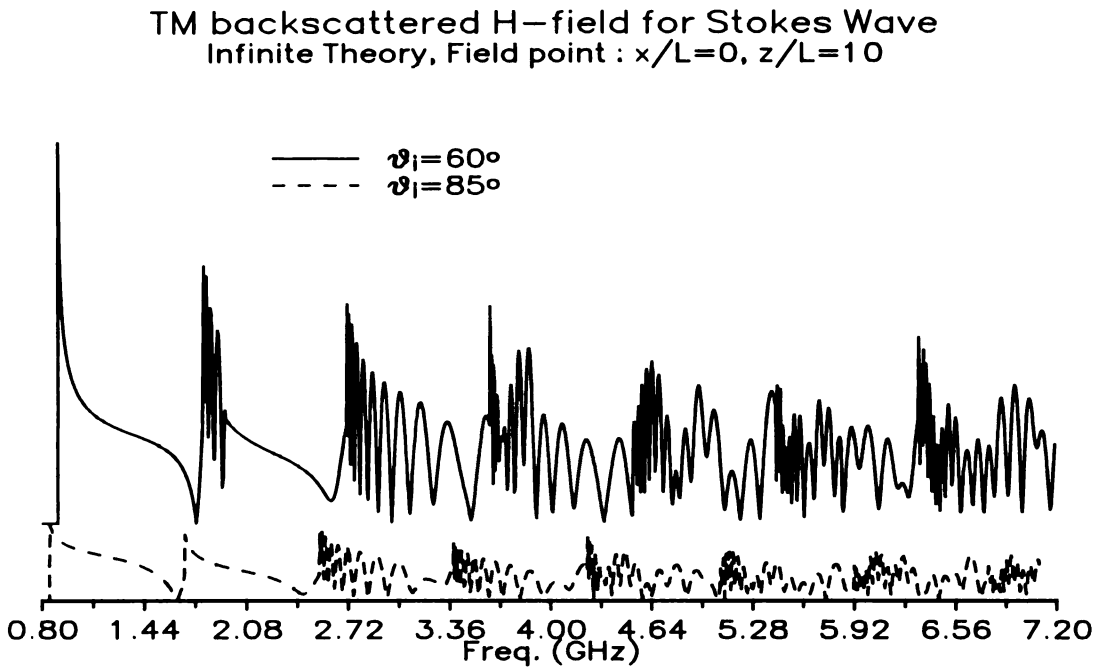

Figure 5.27 TM backscattered magnetic field for the Stokes wave model. Comparison theoretical responses for 60° and 85° incidence.

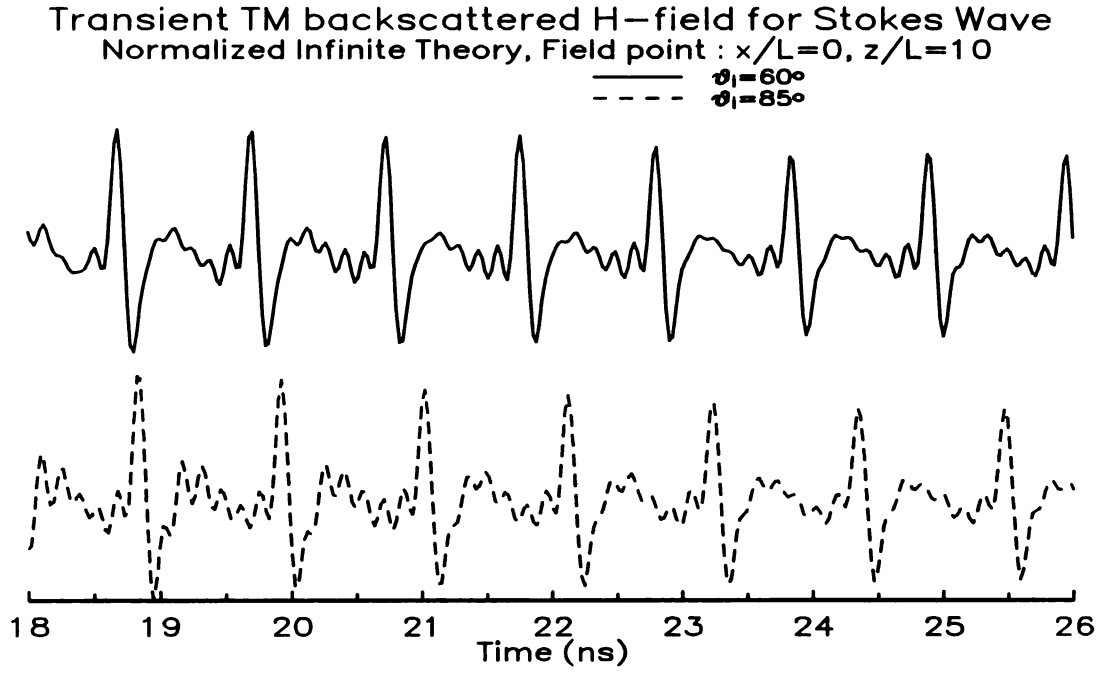

Figure 5.28 Synthesized transient TM backscattered magnetic field for Stokes wave.

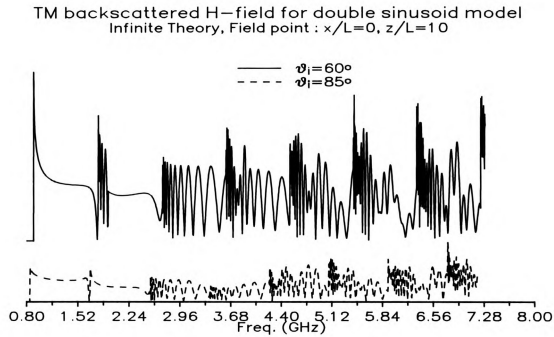

Figure 5.29 TM backscattered magnetic field for the double sinusoid wave model. Comparison theoretical responses for 60° and 85° incidence.

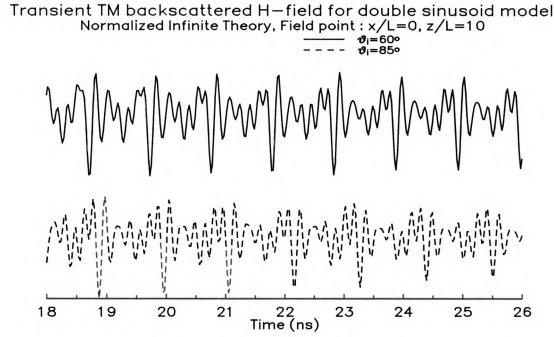

Figure 5.30 Synthesized transient TM backscattered magnetic field for double sinusoid.

5.5.3 Comparison/Evaluation of TM results

The theoretical and experimental results for TM excitation shown in the previous sections provide a qualitative comparison. The basic scattering mechanisms are apparent in both the theoretical and experimental results and give hope for a positive comparison. There are a number of difficulties in performing a comparison between the theoretical and experimental responses. These difficulties have been addressed in the previous chapters and will only be briefly listed again. The experimental models are of course finite and comparison to theory for the infinite surfaces must recognize this fact. The incident wave in the experimental system is not an ideal plane wave. The incidence angle is also affected by the placement of the wave model in the anechoic chamber which creates additional uncertainty. The wave model itself has small imperfections and cannot be perfectly periodic.

Nonetheless, even with all the possible error contributions, the experimental and theoretical results are seen to match quite well. In Figure 5.31 the backscattered field spectra for measured and theoretical techniques are compared. The theoretical responses were found using the theory for an infinite surface. The agreement is readily evident and the spectra are seen to be dominated by the Floquet-mode spikes. Note that the theoretical response was obtained by transforming the original spectrum to the time domain and then time gating the transient response to the equivalent finite surface length. The time-gated transient response was then transformed back to the frequency domain.

The synthesized transient response for the Stokes wave model is shown in Figure 5.32. The agreement is once again quite amazing considering the possible detractors. There is similar agreement for the scattered fields from the double-sinusoid wave model. The spectral and synthesized transient responses of the double-sinusoid model for TM excitation are shown in Figure 5.33 and Figure 5.34. The overall strong agreement once again strengthens the confidence in both the theoretical and experimental methods.

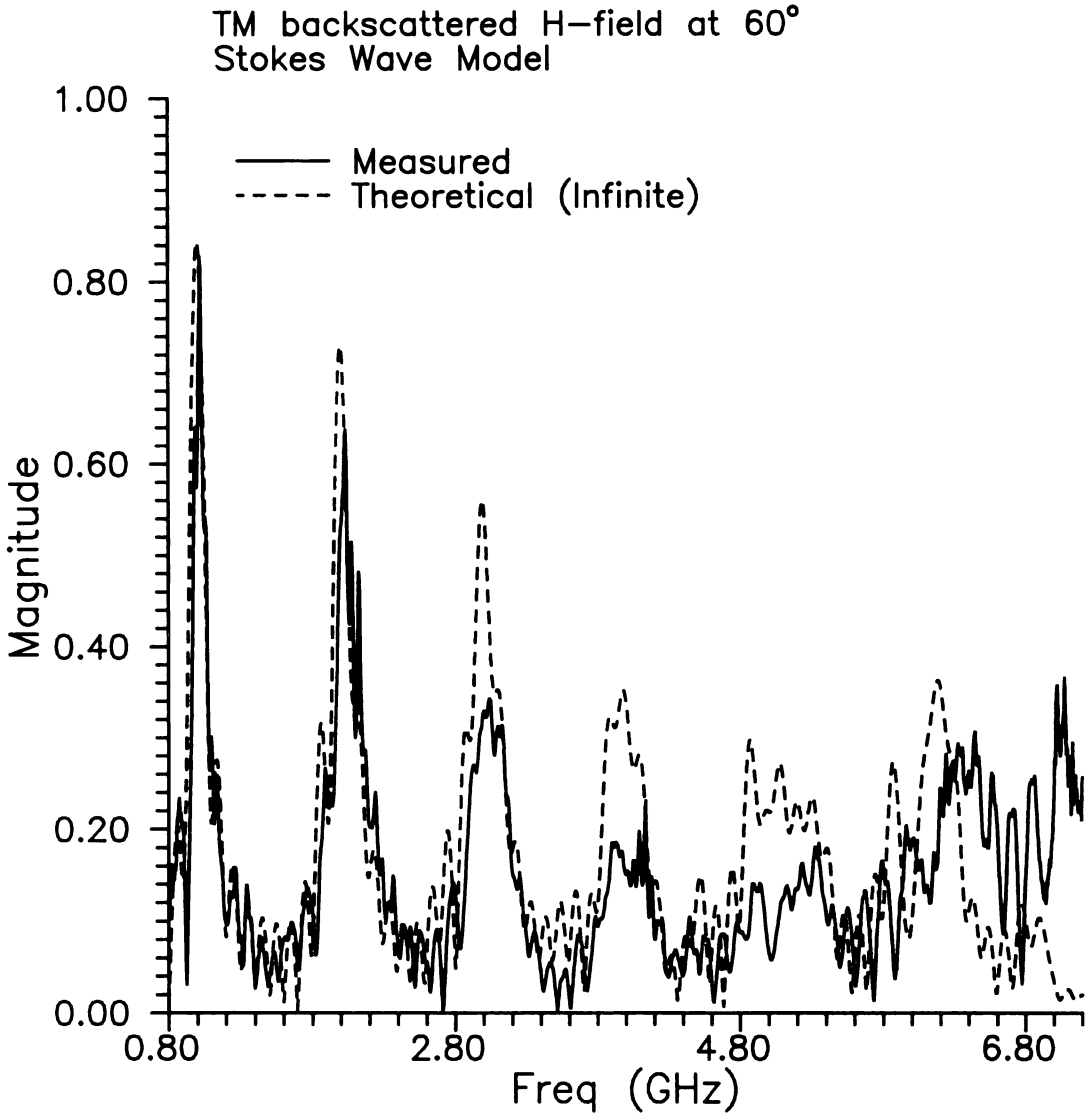

Figure 5.31 TM backscattered magnetic field for the Stokes wave model. Comparison of theoretical and measured responses for 60° incidence.

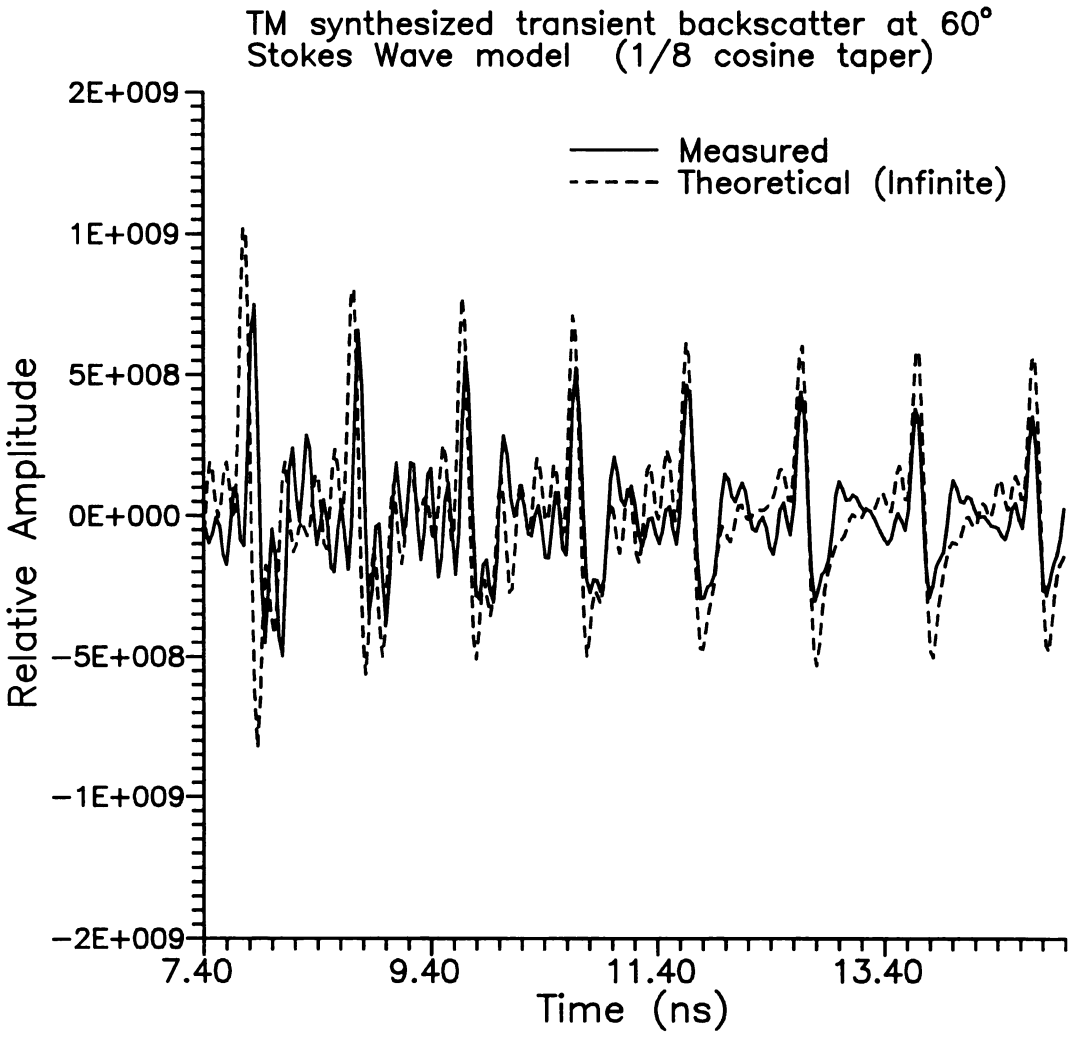

Figure 5.32 Synthesized transient TM backscattered magnetic field for the Stokes wave model. Comparison of theoretical and measured responses for 60° incidence.

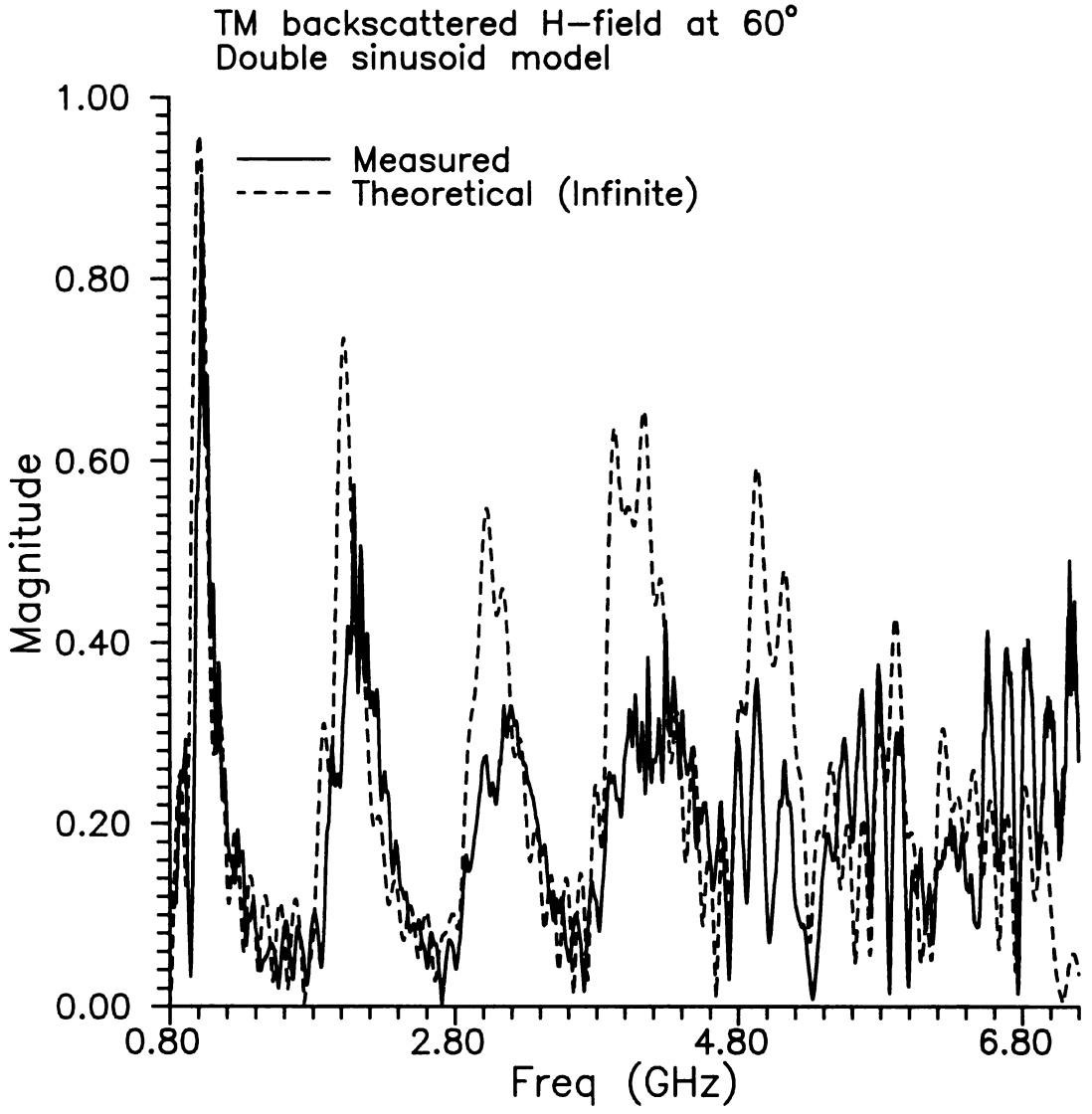

Figure 5.33 TM backscattered magnetic field for the double sinusoid wave model. Comparison of theoretical and measured responses for 60° incidence.

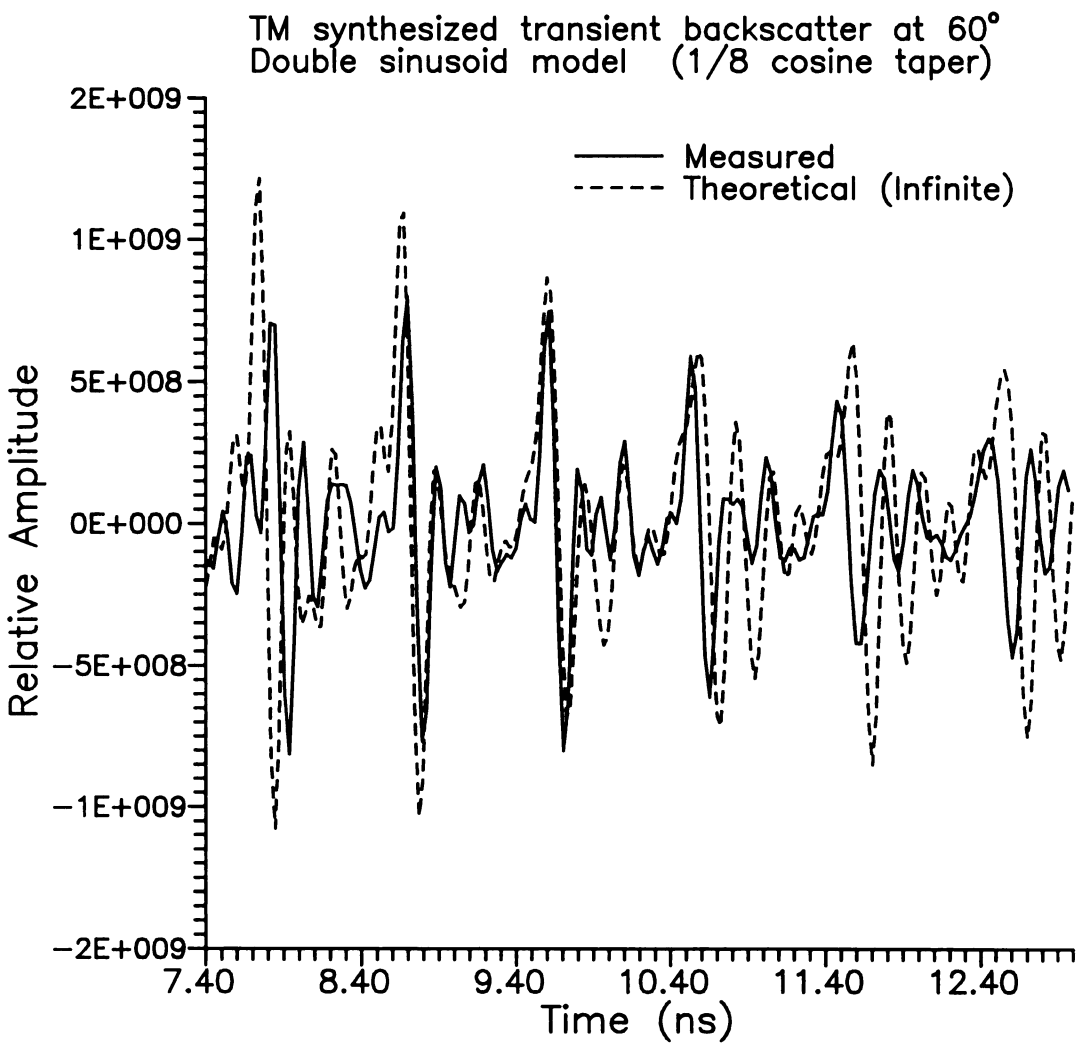

Figure 5.34 Synthesized transient TM backscattered magnetic field for the double sinusoid wave model. Comparison of theoretical and measured responses for 60° incidence.

5.6 Scattering from PEC surfaces for TE excitation.

In section 5.5 the scattered fields for TM pulse interrogation of the Stokes, double-sinusoid and Donelan-Pierson wave models were examined. This section contains the analogous TE excitation results. Since the wave models are PEC the scattered fields for both TE and TM excitations are similar. Therefore only brief explanations are needed in the discussions of the scattering mechanisms. The differences between the polarization states will be highlighted.

5.6.1 Experimental Results for TE Excitation.

The frequency and synthesized transient responses for the three wave models are shown in Figure 5.35 to Figure 5.38. The upper plot is the spectrum for various incidence angles and the lower plot is the corresponding transient response. These plots exhibit the same qualities and scattering mechanisms that were shown for the case of TM excitation in section 5.5.1. These results indicate the quality of the measurement system and reveal the resolution capabilities.

In Figure 5.39 is a comparison of the experimentally measured synthesized transient responses from the Stokes and double-sinusoid wave models. The near grazing angles are shown. The additional features (wave crests) are clearly visible in the double-sinusoid case. The double sinusoid exhibits considerably more structure (dark vertical bands) due to the two-scale roughness. However, the Stokes wave model has a more pronounced multiple scatter, which is evident in the trough regions. The trough regions of the Stokes wave are located between the sets of double dark vertical lines. There are two dark vertical lines for every crest, which represent the specular backscattered pulse. These two observations are intuitively satisfying and will be shown later to agree with the numerical results.

The spectra of the measured backscattered fields for the three wave models at a single incidence angle of 70° are shown in Figure 5.40. The Floquet-mode spikes are once again obvious for the two periodic wave models, while the Donelan-Pierson model

does not exhibit the strong spikes. The backscattered field from the Stokes wave model contains the most energy and this is most likely due to the high surface slope of that wave model.

In Figure 5.41 the corresponding synthesized transient results are compared. The time-domain signals are obtained by performing an Inverse Fast Fourier Transform (IFFT) after a Gaussian Modulated Cosine (GMC) window has been applied in the frequency domain. Only a portion of the transient results are shown in order to enhance the resolution of the plot. The plots reveal the differences between the three models. The Stokes wave has the largest return pulses (due to the large slope) and a multiple scatter can be observed in the trough. The multiple scatter spectral content is in the higher frequencies and could be enhanced in the time-domain with a different weighting function that emphasizes the higher frequencies.

The synthesized transient backscatter from the double sinusoid wave exhibits the scattering center reflections from all of the non-shadowed crests. There is also a multiple scatter that could be enhanced with a different weighting function.

The Donelan-Pierson wave has the smallest return amplitude; this is due to the orientation of the wave. The biggest crest was placed at the front edge, which effectively shadows the remaining crests. The return from the first hump is not shown, but is much larger than the other crests. The transient backscatter does indicate locations of scattering centers, which do match the physical surface shape.

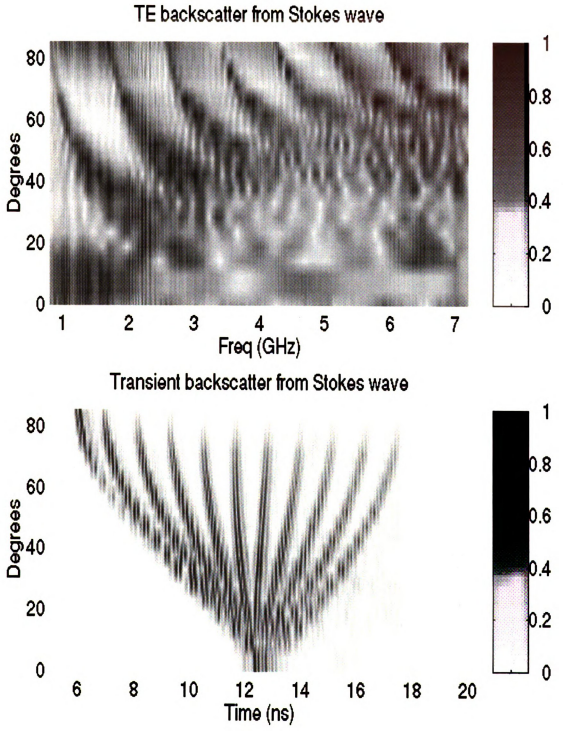

Figure 5.35 Angular dependence of TE scattered fields of the Stokes wave model.

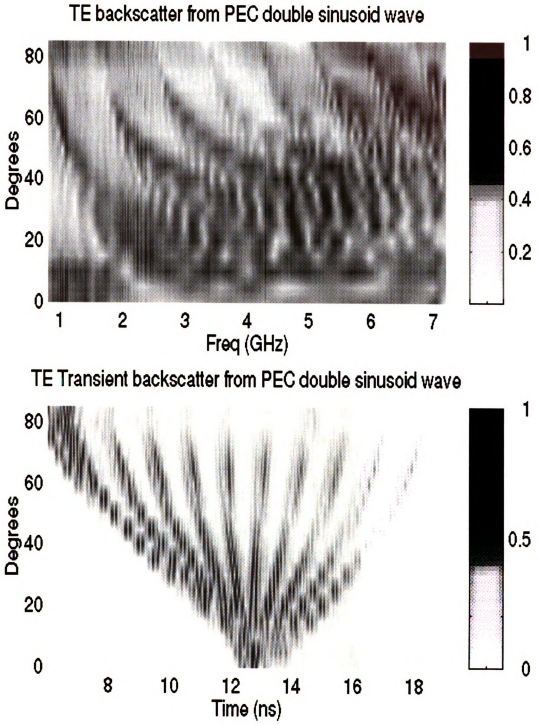

Figure 5.36 Angular dependence of TE scattered field spectrum of the double-sinusoid wave model.

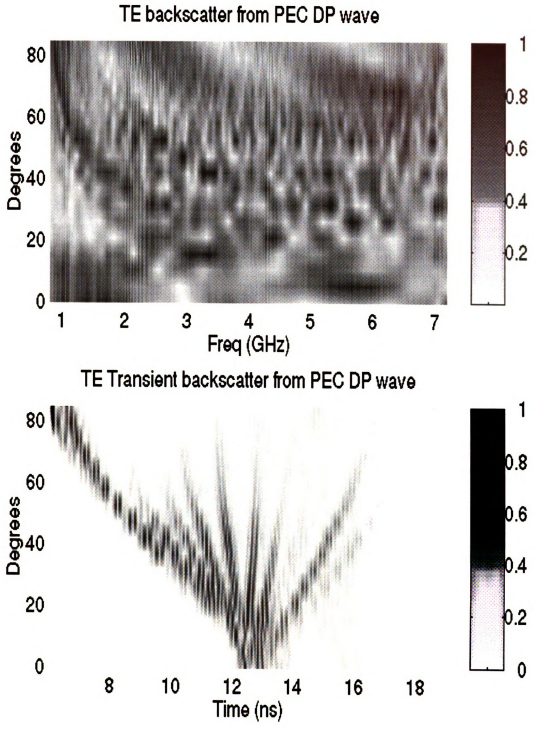

Figure 5.37 Angular dependence of TE scattered fields of the Donelan Pierson wave model.

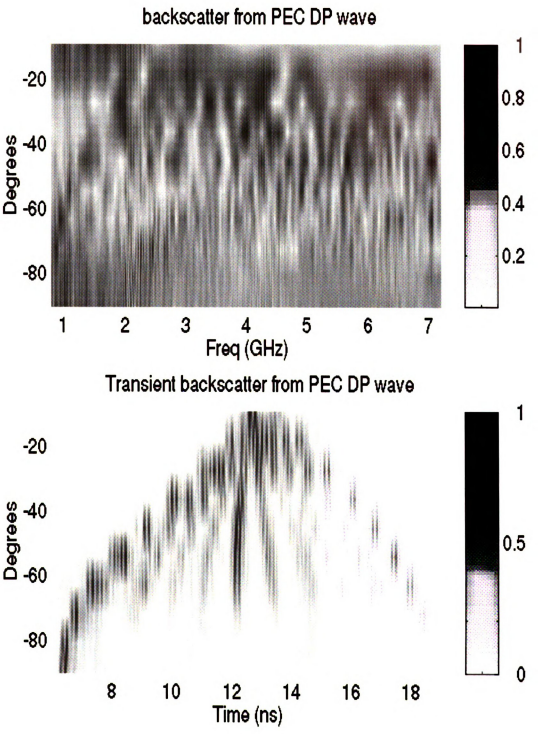

Figure 5.38 Angular dependence of TE scattered fields of the Donelan Pierson wave model.

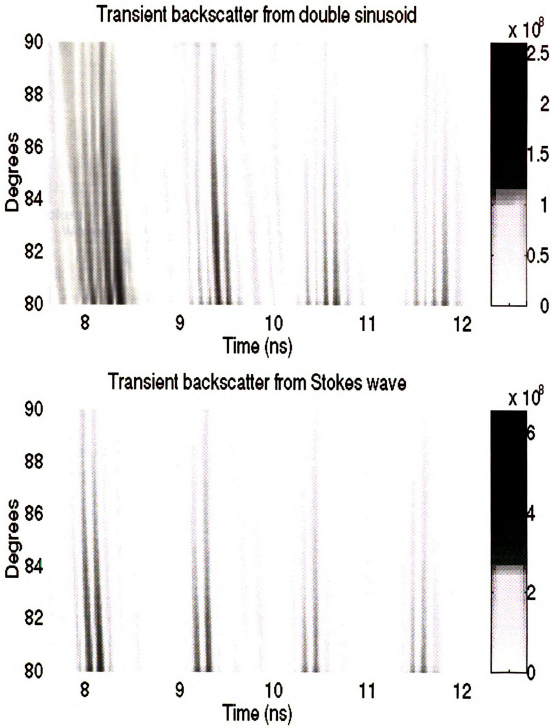

Figure 5.39 Comparison of synthesized transient scattering from the Stokes wave and double sinusoid wave for near grazing incidence angles.

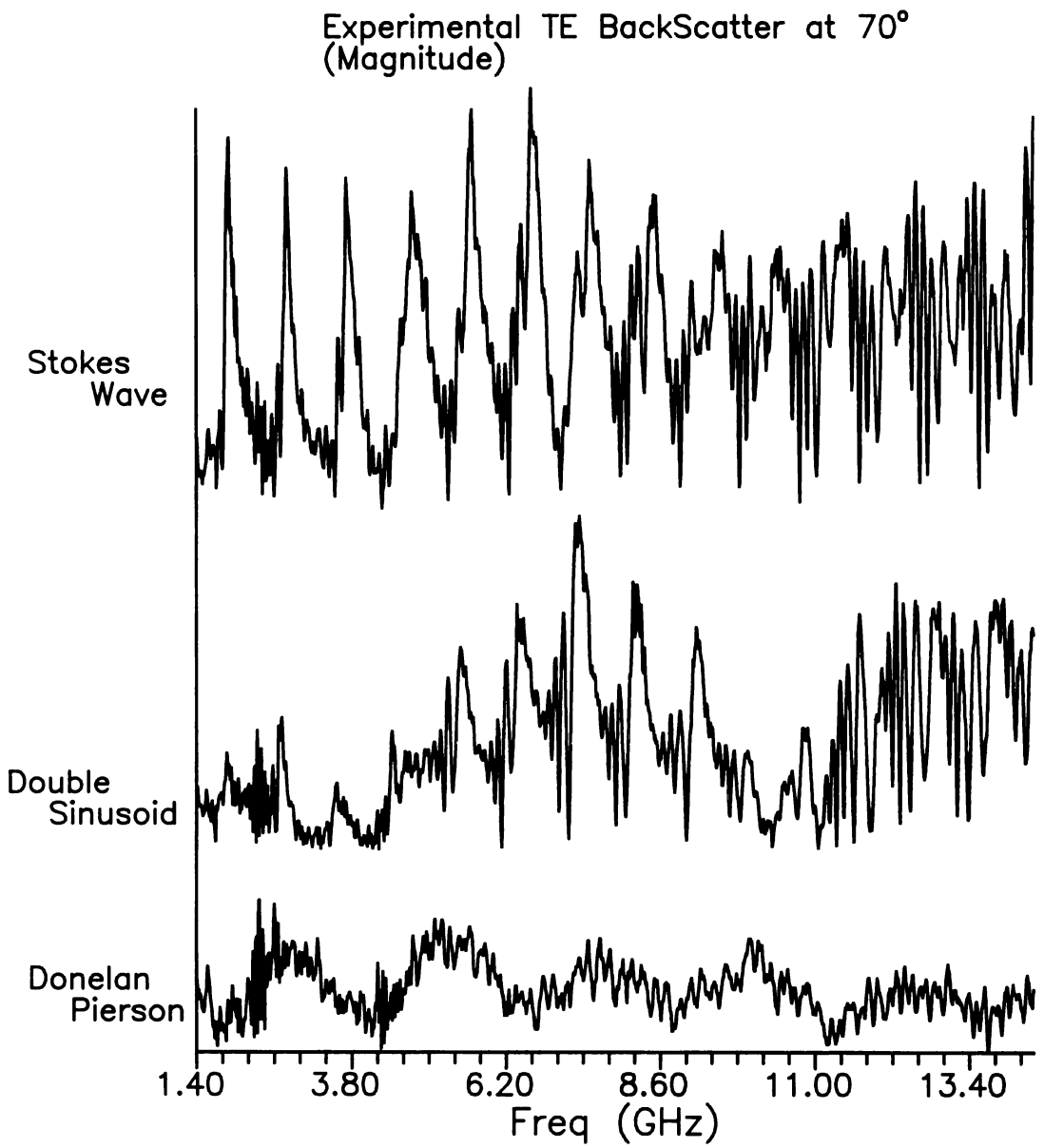

Figure 5.40 Experimental TE scattering from various wave models for an incidence angle of 70°.

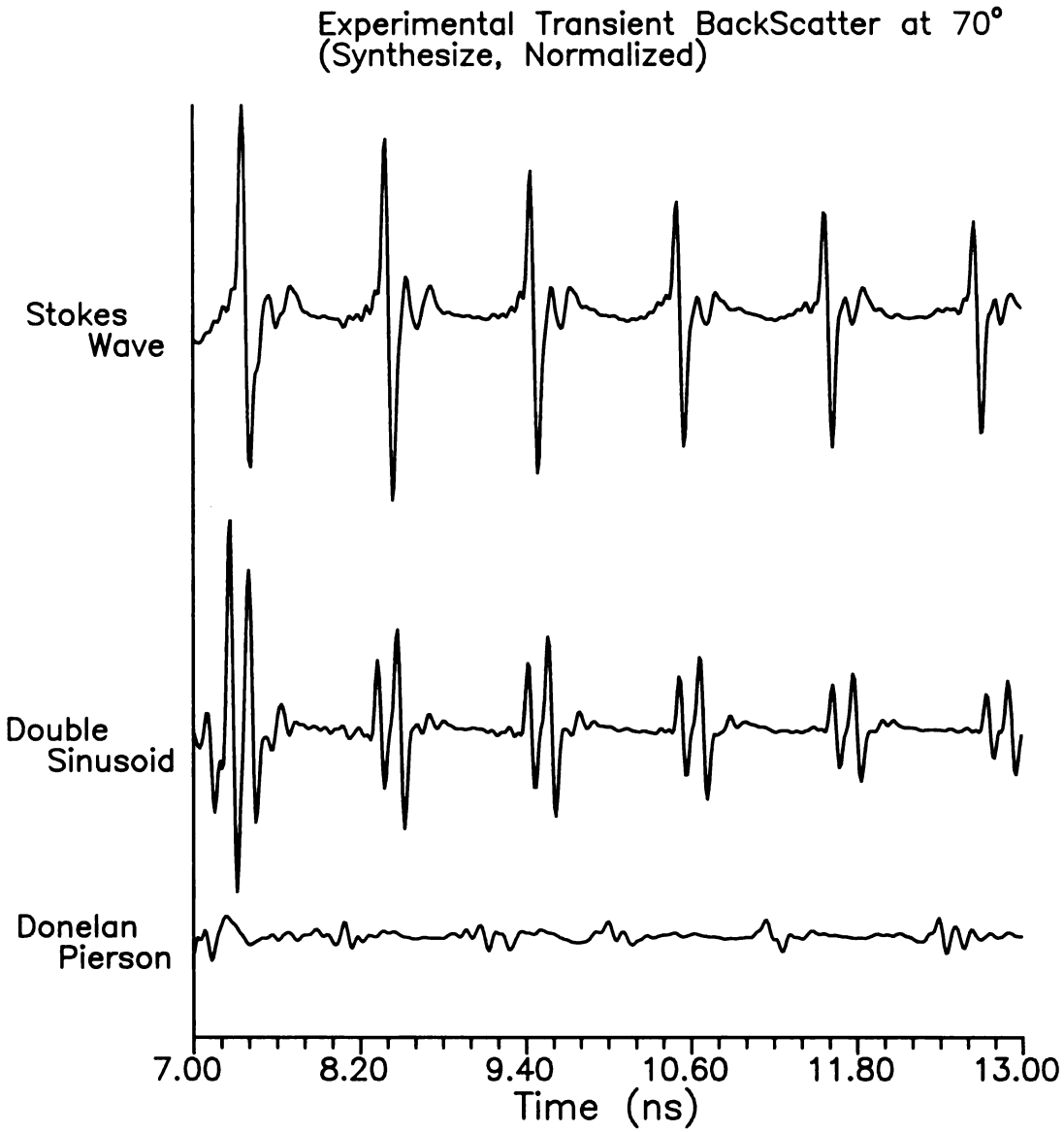

Figure 5.41 Experimental synthesized transient TE scattering from various wave models for an incidence angle of 70°. GMC weighting applied to spectrum before IFFT.

5.6.1a Measurements performed in time domain

The synthesized transient results discussed so far are all of very-large bandwidth (i.e. very-short pulse). The method of frequency domain synthesis works extremely well for stationary (non-time varying) targets, but is less effective for non-stationary targets. A true short-pulse radar can be just as effective on non-stationary targets provided the bandwidth is the same. As explained in section 5.5.1a, the time-domain system at MSU lacks the large bandwidth of the synthesis system. However, that bandwidth is large enough the make some useful and validating comparisons.

Figure 5.42 compares the transient and spectral returns for both the time-domain and frequency-domain systems. The Stokes wave model was used for this comparison. The effective bandwidth of the PPL pulse generator is from DC to roughly 2 Ghz, and the radar horns are effective down to around 0.5 Ghz. In Figure 5.42 the spectral returns are compared for both methods, with the time-domain measurement transformed using the FFT. The agreement between the two methods is excellent over the bandwidth of 0.5-2.0 GHz. The large spike at 2.1 GHz is caused by calibration performed outside of the pulse generator's effective bandwidth. Similar agreement can be seen in the transient results. In this case a GMC window was applied to both spectra and then transformed to the time domain. The transient results are seen to contain 11 return pulses. The first pulse is due to the leading edge of the wave model and the remaining 10 pulses are from the wave crests and are separated by the two-way transit time between neighboring crests.

The backscattered field spectra for double-sinusoid and Stokes wave models are compared in Figure 5.43. The measurement was performed using the frequency-domain system. The comparison reveals that the same low-frequency effect that was observable in the theoretical results is present in the measurements. The effect is that the lower frequencies can only "see" the fundamental harmonic of the double sinusoid model. The

fundamental harmonic of the double-sinusoid model is the same as the Stokes wave period and therefore the spectra are very similar.

The results for the transient backscatter response from double-sinusoid wave model are shown in Figure 5.44. The agreement is once again very positive. These results help to confirm the validity of the synthesis method and provide support for the future use of short pulse radar.

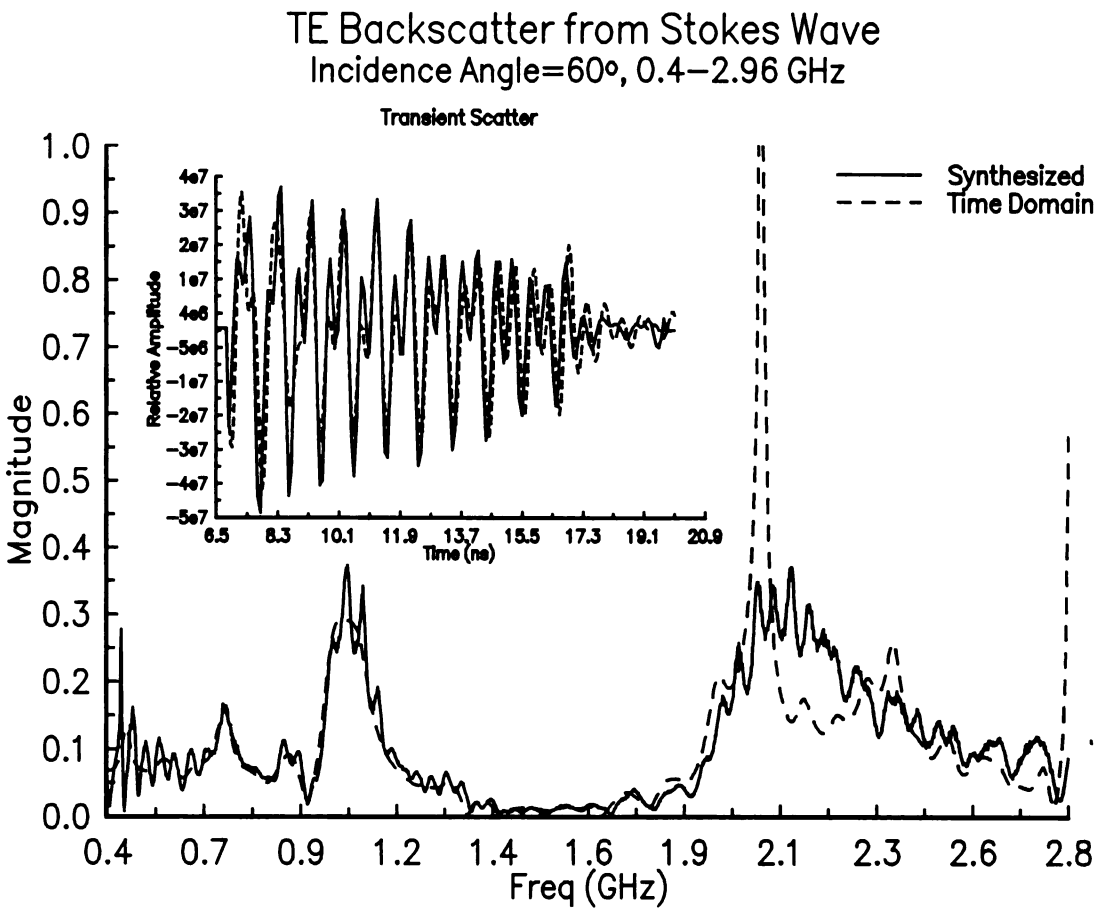

Figure 5.42 Comparison of frequency-domain synthesis measurement with time-domain measurement. Both spectral and transient returns for Stokes Wave interrogated at 60°.

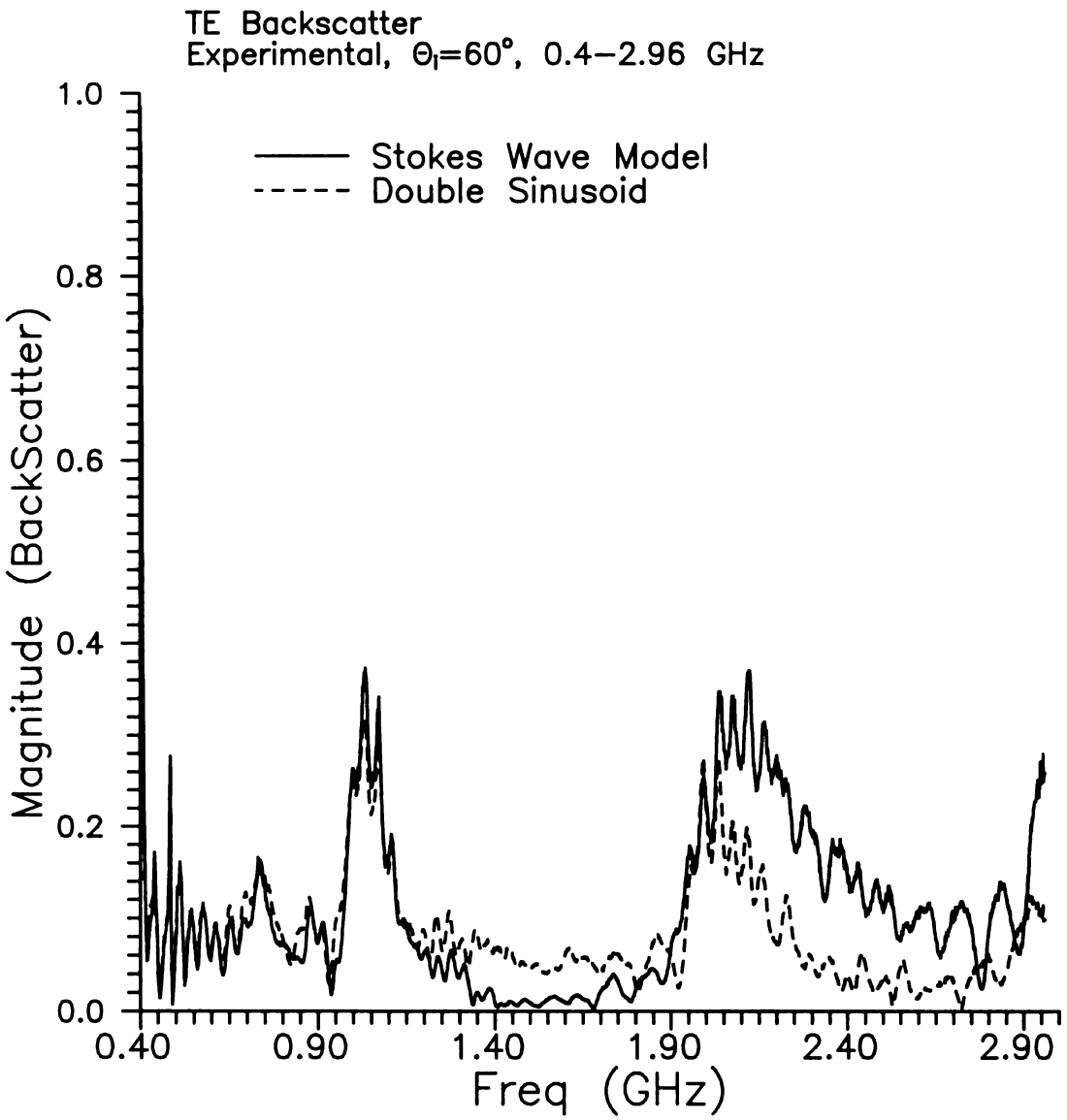

Figure 5.43 Spectra of TE backscatter response for the Stokes and double sinusoid wave models. Measurements were performed using the frequency-domain technique.

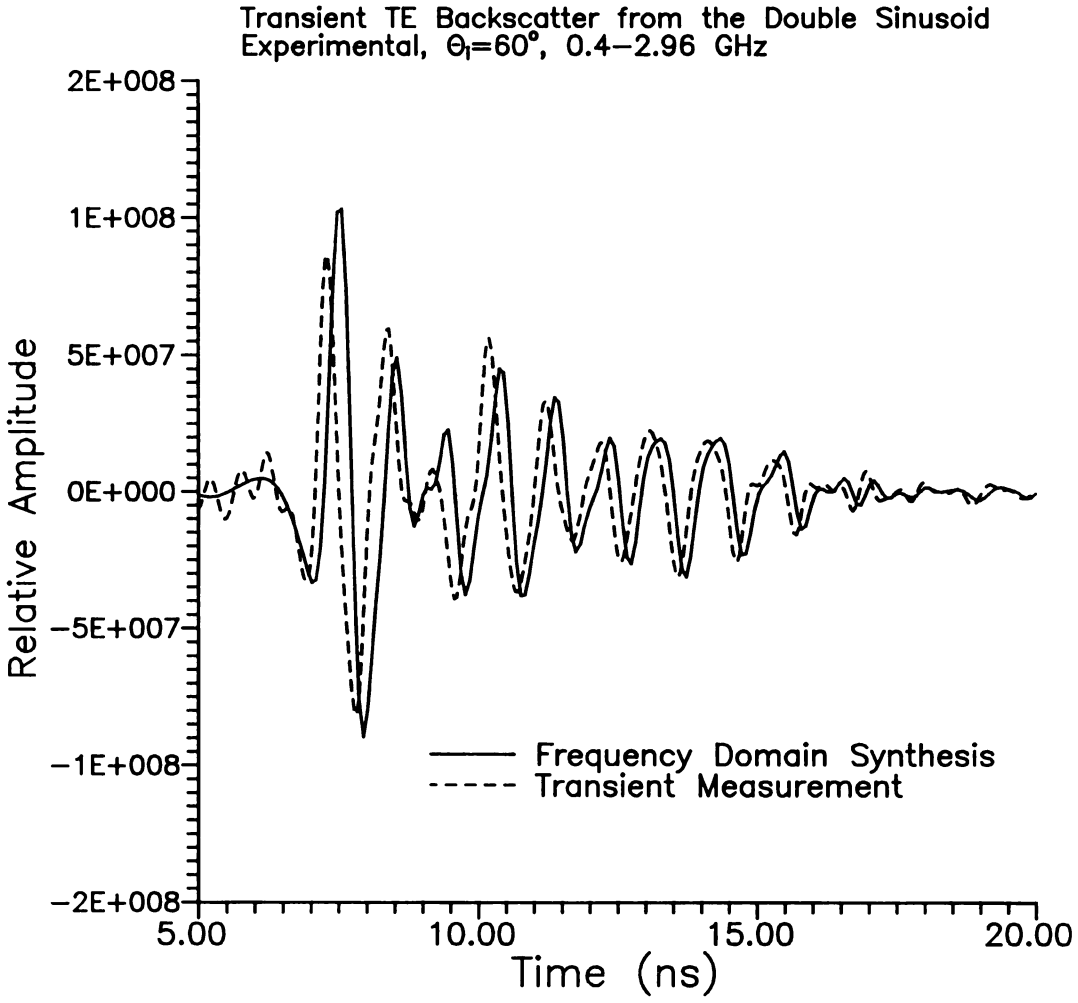

Figure 5.44 Transient TE backscatter response for the double-sinusoid wave model. A comparison of frequency-domain synthesis the time-domain techniques.

5.6.2 Theoretical Results for TE Excitation.

The synthesized transient backscattered fields for the Stokes wave and the double-sinusoid wave are shown in the following figures. The results were computed assuming an infinite PEC surface and utilizing the theoretical methods developed earlier in the chapter.

The transient backscatter from the Stokes wave model are shown in Figure 5.45 and Figure 5.46 for 85° and 60° incidence, respectively. In both figures the observation point is located at two differing heights. The transient backscattered fields depict the periodicity of the wave model as seen by the periodic return pulses. There is also a multiple scatter present in the trough regions between the specular reflections. It is quite interesting to note the difference that the observation point has on the backscattered fields. When the observation point is in close proximity to the wave crest the evanescent Floquet modes contribute to the backscattered fields. This was also noted in the sinusoidal wave models.

There are similar results for the double-sinusoid model. In Figure 5.47 and Figure 5.48 the transient backscattered fields from the double-sinusoid model are shown for the respective incident angles of 85° and 60°. There is a noticeable difference between responses for 85° and 60°. The increased effect of shadowing is evident for the 85° case. This can be seen in the strength of the specular reflections from the wave crests. There is also a prominent multiple scatter for the lower observation height.

The effects of spectral content are examined in Figure 5.49 and Figure 5.50. The synthesized transient backscatter from the double sinusoid wave for an increasingly narrower GMC window are shown in Figure 5.49. The incident pulse can be seen to become very narrow as τ becomes smaller, this results in enhanced resolution. In Figure 5.50 the effects of moving a constant τ GMC window (roughly 1.5 GHz wide) through the spectral response is shown. Different parts of the wave are more active for different frequency bands. For example, the lowest band produces scattering from the

main swell, but as the window is moved up in frequency (f_c increased) the small-scale ripples on the wave become more active and produce reflections.

The same time-frequency analysis is performed on the theoretical response from the Stokes wave. In Figure 5.51 the effect of GMC window width is shown and in Figure 5.52 the effect of GMC window center frequency is examined. The results for the Stokes wave model exhibit the same qualities that were seen with the double-sinusoid model. These results would simulate a less robust UWB/SP system. The loss in bandwidth (or resolution) has an obvious detrimental effect upon wave clutter identification.

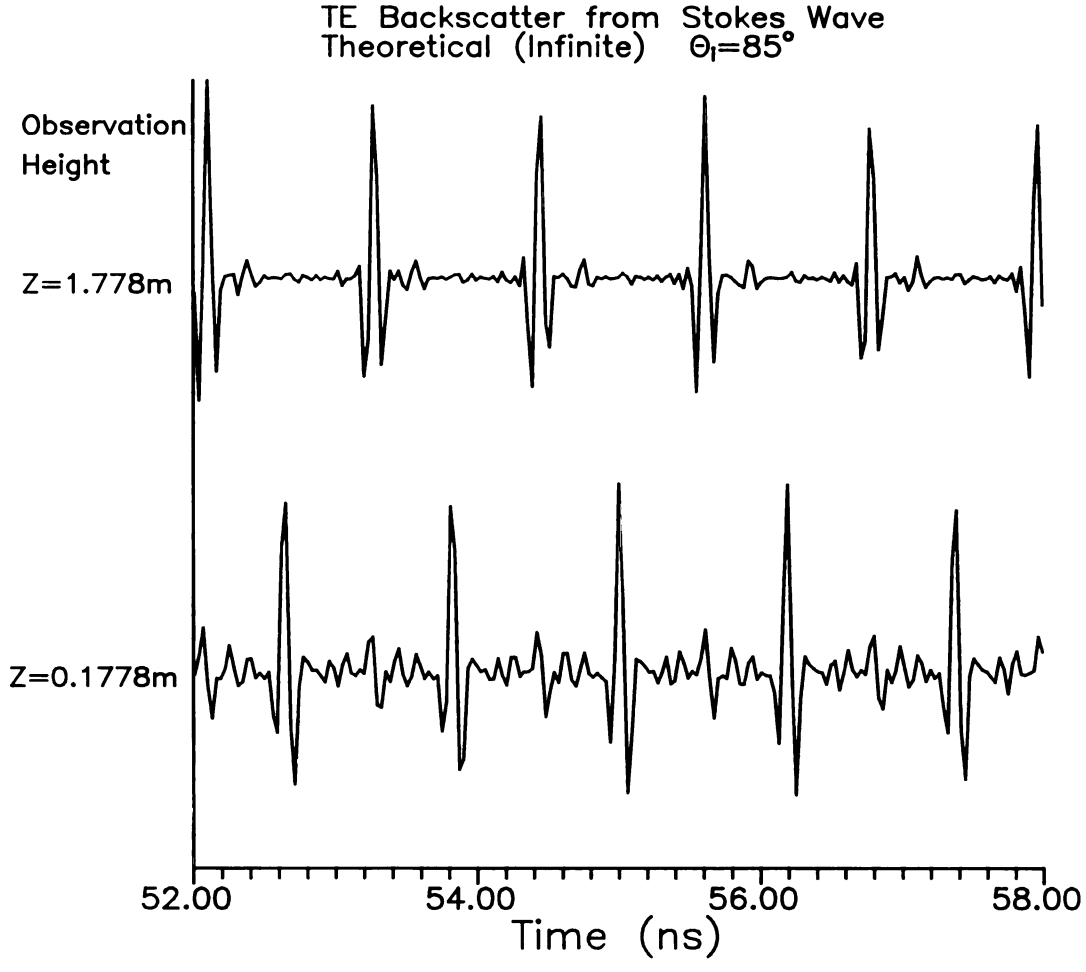

Figure 5.45 Theoretical synthesized transient TE backscattered fields from the Stokes wave model. The response at 85° incidence for two field points is shown.

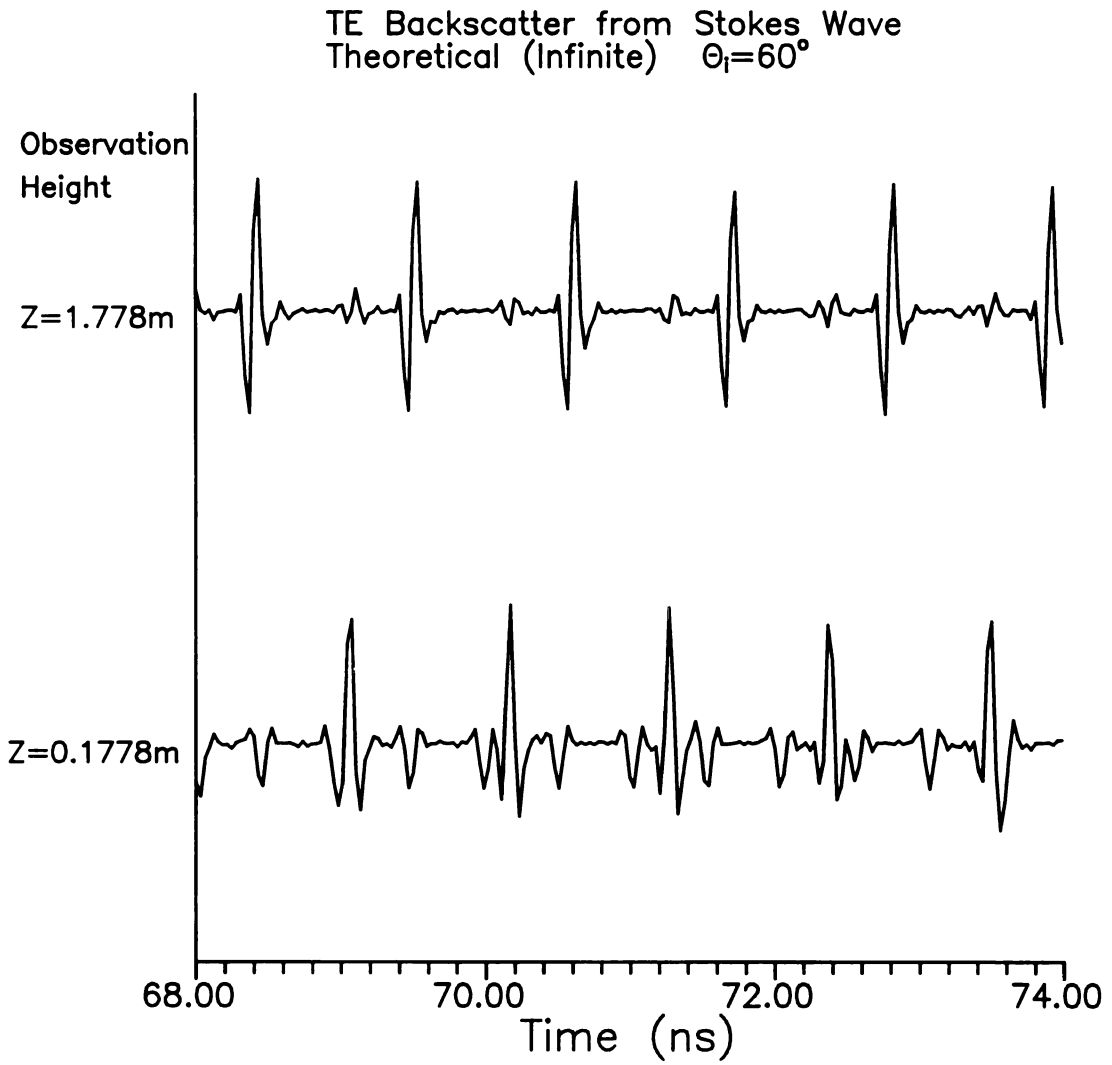

Figure 5.46 Theoretical synthesized transient TE backscattered fields from the Stokes wave model. The response at 60° incidence for two field points is shown.

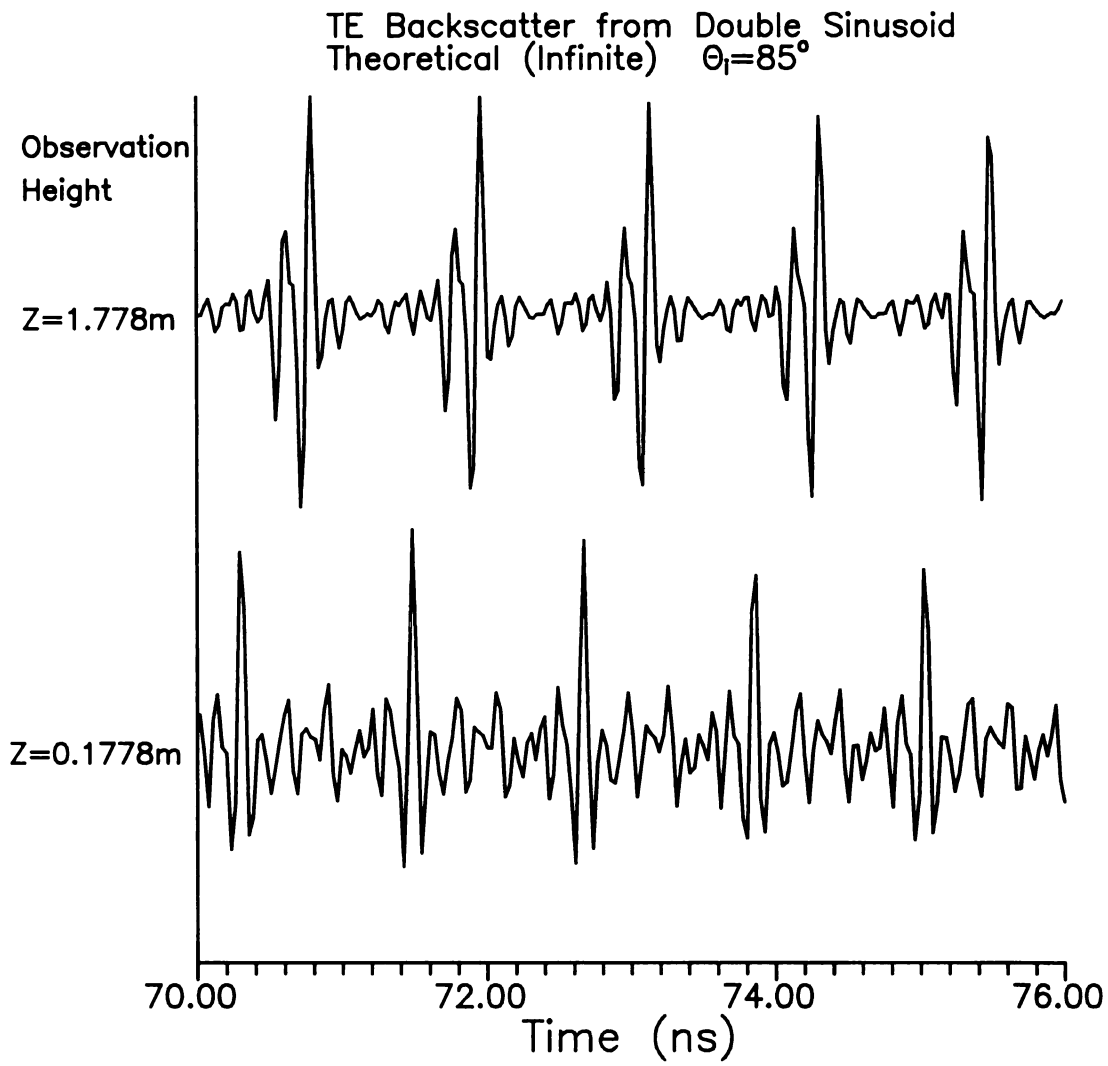

Figure 5.47 Theoretical synthesized transient TE backscattered fields from the double-sinusoid wave model. The response at 85° incidence for two field points is shown.

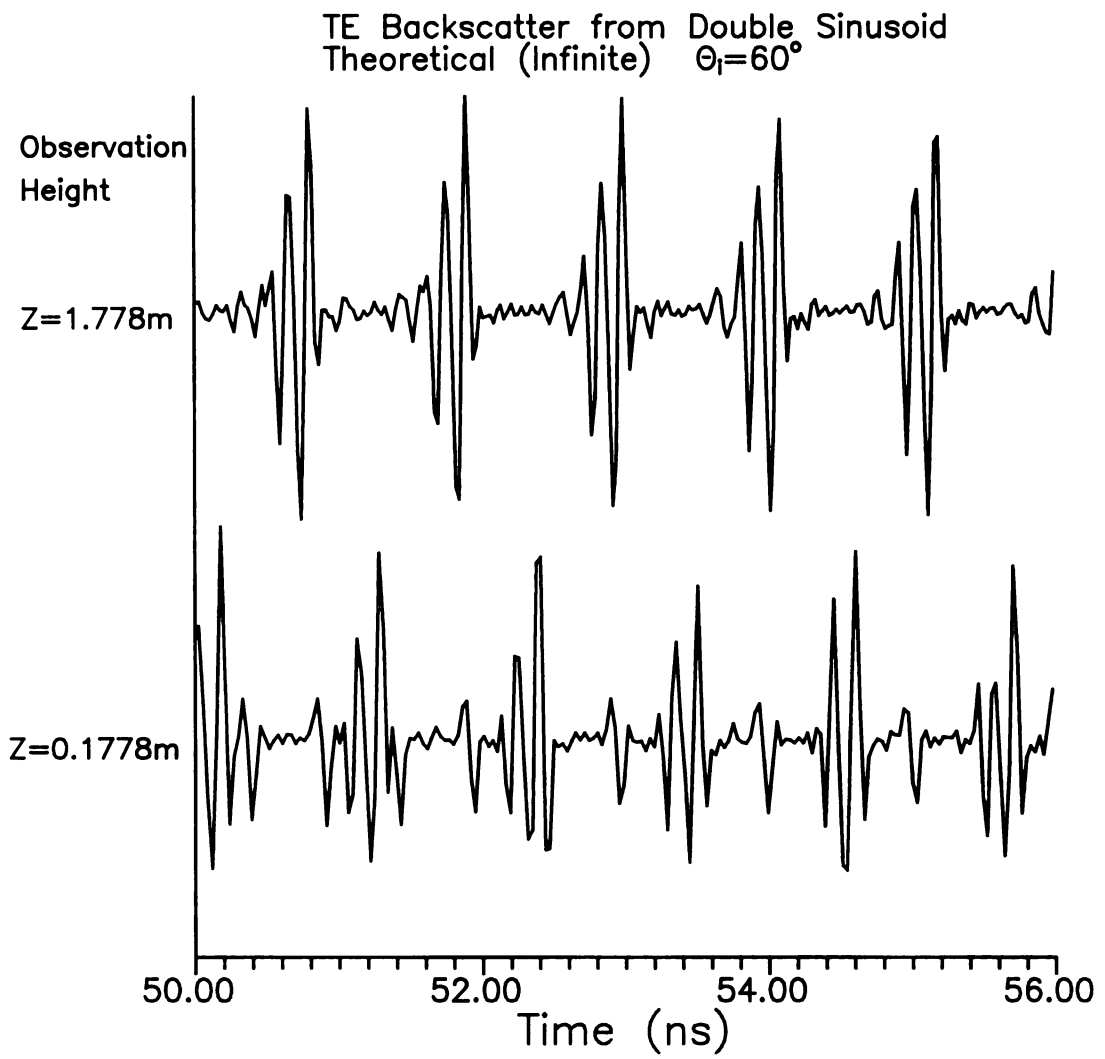

Figure 5.48 Theoretical synthesized transient TE backscattered fields from the double-sinusoid wave model. The response at 60° incidence for two field points is shown.

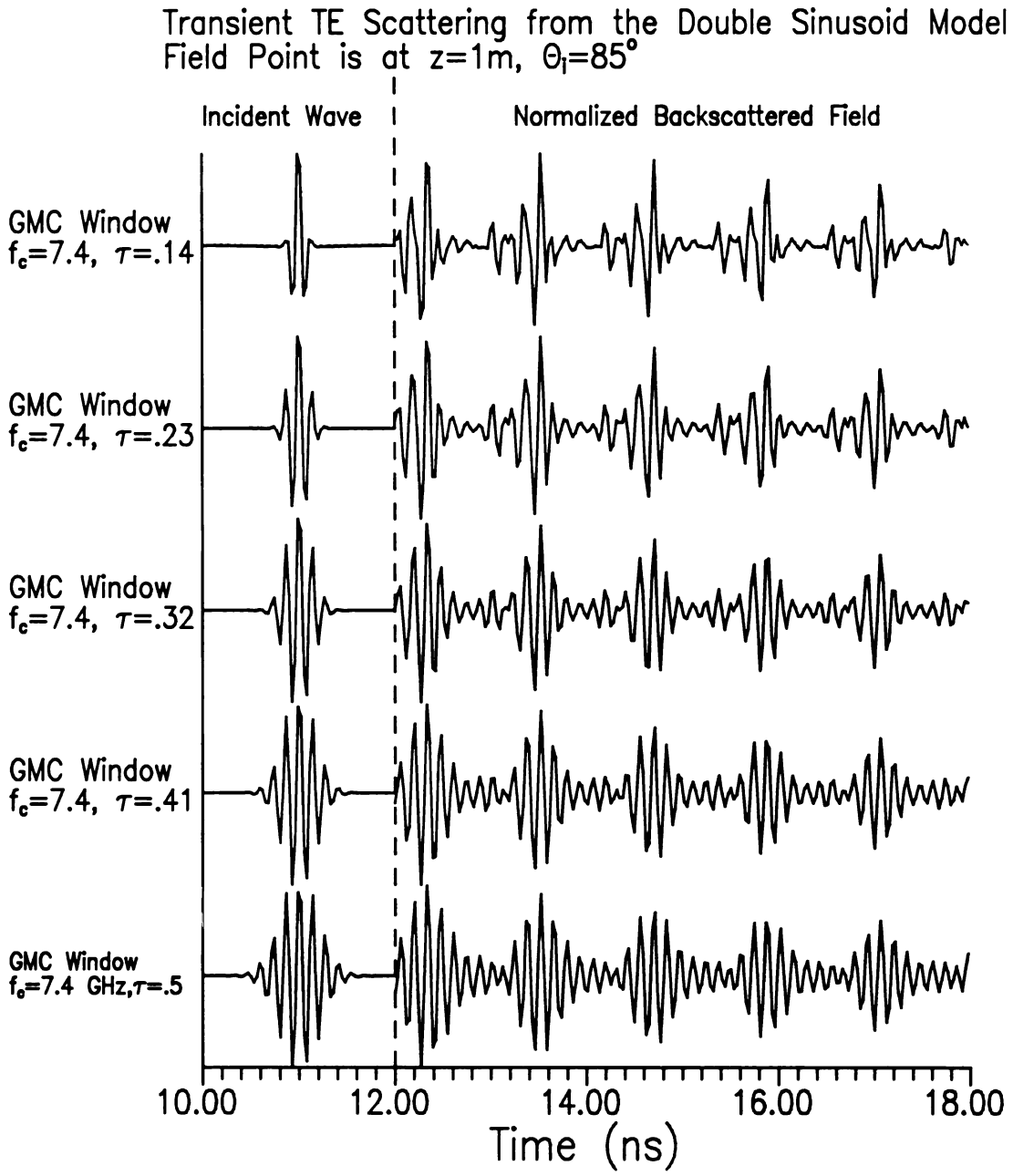

Figure 5.49 Theoretical transient scattering from double-sinusoid wave at 85°, with the effect of GMC window width examined.

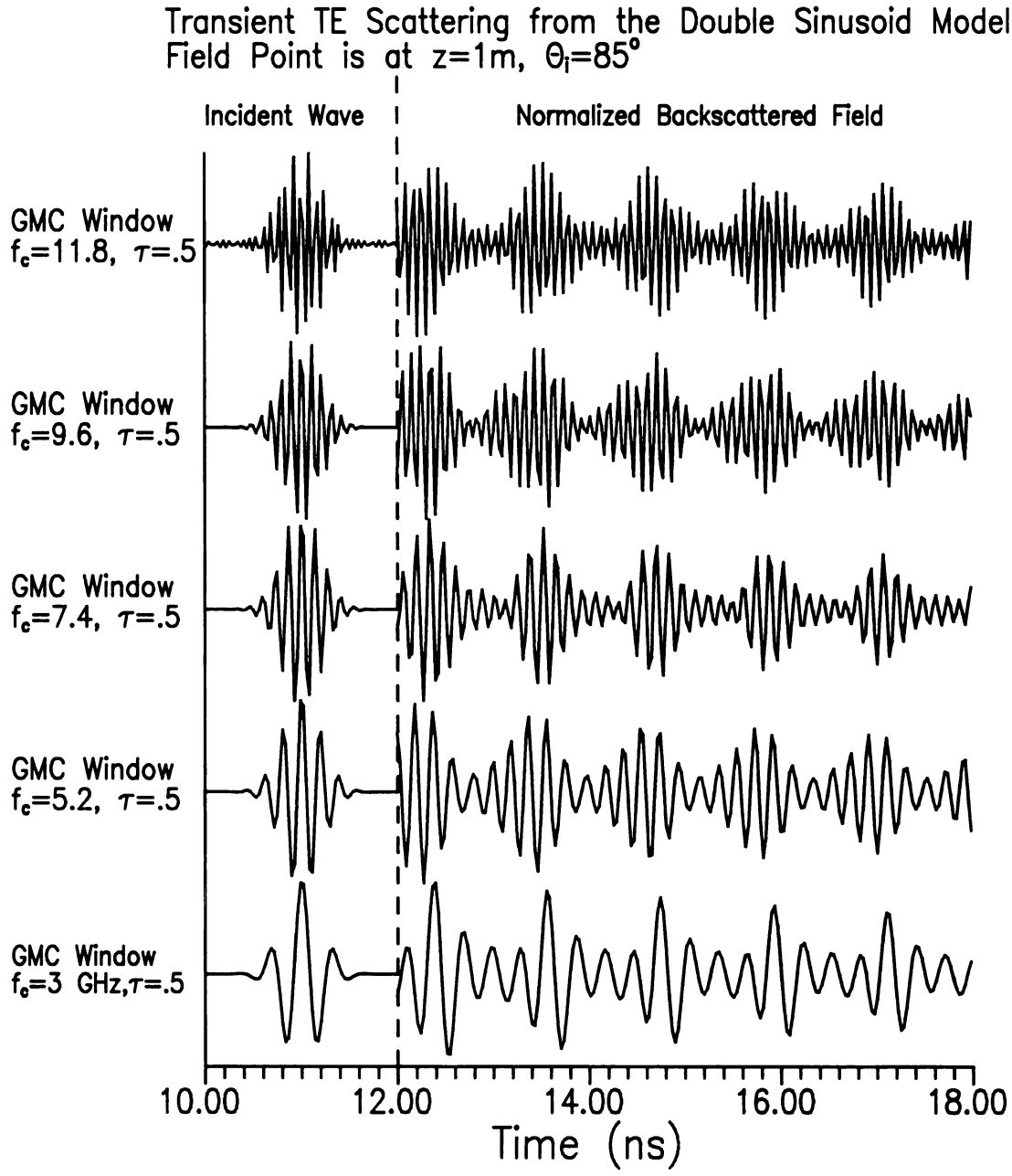

Figure 5.50 Theoretical transient scattering from double-sinusoid wave at 85°, with the effect of GMC window center frequency examined.

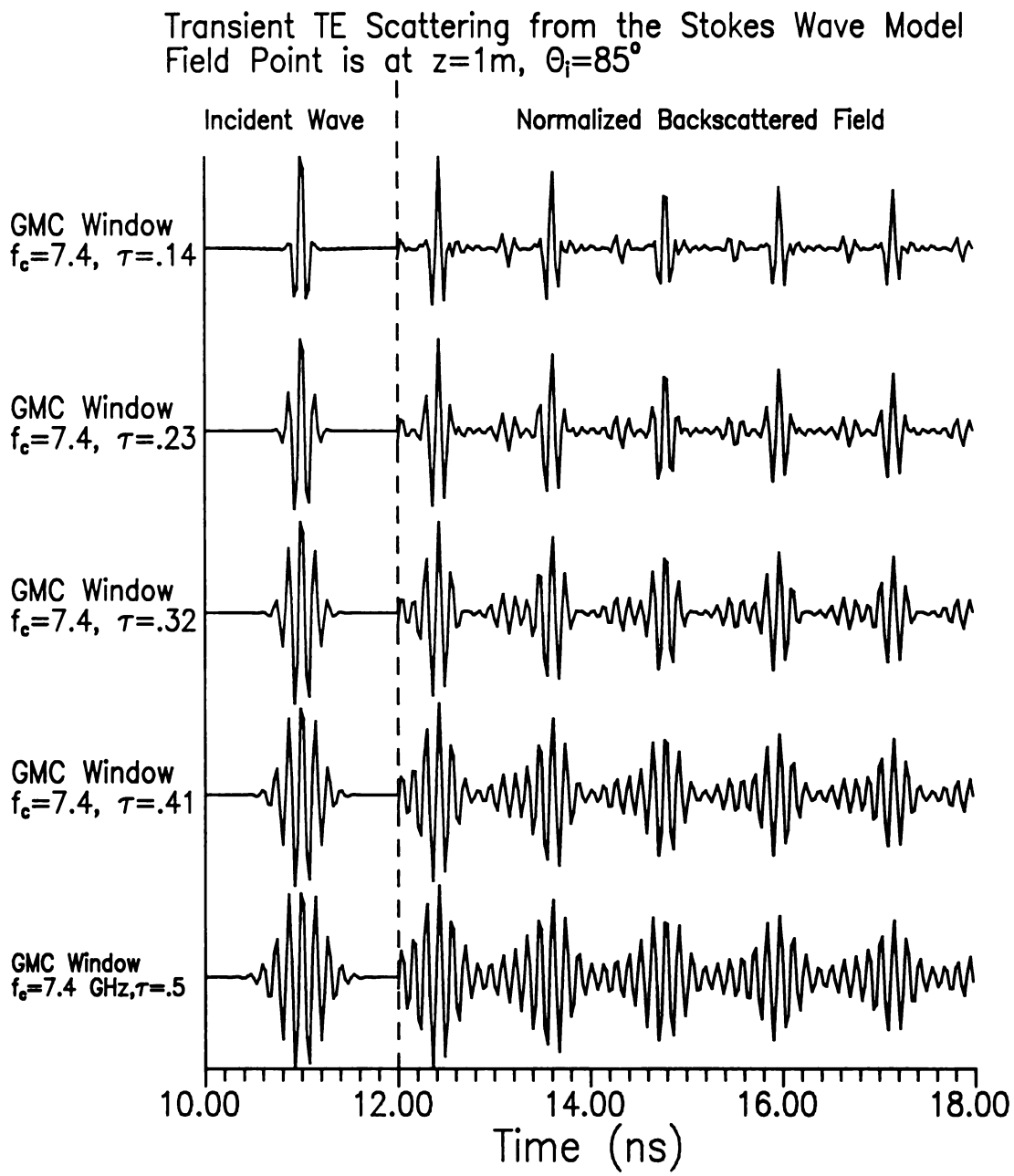

Figure 5.51 Theoretical transient scattering from Stokes wave at 85°, with the effect of GMC window width examined.

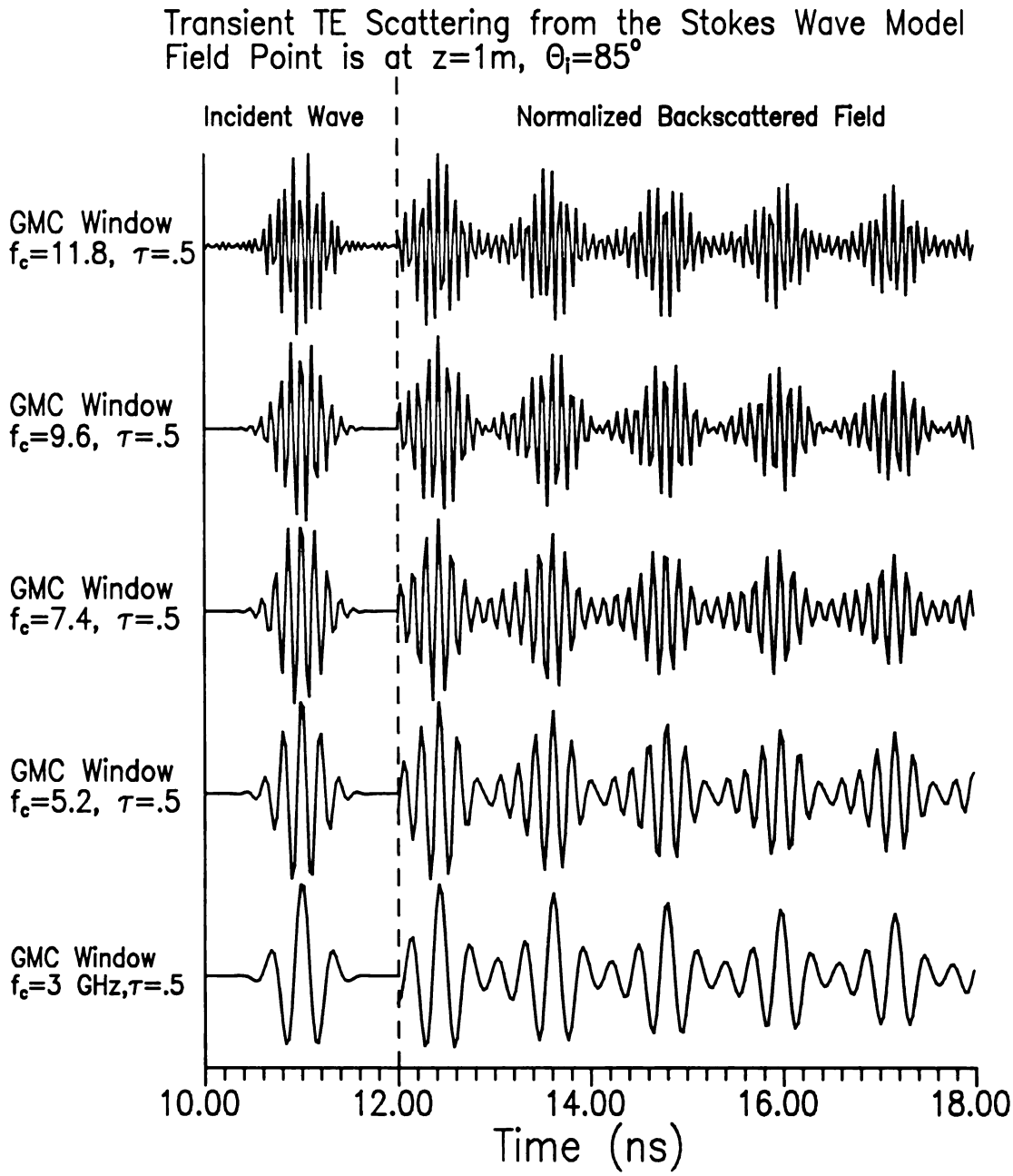

Figure 5.52 Theoretical transient scattering from Stokes wave at 85°, with the effect of GMC window center frequency examined.

5.6.3 Comparison/Evaluation of TE results.

As stated earlier, there is excellent agreement between the theoretical and the experimentally measured backscattered fields. In Figure 5.53 the synthesized transient backscatter from the Stokes wave model is examined. Only a few periods of the wave are shown, but there is very good agreement between the theoretical (infinite periodic surface) backscatter and the frequency-domain synthesis measurements. These results were obtained by weighting the spectral response with a GMC then transforming into the time-domain. Although not shown, the theoretical transient backscatter from the finite model also matched well with the measured data.

In Figure 5.54 the spectral returns are compared. Once again there is excellent agreement. The peaks are due to the periodicity of the wave (Floquet modes) and are slightly spread out due to the apparent period change as viewed from the field point. The theoretical backscatter from the finite length surface did not exhibit this spreading, due to the use of the far-field approximation.

The double sinusoid wave is considered next, and once again there is a strong agreement between the theory and the measurements. In Figure 5.55 the synthesized transient backscatter is compared. The additional wave structure is evident and accurately depicted by the theoretical results. The spectral returns are not shown but are also in good agreement.

The synthesized transient backscatter from the Donelan Pierson wave is compared with the theoretical backscatter from a finite wave. The infinite (periodic) theory can not accurately model the backscatter due to the large shadow produced by the first crest. The finite theory does a fairly good job as seen in Figure 5.56, but due to the far-field approximation the two-way transit times between crests are not accurately depicted. The spectral comparison is also hampered by the far-field approximation, but does show general agreement.

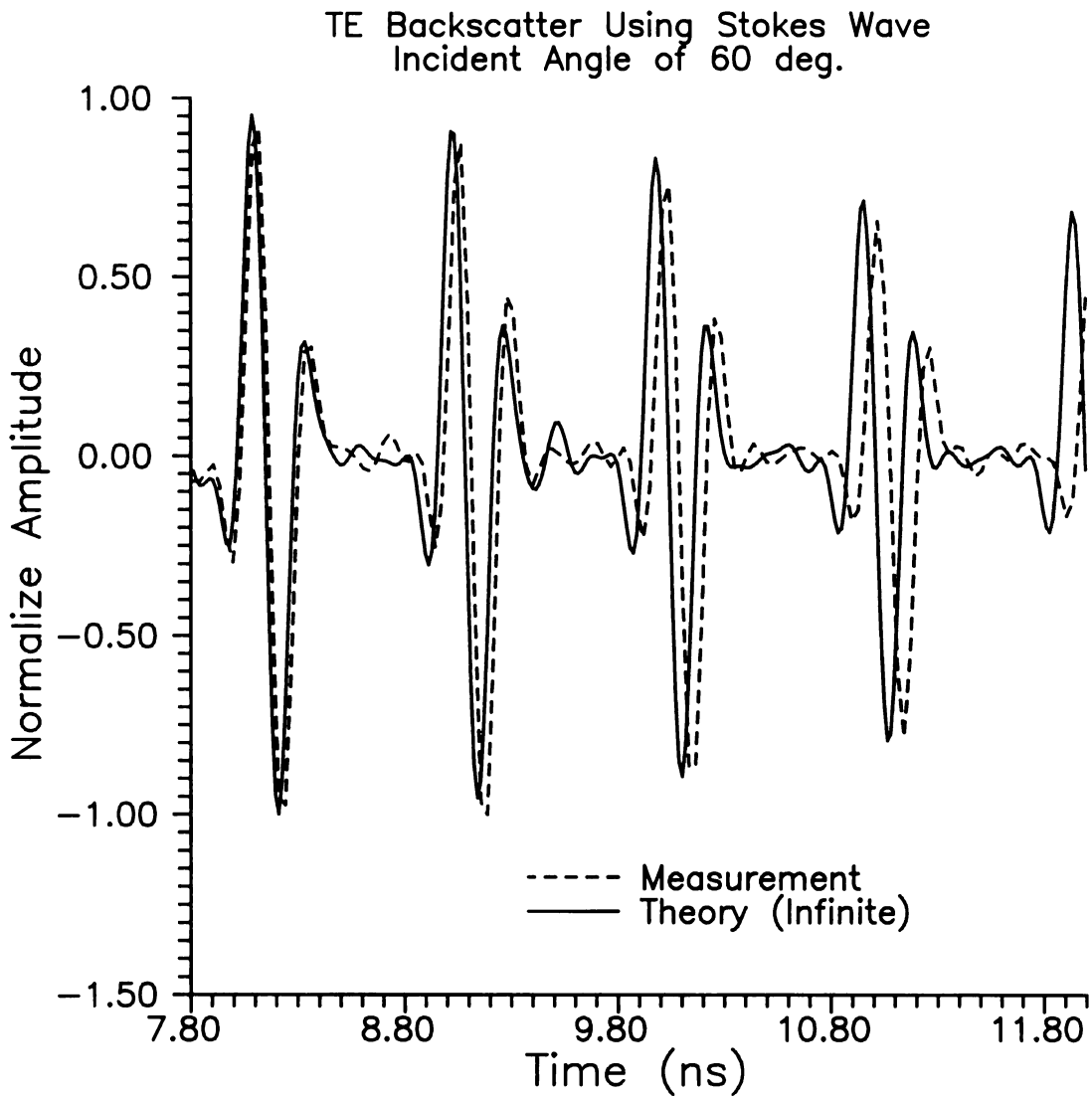

Figure 5.53 Comparison of synthesized transient scattering from Stokes wave with theoretical transient scattering at 60°. Using 0.8-7.2 GHz GMC windowed spectral content.

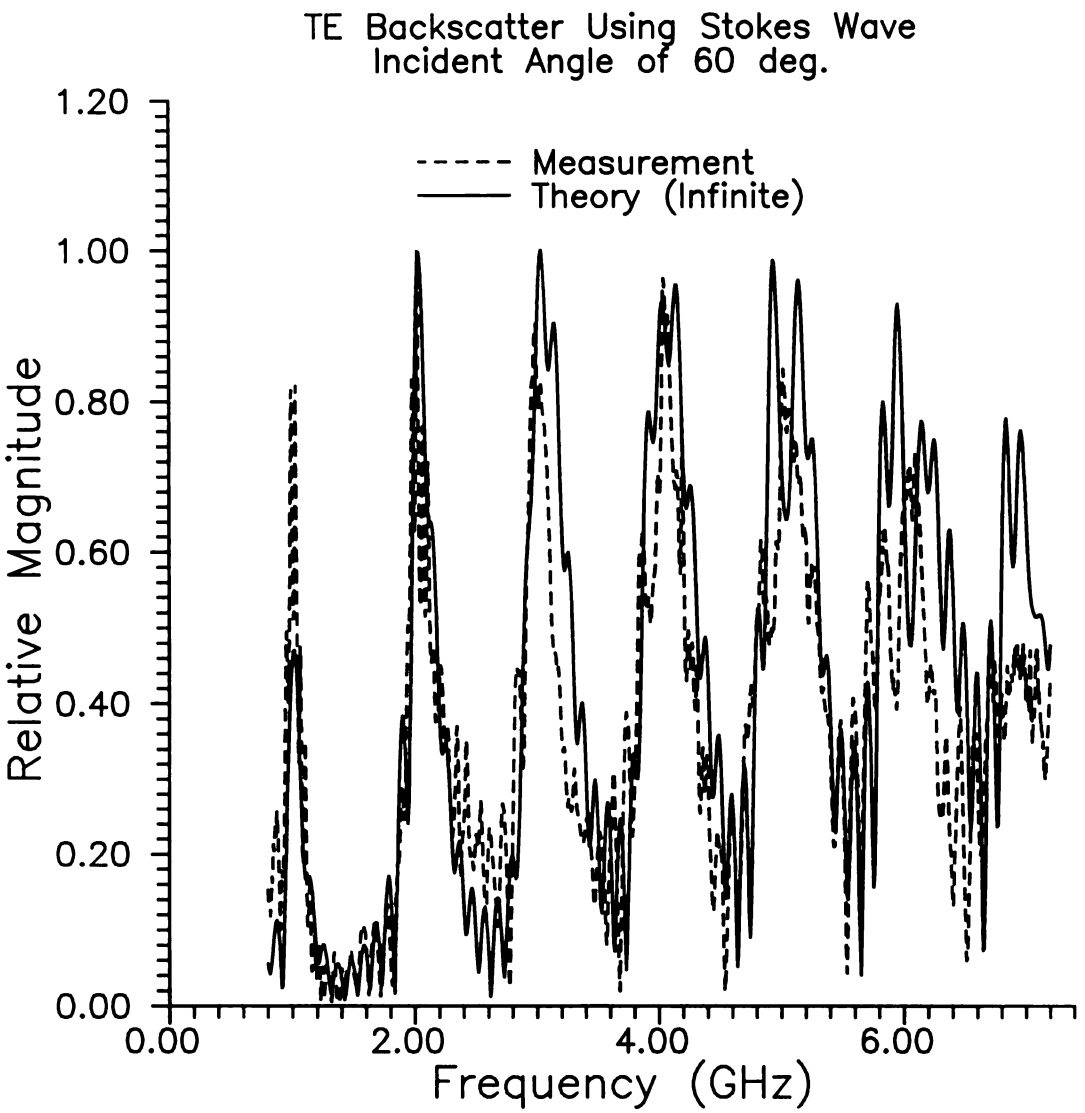

Figure 5.54 Comparison of TE scattering from Stokes wave with theoretical scattering at 60°.

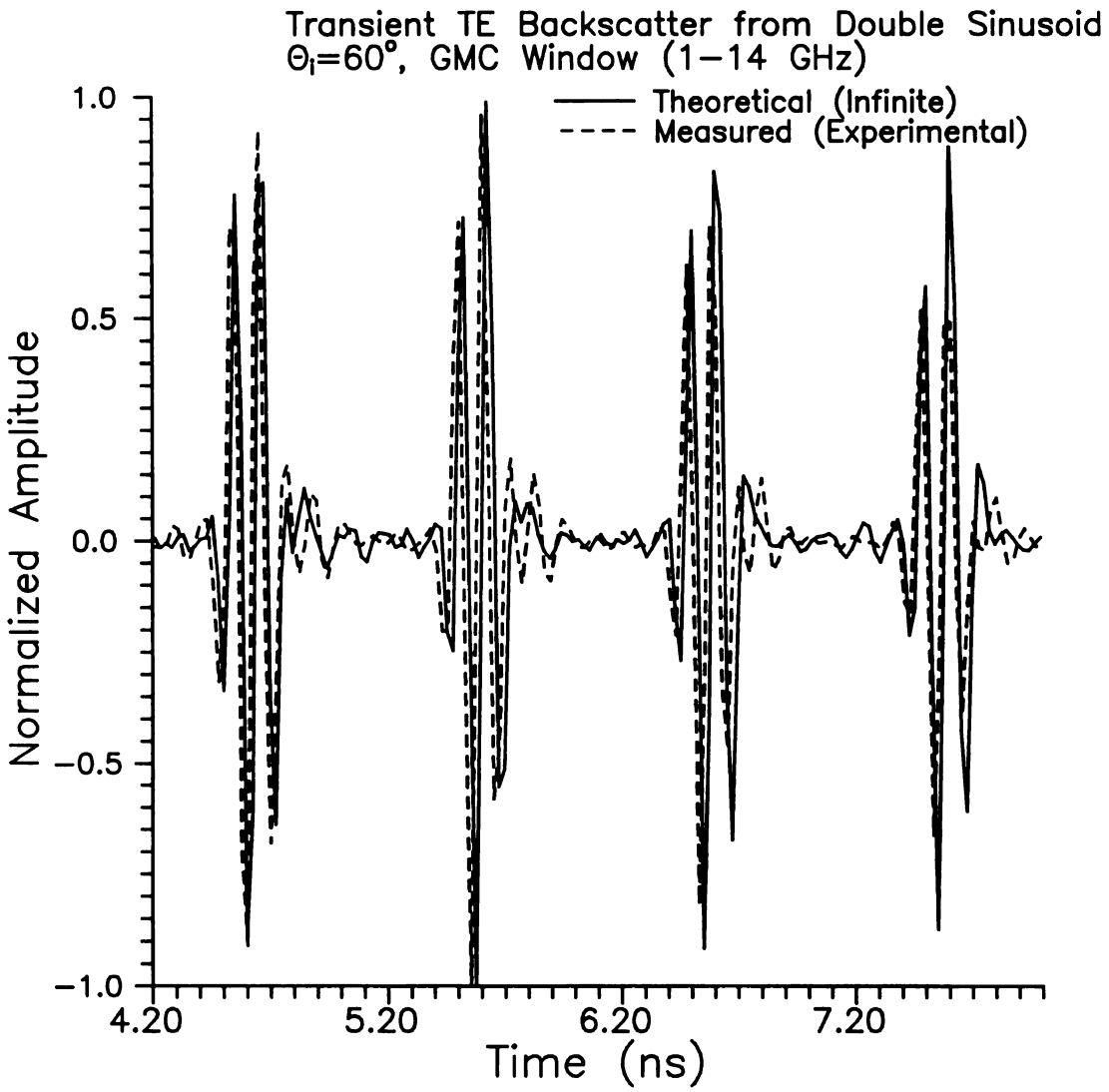

Figure 5.55 Comparison of theoretical and measured transient scattering from the double-sinusoid wave. Angle of incidence is 60°.

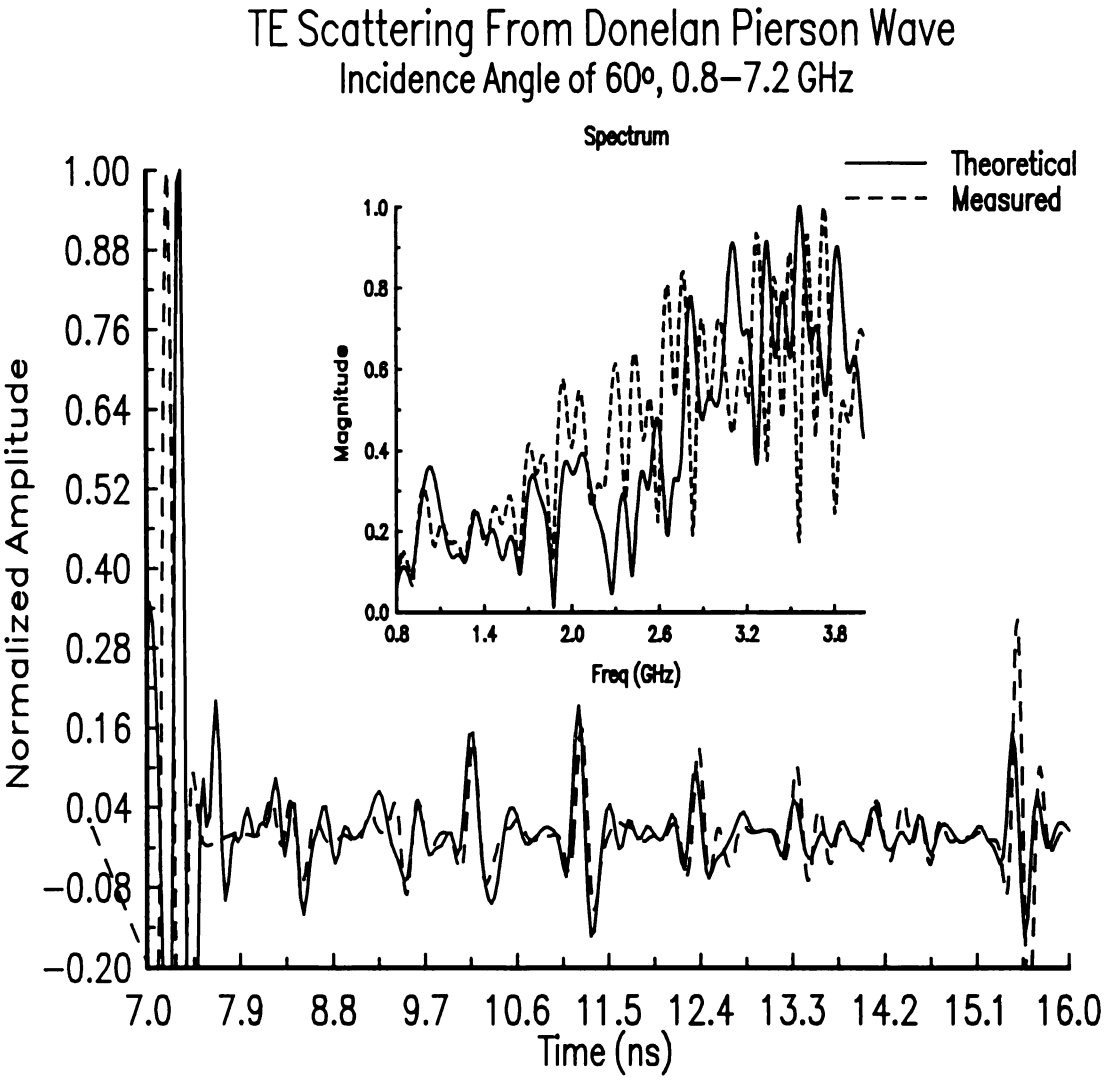

Figure 5.56 Comparison of theoretical and measured scattering from the Donelan Pierson wave. Angle of incidence is 60°.

5.7. Conclusions

The experimental measurements presented in this chapter help to validate the theoretical techniques, and they offer new insights into the scattering from these surface models. The time-frequency nature of the scattering was only qualitatively discussed and will be examined in detail in the future. The identification and analysis of scattering mechanisms was possible through the use of UWB/SP radar on the specifically chosen sea-surface models. These mechanisms include scattering centers (or specular reflection), multiple scattering and sub-structure scattering. The increased bandwidth of the UWB/SP radar scheme is the crucial factor in the improved resolution.

The transient backscatter obtained by the frequency-domain synthesis technique was seen to agree with the true time-domain short-pulse measurements. This furthers the confidence in the theoretical techniques and the measurement techniques. This experiment reveals many of the future strengths of the short-pulse radar; the sea surface can be modelled as a static wave, the extraction of wave features is enhanced, and the spectral-time characteristics are of new importance.

Chapter 6
Transient Scattering of a Beam from Infinite Periodic Surfaces

6.1 Introduction

The preceding chapters have emphasized the improvement of the ocean models. The oceans models included PEC sinusoidal, lossy sinusoidal and non-sinusoidal surfaces. Transient scattering from all of these surfaces was examined for an incident plane wave. In this chapter, the improvement is made in the incident-wave model. The incident wave thus far has been an ideal plane wave, which is of infinite spatial extent. A realistic radar system produces a non-uniform near plane wave of finite extent. The coverage area of the incident wave is called the footprint. Therefore this chapter will examine the transient scattering from a limited-footprint or beam radar.

The incorporation of a non-planar incident field into the previously developed scattering theory is quite simple for the finite length ocean models. However, the formulation for scattered fields from the infinite surface models with beam interrogation is not so trivial. The difficulty arises with the use of the periodic Green's function. The PGF allows for truncation of the problem to just one period of the ocean surface. Therefore the incident beam would also be repeated for every crest of the ocean surface with a progressive phase shift. This chapter will utilize a plane wave expansion to create an incident beam for use with the infinite length ocean models. The plane wave expansion will allow for the continued usage of the scattering theories developed previously for the infinite surfaces.

The preceding chapters introduced two frequency-domain methods to determine the scattered fields from an infinite ocean surface for plane wave excitation. One technique, known as the Rayleigh hypothesis, is only valid for sufficiently smooth

surfaces. A more encompassing integral-equation theory was also developed to provide solutions for rougher surfaces. These two methods can be modified, to a more general non-uniform (beam) incident wave, by properly choosing a number of plane waves. The technique in which a sum of plane waves is formed into a beam is known as the plane-wave expansion. The idea is therefore to repeatedly solve for the scattered fields using specific plane waves. The plane waves are chosen so that the resultant sum is a beam. Thus, the summation of scattered fields from each constituent plane wave results in the scattered field produced by that incident beam.

There are a number of ways in which the constituent plane waves can be determined. One method is to Fourier synthesize the plane waves needed to create a predetermined aperture field, this method is similar to antenna array beam synthesis. Another method, although less general, is to simply create a square wave using Fourier series. This square wave could then be space windowed to create the effect of a single beam. Both methods would ideally involve an infinite number a plane waves to exactly reconstruct the intended pattern. A feasible solution would involve a finite number of plane waves with the smallest number of plane waves needed to accurately create the beam as an optimal choice. By setting this limitation a slightly imperfect beam is expected, in fact the aperture field method will create a periodic beam, which will also need to be space windowed, and the two methods somewhat degrade into one.

6.2 Application of Scattering Theory

The two-dimensional surfaces of the previous chapters will be considered, and also only TE incident fields are analysed. In addition only a sinusoidal surface will be considered; this limitation eases the computational time involved by allowing for the use of the Rayleigh-hypothesis method. The integral equation method could have just as easily been employed, and for rough surfaces, but the computational time involved is rather phenomenal.

The computations are not only repeated for various incidence angles, but must also be iterated over a large bandwidth with a relatively small frequency step size. The frequency domain results are then transformed to obtain the desired transient response. The analytical technique uses two spectral transformations which results in a high computational load. In order to retain any of the valuable techniques developed, the non-uniform beam of interest must be composed of a finite sum of plane waves. This point was brought up in the introduction, and the essential steps in creating a non-uniform beam are presented below.

6.3 Beam Synthesis Techniques

In the introduction two methods for creating a non-uniform beam are mentioned, the first case to be considered will be the more general case, which is the aperture field method. The basic idea behind this method is to Fourier transform one of the spatial variables (x,z) out of the field representation, then match the fields at the aperture to obtain a set of spectral amplitudes that will recreate the same aperture field.

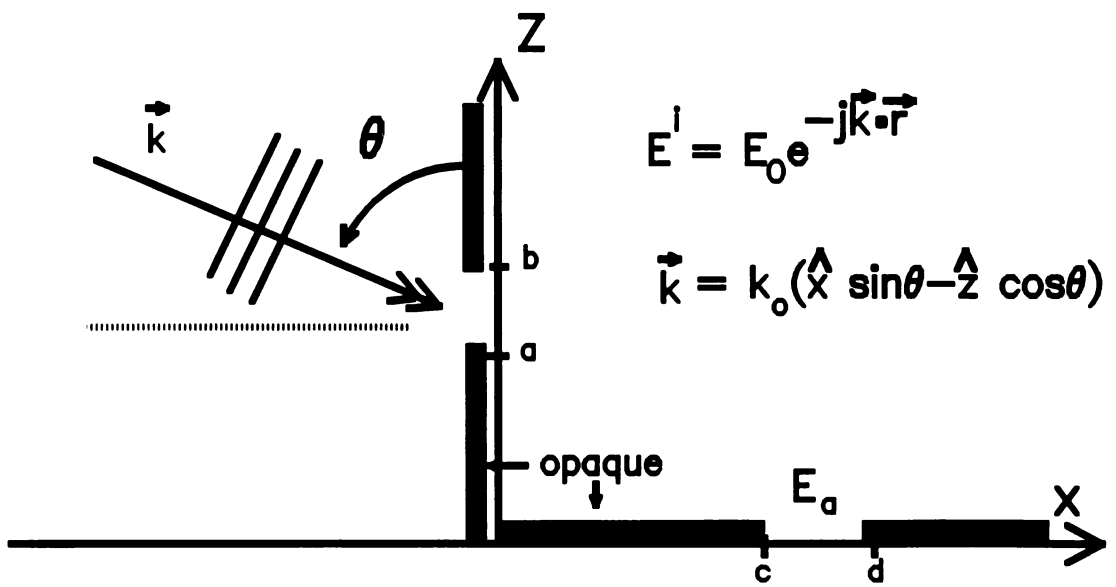

Figure 6.1 Geometry of Beam Synthesis Apertures.

The Fourier transform pair for either component of the field will be denoted as $E(x,z) \rightarrow e(x,k_z)$ or $E(x,z) \rightarrow e(k_x,z)$. The Fourier transform is defined here as

$$\begin{aligned} E(x,z) &= \frac{1}{2\pi}\int_{-\infty}^{\infty} e(k_x,z)\, e^{jk_x x}\, dk_x \\ e(k_x,z) &= \int_{-\infty}^{\infty} E(x,z)\, e^{-jk_x x}\, dx \end{aligned} \tag{6.1}$$

The transformation that is used will be dependent on the aperture orientation. Consider a plane wave incident upon an x-directed aperture (See Figure 6.1). Taking the Fourier transform of the governing Helmholtz equation and solving the resulting differential equation, the spectral domain fields are described by

$$e(k_x,z) = A(k_x)\, e^{jk_z z} + B(k_x)\, e^{-jk_z z} \tag{6.2}$$

where $k_z = \sqrt{k_o^2 - k_x^2}$ and $k_o = \omega\sqrt{\mu_o \epsilon_o}$.

For a beam propagating in the negative z-direction $B(k_x) = 0$, and the space domain field can now be found by taking the inverse transform of $e(k_x,z)$.

$$E(x,z) = \frac{1}{2\pi}\int_{-\infty}^{\infty} A(k_x) e^{j(k_x x + k_z z)} dk_x \tag{6.3}$$

A prescribed aperture field is used to determine the unknown spectral amplitudes $A(k_x)$. Note if the aperture is placed in the z=0 plane then $e(k_x,0) = A(k_x)$ or

$$A(k_x) = \int_c^d E(x,0) e^{jk_x x}\, dx \tag{6.4}$$

The aperture field can be selected by many means; one simple way would be to have the aperture field be equal to the incident plane wave field $E_a = E_o e^{-jk_o \sin\theta\, x}$. For this case the spectral amplitudes can be directly integrated to be

$$A(k_x) = \frac{2E_o e^{j\gamma(c+d)/2}}{j\gamma} \sin(\gamma(d-c)/2) \tag{6.5}$$

where $\gamma = k_x - k_o \sin\theta$. The spectral amplitudes will be maximal at $\gamma = 0$.

In order to perfectly reconstruct the beam needed to produce such an aperture field an infinite number of spectral components are needed, but by properly choosing a

finite number of spectral components a reasonable beam can be created, this beam however will have a periodic nature. The idea of a periodic beam can be more simply realized by just considering a Fourier series, which is the second method.

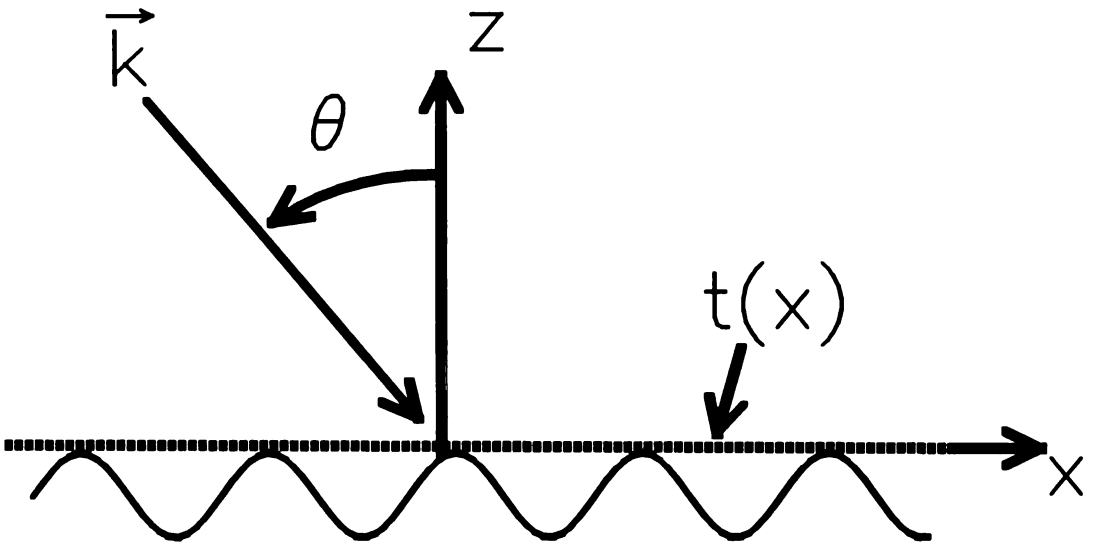

Figure 6.2 Beam synthesis and scattering geometry.

In the Fourier series method the incident field is assumed periodic in the x-direction. This periodicity permits the following representation of the incident field

$$E^i(x,z) = \sum_{n=-\infty}^{\infty} a_n e^{jk_{xn}x} e^{jk_{zn}z} \qquad \ldots \quad k_{xn} = n\frac{\pi}{L}\ ,\ k_{zn}^2 = k_o^2 - k_{xn}^2 \tag{6.6}$$

where $2L$ is period length of the incident field along the x-direction. This field could be thought of as a summation of propagating and evanescent plane waves. The key is to pick a finite number of these plane waves to recreate the periodic incident wave specified.

At this point a similar field matching procedure is performed to determine the Fourier coefficients a_n. Matching at the z=0 plane results in the most compact field representations. At z=0 the incident field is given by

$$E^i(x,0) = \sum_{n=-\infty}^{\infty} a_n e^{jk_{xn}x} \tag{6.7}$$

The field must now be matched to a known distribution to determine the Fourier coefficients. The field distribution that is chosen is non-unique and can be thought of as a transmittance function $t(x)$ (See Figure 6.2). Thus at the z=0 matching plane the two field distributions can be equated, resulting in

$$E_o t(x) e^{-jk_{ox}x} = \sum_{n=-\infty}^{\infty} a_n e^{jk_{xn}x} \tag{6.8}$$

where E_o and $k_{ox} = k_o \sin\theta$ describes a plane-wave field incident upon the transmittance screen at z=0.

The Fourier coefficients are then found in the usual manner utilizing the orthogonality of the circular exponential function. This is accomplished by integrating both sides of (6.8) by

$$\int_{-L}^{L} \{f(x)\}\ e^{-jm\pi x/L}\, dx \tag{6.9}$$

which results in

$$a_n = \frac{E_o}{2L} \int_{-L}^{L} t(x) e^{-j(k_{ox} + n\pi/L)x}\, dx \tag{6.10}$$

There are a number of interesting transmittance functions, but the Gaussian transmittance function has proven to be the most useful and easiest to implement. The Gaussian transmittance function is given by

$$t(x) = e^{-\left(\frac{x}{w}\right)^2} \tag{6.11}$$

where w is a width factor and $w \ll L$.

It is interesting to note the similarities between the two methods, which is completely analogous to the connection between the Fourier integral and Fourier series.

The discrete Fourier coefficients a_n of Eqn. (6.10) and continuous coefficients $A(k_z)$ of Eqn. (6.4) are analogous. The aperture method could also be replaced with a transmittance screen which would result in a spatial Fourier transform.

6.3.1 Examples of Gaussian Beam.

In Figure 6.3 the amplitude of the Fourier coefficients (a_n) are shown for a Gaussian beam with a width of 1.0 meter ($w = 0.5m$). The incidence angle is 70° which would correspond to $k_{ox} = -37\,r/m$ for an excitation frequency of 2 GHz. A spatial Gaussian beam has a Gaussian shaped Fourier transform where the width of the Gaussian curves are inversely proportional in each domain. An analogous effect occurs in the discrete case and is obvious in the figure. The 21 strongest modes are plotted. The small amplitudes at the curve ends indicate that the spatial beam should be well constructed.

The reconstructed beam can be seen in Figure 6.4. The beam is well represented by the 21 modes that are included. The width of the Gaussian beam and the repetition period of the beam are seen to correspond to the predicted values of $2L = 10m$ and $2w = 1.0m$. If a narrower beam was required a broader spectrum would be needed and the number of important modes would increase. For this case 21 modes is sufficient to create a beam with small side-lobes. The implication is that scattered fields will have to computed 21 times, for each individual plane wave that makes up the beam.

An important detail regarding Figure 6.3 is the classification of evanescent and propagating modes. These are with respect to the z-direction are a consequence of k_{zn}. When $|k_{xn}| > k_o$ the plane waves become evanescent in the z-direction and therefore the placement of the transmittance screen becomes important. The transmittance screen should be placed as close to the ocean surface as possible, as shown in Figure 6.2. In this fashion the effects of dispersion and decay are minimized and a good beam can illuminate the surface.

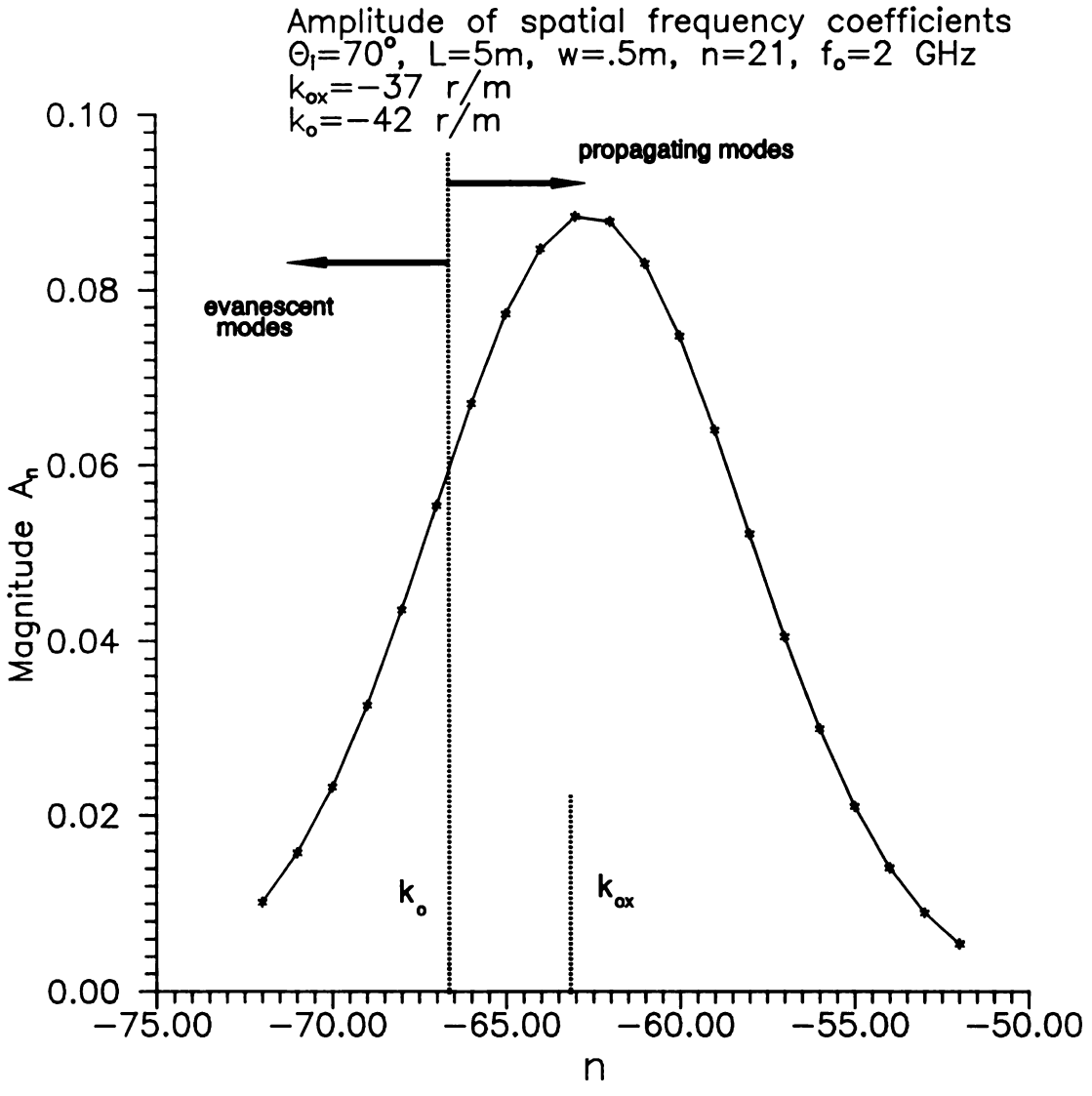

Figure 6.3 Spectral Amplitudes for a Gaussian Incident Beam Parameters are L=5.0m and w =.5m.

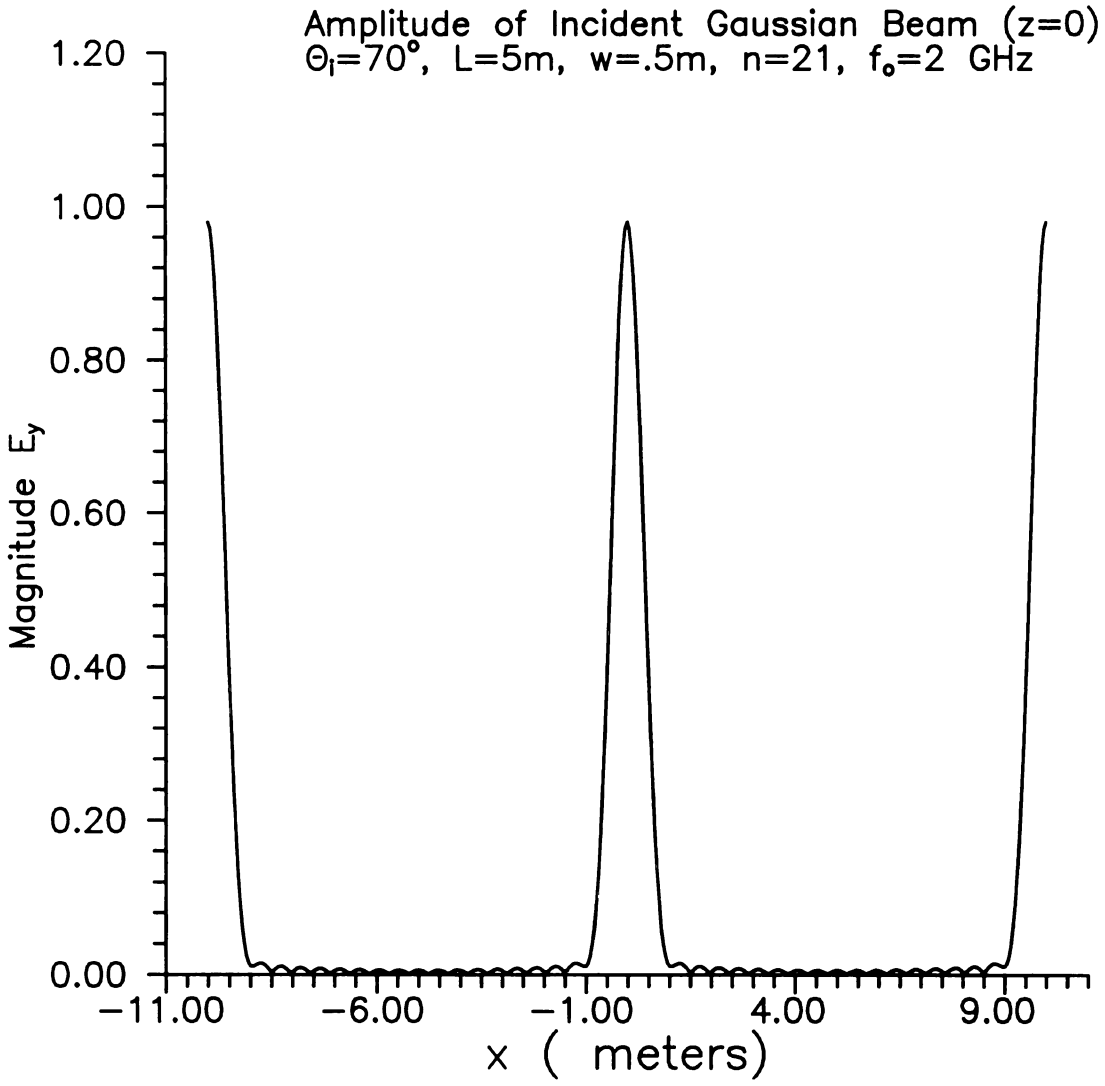

Figure 6.4 Gaussian Incident beam created from 21 terms of the Fourier Series, where L=5.0 m, w=.5 m, and θ =70°

6.4 Transient Scattering Results.

The induced surface currents for a TE incident Gaussian beam are examined in Figure 6.5 and Figure 6.6. For both examples the Gaussian beam is 1.0m wide with a repetition period of 10.0m. The beam is illuminating a PEC sinusoidal surface with a period of 0.1m and a height of 0.007 m and the excitation frequency is 2 GHz. In Figure 6.5 the beam is incident from 30° and the resulting induced surface currents are shown. The plot reveals the width of the beam through the fact that the induced currents are strongest where the beam is of greatest amplitude. In Figure 6.6 the response for an incidence angle of 70° is shown. The beam is composed of 21 modes and was shown in Figure 6.4. The induced currents reveal an increased shadowing effect which is expected for the near grazing incidence angle.

In Figure 6.7 and Figure 6.8 are the induced currents for just the central illuminated regions of the two previous figures. These plots highlight the differences between the incidence angles of the Gaussian beams. The case of 70° incidence exhibits a much greater shadowing for each individual wave crest and for the overall illuminated wave packet. It is also interesting to note the difference in current amplitude. The 30° response exhibits a greater amplitude; this effect was noted in previous chapters and was expected for beam illumination as well.

The backscattered fields for a single plane wave (not a beam) are shown in both the frequency and time domains in Figure 6.9 and Figure 6.10. These results will be used as a comparison with the responses for beam illumination. In Figure 6.9 the backscatter spectra from a PEC sinusoid for incidence angles of 70° and 85° are shown. The synthesized transient responses of the respective spectra are shown in Figure 6.10. Indicated in this figure by T is the two-way transit time between consecutive wave crests. This two-way transit time does agree with the expected time for the ocean surface period of 0.1m. In Figure 6.11 is the extended transient response for an incidence angle of 85°. This plot is important because it reveals that a plane wave uniformly illuminates

the entire (infinite) sinusoidal surface. The transient response due to a beam, which will not illuminate all of the wave crests, should reflect the non-uniform illumination.

The frequency response for Gaussian beam illumination is shown in Figure 6.12 and Figure 6.13. The beam and PEC sinusoidal surface parameters are the same as those of the induced current plots (Figure 6.5 and Figure 6.6). In Figure 6.12 the response for a 30° beam is shown for various field point locations. The field points are varied along the x-direction and quite a large variation between the respective responses. The spectrum produced by beam illumination is also quite different than that produced by a single plane wave. It is interesting that beam illumination produces spectra that resemble the response from a finite surface, with the well defined and spread out Floquet-mode spikes. This is intuitively expected because the limited footprint beam effectively reduces the infinite surface to a finite structure. The 70° case is shown in Figure 6.13 and exhibits the same phenomena as the 30° case.

The corresponding synthesized transient responses are shown in Figure 6.14 and Figure 6.15. These results show the transient backscatter due to a Gaussian beam illumination. In Figure 6.14 the interrogating beam has an incidence angle of 30°. The figure shows the transient backscatter at the three field points displayed in the frequency response plot of Figure 6.12. The plot reveals that only the illuminated portion of the sinusoidal wave is producing backscatter. The change in field point location exhibits the expected behavior, which is a time shift in the backscatter wave packet. The decay in the return wave packet amplitude is due to the increased distance the scattered wave had to travel. Although it is not shown, the incident wave is periodic with a spatial period of 10m and backscatter would also be produced from the additional incident beams.

In Figure 6.15 the incidence angle is increased to 70° (near grazing). The envelopes of the backscatter wave packets are somewhat distorted in shape. This is explained by comparing the induced surface currents of Figure 6.5 and Figure 6.6. The induced currents on the 70° incidence have a different distribution than the 30° case.

The difference between the single plane-wave excitation and the beam illumination is quite evident in the transient responses. This is highlighted in Figure 6.16, where the transient response for a 30° beam is shown. If this surface had been illuminated with a single plane wave the three location points would have identical backscatter responses due to the infinite spatial extent of both the incident wave and sinusoidal surface. But it is clear from this figure that beam illumination induces non-uniform surface currents, which create the footprint-limited wave-packet backscatter.

The synthesized transient backscatter for an incident Gaussian beam is shown in Figure 6.17. The field point location is varied along the vertical axis and the log magnitude of the transient backscatter response is plotted versus time. The upper plot is for a 70° incident beam and is contrasted with a 30° incident beam in the lower plot. The backscatter from the 30° beam is greater in magnitude and less spread out than the 70° case. This was seen previously and is expected since the 70° beam has a larger footprint.

In Figure 6.18 the total transient scatter from a PEC sinusoid wave is shown for a Gaussian beam incident pulse. The figure displays the backscatter as well as the prominent specular forward scatter. The forward scatter are the narrow diagonal lines with a positive slope. The forward scattered waves that occurs at the later times is due to the periodicity of the incident beam.

6.5 Conclusions

In this chapter the scattering of a spatially limited incident beam by an infinite periodic surface was examined. The construction of the beam was such that the previous theoretical developments could be still used to determine the scattered fields. This was accomplished with the idea of a plane-wave decomposition. The beam was decomposed into a finite number of plane waves, which can be used with the existing scattering theories. The restriction of the number of constituent plane waves resulted in a spatially periodic beam. This unwanted characteristic could be mitigated by spatial windowing.

The results that were obtained were not verified with experimental measurements but the confidence level is high regarding their correctness. The information gained from previous experiments and theoretical results from the finite surfaces was closely related to the beam excitation. The correlation between the two was noted in both the time and frequency domains. The most notable, and expected difference between the single plane wave and beam excitation is the spatial non-uniformity of the scattered fields. This was shown by examining the spectral and transient responses at a number of field points in the horizontal plane.

The usefulness of the beam excitation is its the ability to model a limited footprint radar system in a infinite sea-surface environment. In the future this model will be used for realistic radar simulations in which targets in the ocean environment are sought.

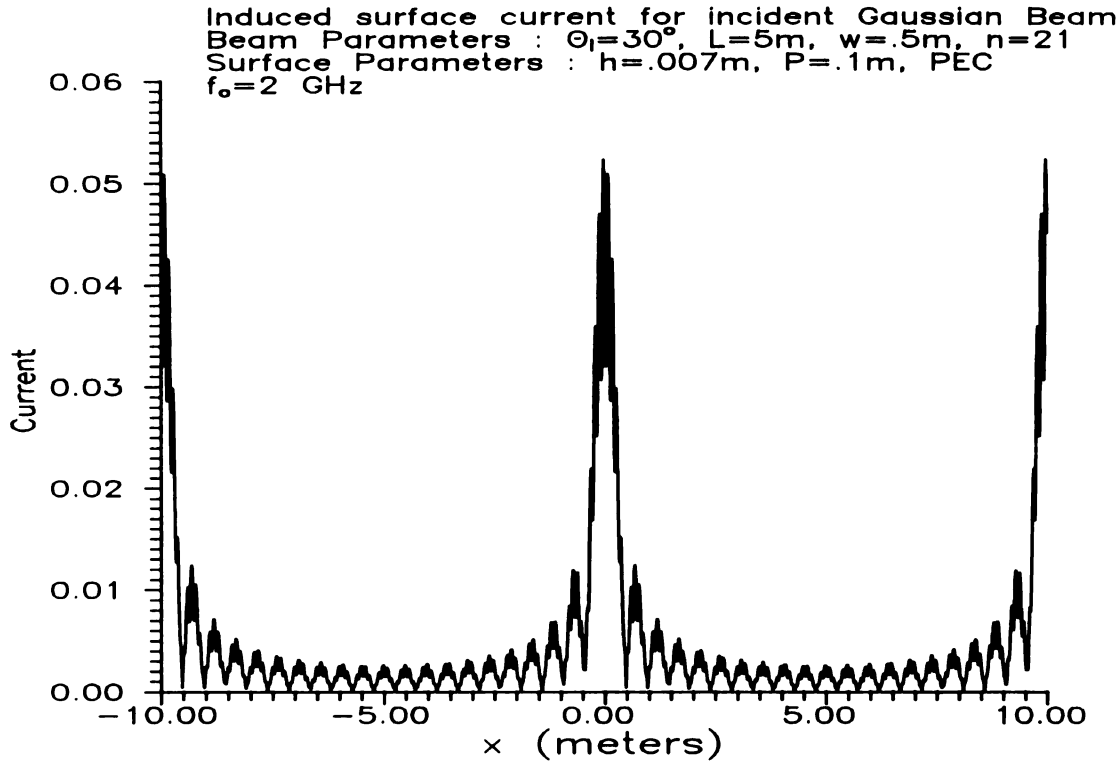

Figure 6.5 Induced Surface currents on PEC surface, for 30° Gaussian beam illumination.

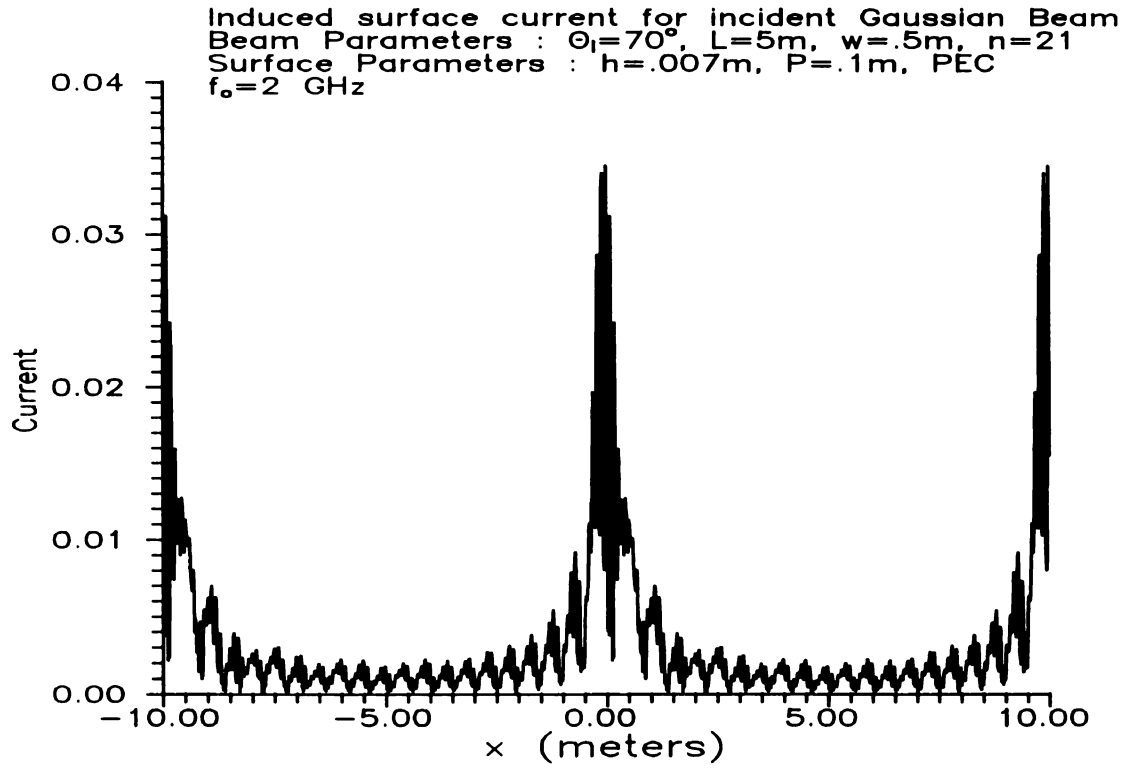

Figure 6.6 Induced surface currents on PEC surface for 70° beam illumination.

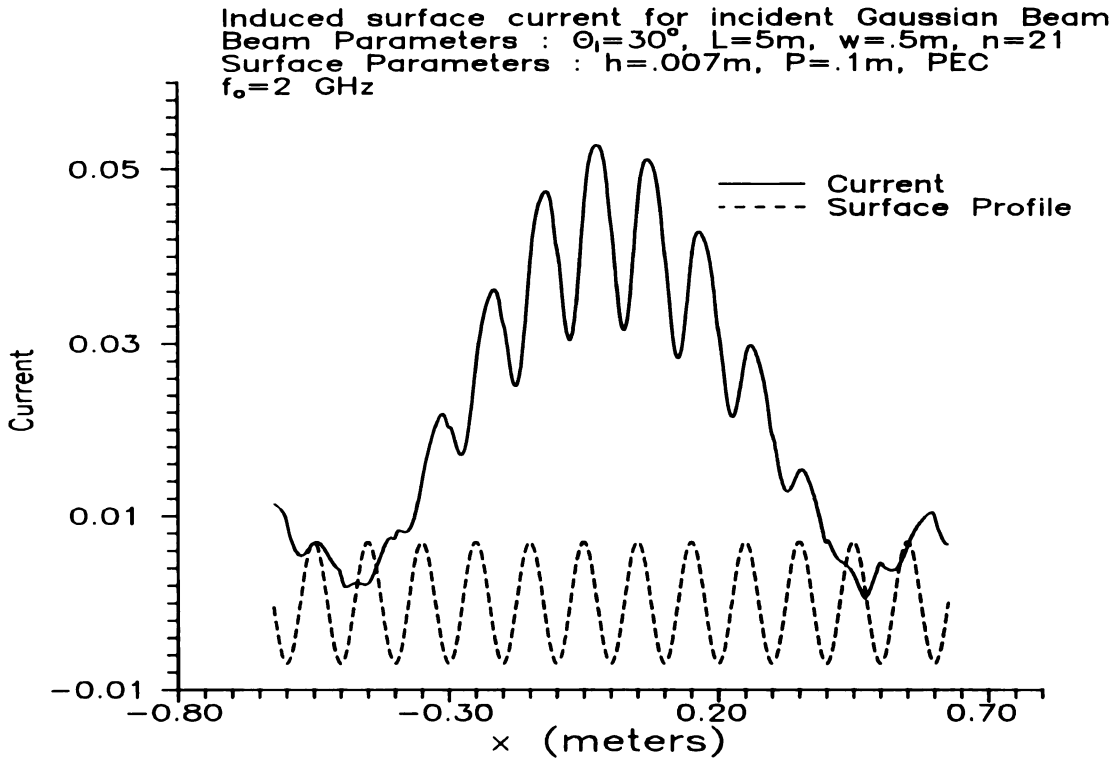

Figure 6.7 Induced surface currents on PEC surface for 30° beam illumination.

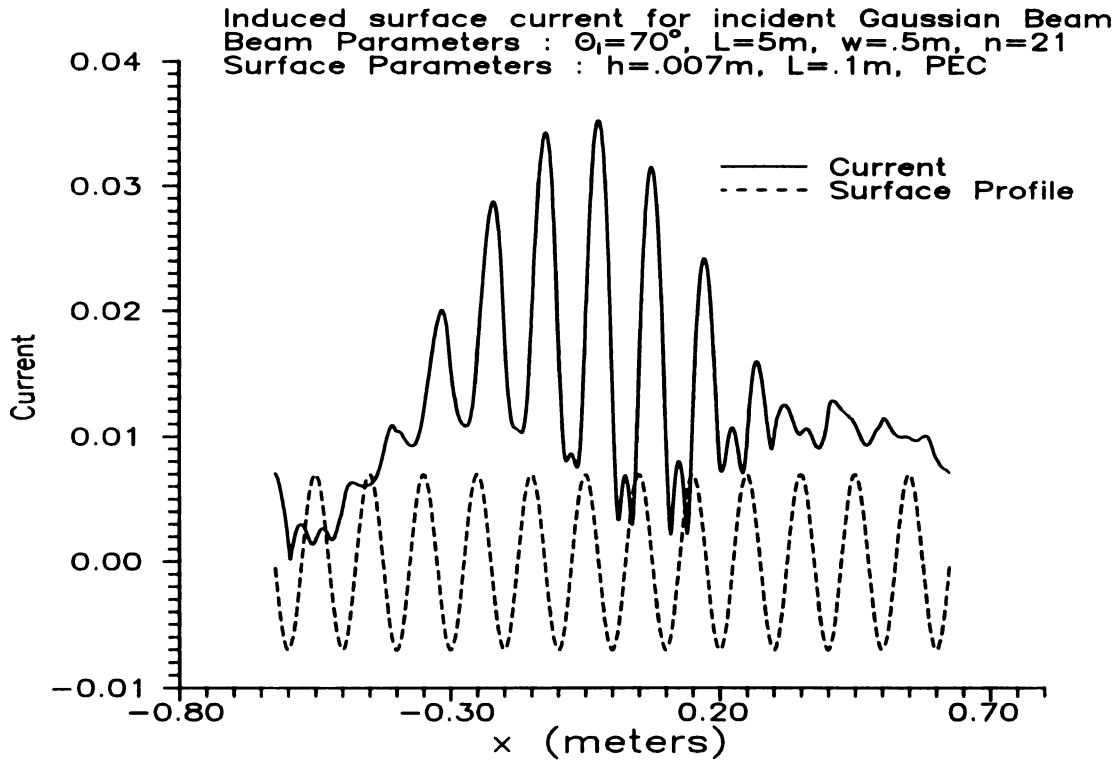

Figure 6.8 Induced surface currents on PEC surface for 70° beam illumination.

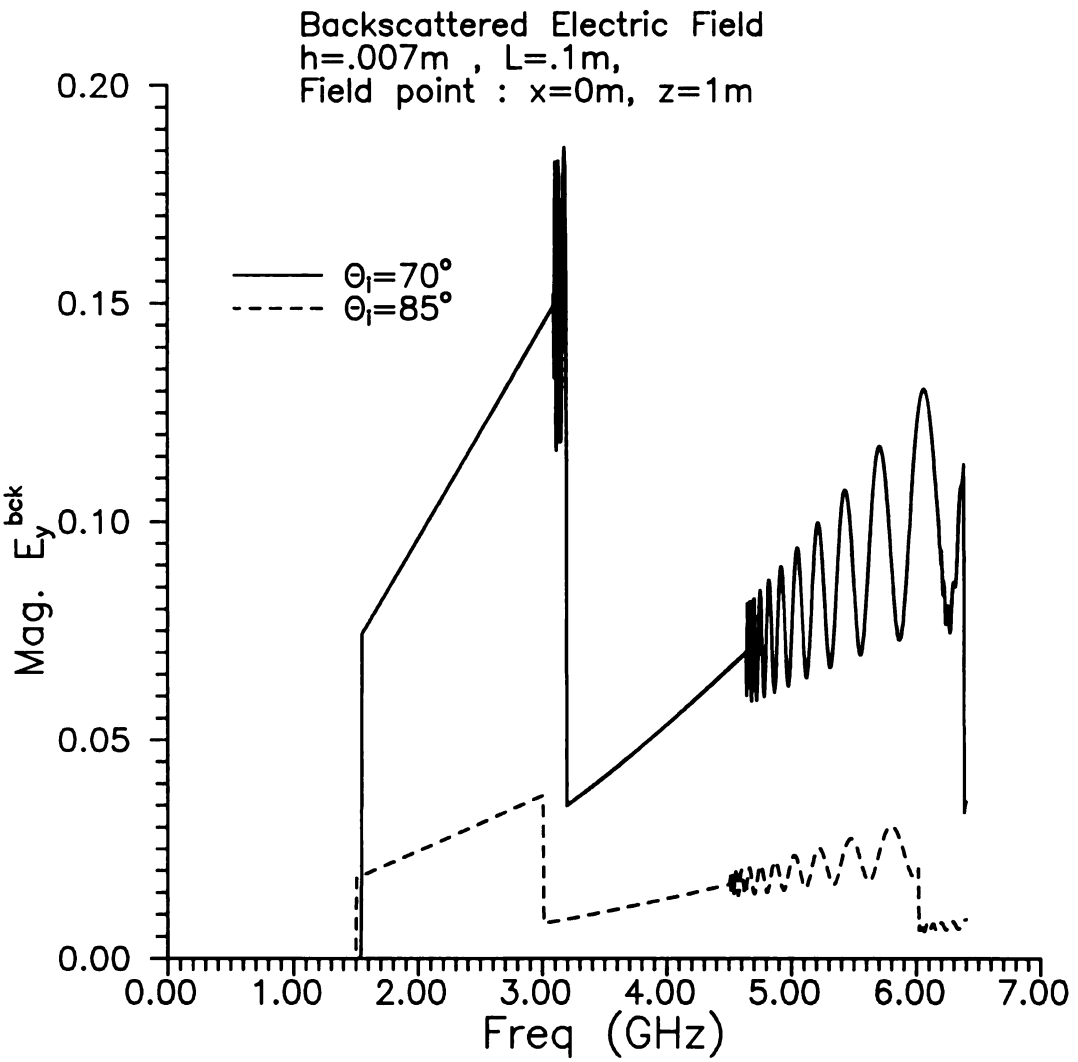

Figure 6.9 Frequency response of backscatter from a PEC surface for a single plane wave.

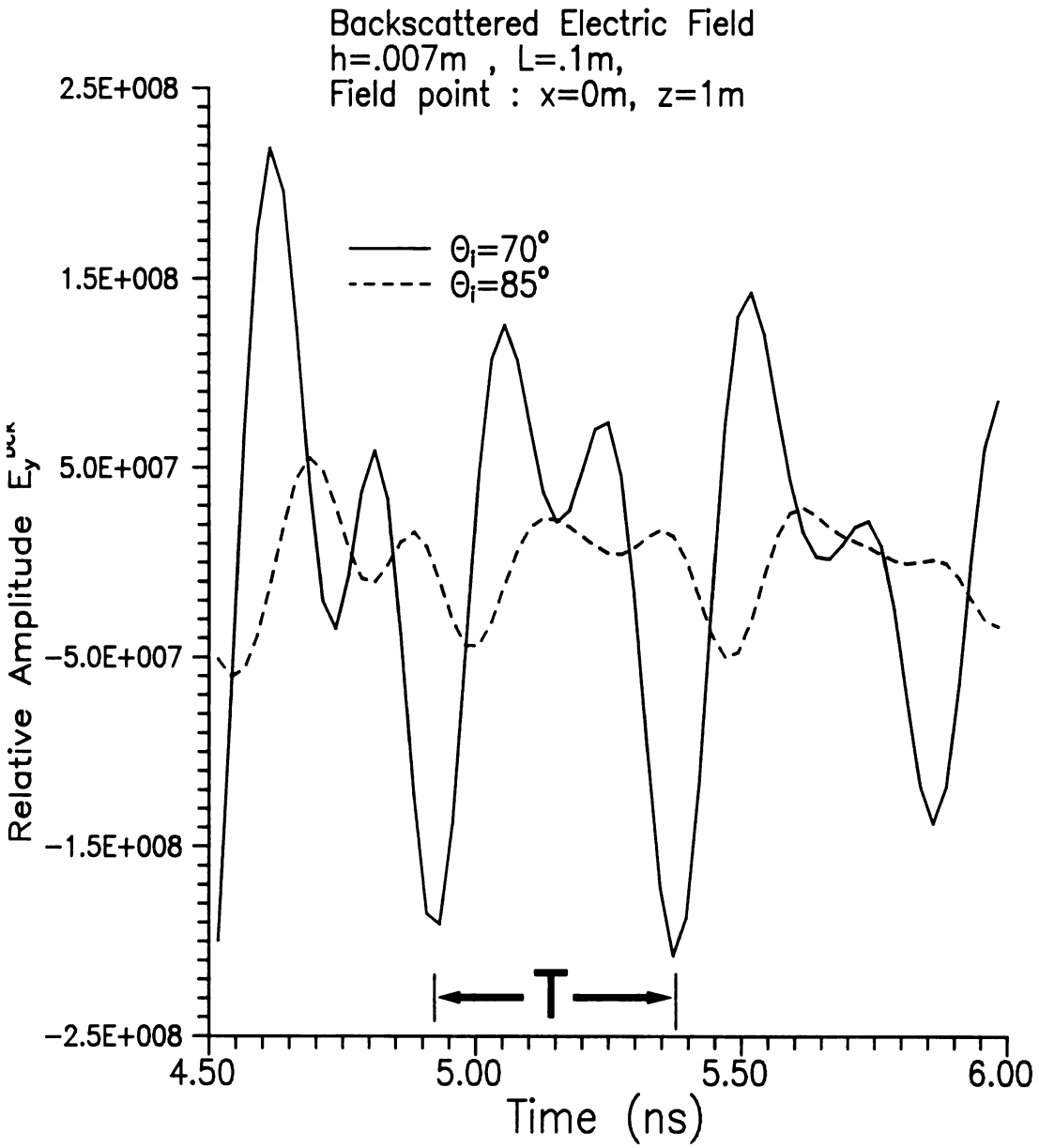

Figure 6.10 Transient backscatter from a PEC surface for single plane wave pulse illumination.

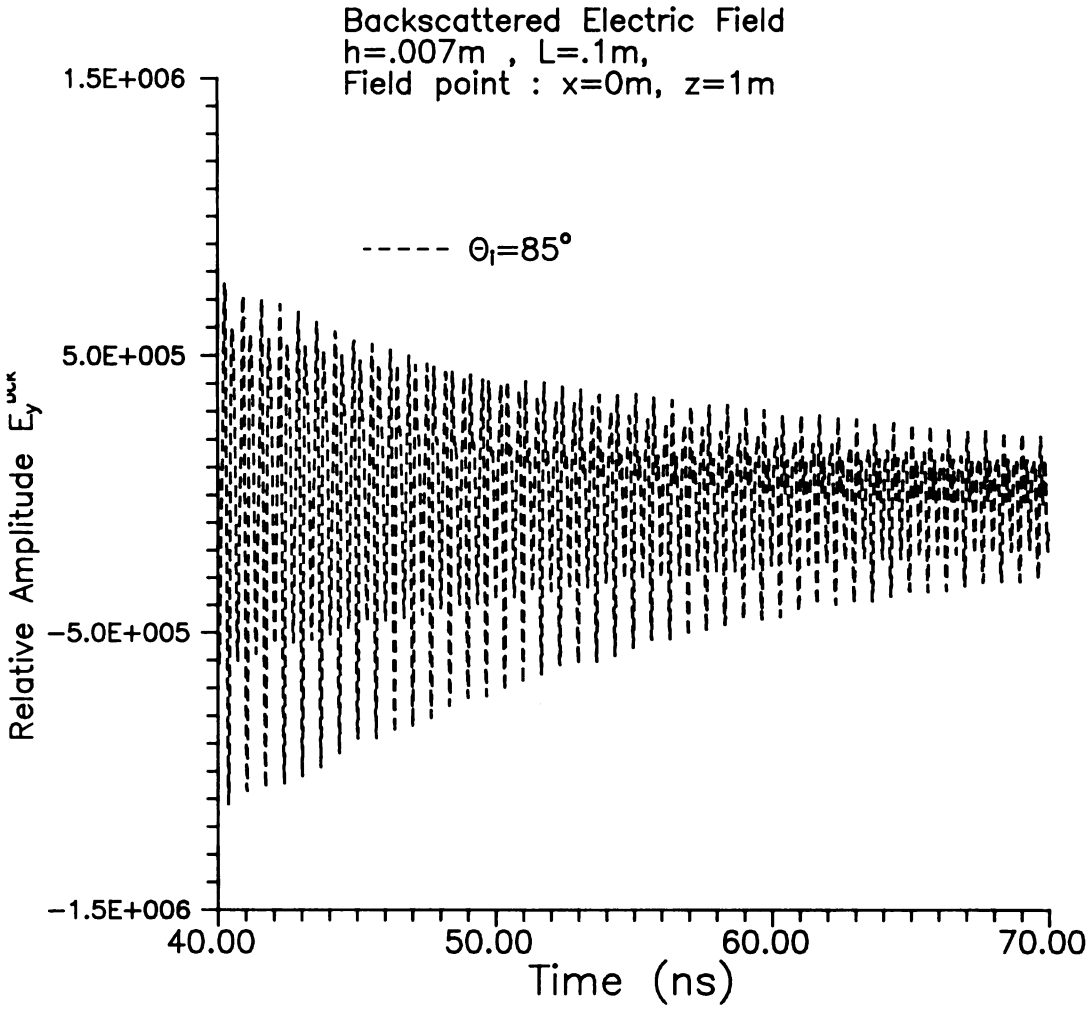

Figure 6.11 Transient backscatter for single plane wave incident.

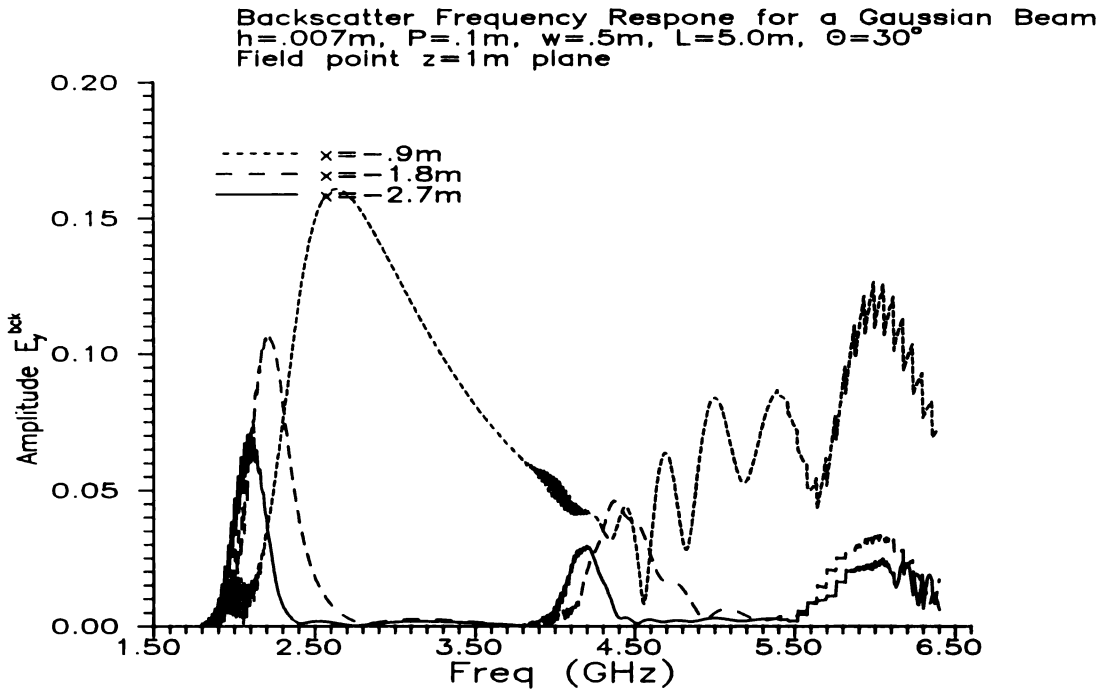

Figure 6.12 Spectrum of backscattered field for an incident Gaussian beam (θ=30°)

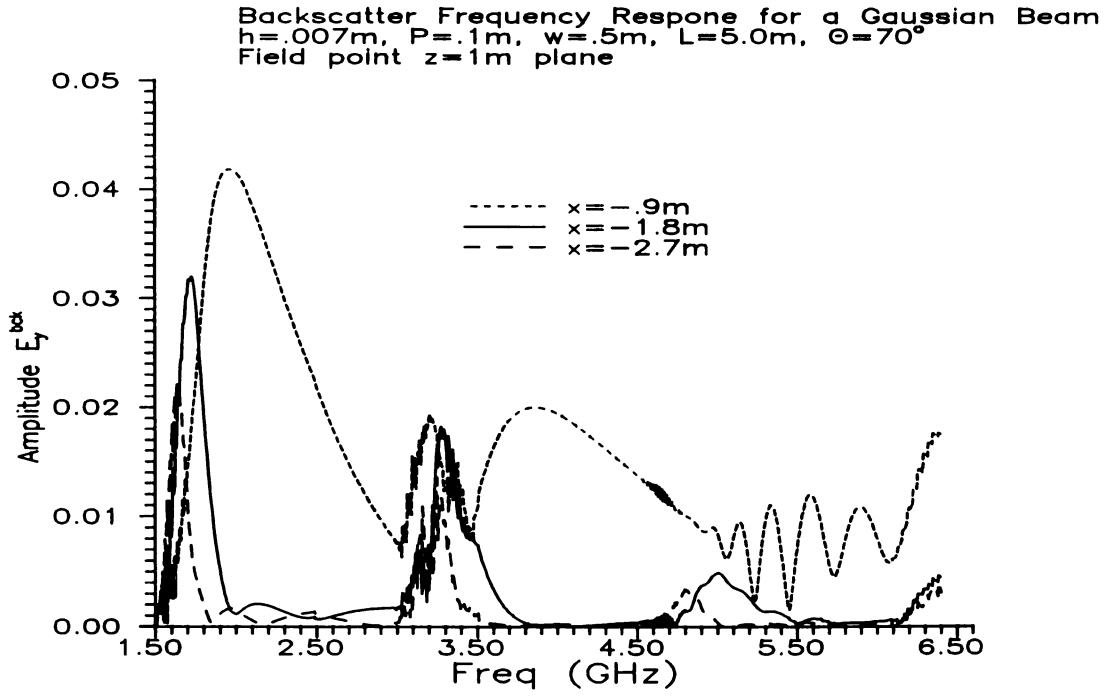

Figure 6.13 Frequency response of backscattered field for an incident Gaussian beam (L=5.0m, w=0.5m, n=21 θ=70°)

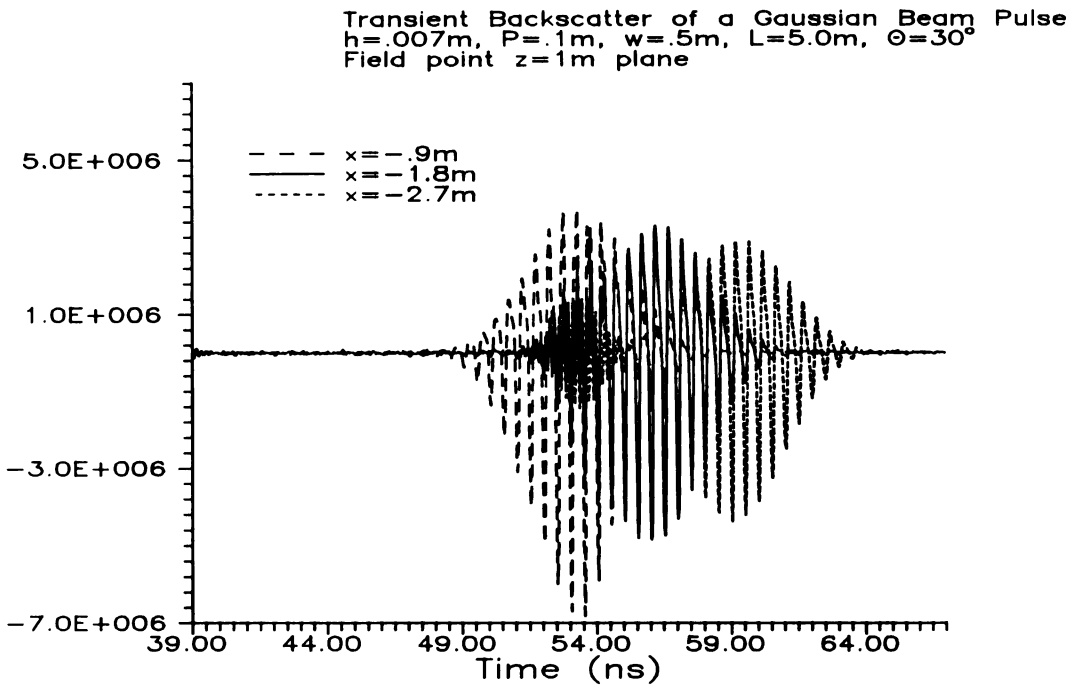

Figure 6.14 Transient backscattered field for an incident Gaussian beam pulse (θ=30°).

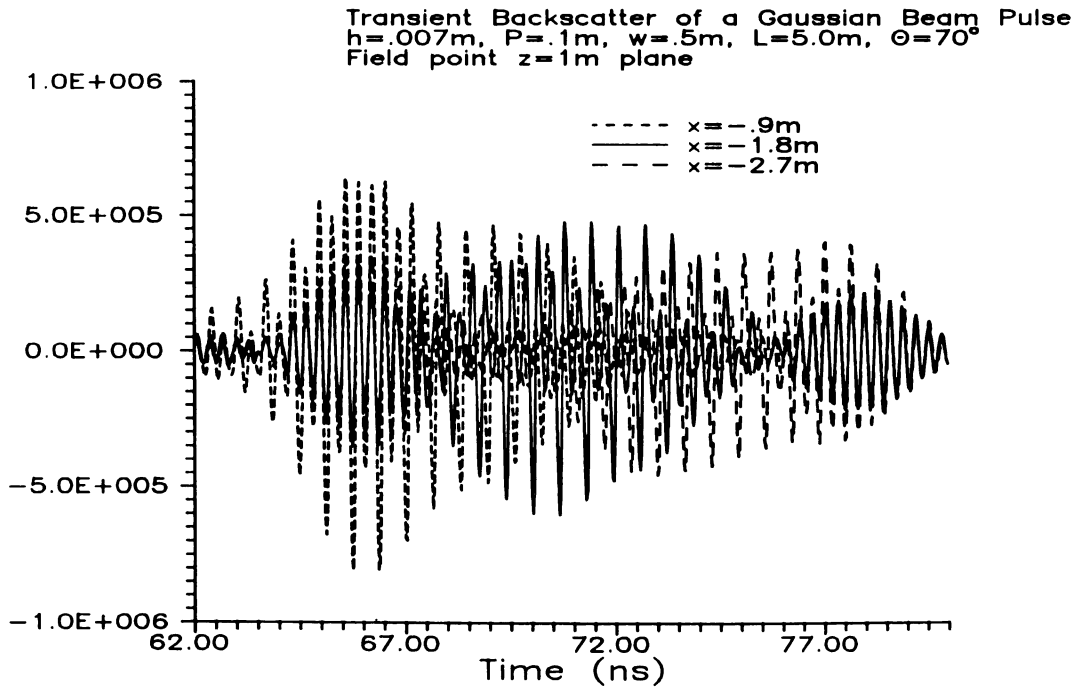

Figure 6.15 Transient backscattered field for an incident Gaussian beam pulse (θ=70°).

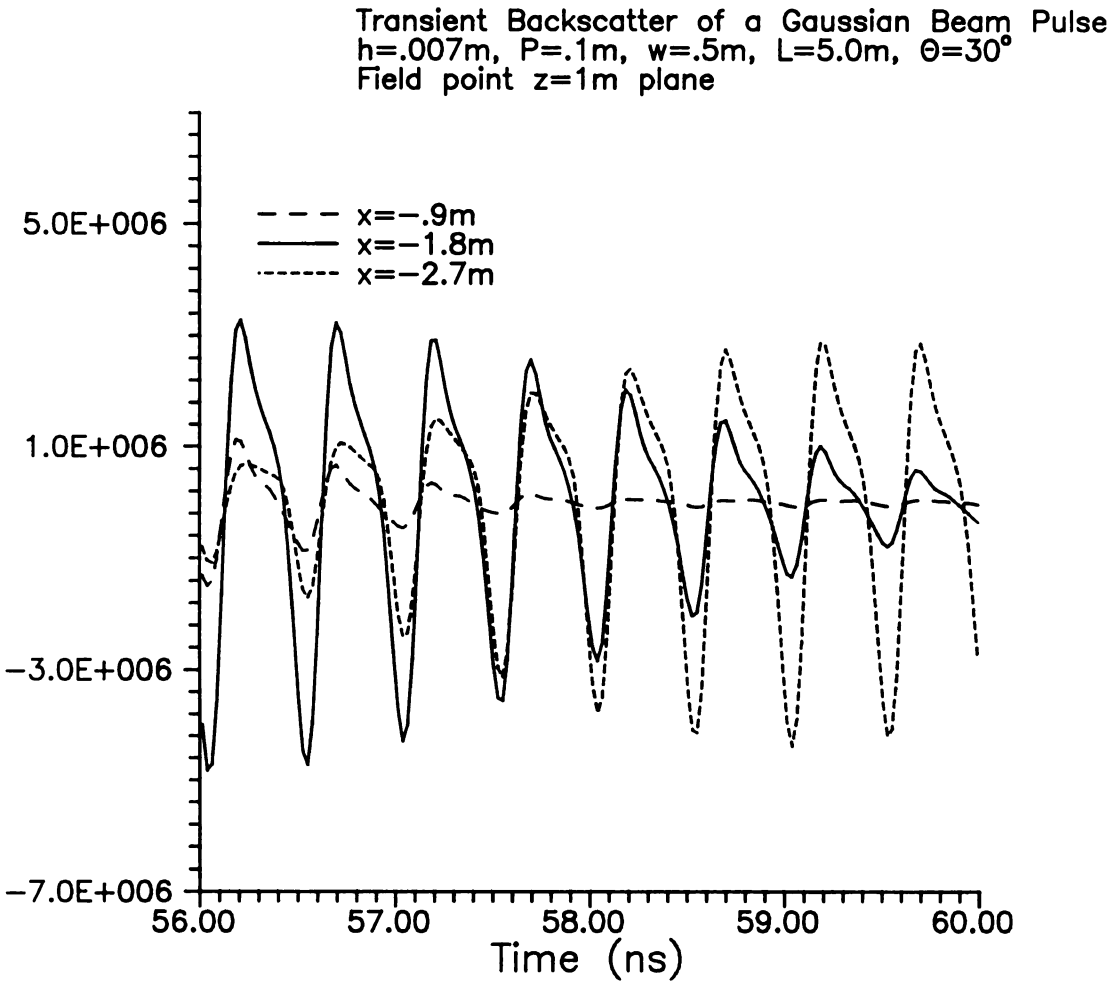

Figure 6.16 Transient backscattered field for an incident Gaussian beam pulse (L=5.0m, w=0.5m, θ=30°)

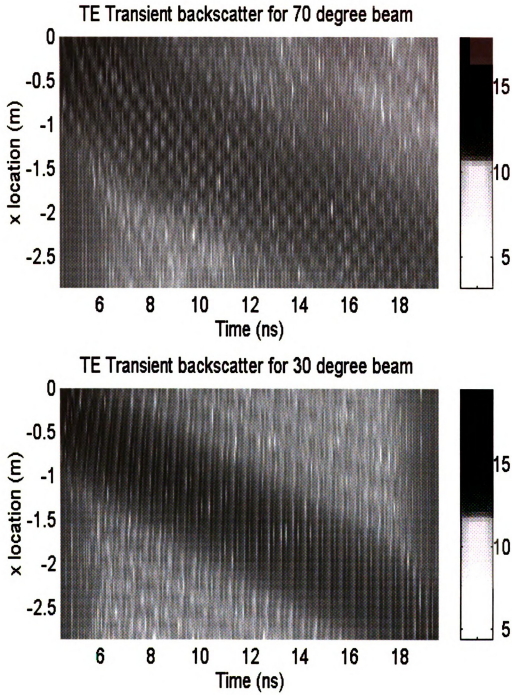

Figure 6.17 Synthesized transient backscatter response for Gaussian beam pulse incident at 30° and 70°. (Beam parameters : n=21, w=.5m, L=5m) (Surface parameters : P=0.1m, h=0.007m, PEC sinusoid)

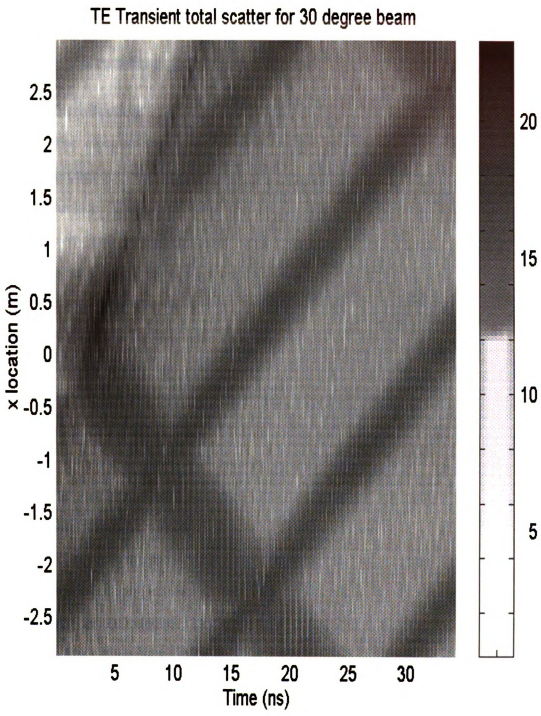

Figure 6.18 Synthesized transient total scatter response for Gaussian beam pulse incident at 30°. (Beam parameters : n=21, w=.5m, L=5m) (Surface parameters : P=0.1m, h=0.007m, PEC sinusoid)

Chapter 7
Transient Scattering from a Three Layer Medium

7.1 Introduction

The electrical characteristics of the ocean have been considered in numerous places throughout this thesis. The most elementary model was the perfectly conducting (PEC) surface. The ocean model was later improved to be a lossy layer, in which the conductivity and permittivity were parameters. In this chapter the composition of the ocean is once again upgraded. A planar interface is added within the ocean layer. This interface separates two electrically dissimilar layers and creates a three layer geometry. The new geometry is shown in Figure 7.1.

The additional layer allows for the modelling of a number of ocean attributes. The most obvious would be the ocean floor, but is rather uninteresting except in very shallow water. A more interesting scenario is that of a ducting layer, which is a physical ocean effect that has the possibility of trapping electromagnetic waves [57,58]. The third layer could also model a salinity or temperature gradient, where the electrical characteristics of the ocean may be varying.

The problem has been simplified by introducing just an infinite planar layer. The general case of an additional periodic layer is possible but greatly intensifies the computational difficulties. The computational complexity is relatively unchanged with the addition of a planar layer. The three layer problem can be solved by extending both of the frequency domain methods used for the PEC and two-layer cases. Namely, the classical mode matching in conjunction with the Rayleigh hypothesis and the integral equation methods.

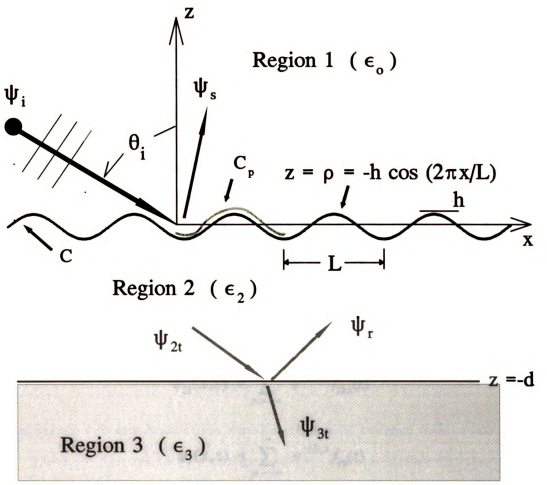

Figure 7.1 Configuration of three medium scattering problem.

7.2 Floquet mode-matching/Rayleigh hypothesis.

The extension of the Floquet mode-matching method is straightforward. The additional layer neither creates nor destroys any of the modes induced by the periodic interface. Therefore a mode by mode reflection and transmission occurs at the planar interface in which the typical reflection and transmission coefficients hold. There still must be a mode matching procedure performed at the periodic interface which will now contain an additional upward space harmonics (ψ_r).

The geometry is shown in Figure 7.1. A TM plane wave is assumed incident upon the sinusoidal interface at an angle of θ_i. The generating field quantity is $H_y(x,z)$ and

will be denoted as $\psi(x,z)$. The corresponding electric field quantities can be found via Maxwell's equations. The sinusoidal interface, which separates air and sea, is represented by $\rho(x)$. The planar interface is located below the sinusoidal interface at z=-d meters.

The TM incident wave is given by

$$\psi_i = A_o e^{-j\beta x} e^{jqz} \tag{7.1}$$

where $\beta = k_o \sin\theta_i$, $q = k_o \cos\theta_i$ and $k_o = \omega\sqrt{\epsilon_o \mu_o}$.

The fields in each of the regions can be represented by the Floquet mode expansion. This is due to the expected periodicity of the fields and was discussed in detail in chapter 3. The fields in each region are therefore given by

$$\psi_s(x,z) = \sum_{n=-\infty}^{\infty} e^{-j\beta_n x} f_{sn}(z) \tag{7.2}$$

$$\psi_{2t}(x,z) = \sum_{n=-\infty}^{\infty} e^{-j\beta_n x} f_{2tn}(z) \tag{7.3}$$

$$\psi_r(x,z) = \sum_{n=-\infty}^{\infty} e^{-j\beta_n x} f_{rn}(z) \tag{7.4}$$

$$\psi_{3t}(x,z) = \sum_{n=-\infty}^{\infty} e^{-j\beta_n x} f_{3tn}(z) \tag{7.5}$$

where $\beta_n = \beta + 2n\pi / L$.

The above wave functions must all satisfy the homogenous Helmholtz equation in their respective regions. The application of the Helmholtz equation upon the wave functions determines the functional z-dependence of the unknown field quantities. This operation was performed in chapter 3 and chapter 4. The resulting field representations are

$$\psi_s = \sum_{n=-\infty}^{\infty} B_n e^{-j\beta_n x} e^{-jq_{1n} z} \tag{7.6}$$

$$\psi_{2t} = \sum_{n=-\infty}^{\infty} C_n \, e^{-j\beta_n x} \, e^{j q_{2n} z} \tag{7.7}$$

$$\psi_r = \sum_{n=-\infty}^{\infty} D_n \, e^{-j\beta_n x} \, e^{-j q_{2n}(z+d)} \tag{7.8}$$

$$\psi_{3t} = \sum_{n=-\infty}^{\infty} G_n \, e^{-j\beta_n x} \, e^{j q_{3n}(z+d)} \tag{7.9}$$

where

$$q_{1n} = \sqrt{k_o^2 - \beta_n^2}$$

$$q_{2n} = \sqrt{k_2^2 - \beta_n^2}$$

$$q_{3n} = \sqrt{k_3^2 - \beta_n^2}$$

$$k_2 = \omega\sqrt{\epsilon_2 \mu_o} \quad , \quad k_3 = \omega\sqrt{\epsilon_3 \mu_o}$$

and the branch cuts are chosen such that the required exponential decay occurs.

There are four unknown modal coefficients, and this implies that four boundary conditions are needed to completely specify the problem. There are two boundary conditions associated with the sinusoidal surface as well as two with the planar interface. The boundary conditions are the continuity of the tangential magnetic and electric fields across the boundary. The boundary conditions in terms of the wave function are given by

$$\frac{\partial \psi_1}{\partial n} = \frac{\epsilon_o}{\epsilon_2} \frac{\partial \psi_2}{\partial n} \quad ; \quad \psi_1 = \psi_2 \quad at \quad z = \rho \tag{7.10}$$

$$\frac{\partial \psi_2}{\partial z} = \frac{\epsilon_2}{\epsilon_3} \frac{\partial \psi_{3t}}{\partial z} \quad ; \quad \psi_2 = \psi_{3t} \quad at \quad z = -d \tag{7.11}$$

where $\psi_1 = \psi_i + \psi_s$, $\psi_2 = \psi_{2t} + \psi_r$ and $\frac{\partial}{\partial n}$ denotes normal derivative.

The remaining steps are identical to those performed in chapter 3 and chapter 4. Namely, the field representations of equations (7.6) through (7.9) are substituted into the auxiliary equations (7.10) and (7.11). Galerkin's method is then applied to isolate the unknown modal coefficients. This was demonstrated in earlier chapters and is accomplished by applying the following operator

$$\int_0^L \{...\}\ e^{j\beta_m x}\, dx \tag{7.12}$$

where L is the period length of the sinusoidal surface.

Note that for the z=-d boundary condition (7.11) the equations are orthogonal. Therefore, it is possible to solve for D_n and G_n in terms of C_n. The relations are given by

$$D_n = e^{-j q_{2n} d} R_n C_n \tag{7.13}$$

$$G_n = e^{-j q_{2n} d} T_n C_n \tag{7.14}$$

Where,

$$R_n = \frac{\epsilon_3 q_{2n} - \epsilon_2 q_{3n}}{\epsilon_3 q_{2n} + \epsilon_2 q_{3n}} \tag{7.15}$$

$$T_n = \frac{2\epsilon_3 q_{2n}}{\epsilon_3 q_{2n} + \epsilon_2 q_{3n}} \tag{7.16}$$

and coefficients R_n and T_n are the typical reflection and transmission coefficients associated with a planar interface, except that they could be different for any given mode.

The remaining unknowns B_n and C_n are found from the boundary condition at the sinusoidal interface (7.10). These coefficients are coupled and the application of Galerkin's method results in the following set of equations

$$\sum_{n=-\infty}^{\infty} B_n K_{mn} - \sum_{n=-\infty}^{\infty} C_n \left(K_{mnt} + R_n e^{-j q_{2n} d} K_{mnr} \right) = -A_o A_m \tag{7.17}$$

$$\sum_{n=-\infty}^{\infty} B_n L_{mn} - \frac{\epsilon_o}{\epsilon_2} \sum_{n=-\infty}^{\infty} C_n \left(L_{mnt} + R_n e^{-j q_{2n} d} L_{mnr} \right) = A_o F_m \qquad (7.18)$$

where,

$$L_{mnr} = e^{-j q_{2n} d} L_{mn} \Big|_{q_{1n} = q_{2n}}$$

$$K_{mnr} = e^{-j q_{2n} d} K_{mn} \Big|_{q_{1n} = q_{2n}}$$

and L_{mn}, L_{mnt}, K_{mn}, K_{mnt}, A_m and F_m remain the same as the two layer case of chapter 4, section 2.

The numerical implementation of (7.17) and (7.18) is accomplished by truncating the infinite number of equations and creating a square matrix. A square matrix is produced by restricting the number of m and n entries to be the same. The convergence of the solution is discussed in chapters 3 and 4.

7.3 PGF IE Technique

The extension of the integral equation technique to the three layer problem is simplified by the restriction of the additional layer to be planar. The planar layer can be handled analytically, whereas a periodic layer requires a numerical approach. The approach is similar to that taken with the two layer problem of chapter 4.

The region below the sinusoidal surface is replaced with the upper region medium, thus creating a homogenous medium. An equivalent volume polarization current is placed in the lower region. This polarization current induces the same fields in the upper region that the original configuration would. The key aspect is that a homogenous Green's function can be employed to find the scattered fields produced by the polarization current (replaced by equivalent surface fields). The Green's function for this upper region case remains unchanged (from the two layer problem) and is known as the primary Green's function, which is given by

$$G_i^P(x,z|x',z') = -\frac{j}{2L}\sum_{n=-\infty}^{\infty}\frac{e^{-j\beta_n(x-x')}e^{-jq_{in}|z-z'|}}{q_{in}} \tag{7.19}$$

where i designates the region (1 or 2) and q_{in} is the same as in section 2.

In fact the integral equation (IE) obtained from closure in region 1 remains unchanged (See Chapter 4 and Appendix C), and is given by

$$\frac{1}{2}\psi(\vec{\rho}) - PV\int_{C_p}\psi(\vec{\rho}')\frac{\partial G_1^P(\vec{\rho}|\vec{\rho}')}{\partial n'} - G_1^P(\vec{\rho}|\vec{\rho}')\frac{\partial\psi(\vec{\rho}')}{\partial n'}\,dl' = \psi_i(\vec{\rho}) \tag{7.20}$$

However, when the upper region medium is replaced with the region 2 medium and polarization currents are placed in the upper region, there is an additional planar layer (Region 3) that must be taken into account. The medium is no longer homogenous and therefore the primary Green's function does not adequately describe the induced fields. The Green's function for region 2 must be augmented to include the effects of the additional planar layer below. This can be done analytically because of the ideal geometry of the additional layer. The new Green's function (G_s) is composed of the primary Green's function and a reflected Green's function (G^r)

$$G_2 = G_2^P + G^r \tag{7.21}$$

where

$$G^r(x,z|x',z') = -\frac{j}{2L}\sum_n R_n\frac{e^{-j\beta_n(x-x')}e^{-jq_{2n}(z+z'+2d)}}{q_{2n}} \tag{7.22}$$

In this manner the problem can once again be thought of as a homogenous medium, where the reflected Green's function accounts for region 3. Therefore, the same procedure that was used in chapter 4 for the two-layer problem can be used here to obtain the other coupled integral equation.

The IE equation obtained by closure in the lower region remains unchanged in form from the two-layer problem. The Green's function kernels must be appropriately changed in the IE, which is given by

$$\frac{1}{2}\psi(\vec{\rho}) + PV\int_{C_p} \psi(\vec{\rho}')\frac{\partial G_2(\vec{\rho}\,|\,\vec{\rho}')}{\partial n'} - \frac{\epsilon_2}{\epsilon_o} G_2(\vec{\rho}\,|\,\vec{\rho}')\frac{\partial \psi(\vec{\rho}')}{\partial n'}\ dl' = 0 \qquad (7.23)$$

The derivation of the reflected Green's function is straightforward. In region 2 the homogenous Helmholtz equation must hold, and is given by

$$(\nabla^2 + k_2^2)\ G^r(x,z\,|\,x',z') = 0 \qquad (7.24)$$

Because the scattered field will be periodic in the x-direction, G^r can be represented using Floquet's Theorem as

$$G^r(x,z\,|\,x',z') = \sum_{n=-\infty}^{\infty} g_n^r(z\,|\,x',z')e^{-j\beta_n x} \qquad (7.25)$$

Substituting the reflected Green's function (7.25) into the Helmholtz equation (7.24) yields

$$\sum_{n=-\infty}^{\infty} \left\{ [\frac{\partial^2}{\partial z^2} + q_{2n}^2]\ g_n^r \right\} e^{-j\beta_n x} = 0 \qquad (7.26)$$

Using the orthogonality of $e^{-j\beta_n x}$, (i.e. $\{..\} = 0$)

$$\frac{\partial^2 g_n^r}{\partial z^2} + q_{2n}^2\ g_n^r = 0 \qquad (7.27)$$

The known general solution of the above differential equation can be simplified by the physics of the problem. The solution for the modal reflected Green's functions are given by

$$g_n^r(z\,|\,x',z') = A_n(x',z')\ e^{-jq_{2n}(z+d)} \qquad (7.28)$$

Following a similar development for the transmitted Green's function, which is located in region 3,

$$g_n^t(z\,|\,x',z') = B_n(x',z')\ e^{jq_{3n}(z+d)} \qquad (7.29)$$

The Green's functions represent the magnetic field produced by a line source. These fields must still obey the boundary conditions at the z=-d plane. The boundary conditions are given by

$$\frac{\partial G_2^p}{\partial z} + \frac{\partial G^r}{\partial z} = \frac{\epsilon_2}{\epsilon_3}\frac{\partial G^t}{\partial z} \quad ; \quad G_2^p + G^r = G^t \quad at\ z = -d \tag{7.30}$$

The unknown reflection and transmission coefficients (A_n and B_n) can be determined by applying the boundary conditions at z=-d. Substituting the definition of the Green's functions into the boundary condition equations result in

$$\sum_{n=-\infty}^{\infty}\left[\frac{-j}{2L}\frac{e^{j\beta_n x'}e^{-jq_{2n}(z'+d)}}{q_n} + A_n - B_n\right]e^{-j\beta_n x} = 0 \tag{7.31}$$

$$\sum_{n=-\infty}^{\infty}\left[\frac{-j}{2L}e^{j\beta_n x'}e^{-jq_{2n}(z'+d)} - q_{2n}A_n - \frac{\epsilon_2}{\epsilon_3}q_{3n}B_n\right]e^{-j\beta_n x} = 0 \tag{7.32}$$

The orthogonality of $e^{-j\beta_n x}$ simplifies these equations to

$$\frac{-j}{2L}\frac{e^{j\beta_n x'}e^{-jq_{2n}(z'+d)}}{q_n} + A_n - B_n = 0 \tag{7.33}$$

$$\frac{-j}{2L}e^{j\beta_n x'}e^{-jq_{2n}(z'+d)} - q_{2n}A_n - \frac{\epsilon_2}{\epsilon_3}q_{3n}B_n = 0 \tag{7.34}$$

for all n.

The two equations for each set of unknown modal reflection and transmission coefficients can easily be solved to yield

$$A_n = R_n\frac{-j}{2L}\frac{e^{j\beta_n x}e^{-jq_{2n}(z'+d)}}{q_{2n}} \tag{7.35}$$

$$B_n = T_n\frac{-j}{2L}\frac{e^{j\beta_n x}e^{-jq_{2n}(z'+d)}}{q_{2n}} \tag{7.36}$$

where R_n and T_n are given by (7.15) and (7.16), respectively.

Therefore, the reflected Green's function can be written as

$$G^r(x,z\,|\,x',z') = \frac{-j}{2L}\sum_{n=-\infty}^{\infty} R_n \frac{e^{-j\beta_n(x-x')}e^{-jq_{2n}(z+z'+d)}}{q_{2n}} \tag{7.37}$$

A coupled pair of integral equations (7.20) and (7.23) are created by enforcing the boundary conditions at the sinusoidal interface. A MoM numerical solution can be implemented by expanding surface field quantities with a pulse function basis set and point matching. The procedure for these steps are found in chapter 4, section 3.

Subsequent to the numerical solution for the surface fields ψ and $\partial\psi/\partial n$, the scattered magnetic field in the middle layer can be determined by

$$H_2(x,z) = -\int_L \left[\psi(x',z')\frac{\partial G_2}{\partial n'} - \frac{\epsilon_2}{\epsilon_o}\frac{\partial \psi}{\partial n'}\, G_2(\vec{\rho}\,|\,\vec{\rho}')\right] dl' \tag{7.38}$$

where $G_2 = G_2^P + G^r$.

The methods described above are frequency domain techniques. The desired transient response must be synthesized from a representative spectral response. This is the identical approach taken in chapters 3 and 4.

7.5 Numerical Results

The case of a sinusoidal surface (wavelength L, amplitude h) located above a perfectly conducting layer will be considered numerically. In Figure 7.2 the induced surface fields on one period of the sinusoidal surface for a near grazing (85°) TM incident plane wave is compared with the induced field when the third layer is absent. The PEC third layer is located (d/L=.1) below the non-conducting sinusoidal layer, whose parameters are L=0.1m and h/L=0.04. The additional third layer has a marked effect on the induced fields. A change in the induced surface fields will result in different scattered fields. This can be seen with frequency response of the backscattered fields shown in Figure 7.3. In this figure the parameters of the sinusoidal surface and the third layer are the same as in Figure 7.2.

In Figure 7.4 the corresponding synthesized transient backscattered fields are shown. The comparison of a PEC third layer and no third layer is shown. The effect of third layer is very evident in the additional peaks of the backscattered returns. The peaks are due to multiple reflections (trapped waves) between the sinusoidal layer and the PEC third layer. The initial return pulses are very similar for the two cases and then deviate after the 10ns point. This is expected because of the time delay of the incident pulse in traversing the middle layer.

In the final figure (Figure 7.5) the transient total scattered field (backscatter + forward scatter) in the middle layer, is depicted for the same case. Once again, the effect of the PEC third layer is seen by the enhanced returns after the initial pulse passes.

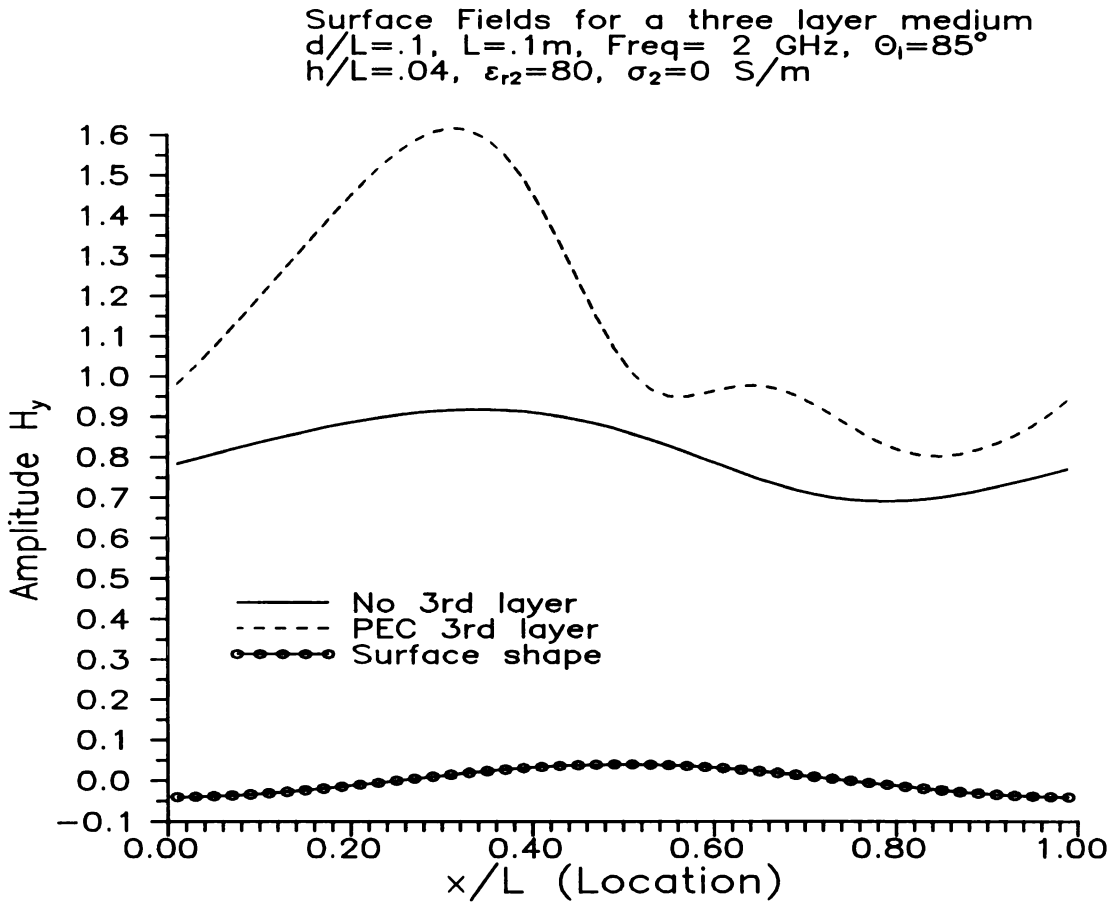

Figure 7.2 Comparison of induced surface fields for TM excitation of three layered medium where the upper layer has a sinusoidal interface (PGF IE).

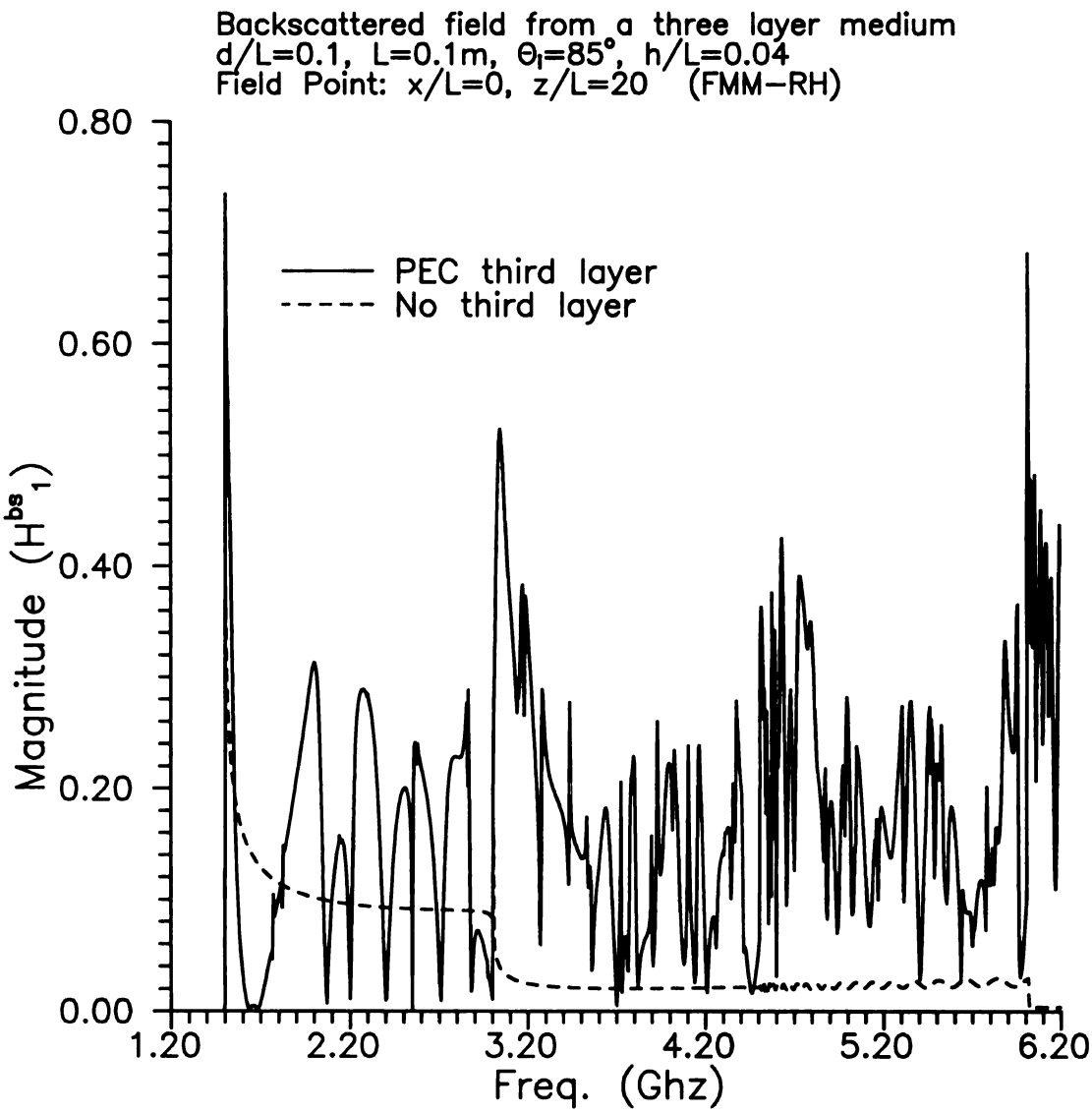

Figure 7.3 Frequency response of backscattered fields for a TM plane wave incident upon a three layer medium.

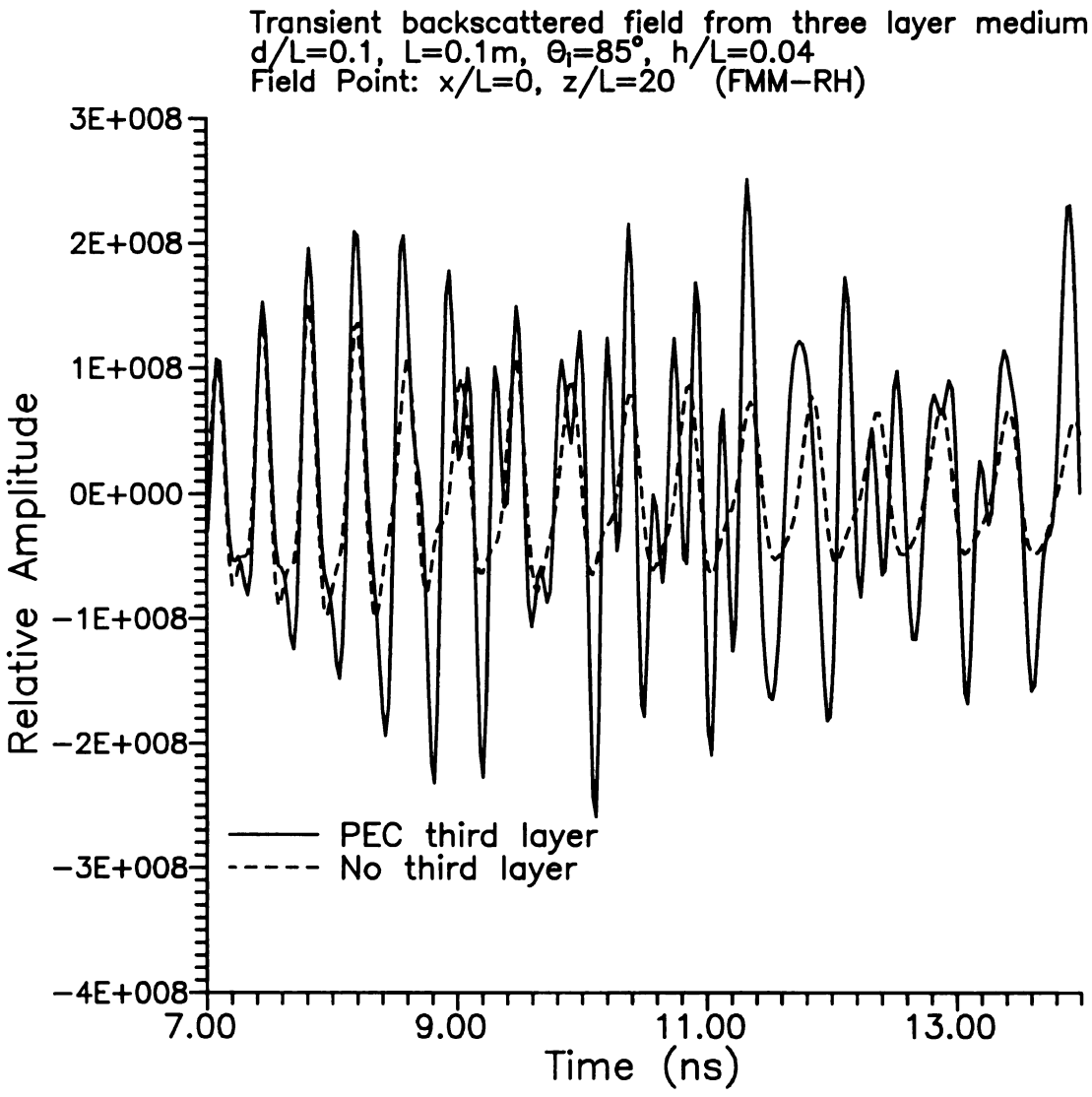

Figure 7.4 Transient backscattered fields from a three layer medium where the upper interface is sinusoidal.

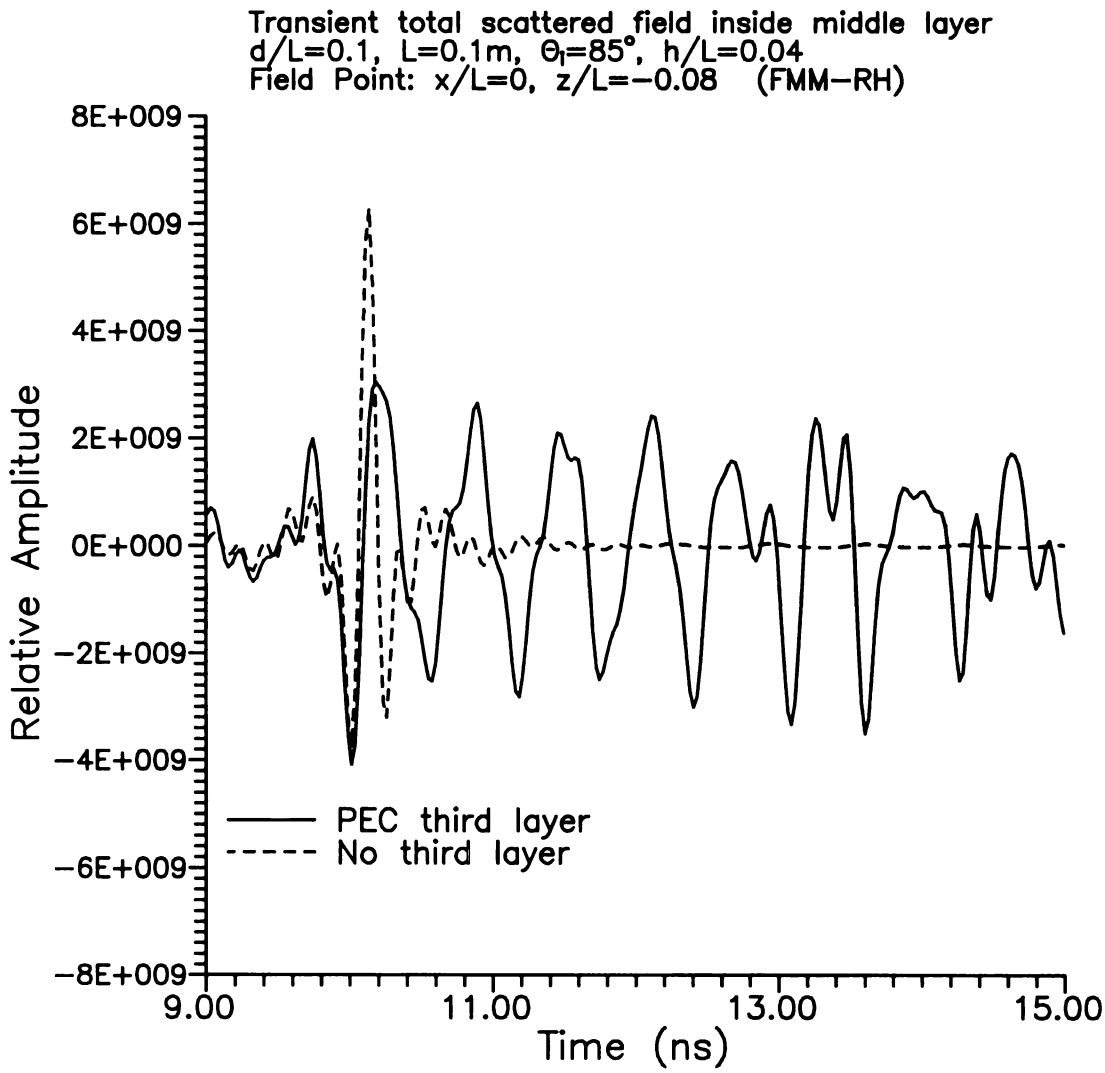

Figure 7.5 Transient total scattered field inside the middle layer of a three layer medium where the upper layer has a sinusoidal interface.

7.6 Conclusions

A number of improvements have been made concerning the theoretical scattering models. A three layer ocean model has been analysed. An additional planar layer which can be located above or below a rough periodic surface and is composed of a general homogenous medium has been added to the existing theory. This additional layer could possibly model a number of physical ocean characteristics, such as a temperature gradient layer, or salinity gradient layer, or a ducting region or even a large submerged conductor. Not only has the ocean model been improved, which will produce better results, but the possibility of surface wave (or trapped wave) propagation can now be examined. Which could shed new light on the target detection problem.

Two frequency domain methods have been employed to solve for the scattered fields from a three layer periodic medium. Both methods are direct extensions to the techniques developed for the two layer problem. The classical Floquet Mode-Matching method has been extended as well as the rigorous Integral Equation (IE) method.

Chapter 8
Conclusions and Future Study

8.1 Summary

In this thesis a basic study of the applicability of a shipboard UWB/SP radar in the ocean environment was investigated. The study was both theoretical and experimental. The experimental measurement techniques were summarized in chapter 2. A detailed survey of the measurement, calibration and post-processing methods was included along with a comparison of the time-domain and frequency-domain-synthesis measurement techniques. The experimental measurements were crucial in verifying the analytic methods.

A realistic UWB/SP radar would emit an actual transient pulse. This would be very similar to the time-domain measurement system at MSU. However, the time-domain system at MSU lacks the bandwidth a UWB/SP could attain. Therefore, a frequency-domain-synthesis measurement facility was created, which can yield the necessary bandwidth. The legitimacy of the frequency domain synthesis technique was, however, in question. The favorable comparison of the time-domain and frequency-domain-synthesis measurement techniques in this thesis was, therefore, quite satisfying.

The remaining chapters concentrated on the elucidation of electromagnetic scattering from an ocean surface. The Floquet mode-matching technique with the aid of the Rayleigh hypothesis was described in detail for use with infinite sinusoidal surfaces. Integral equation methods were also developed, in chapters 3 and 4, for use with infinite periodic and finite ocean surfaces. The numerical implementation of both methods was discussed and a wide range of results shown. The rigorous IE method was the primary choice for most applications. The FMM/RH technique provided numerous results and

served to validate the IE theory. These frequency-domain methods all required an IFFT to yield the desired transient response. The experimental measurements were compared with great success with the theoretical response from the ocean models utilized in this study.

The ocean models were chosen to systematically test the analytic techniques and to methodically increase the physical understanding. A PEC sinusoid was the starting point. The ocean model was improved to a lossy sinusoidal interface. A planar third layer was added to further improve the ocean modelling capabilities. The final and most important addition was the case of non-sinusoidal and aperiodic surfaces. The transient responses were examined in the hopes of improving the fundamental understanding and to provide possible applications of UWB/SP radar.

In chapter 6 a limited-footprint UWB/SP radar system was simulated. The incident beam was constructed from monochromatic plane waves. The construction of the illuminating beam allowed for simple use of the previously developed scattering theories and was applicable to any of the ocean surface realizations.

8.2 Major contributions and findings.

The most important and new contribution is the short-pulse transient response of these ocean-like surfaces. The underlying physics has never been examined for such excitation. Therefore, the rigorous IE method was needed to include all possible physical effects. The bulk of the analytic techniques were for the first time rigorously implemented. The earlier workers in this field had relied on numerous assumptions to decrease the numerical complexity of the problems. Analytically, the application of beam excitation to an infinite surface was a new contribution, along with the extension of the FMM/RH and IE method to two and three layer structures.

The transient responses from the ocean models revealed many new attributes associated with the short-pulse excitation. The backscattered fields were seen to be dominated by surface slope and wave crests. The resolution of the UWB/SP system

allowed for individual wave crest reflections to be seen. The larger sloped waves, such as the Stokes wave, had enhanced backscatter and multiple specular reflections. The resolution capabilities of the UWB/SP radar would also mitigate multipath effects.

The wide bandwidth of spectral response, inherent in the transient returns, provided new and interesting findings. The Floquet-mode spikes associated with periodic surfaces were unmistakable in both the theoretical and experimental results. The frequency selectivity of the total scattered field points to a possible application with target detection. A target would be illuminated by this total scattered field and its response would be affected by this selectivity.

The comparison of the various wave models was new and enlightening. The frequency and transient response from the double-sinusoid model was compared with sinusoidal, Stokes and Donelan Pierson wave models. The correlation between the frequency band and the scattered fields from the wave models were quite amazing. The lower frequencies could resolve the main swell, while the high frequencies were responsible for multiple scattering or small features.

The success of the experimental measurements and the validation of the theoretical models was a major contribution. The measurements also provided the impetus for seeking a link between the infinite and finite surface responses. The theoretical and experimental scattering from the finite surfaces were compared quite favorably with the response from an infinite surface. The beam excitation of an infinite surface was also seen to resemble the response from a finite surface.

8.3 Future research

There are numerous avenues in which these fundamental ideas can be expanded. The utilization of approximations for the theoretical methods should be examined. The results in this thesis have all been rigorous and it would be numerically prudent to research possible approximations. These approximations would also be needed if the

wave length of the ocean was to be increased. The ocean models could also be improved by including some randomness or aperiodicity.

The transient scattered fields from the ocean models are the first step in developing new target detection and identification techniques. The incorporation of a target in the scattered response is now necessary in order to proceed in developing target detection schemes. The future workers in these areas will benefit from the ideas set forth in this thesis.

Appendix A

Appendix A

Periodic Green's Function Derivation

The periodic Green's function (PGF) is defined as the solution to

$$\frac{\partial^2 G}{\partial x^2} + \frac{\partial^2 G}{\partial z^2} + k^2 G = -\sum_{m=-\infty}^{\infty} e^{-jm\beta L}\delta[x-(x'+mL)]\,\delta(z-z') \tag{A.1}$$

and consequently has the periodicity property $G(x+mL,z|x',z') = \exp(-jm\beta L)\,G(x,z|x',z')$. As a result of the latter periodicity, $G(x,z|x',z')$ has the Floquet-mode series representation

$$G(x,z|x',z') = \sum_{n=-\infty}^{\infty} g_n(x',z|z')\,e^{-j\beta_n x} \tag{A.2}$$

where the g_n are Floquet-mode amplitudes and $\beta_n = \beta + 2n\pi/L$. Since representation (A.2) has the requisite periodicity, then it is sufficient that G satisfy

$$\frac{\partial^2 G}{\partial x^2} + \frac{\partial^2 G}{\partial z^2} + k^2 G = -\delta(x-x')\,\delta(z-z') \tag{A.3}$$

in the first period $0<x<L$ of the ocean surface. Substituting representation (A.2) into definition (A.3) leads to

$$\sum_{n=-\infty}^{\infty} h_n(x',z|z')\,e^{-j\beta_n x} = -\delta(x-x')\,\delta(z-z') \tag{A.4}$$

where h_n is defined by

$$\left(\frac{\partial^2}{\partial z^2} + q_n^2\right) g_n(x',z|z') = h_n(x',z|z') \tag{A.5}$$

with wavenumber parameter q_n defined by $q_n^2 = k^2 - \beta_n^2$.

Expression (A.4) leads to

$$\sum_{n=-\infty}^{\infty} h_n \int_0^L e^{j\beta_n x} e^{-j\beta_n x} dx = -\delta(z-z') \int_0^L \delta(x-x') e^{j\beta_n x} dx \tag{A.6}$$

and exploiting the Floquet-mode orthogonality property

$$\int_0^L e^{j\beta_m x} e^{-j\beta_n x} dx = L\delta_{mn} \tag{A.7}$$

provides

$$h_n(x',z|z') = -\frac{e^{j\beta_n x'}}{L} \delta(z-z') \quad . \tag{A.8}$$

Using result (A.8) in definition (A.5) results in

$$\left(\frac{\partial^2}{\partial z^2} + q_n^2\right) g_n(x',z|z') = -\frac{e^{j\beta_n x'}}{L} \delta(z-z') \tag{A.9}$$

which is a differential equation for the Floquet-mode amplitude coefficients $g_n(x',z|z')$.

A solution to (A.9) is obtained by the Fourier transform technique, in which the transform $\tilde{g}_n(x',\zeta|z) = \mathcal{F}_z\{g_n(x',z|z')\}$, where ζ is the spatial-frequency transform variable, is introduced through the transform pair

$$\begin{aligned} \tilde{g}_n(x',\zeta|z') &= \int_{-\infty}^{\infty} g_n(x',z|z') e^{-j\zeta z} dz \\ g_n(x',z|z') &= \frac{1}{2\pi} \int_{-\infty}^{\infty} \tilde{g}_n(x',\zeta|z') e^{j\zeta z} d\zeta \end{aligned} \tag{A.10}$$

Transforming (A.9) term by term leads, subsequent to application of the differentiation theorem, to

$$-\left(\zeta^2 - q_n^2\right) \tilde{g}_n(x',\zeta|z') = -\frac{e^{j\beta_n x'} e^{-j\zeta z'}}{L} \tag{A.11}$$

Solving for $\tilde{g}_n$ and inverse transforming yields

$$g_n(x',z|z') = \frac{e^{j\beta_n x'}}{2\pi L}\int_{-\infty}^{\infty}\frac{e^{j\zeta(z-z')}}{(\zeta-q_n)(\zeta+q_n)}\,d\zeta \qquad \textbf{(A.12)}$$

where the only singularities of the integrand are simple poles at $\zeta = \pm q_n$. Here $q_n = -j\sqrt{\beta_n^2 - k^2}$ with branch cut chosen such that $Im\{q_n\} < 0$ to insure that $+q_n$ resides in the lower half of the complex ζ-plane. The integral in (A.12) can be evaluated by contour integration. Since $\exp[j\zeta(z-z')] = \exp[-\zeta_i(z-z')]\exp[j\zeta_r(z-z')]$, the real axis integration contour should be closed along an infinite semicircle in the upper half plane (enclosing the pole at $\zeta = -q_n$) for $z > z'$, leading to the residue contribution

$$g_n(x',z|z') = -\frac{je^{j\beta_n x'}e^{-jq_n(z-z')}}{2Lq_n} \quad . \qquad \textbf{(A.13)}$$

If $z < z'$, then closure should be made along an infinite semicircle in the lower half plane (enclosing the pole at $\zeta = q_n$), leading to the residue contribution

$$g_n(x',z|z') = -\frac{je^{j\beta_n x'}e^{-jq_n(z'-z)}}{2Lq_n} \quad . \qquad \textbf{(A.14)}$$

The expressions in (A.13) and (A.14) can be combined in the form

$$g_n(x',z|z') = -\frac{je^{j\beta_n x'}e^{-jq_n|z-z'|}}{2Lq_n} \qquad \textbf{(A.15)}$$

and exploiting result (A.15) in Floquet-series representation (A.2) provides the desired periodic Green's function

$$G(x,z|x',z') = -\frac{j}{2L}\sum_{n=-\infty}^{\infty}\frac{e^{-j\beta_n(x-x')}e^{-jq_n|z-z'|}}{q_n} \quad . \qquad \textbf{(A.16)}$$

An alternate derivation of the Periodic Green's Function can be found in [15].

Appendix B

Appendix B

Sea Surface Realizations

There has been, and continues to be, an enormous amount of research directed at accurately and dependably depicting ocean waves. This appendix will provide some of the details of the sea surface models employed throughout this thesis. The most primitive model is the sinusoid, this model is not only periodic, but also very smooth, with relatively small surface slopes.

The multiple sinusoid model, is also smooth and periodic, but it contains some larger surface slopes and mimics two-scale roughness. Two-scale roughness is an important feature to test the scattering theory against. Many theoretical methods use approximations that 'fall apart' when confronted with two-scale roughness.

The Stokes Wave [52] has also been extensively examined, this wave is rather smooth and periodic, but it contains extremely large surface slopes. The large surface slopes are also an important wave feature. Once again some scattering theories break down for larger surface slopes (e.g. Rayleigh Hypothesis). The Stokes wave is also a form of a cycloidal wave, and can be expressed mathematically by,

$$\begin{aligned} kx &= \beta k \sin(\theta) + \theta \\ \eta &= -\beta \cos(\theta) + \frac{2}{3}k^3(\beta - \frac{3}{8}\beta^3)^4 \cos(2kx) \end{aligned} \tag{B.1}$$

where η is the surface function (vertical displacement) and x is the horizontal displacement. θ is the parameter of this parametric curve. The β,k are wave shaping constants.

The final sea surface realization that has been considered is the Donelan-Pierson wind driven wave [53-56]. This model has been derived from actual ocean

measurements, and represents the most accurate model in consideration. The Donelan-Pierson spectrum is the spectral representation of the spatial frequencies contained in the wave, and this spectrum is dependent on wind speed.

$$f(K) = \xi(K)\sqrt{\Phi_{DP}(|K|)\,|K|\,\frac{\Delta K}{2}} + \xi^*(-K)\sqrt{\Phi_{DP}(|K|)\,|K|\,\frac{\Delta K}{2}}$$

where $\xi(K)$ is a complex Gaussian random function, with unit variance, and no correlation between disjoint spatial wave numbers (K).

The Donelan-Pierson spectrum Φ_{DP} is given by,

$$\Phi_{DP}(|K|) = \frac{1.62x10^{-3}\ \bar{U}}{|K|^{3.5}\ g^{.5}} \cdot e^{\frac{-g^2}{|K|^2\,(1.2\bar{U})^4}} \cdot 1.7^{F(\bar{U},|K|)} \cdot h \qquad \textbf{(B.3)}$$

where

$$F(\bar{U},|K|) = \exp\left[-1.22\left(\frac{1.2\ \bar{U}\sqrt{|K|}}{\sqrt{g}} - 1\right)^2\right]$$

$$K_\rho = \frac{g}{(\ 1.2\ \bar{U}\ )^2}$$

$$h = \begin{cases} 1.24 & \ldots\ 0 < |K|/K_\rho < 0.31 \\ 2.61\ (|K|/K_\rho)^{.65} & \ldots\ 0.31 < |K|/K_\rho < 0.9 \\ 2.28\ (K_\rho/|K|)^{.65} & \ldots\ 0.9 < |K|/K_\rho < 10.0 \end{cases}$$

The constants g and $\bar{U}$ are 9.81 m/s^2 and average wind speed at 10m above ocean surface, respectively.

A linear realization of the Donelan Pierson spectrum is to apply,

$$\sqrt{\Phi_{DP}(K)\ \Delta K} \qquad \textbf{(B.4)}$$

as a spatial filter to a collection of uncorrelated, unit-variance complex variables.

In Figure B.1 the Donelan Pierson spectrum (or spatial filter) is shown for a number of wind speeds. The spatial frequency K_ρ marks the peak of the spectrum. The

wind wave will be composed of an infinite continuous spectrum of spatial frequencies, but depending on wind speed the majority of spatial frequencies will come from a particular spatial frequency band. As the wind speed increases the peak in the spectrum is decreasing in spatial frequency, but is increasing in magnitude, this implies that larger wavelength and larger amplitude waves are being driven. This is consistent with practical experience; when the wind speed is low, only small ripples are seen, and as the wind speed increases larger waves appear (whitecaps).

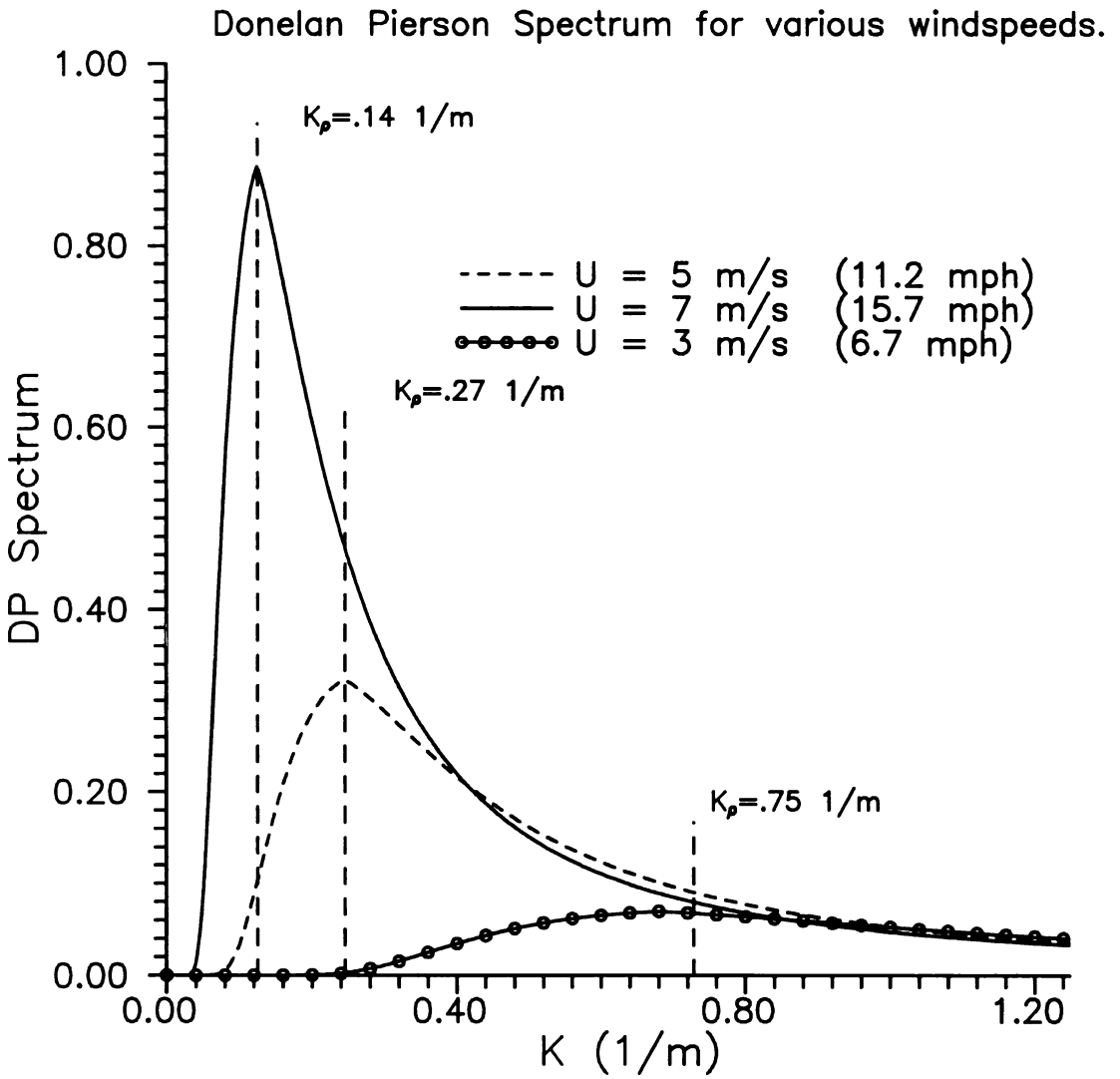

Figure B.1 The Donelan Pierson spectrum of wind driven waves for various wind speeds.

Appendix C

Appendix C

Extinction theorem integral equation formulation

This appendix provides the details for utilizing the extinction theorem in the formulation of the integral equations used throughout this thesis. This subject is covered in many graduate level electromagnetic books [49], but is included here due to the extensive reliance upon the technique.

The configuration of the two-dimensional two-region problem is shown in Figure C.1. There is a source region ($Q(\vec{\rho})$), two surface regions separated by a closed contour (C) and a small surface containing the observation point surround by C_1. Region 1 is characterized by wavenumber k_1 and the scalar wave function $\psi_1(\vec{\rho})$, while region 2 is characterized by k_2 and $\psi_2(\vec{\rho})$.

The wave function in region 1 must obey the forced Helmholtz equation due to the location of the source in region 1,

$$(\nabla^2 + k_1^2)\,\psi_1(\vec{\rho}) = -Q(\vec{\rho}) \tag{C.1}$$

The Green's function for that region can be defined as

$$(\nabla^2 + k_1^2)\,g_1(\vec{\rho},\vec{\rho}') = -\delta(\vec{\rho} - \vec{\rho}') \tag{C.2}$$

At this point the use of the 2-D Green's theorem over the entire surface area of region 1 is necessary. The 2-D Green's theorem is given by

$$\int_s (u\,\nabla^2 v - v\nabla^2 u)\,ds = \int_c \left(u\frac{\partial v}{\partial n} - v\frac{\partial u}{\partial n}\right) dl \tag{C.3}$$

By letting $u = \psi(\vec{\rho})$ and $v = g_1(\vec{\rho},\vec{\rho}')$ and utilizing equations (C.1) and (C.2), Green's theorem can be seen to yield

$$\psi_i(\vec{\rho}) = -\int_{C+C_1} \left[\psi(\vec{\rho}\,') \frac{\partial g_1(\vec{\rho},\vec{\rho}\,')}{\partial n'} - g_1(\vec{\rho},\vec{\rho}\,') \frac{\partial \psi(\vec{\rho}\,')}{\partial n'}\right] dl' \qquad \text{(C.4)}$$

where $\psi_i(\vec{\rho}) = \int_{source} g_1(\vec{\rho},\vec{\rho}\,')\, Q(\vec{\rho}\,')\, ds'$ and is the surviving surface integral. The line integral at infinity (C_∞) has no contribution due to the radiation condition.

The location of the observation point ($\vec{\rho}$) will effect the evaluation of the integral in (C.4).

$$\left.\begin{array}{ll} \vec{\rho} \in \textit{region } 1 & \psi_1(\vec{\rho}) \\ \vec{\rho} \in \textit{region } 2 & 0 \\ \vec{\rho} \in C & \frac{1}{2}\psi_1(\vec{\rho}) \end{array}\right\} = \qquad \text{(C.5)}$$

$$\psi_i(\vec{\rho}) + PV\int_C \left[\psi_1(\vec{\rho}\,') \frac{\partial g_1(\vec{\rho},\vec{\rho}\,')}{\partial n'} - g_1(\vec{\rho},\vec{\rho}\,') \frac{\partial \psi_1(\vec{\rho}\,')}{\partial n'}\right] dl'$$

where PV indicates a principal-value integration and is only needed if $\vec{\rho}$ is on C, where there is a source-point singularity.

When $\vec{\rho}$ is in region 2 there is a null field and this is known as the extinction theorem. Since there is no field in region 2 for this equivalent problem the medium in region 2 is arbitrary. Throughout this thesis region 2 is replaced with the same medium as region 1, which allows for the use of a homogenous Green's function. Equation (C.5) is also a statement of Huygen's principle.

A similar development can be followed for the fields (wave function) in region 2. In this case there is no source and therefore no incident field. The resulting integral equation for the wave function is given by

$$\left.\begin{array}{ll} \vec{\rho} \in \textit{region } 2 & \psi_2(\vec{\rho}) \\ \vec{\rho} \in \textit{region } 1 & 0 \\ \vec{\rho} \in C & \frac{1}{2}\psi_2(\vec{\rho}) \end{array}\right\} = PV\int_C \left[\psi_2(\vec{\rho}\,') \frac{\partial g_2(\vec{\rho},\vec{\rho}\,')}{\partial n'} - g_2(\vec{\rho},\vec{\rho}\,') \frac{\partial \psi_2(\vec{\rho}\,')}{\partial n'}\right] dl' \qquad \text{(C.6)}$$

Equations (C.6) and (C.5) form the backbone of the integral equation formulation used throughout this thesis. The typical application is to enforce the two equations at the sea-

surface interface (C) with the boundary conditions linking the field quantities. This results in a pair of coupled integral equations for the unknown surface field quantities.

The special case of a PEC interface decouple the equations and only requires the use of (C.5).

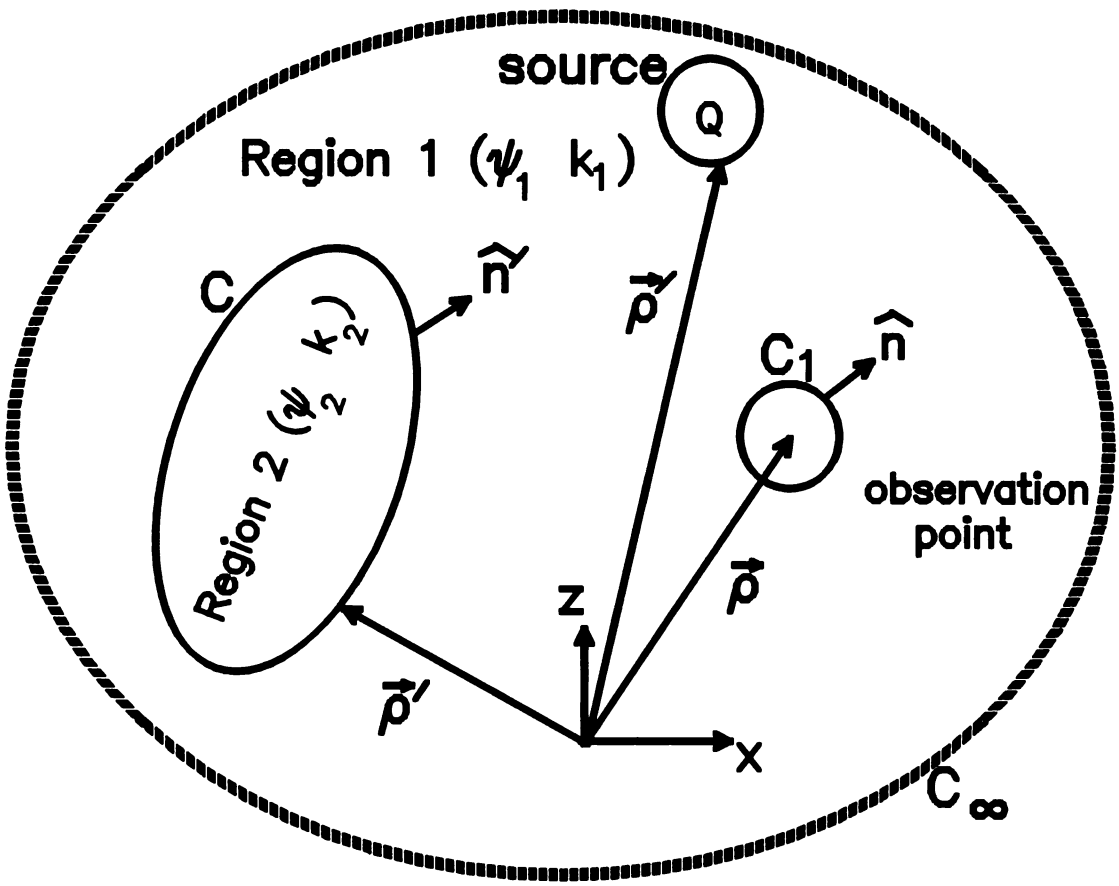

Figure C.1 Generic configuration of a 2-D two-region problem.

Bibliography

Bibliography

1. J.D. DeLorenzo and E.S. Cassedy, "A Study of the Mechanism of Sea Surface Scattering," *IEEE AP-S*, Vol. AP-14, No. 5, pp. 611-620, Oct. 1966.

2. J.W. Wright, "Backscattering from Capillary Waves with Application to Sea Clutter," *IEEE AP-S*, Vol. AP-14, No. 6, pp. 749-754, Nov. 1966.

3. J.W. Wright, " A New Model for Sea Clutter," *IEEE AP-S*, Vol. AP-16, No. 2, pp. 217-223, March 1968.

4. F.G. Bass, et. al., "Very High Frequency Radiowave Scattering by a Disturbed Sea Surface, Parts I and II," *IEEE AP-S*, Vol. AP-16, No. 5, pp. 554-568, Sept. 1968.

5. L.B. Wetzel, "A model for sea backscatter intermittency at extreme grazing angles," *Radio Science*, Vol. 12, No. 5, pp. 749-756, 1977.

6. D.E. Barrick, "First-order theory and analysis of MF/HF/VHF scatter from the sea," *IEEE AP-S*, Vol. AP-20, No. 1, pp. 2-10, 1972.

7. D.E. Barrick and W.H. Peake, "A review of scattering from surfaces with different roughness scales," *Radio Science*, Vol. 3, pp. 865-868, 1968.

8. *Ultra-Wideband, Short-Pulse Electromagnetics*, edited by H.L. Bertoni, L. Carin and L. Felsen, Plenum Press, New York, 1993.

9. *Ultra-Wideband, Short-Pulse Electromagnetics 2*, edited by L. Carin and L. Felsen, Plenum Press, New York, 1994.

10. D.R. Wehner, *High Resolution Radar*, Artech House, Norwood, Mass., 1987.

11. M.L. Skolnik, *Introduction to Radar Systems*, McGraw Hill, New York, 1980.

12. A. Ishimaru, *Electromagnetic Wave Propagation, Radiation and Scattering*, Prentice-Hall, Englewood Cliffs, New Jersey, 1991.

13. P. Beckmann and A. Spizzichino, *Scattering of Electromagnetic Waves from Rough Surfaces*, Pergamon, London, 1963.

14. A. Wirgin, "Reflection from a corrugated surface," *JASA*, vol 68, pp. 692-699, Aug. 1980.

15. J.A. Kong, *Electromagnetic Wave Theory*, John Wiley, New York, 1990.

16. R.E. Collin, *Field Theory of Guided Waves, 2nd Ed.*, IEEE Press, New York, 1991.

17. R.E. Collin, "Full Wave theories for rough surface scattering: An updated assessment," *Radio Science*, vol. 29, pp. 1237-1254, Sep.-Oct. 1994.

18. R.E. Collin, "Electromagnetic Scattering from Perfectly Conducting Rough Surfaces (A New Full Wave Method)," *IEEE Trans. Ant. Prop.*, vol. 40, pp. 1466-1477, Dec. 1992.

19. E. Bahar, "Full-Wave Solutions for the Scattered Radiation Fields from Rough Surfaces with Arbitrary Slope and Frequency," *IEEE APS.*, vol. AP-28, pp. 11-21, Jan. 1980.

20. Y. Takakura, "Rigorous integral approach to the problem of scattering from a modulated periodic medium obtained through conformal mapping," *JOSA*, Vol. 12, No. 6, pp. 1283-1289, June 1995.

21. R.H. Ott et al., "VHF radar sea scatter and propagation at grazing angles less than 1°," *Radio Science*, vol. 30, pp. 361-370, Mar.-April 1995.

22. J.A. DeSanto, "Scattering from a perfectly reflecting arbitrary periodic surface: An exact theory," *Radio Science*, vol. 16, pp. 1315-1326, Nov.-Dec. 1981.

23. J.A. DeSanto, "Exact spectral formalism for rough-surface scattering," *JOSA*, vol. 2, pp. 2202-2206, Dec. 1985.

24. G.G. Zipfel Jr. and J.A. DeSanto, "Scattering of a scalar wave from a random rough surface: A diagrammatic approach," *J. Math Phys.*, vol. 13, pp. 1903-1911, Dec. 1972.

25. J.A. DeSanto, "Scattering from a sinusoid: derivation of linear equations for the field amplitudes," *JASA*, vol. 57, pp. 1195-1197, May 1975.

26. K.A. Zaki and A.R. Neureuther, "Scattering from a perfectly conducting surface with a sinusoidal height profile: TE Polarization," *IEEE Trans. Ant. Prop.*, vol. AP-19, pp.208-214, Mar. 1971.

27. F. Schwering and G. Whitman, "Scattering by periodic metal surfaces with sinusoidal height profiles-A theoretical approach," *IEEE Trans. Ant. Prop.*, vol. AP-25, pp.869-876, Nov. 1977.

28. F. Schwering and G. Whitman, "Scattering from a perfectly conducting surface with a sinusoidal height profile: TM Polarization," *IEEE Trans. Ant. Prop.*, vol. AP-19, pp. 747-751, Nov. 1971.

29. A.K. Jordan and R.H. Lang, "Electromagnetic scattering patterns from sinusoidal surfaces," *Radio Science*, vol. 14, pp. 1077-1088, Nov.-Dec. 1979.

30. P.C. Waterman, "Scattering by periodic surfaces," *JASA*, vol. 57, pp.791-802, April 1975.

31. R.F. Millar, "On the Rayleigh assumption in scattering by a periodic surface," *Proc. Cambridge Phil. Soc.*, vol. 65, pp. 773-791, 1969.

32. R.F. Millar, "On the Rayleigh assumption in scattering by a periodic surface II," *Proc. Cambridge Phil. Soc.*, vol. 69, pp. 217-225, 1971.

33. R.F. Millar, "The Rayleigh hypothesis and a related least-squares solution to scattering problems for periodic surfaces and other scatterers," *Radio Science*, vol 8, pp. 785-796, Aug.-Sep. 1973.

34. J.L. Utresky, "The scattering of plane waves from periodic surfaces," *Ann. Phys.*, vol. 33, pp. 400-427, 1965.

35. P.M. van den Berg and J.T. Fokkema, "The Rayleigh hypothesis in the theory of reflection by a grating," *JOSA*, vol. 69, pp. 27-31, Jan. 1979.

36. P.M. van den Berg and A.T. de Hoop, "Reflection and Transmission of Electromagnetic Waves at a Rough Interface Between Two Different Media," *IEEE Trans. Geosci. Remote Sens.*, vol. GE-22, pp. 42-52, Jan. 1984.

37. J.E. Ross, "Application of Transient Electromagnetic Fields to Radar Target Discrimination," PhD dissertation, Michigan State University, 1992.

38. M.A. Morgan and N.J. Walsh, "Ultra-Wide-Band Transient Electromagnetic Scattering Laboratory," *IEEE AP-S*, Vol. AP-39, No. 8, pp. 1230-1234, August 1991.

39. M.A. Morgan, "Ultra-Wideband Impulse Scattering Measurements," *IEEE AP-S*, Vol. 42, No. 6, pp. 840-846, June 1994.

40. R.W.P King, *Theory of Linear Antennas*, Harvard University Press, Cambridge, Mass., 1956.

41. L. Carin and L. Felsen, "Time Harmonic and Transient Scattering by Finite Periodic Flat Strip Arrays: Hybrid (Ray)-(Floquet Mode)-(MoM) Algorithm," *IEEE Trans. Ant. Prop.*, vol. 41, pp. 412-421, April 1993.

42. M.E. Veysoglu, R.T. Shin, and J.A. Kong, "A finite-difference time-domain analysis of wave scattering from periodic surfaces: Oblique incidence case," *JEWA*, vol. 7, pp. 1595-1607, Dec. 1993.

43. A. Norman, et. al., "Transient scattering of a short pulse from a conducting sinusoidal surface," *JEWA*, Vol. 10, No. 4, pp. 461-487, 1996.

44. M.E. Veysoglu et al., "Polarimetric passive remote sensing of periodic surfaces," *JEWA*, vol. 5 no. 9, pp.997-1005, 1991.

45. M.E. Knotts and K.A. O'Donnell, "Multiple scatterings by deep perturbed gratings," *JOSA*, vol. 11, pp. 2837-2843, Nov. 1994.

46. R.A. Depine and D.C. Skigin, "Scattering from metallic surfaces having a finite number of rectangular grooves," *JOSA*, vol. 11, pp. 2844-2850, Nov. 1994.

47. P. Tran and A.A. Maradudin, "The scattering of electromagnetic waves from a randomly rough 2D metallic surface," *Optics Comm.*, Vol. 110, pp. 269-273, Aug. 1994.

48. R.F. Harrington, *Time-Harmonic Electromagnetic Fields*, McGraw-Hill, New York, 1961.

49. W.C. Chew, *Waves and Fields in Inhomogenous Media*, Von Nostrand Reinhold, New York, 1990.

50. A.W. Mathis and A.F. Peterson, "A comparison of Acceleration Procedures for the Two-Dimensional Periodic Green's Function," *IEEE AP-S*, Vol. 44 No. 4 pp 567-572, April 1996.

51. S. Singh and R. Singh, "A Convergence Acceleration Procedure for Computing Slowly Converging Series," *IEEE MTT*, Vol. 40, No. 1, pp. 168-173, Jan. 1992.

52. B. Kinsman, *Wind Waves, their generation and propagation on the ocean surface*, Prentice Hall, NJ, 1965.

53. M.A. Donelan and W.J. Pierson, "Radar Scattering and Equilibrium Ranges in Wind-Generated Waves with Application to Scatterometry," *JGR*, Vol. 92, No. C5, pp. 4971-5029, May 15, 1987.

54. C.L. Rino, et. al., "Numerical simulation of backscatter from linear and nonlinear ocean surface realizations," *Radio Science*, Vol. 26, No. 1, pp. 51-71, Jan. 1991.

55. B.J. West, et. al., "A New Method for Surface Hydrodynamics," *JGR*, Vol. 92, No. C11, pp. 11803-11824, Oct. 15, 1987.

56. S.L. Broschat, "The Phase Perturbation Approximation for Rough Surface Scattering from a Pierson-Moskowitz Sea-Surface," *IEEE Geoscience and Remote Sensing*, Vol. 31 No. 1, pp. 278-283, Jan. 1993.

57. S.T. Peng, T. Tamir and H.L. Bertoni, "Theory of Periodic Dielectric Waveguides," *IEEE MTT*, Vol. MTT-23, No. 1, pp. 123-133, Jan. 1975.

58. R.A. Paulus, "Evaporation Duct Effects on Sea Clutter," *IEEE AP-S*, Vol. 38, No. 11, pp. 1765-1771, Nov. 1990.